A Quasi-Real-Time Inertialess Microwave Holographic Imaging System

by

C.S.Nilsen, M.Sc.

A Thesis submitted for the degree of Doctor of Philosophy
University of Cape Town
October 1980

ERRATA

Page 6, line 1 : For "Artic" read "Arctic"

" line 18 : For "(35,37)" read "(35-37)"

Page 7, lines 5 & 6 : For "the aperture is normal to the object plane" read "the plane of the aperture, while parallel to the object plane, is displaced from the latter along the direction of their common normal".

Page 10, line 19 : For "signal-to-raise" read "signal-to-noise"

Page 11, line 15 : For "Ghz" read "GHz"

Page 17 : In equation 3.2 and the following equations, a (constant) factor, e^{j2kz}, has been omitted.

Page 25 : Equation 3.29 should read : "$\Delta z = 2(\lambda z^2/L^2)$"

Page 26, last line of second paragraph : Delete "(greater)"

Page 30, line 12 : For "as close as to" read "as close to"

Page 62, 6 lines from bottom : For "date" read "data"

Page 72, line 2 : For "lease" read " least"

Page 111, second last line : Delete "maximum". For "preceeds" read "precedes"

Page 118, line 8 : For "disributor" read " distributor"

Page 124, line 5 : In ref. 31, "vol. 59" should be "vol. 57"

Passim : For "Raleigh" read "Rayleigh"

" : For "mS" read "ms" (milliseconds)

ACKNOWLEDGMENTS

The author acknowledges the assistance and cooperation of the following persons in the execution of the work reported in this thesis:

Professor N.C. de V. Enslin, Head of the Department of Electrical Engineering at the University of Cape Town, for the research and workshop facilities made available,

Professor J.L.N. Besseling for his supervision and encouragement latterly,

Mr. Frans Weehuizen for the availability and maintenance of computer facilities,

Mr. W. Meissner of Plessey (S.A.) for the donation of several microwave klystron sources,

Mr. Philipp Wagner for his assistance with the array antennae,

Mr. P. Pare for his help in developing computer data logging techniques and in performing a survey of the antenna arrays.

In addition, the author wishes to record here his appreciation of the guidance and supervision of Dr. D.N. Swingler, his former supervisor, both during and after the period of the latter's association with the University of Cape Town. He is especially appreciative of the recent opportunity made available to discuss this work.

Experimental results from an early version of the microwave imaging system considered in this thesis were reported in the following publication:

C.S.Nilsen and D.N.Swingler, "Quasi-real-time inertialess microwave holography", Proc.IEEE, vol.65, pp.491-492, March 1977.

SYNOPSIS

This thesis records the theoretical analysis and hardware development of a laboratory microwave imaging system which uses holographic principles. The application of an aperture synthesis technique and the electronic commutation of all antennae has resulted in a compact and economic assembly which requires no moving parts and which, consequently, has a high field mapping speed potential.

The relationship of this microwave holographic system to other established techniques is examined theoretically and the performance of the imaging system is demonstrated using conventional optically- and numerically-based reconstruction of the measured holograms.

The high mapping speed potential of this system has allowed the exploitation of an imaging mode not usually associated with microwave holography. In particular, a certain antenna array specification leads to a versatile imaging system which corresponds closely in the laboratory scale to the widely used synthetic aperture radar principle. It is envisaged that the microwave holographic implementation of this latter principle be used as laboratory instrumentation in the elucidation of the interaction of hydrodynamic and electromagnetic waves. Some simple demonstrations of this application have been presented, and the concluding chapter also describes a suitable hardware specification.

This thesis has also emphasised the hardware details of the imaging system since the development of the microwave and other electronic components represented a substantial part of this research and because the potential applications of the imaging principle have been found to be intimately linked to the tolerances of the various microwave components.

CONTENTS

CHAPTER 1

Introduction to Quasi-Real-Time Inertialess Microwave Holography

The aquisition of information pertaining to an object via an image obtained by electromagnetic remote sensing is a common requirement and a variety of techniques is applicable in various wavelength regions of the spectrum. This thesis is concerned with the practical development and hardware deployment of a high speed synthetic aperture imaging system which utilises specifically holographic techniques in the microwave region.

Holography, first described by Gabor in 1948[1], is a two-step process, in which an image is rendered from an intermediate recording of a wavefront in the object diffraction field. A recording of such a field wherein both phase and amplitude are preserved, is a hologram, and is generated by the interference between the object wave and a reference wave. In some cases the reference wave is available as a separate wavefront, but it may also be synthesised by the recording process. The hologram, whether derived from electromagnetic or mechanical radiation, is usually understood to be a planar or quasi-planar map. Holograms are characteristically diffuse recordings as there is in general no one-to-one correspondence between object and hologram detail and potentially three object dimensions are accomodatable in two hologram dimensions.

In the microwave domain, holograms may have physical existence as analogue recordings or may be no more than temporary data maps stored in memory devices. A great number of competing techniques is available in the microwave domain for the recording of the hologram, but all must in some way generate a two dimensional, and often planar, map. The two map dimensions are usually spatial, but there are techniques on the fringes of microwave holography using temporal[2,3] and spectral[4,5] properties of the radiation to synthesise the

second dimension. A hierarchy of microwave holographic mapping within general microwave imaging (Fig. 1.1) is given together with an indication of the applicable technology.

Continuous two dimensional object field maps are possible using thermographic techniques [6,7], typically with liquid crystal panels, but the majority of reported examples have been sampled holograms. Some form of data sampling is obviously a prerequisite for any computer-based numerical reconstruction.

Large areal arrays of transmitting or receiving sensors[8] may be used to define the required hologram aperture, but such schemes, although possessing the great advantage of high mapping speed potential, may be impractical economically or may pose data collection problems. Such arrays appear to be more a feature of acoustic holography [9,10] than of practical microwave holography. The aperture need not always be completely filled on a regular matrix, but may be judiciously and effectively pruned by random element removal; this approach has been suggested by Steinberg [11,12] for a "radio camera" optimised for very high angular resolution.

Serial or sequential data collection may be admissible given a sufficiently stable object environment, and in such cases a single transmitting, a single receiving, or a combined transmit-receive sensor (the latter possessing an enhanced resolution capability) may be scanned over the required aperture. [13-26] This aperture is commonly covered by either raster or rotationally symmetric scan formats. A variant of this scheme employs field perturbation devices, either physically scanned (such as the spinning dipole system[27,28] or as panels of solid state [29] or plasma tube [30] modulators. The characteristic modulation impressed on the object field is remotely retrieved by a single sensor. Such schemes tend to be more economic than microwave sensor arrays, although their sensitivity may not be as good. Where speed requirements militate against point-by-point field sampling,

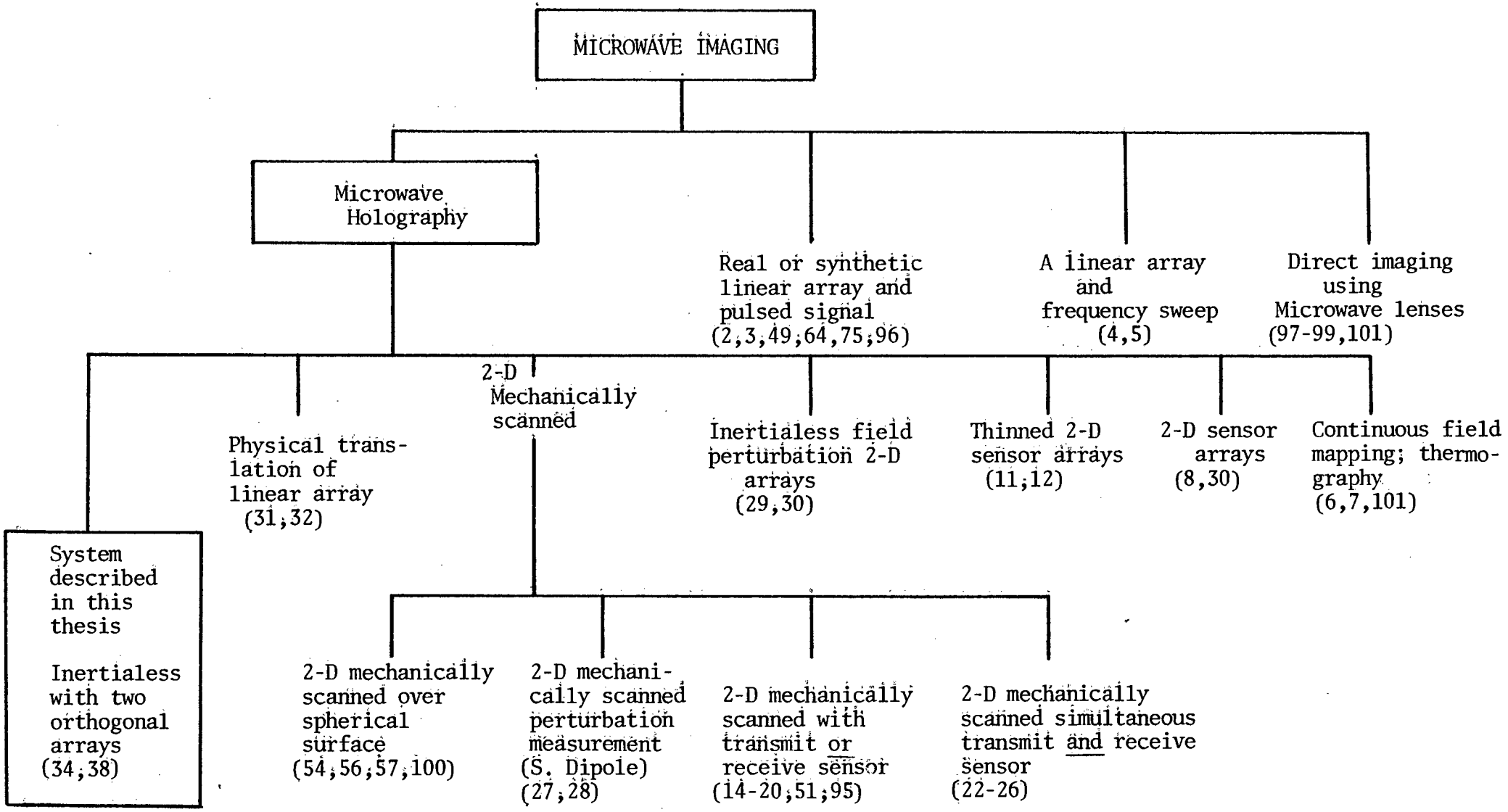

Fig. 1.1 A Hierarchy of microwave holographic imaging

the translation of a linear array of sensors (receiving or transmitting) over a baseline normal to the array long axis allows the synthesis of an aperture whose area is the product of array length and its displacement. [21,31,32]

The requirement of array movement may be eliminated if two mutually orthogonal linear arrays of complementary (that is, transmitting and receiving) sensors are used instead. Such an arrangement is used in the imaging system described in this thesis, and it synthesises an aperture equal to the product of array lengths and is sampled at intervals determined by the sensor distribution in their respective axes. It has the great advantage of synthesising an areal array of N^2 sensors whilst using only two arrays of N elements each. The resulting crossed-array detector is physically similar to the Mill's cross antenna [33] used in radioastronomy, and it was described by Wells [34] in 1970 as a potentially very high speed holographic system which required no moving parts. Both mono- and multiple-frequency variants have been proposed for acoustic imaging purposes [39-41], and a few examples of microwave versions have been reported. [35-38] The discrete nature of the synthetic aperture realised in this system is inherently suited to computer-based data capture and to the subsequent image reconstruction process, and the choice of antenna spacing allows a tradeoff to be made between the unambiguous field of view and the lateral image resolution. The reference wave function is synthesised by the scanning operation and its parameters are readily adjustable so that the offset [21] reference wave technique of Leith and Upatniek can be simulated.

A significant variant of this crossed array technique is that described by Ogura and Iizuka. [42-45] Two complementary sensor arrays, both linear, are mutually separate and are coaxially mounted, and are combined in a system optimised for high range resolution. A notable system feature was the irregular (quadratic) antenna spacing which naturally coded the incident wavefront in a form more suited to reconstruction.

The high range resolution was attained at the expense of resolution in the other axis, and it compared favourably with the range resolution attainable by more traditional pulsed techniques yet used essentially monofrequency transmissions. Their technique is only quasi-holographic, as three dimensional imagery is not immediately possible. As such it might be compared with other quasi-holographic techniques, such as synthetic aperture radar [46] and the implicit pulsed technique described by Karg.[2,3] In the latter, a one dimensional array (itself created by aperture synthesis) generates line holograms corresponding to planar object sections at a number of different wavelengths. The series of two dimensional images reconstructed from the line hologram sequence is summed and the resulting composite image has a depth resolution commensurate with the total bandwidth used .

Farhat [4,5] has proposed a swept frequency imaging system. Under certain conditions, the object diffraction field is a simple function of frequency. A linear sensor array samples the object wave at the various frequencies and a hologram axis is synthesised normal to the sensor array by the process. The hologram data can be formatted for either optical or digital computer-based reconstruction.

Early applications of microwave holography were largely confined to the demonstration of systems for imaging of objects obscured by optically opaque dielectric media.[6,18,20,21,28,47,48] A notable and very successful exception has been synthetic aperture radar (SAR), initially developed in the early 1950's [46,49], but, as previously noted, quasi-holographic in character. A true holographic version of this system was demonstrated by Larson [31,32]. A linear microwave mixer (that is, receiving) array fixed beneath an aircraft at right angles to the flightline generated a strip hologram which yielded terrain imagery on reconstruction. The aperture synthesised in the flight path direction was governed by the system "footprint" in the normal SAR manner. The reconstruction

process generated a planar image, but a technique derived from microwave holographic interferometry [18,50-52] was optionally used to superimpose contours on the image. [32]

The increasing specification of near-field measurements for the derivation of far-field radiation patterns of radio and radar antennae is a process amenable to holographic insight and is being actively developed. [53-57]

Regarding the record of differential phase shifts (measured at a ground station) between two harmonically related continuous wave transmissions from a navigation satellite as a one dimensional complex hologram has allowed Schmidt and Tourianen [58] to image ionospheric irregularities. Their technique treated the lower frequency emission as the object wave. The higher frequency emission was regarded as a reference wave which was assumed to have been little perturbed in the ionospheric transit.

Path profile in microwave communications links can be inferred from so-called height-gain data using holographic interpretation[59,60,86]; the Fresnel zone field resulting from the obstacles between the link terminations is treated as an interference pattern generated by the interaction of the direct (reference) wave and an object wave scattered by the obstacles.

An example of a remote label reading system proposed and demonstrated by Constant [61] is entirely holographic in concept, although it was explained in pulse compression terms. A one dimensional synthetic aperture is generated by the uniform relative motion of a wayside transmitter-receiver interrogator unit and a vehicle mounted label binary encoded with an imprinted dipole resonator sequence. The sensor output is processed by a pulse compression filter, and the compressed data constitutes a line image of the label.

A coaxial array synthetic aperture variant of the system considered in this thesis was developed as a precision ranging system, and it was intended for the airborne continuous

evaluation of ice thickness in the Canadian Artic; it was designated HISS. (Holographic Ice Surveying System)[42-45,62] The reconstruction of the profile found beneath the helicopter radar platform was based entirely on numerical techniques and a special purpose computer was evolved to match the displayed ice profile to the speed of flight.

The orthogonal linear array aperture synthesis scheme was conceived and developed as a high-speed sonar holographic mapping system. Wells [34] considers a fundamental limitation due to the interaction of sensor sampling rate and the characteristic velocity of propagation of radiation in the medium, an effect which hampers other acoustic synthetic aperture sensors as well. [63] This effect is, however, quite insignificant in the electromagnetic domain and in the context of the envisaged applications. Although some simulations, using both monofrequency and wide spectrum radiation have been reported [39-41], there have been few microwave hardware interpretations of this orthogonal array concept.[35,37] Quite apart from the hardware economy (witness N^2 field samples available from only 2N sensors at a single frequency), the property of physical orthogonality leads to simplified image reconstruction algorithms, which are usable not only in the limit of large object ranges.

The system described in this thesis implements the orthogonal array concept as a crossed array in the microwave domain and has been exercised in the conventional imaging modes using both optically- and numerically-based reconstruction procedures. The advent of computer-based reconstruction has had profound implications for the hardware specification and the design of microwave holographic equipment. Obtrusive signals (such as the unwanted signals arising from the direct transmission between sensors of the transmitting and receiving arrays) and hardware systematic errors can in many cases be compensated, and one such technique , reported herein, was routinely used to improve the dynamic range performance.

A variant of the quasi-planar imaging mode (very similar to that used in synthetic aperture radar [64]) has also been demonstrated. In contrast to Larson's holographic radar[31,32] in which the hologram aperture was approximately coplanar with the object terrain, the aperture is normal to the object plane. The illumination mode is similar to that used in SAR, and the system has the decided advantage, in comparison with SAR, of range resolution which improves with reducing range; a secondary advantage is the relative freedom from spurious image artifacts introduced by certain hardware errors.

The high speed hologram recording property has been used to attempt the imagery of object scenes in linear motion. The motivation for this mode of operation is found in the very significant and growing interest attached to the remote sensing of many aspects of sea state via various electromagnetic probes, [68-71,75-84] of which the SAR sensor is of major importance. The complexity of the interaction between hydrodynamic and electromagnetic waves suggests controlled laboratory-scale experiments for testing theoretical models [85], and in particular a sensor which can mimic the SAR mode of operation is clearly required. The effects of object motion on SAR imagery have been widely reported [65-74], and a similar approach has been invoked to explain image modulation arising from object motion in the orthogonal array microwave holographic system.

It would appear that microwave holography is a suitable instrumentation tool for the laboratory evaluation of the wave-wave phenomena and that, as an example, given reasonable hardware and reconstruction process linearity, object doppler information is available. Object scenes such as those found in wind/wave tanks are intrinsically quasi-planar and microwave holography can offer useful range and azimuthal resolution without having to refocus antennae mechanically or having to resort to extreme transmission bandwidths. The crossed axis version of the orthogonal array concept is particularly suited

as a wave-wave probe, and a hardware specification has been suggested which both optimises its simulation of the SAR process and also results in a simpler microwave assembly, without compromising its performance as a conventional imaging system. The upper limits to scanning speed using the inertia-less crossed-array system are set only by hardware and ultimately economic limitations, and the system is sparing in the use of such hardware.

CHAPTER 2

2.1 Hardware Implementation of Inertialess Microwave Holographic Imaging System

Wells [34] has regarded the orthogonal array imaging system as an example of two-dimensional aperture synthesis using one-dimensional arrays. The operation of this system can be illustrated by a phased array analogy. A conventional phased array radar has access to individual elements of the transmitting and receiving arrays and would assign programmed phase shifts to these elements. The intersection of the respective beams, focussed at the same distance, would define both the position and spatial resolution of an image point. (Fig.2.1) The phased array performs the imaging process in a single stage. A simpler holographic implementation realizes the same imaging principle by á posteriori manipulation of data gathered using only two elements of complementary type at a given moment. Holographic imaging is the result of a two stage process, and the necessary beamforming is performed in the latter reconstruction stage.

The hardware required for the holographic system is intrinsically quite modest. If it assumed that elements of both receiving and transmitting arrays can be arranged, selected and activated in some known sequence, and that these elements are only accessible to the peripheral microwave circuitry via one port on each array, then just one source and one detector are required. It is preferable that the detection circuitry be capable of representing the received signal in complex notation. The subsequent image reconstruction procedure can be performed by both direct computation and analogue means, [8,14,17,24,31,32,47,87,88] the most common example of the latter being coherent optical processing.

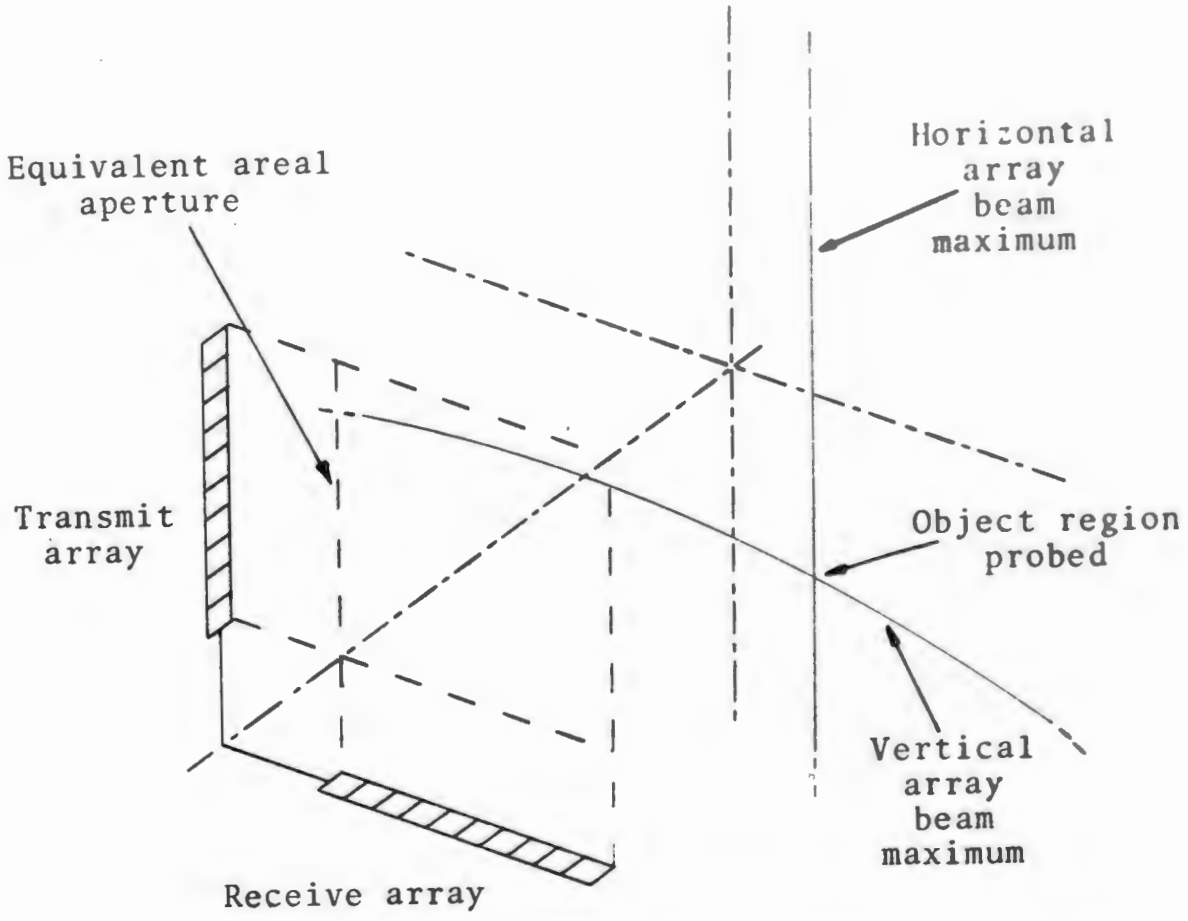

Fig. 2.1 Simplified Imaging Analogy

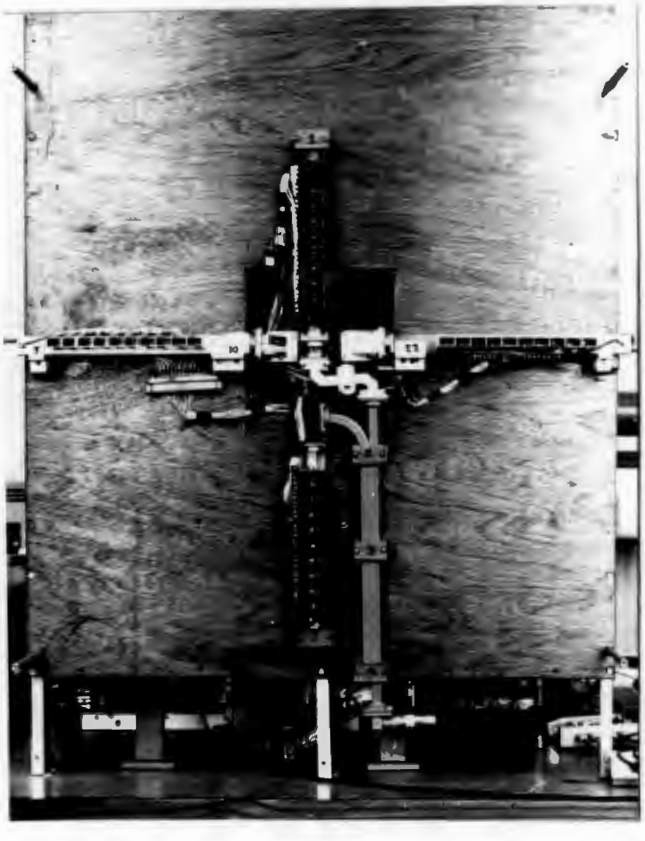

Fig. 2.2 Front view of prototype microwave arrays

2.2 Array Realisations

The orthogonal array technique requires that a number of antennae be available disposed as two linear arrays, and that synchronous detection of the signal received with all possible pairs of transmit and receive antennae, used in sequence, yields the required hologram data. The practical implementation of this microwave hologram system requires a simple, repeatable and economic array antenna design. It is further convenient if a prototype array can be equally well operated in transmitting or receiving mode for the purposes of testing and calibration.

Array designs reported in the literature include equally spaced antennae commutated by cascaded mechanical waveguide switches arranged in binary sequence [35], and electronic PIN diode switches [44]. The former is regarded as a form of inertialess holographic system in that there is no physical transport of an antenna in the field mapping process; however, mapping rates can be ultimately inertially limited rather than by any consideration of adequate signal-to-raise ratio.

A significant and potentially very useful variant, applicable to a receive array function, uses separate microwave mixers with individual antennae [32]. Reference wave distribution to every mixer of the array at a frequency offset from that of the source raises the possibility of individually correcting receive channel amplitude and phase errors by purely hardware means at the intermediate frequency. Such a provision is particularly useful if reconstruction techniques are confined to those possible using analogue optical processors, but reconstruction schemes based on the digital computer afford relatively easier compensation of receiver errors particularly if the hologram data is available in amplitude and phase format.

The transmitted power would ideally follow one path from source to selected antenna, as in [35] and [44], but practical consideration of component availability and economics have dictated a less efficient approach leading to power levels at each antenna much below that of the source.

2.3 Array Design

A slotted waveguide radiator, as used extensively in radar systems [89], was selected as a basic signal distributor. Individual stub waveguides in front of each slot enclosed diode switch elements and in addition served as polarising filters. An antenna spacing of less than one free space wavelength was deemed necessary and slot spacing was chosen as 20.2mm. The waveguidelength was double this value, 40.4mm, and the free space wavelength of 30.3mm corresponded to 9.9Ghz. The waveguide distributor was designed as a resonant array as this promised straightforward establishment of equal slot power densities and (ideally) zero relative phase shift between slots. 20 elements were incorporated in each array. (Fig.2.2)

The arrays, although spatially orthogonal, had to be co-polarised. As standard X-band waveguide has outside dimensions of 12 x 25.4mm, it was necessary to fabricate a special reduced cross-section waveguide of internal width 18mm. The closeness of this dimension to the cut-off dimensions of 15.2mm at the chosen wavelength necessitated close machining tolerances to avoid excessive antenna relative phase errors. These reduced-section elements were incorporated in the horizontal array seen in Fig.2.2.

Low transmitted power levels (of the order of a few milliwatts) did not justify PIN diode switches, and cheap, low capacitance germanium small signal diodes were used in each element as shunt switches. A useful feature of the switch design was the very low power consumed in the "OFF" or zero transmission state, since any element is inactive 95% of the

time in a twenty element array. The diode parisitic capacitance (about 0.2pF) in reverse biased condition and the package inductance formed a series resonant circuit shunting the waveguide.

A slight improvement in antennae isolation (that is, "OFF" state transmission) and a great improvement in system sensitivity was effected by "marking" each active antenna with a square wave tone unique to that axis; the received signal components at the sum of the two modulation frequencies were recovered by post-mixer synchronous detection. The two frequencies used were 148.327 kHz and 188.601 kHz and were derived from oscillators controlled by available crystals. (Fig. 2.3) The bandwidth required at the sum frequency (336.928 kHz) as a result of the selected antenna commutation rate was not encroached by any harmonic of the two modulation frequencies.

The arrays were developed as four separate ten-element subarrays (Fig. 2.2) and signal combination in each axis was by a 3dB directional coupler (Fig. 2.3). A travelling wave amplifier of 27dB gain was interposed in the path between receive array combiner and mixer.

A klystron source at 9.9GHz developed approximately 200mW when operated with forced air cooling and substantially above its rated anode and reflector voltages. Two isolators and a reference directional coupler preserved spectral monochromaticity of the source and reference signal as the transmitting array was switched and tone modulated.

2.4 Received Signal Hardware Processing

Synchronous detection at 9.9GHz of the amplified receive array output required two balanced mixers with reference inputs equal in magnitude and in phase quadrature. Typical

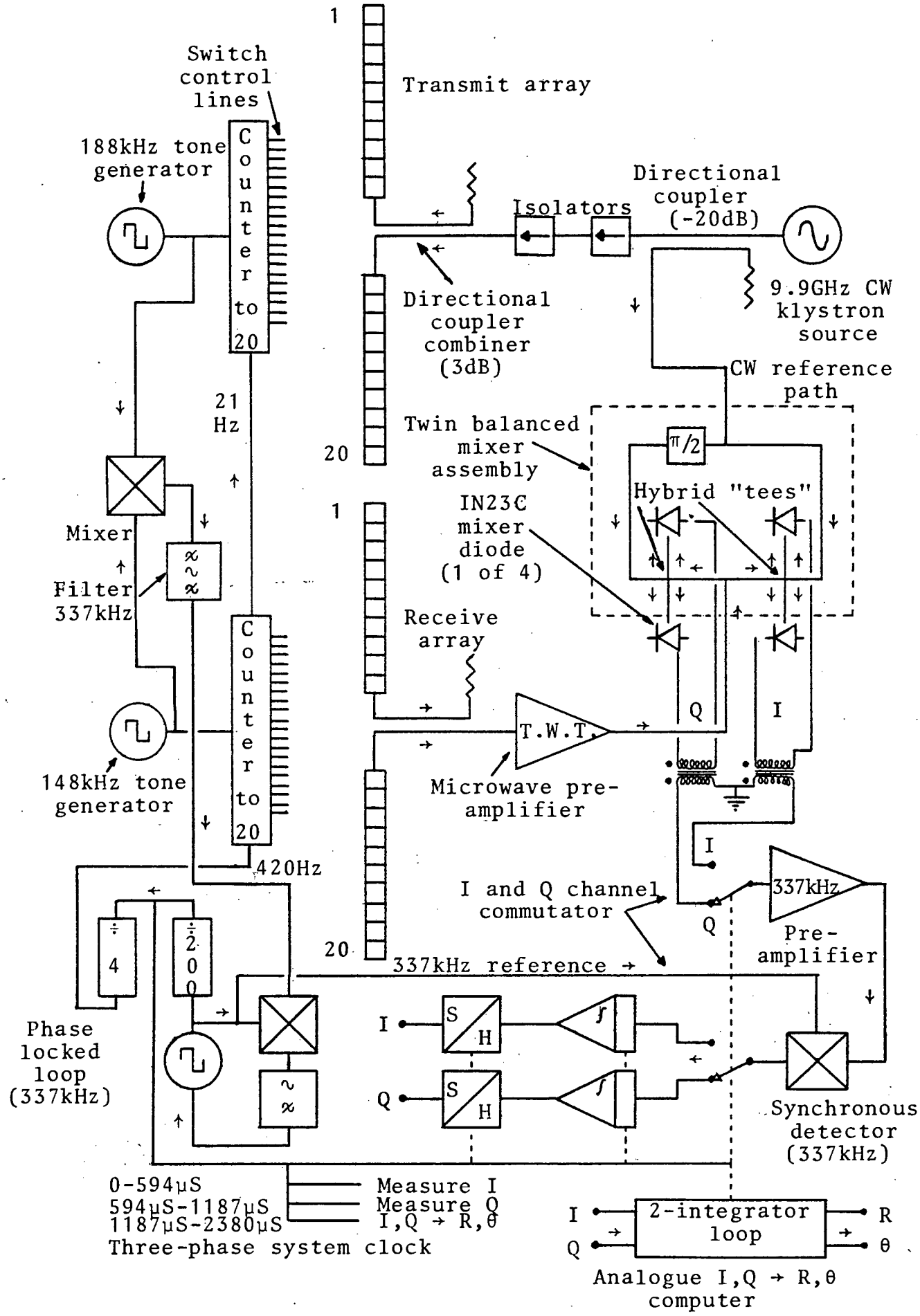

Fig. 2.3 Simplified microwave and low frequency processing

mixer outputs of a few tens of microvolts at the selected sum frequency of 336.928kHz were boosted by a narrow band tuned amplifier. A feature of the system was the commutation of this amplifier between mixer outputs so that any transfer function tracking problems possible in a two channel system were sensibly eliminated.[90]

The inphase and quadrature (hereafter I and Q respectively) components at the sum frequency were recovered by synchronous detection.

The time epoch allocated to a particular component of the signal received from a given transmit and receive antenna pair was known, and since the received signal suffered essentially no delay, it was a simple matter to incorporate a pair of operational integrators, switched in sequence, to realize a matched filter function.

Additional circuitry comprised sample and hold devices to memorize I and Q components between commutation intervals and circuitry to recognize the beginning of an array commutation sequence and to signal the computer external interrupt facility to begin analogue to digital conversion and storage of the I and Q components. These were represented as 12 bit numbers, including the sign. Data handling was via an assembler language program linked to a higher level language program used for image reconstruction purposes.

The time taken to acquire 400 pairs of I and Q components was arbitrarily selected very early in the development program as approximately 1 second, the time allocated to each antenna pair being thus 2.38mS. This period was further divided into four parts. Two initial periods of about 600μS each were allocated to estimation of the I and Q components, in that sequence, and the remaining time was intended for analogue computation of the polar (that is, amplitude and phase) representation of these components.

In the event, and in the presence of significant amplitude signal components arising from direct coupling between transmitting and receiving antennae, unwanted background signals and constant I and Q offsets arising in the commutation and synchronous detection process, it proved more useful to assemble the useful hologram data instead after two passes; that is, with the object introduced only in the second pass. This (subtractive) mode allowed clearer imagery of smaller objects in considerable clutter. The clutter level was such that there was usually no detectable change in signal levels monitored in phasor representation on an oscilloscope when the object was introduced.

An analogue polar-coordinate computer was incorporated (Fig.2.3) which took the I and Q components as inputs and delivered output voltages proportional to amplitude and phase of the (complex) received signal. It was little used for imaging purposes, but was useful in preliminary testing of subarrays and in general testing of microwave components whenever unambiguous phase data (over 2π radians) was required. Other examples of its use were the location of subarray elemental radiators' phase centres and the evaluation of helical antennae characteristics reported in Appendix II. An investigation of microwave tomography (Appendix III) was also made possible using this processor.

The "marking" or modulation of the individual array antennae was used in the measurement of antennae phase and amplitude errors. This investigation was carried out as part of an undergraduate project using computer acquisition of data. Prior to this investigation, individual subarrays had been tested using the analogue computer. In these investigations, an unmodulated source illuminated an object consisting of a high gain exponentially flared horn antenna having as termination a germanium diode shunt switch backed by a short circuit one quarter waveguidelength behind the plane of the diode. The diode was switched between "ON" and "OFF" states

and reflected incident continuous wave radiation as an essentially double sideband (suppressed carrier) signal. The array under test was used as a receiver and commutated in the normal way with a "mark" frequency complementary to that used by the reflective object, such that the received signal was characterized by modulation, at inter alia, the required sum frequency of 336.928kHz. Reflections from objects other than the reflective "cooperative target" were ignored by the processor due to their lack of temporal modulation, and effective measurements of the array errors could be made in an environment far from anechoic. Similar techniques are standard in field perturbation measurements using microwave homodyne illuminator and detector instrumentation. [91-93]

A simpler microwave configuration was used to measure the phase centreposition, in both polarisations, of the radiator designs selected for transmit and receive elements. This information was then used to predict wavefront curvature across the array in various geometries. A least squares fit of this prediction to temporally averaged measured data was the basis of the undergraduate investigation. [38]

The measured systematic amplitude and phase errors of the array antennae were found to be of a satisfactorily low level so that error correction was not deemed necessary in the processing of data leading to the imagery presented in this thesis.

A most useful feature of the holographic system was the facility with which component evaluation could be performed once the basic source and two channel mixer and associated signal processor were available. Using simple reflective switches and little other hardware most of the functions of a microwave network analyser (which was not available) could be simulated, albeit at a single carrier frequency.

CHAPTER 3

3.1 The Theory of the Technique

This chapter describes the theoretical basis of the orthogonal array imaging system. The imaging process is initially examined using the simple Fresnel paraxial field descriptions and the spatial resolution attainable in all axes is derived. The use of the simplest reconstruction process may produce characteristic image distortion if applied indiscriminately, and a more accurate reconstruction process is appropriate in these cases.

Practical considerations dictate that the arrays consist of discrete antenna elements, and the resulting sampled holograms impose certain limits to the object regions unambiguously accessible to the system. The object region accessibility is found to depend also on the choice of reconstruction process.

It is found possible to manipulate the form of the reference wavefront synthesised in the imaging process by controlling array antenna spacing and a series of simulations demonstrating this property is presented.

3.2 Hologram Formation

The holographic recording system and object geometry are shown in Fig. 3.1. The object is assumed to be quasi-planar and is conventionally described by a reflectance function $A(u,v)$. The object is distant z from two spatially orthogonal arrays of transmitting and receiving antennae. It is assumed that the antenna arrays are continuous and that the measurement of received signal amplitude and phase is made using continuous wave radiation. A transmitting element at y illuminates the object plane while the receiving array maps the reflected field in the other axis. The received signal is a phase-shifted and amplitude attenuated sample of the transmitted continuous wave signal. The total phase shift from source to the phase and amplitude receiver is:

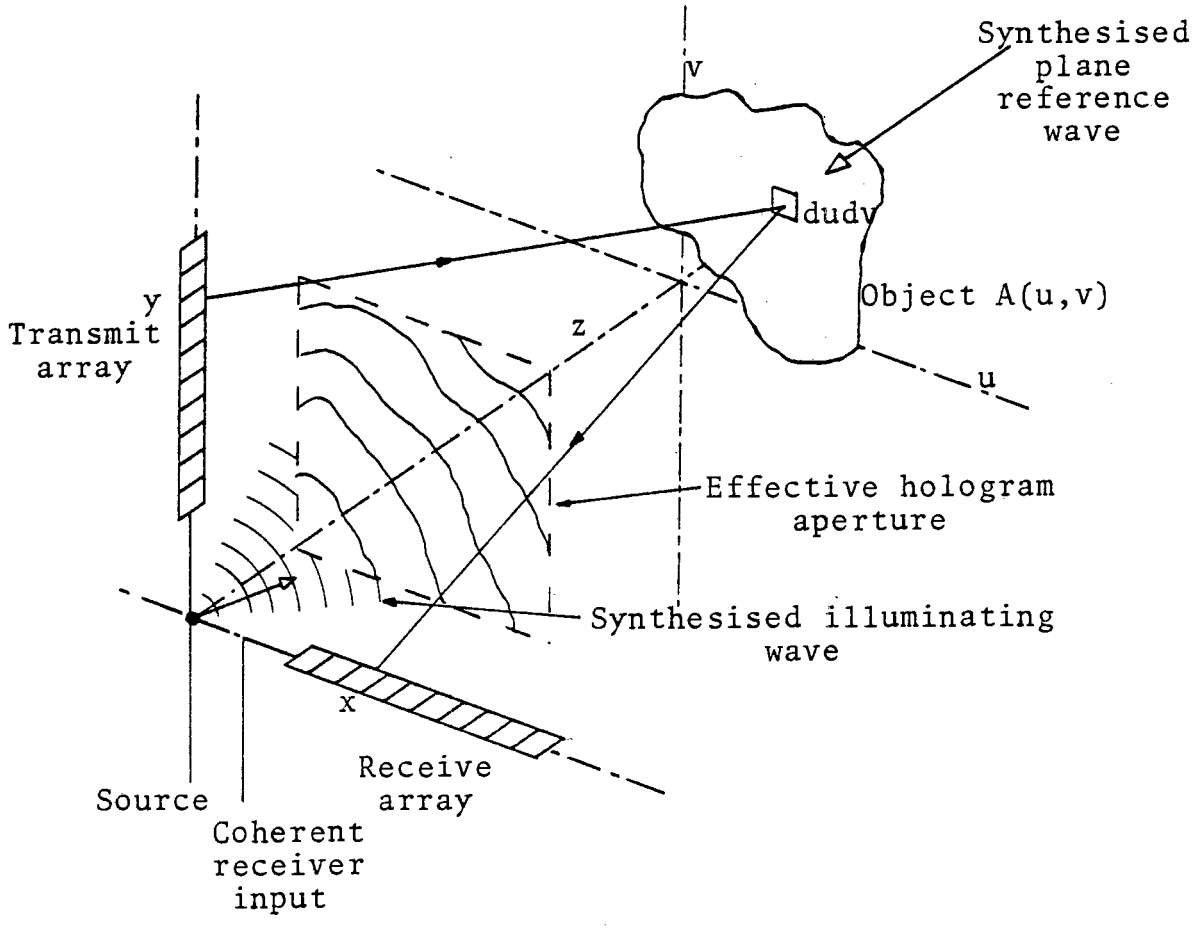

Fig. 3.1 Hologram recording system and object geometry

$$px + py + k((u-x)^2+v^2+z^2)^{\frac{1}{2}} + k((v-y)^2+u^2+z^2)^{\frac{1}{2}} + \text{constant} \quad - 3.1$$

where p and k are the wavenumbers respectively of the array transmission lines and the medium between array and object planes. The constant term absorbs phase shifts in the connections to source, reference coupler and mixer. For paraxial ray paths, the Fresnel approximation leads to the following complex received field representation:

$$e^{jp(x+y)} \cdot \iint_{uv} A(u,v) . e^{j\frac{k}{2z}((u-x)^2+v^2+(v-y)^2+u^2)} .dudv \quad ---- \quad 3.2$$

This can be re-arranged as:

$$e^{jp(x+y)} \cdot \iint_{uv} A(u,v) . e^{j\frac{k}{2z}(u^2+v^2)} . e^{j\frac{k}{2z}((u-x)^2+(v-y)^2)} .dudv \quad 3.3$$

or, using the convolution notation, as:

$$e^{jp(x+y)} . (A(x,y) . e^{j\frac{k}{2z}(x^2+y^2)} \otimes e^{j\frac{k}{2z}(x^2+y^2)}) \quad --------- \quad 3.4$$

where $\otimes$ denotes the convolution operation. The field measured with all possible combinations of transmit and receive elements may be interpreted as equivalent to that found in a plane formed by the projection of transmit and receive apertures. (Fig. 3.1) The object region is, in this analogy, illuminated by a transmitter placed at the intersection of array axes, and the reflected field is mapped over the projected aperture. The sensor commutation also synthesises a plane reference wave. Given a square law detector, the resulting hologram has the following fields incorporated:

$$h(A,B) = |A|^2 + |B|^2 + A^*B + AB^* \quad ---------- \quad 3.5$$

where A and B refer to the object and reference waves respectively, and * indicates complex conjugation. Comparing the fourth term of eq. 3.5 with eq. 3.4, A represents the bracketed term, and B^* the complex conjugate of the synthetic reference wave $\exp(-jp(x+y))$.

In optical holography, holograms corresponding to eq. 3.5 are most common [1], but in microwave holography a variety of detection techniques allow more direct extraction of the object

wave information. A system employing a balanced mixer, or using modulation techniques to "mark" both transmitting and receiving antenna pair (such as has been used in this thesis) will generate bipolar real data corresponding to the hologram $h_r(A,B)$, where:

$$h_r(A,B) = A^*B + AB^* \quad \text{---------- 3.6}$$

A more sophisticated receiver which has two balanced mixers with reference inputs in phase quadrature can generate data components which directly represent the complex hologram $h_c(A,B)$:

$$h_c(A,B) = AB^* \quad \text{---------- 3.7}$$

This approach was latterly used in this thesis. A network analyser used as a coherent receiver in Hayward, Rope, Tricoles and Yue's similar microwave imaging system performed essentially the same role.[35]

3.3 Image Reconstruction

3.3.1 Paraxial Theory

The simple form of the hologram in complex format obtained in eq. 3.4 under the assumption of paraxial propagation suggests image recovery from the hologram by an inverse convolution operation. The image amplitude is:

$$I(u',v') = \left(e^{jp(u'+v')} \cdot \left(A(u',v') \cdot e^{j\frac{k}{2z}(u'^2+v'^2)} \otimes e^{j\frac{k}{2z}(u'^2+v'^2)}\right)\right) \otimes e^{-j\frac{k}{2z}(u'^2+v'^2)} \quad \text{----- 3.8}$$

This can be expanded as:

$$I(u',v') = \iiiint_{xyuv} A(u,v) \cdot e^{j\frac{k}{2z}(u^2+v^2)} \cdot e^{j\frac{k}{2z}(x^2+y^2)} \cdot e^{j\frac{k}{2z}(u^2+v^2)} \cdot e^{-j\frac{k}{z}(ux+vy)} \cdot e^{-j\frac{k}{2z}(u'^2+v'^2)} \cdot e^{j\frac{k}{z}(u'x+v'y)} \cdot e^{-j\frac{k}{2z}(x^2+y^2)} \cdot e^{jp(x+y)} \cdot dudvdxdy \quad \text{---------- 3.9}$$

The cancellation of the third and eighth terms constitutes the focussing condition. Hence:

$$I(u',v') = e^{-j\frac{k}{2z}(u'^2+v'^2)} \iiiint_{xyuv} A(u,v).e^{j\frac{k}{z}(u^2+v^2)} .e^{-j\frac{k}{z}(v-v'-\frac{pz}{k})y} .e^{-j\frac{k}{z}(u-u'-\frac{pz}{k})x} .dudvdxdy \quad \text{- 3.10}$$

$$= e^{-j\frac{k}{2z}(u'^2+v'^2)} \iint_{uv} A(u,v).e^{j\frac{k}{z}(u^2+v^2)} .L^2.\text{sinc}(\tfrac{kL}{2z}(u-u'-\tfrac{pz}{k})).\text{sinc}(\tfrac{kL}{2z}(v-v'-\tfrac{pz}{k})).dudv \quad \text{- 3.11}$$

$$= e^{-j\frac{k}{2z}(u'^2+v'^2)} (A(u',v').e^{j\frac{k}{z}(u'^2+v'^2)} \otimes \text{sinc}(\tfrac{kL}{2z}(u'+\tfrac{pz}{k})).\text{sinc}(\tfrac{kL}{2z}(v'+\tfrac{pz}{k}))) \quad \text{---------- 3.12}$$

The sinc() impulse response terms of eq. 3.12 are defined:

$$\text{sinc}(x) = \frac{\sin x}{x}$$

The image plane coordinates are (u',v') and the array lengths in each axis are taken as L. The complex image amplitude is seen from eq. 3.14 to be modified by a phase term and shifted an amount $\frac{pz}{k}$ in both axes. This image shift is a consequence of the reference wave synthesised by the holographic mapping process. The image is also limited in spatial resolution by the smoothing effect of the aperture impulse response "sinc" functions. Conventionally, the image intensity is taken to characterise the object, rather than the image amplitude, in which case:

$$\text{Image intensity} = I(u',v').I(u',v')^* = |I(u',v')|^2 \quad \text{---------- 3.13}$$

The lateral resolution available in the imaging process is dependent on the form of the system impulse response. Using the conventional Raleigh criterion, the lateral resolution is $\frac{\lambda z}{L}$. This is the same as that expected of a filled aperture L x L occupying the same hologram plane.

The paraxial reconstruction process may be regarded as a modified Fourier transformation of the hologram data; re-writing eq. 3.8:

$$I(u',v') = \iint_{xy} (e^{jp(x+y)} .(A(x,y).e^{j\frac{k}{2z}(x^2+y^2)} \otimes e^{j\frac{k}{2z}(x^2+y^2)})).e^{-j\frac{k}{2z}((x-u')^2+(y-v')^2)} .dxdy$$

$$= e^{-j\frac{k}{2z}(u'^2+v'^2)} \left(\iint_{xy} e^{jp(x+y)} . (A(x,y) . e^{j\frac{k}{2z}(x^2+y^2)} \otimes e^{j\frac{k}{2z}(x^2+y^2)} \right) .$$

$$e^{-j\frac{k}{2z}(x^2+y^2)} . e^{j\frac{k}{z}(xu'+yv')} .dxdy \text{ --------- } 3.14$$

= (complex weight).Fourier transform((Hologram data).
(Focussing factor))

The image formation operation can be separated into two steps. The first is the weighting of the hologram data by a paraxial focussing term, and the second is the spatial frequency transformation of the weighted hologram. This transformation is conveniently scheduled as sequential x and y axis operations.[35] The popularity of the paraxial processor is due to the simple and potentially rapid implementation of the reconstruction process. The focussing criterion is no more than the addition of a phase term to each data point in the complex hologram, and the transformation can be performed separately, as sequential row-and-column Fourier transformations. Sidelobe control in the final image can be effected at the intermediate weighted hologram stage by a suitable apodisation overlay.

3.3.2 Paraxial Reconstruction Processes

Different authors have described the paraxial reconstruction process in different ways. The notions of "backpropagation" and "backpropagator"[26,87] suppose the propagation of the reconstructing radiation from the hologram to the image plane, or opposite to the original object wave propagation in the hologram mapping stage. The convolution expression (eq. 3.8) has a negative exponent indicative of this direction.

The paraxial imaging process supposes the object field to be the superposition of overlapping paraboloidal wavefronts emanating from the point scatterers comprising the object. A "matched filter" imaging process generates paraboloidal wavefronts with the centres of symmetry overlying suspected image detail.[34] By analogy with the (one-dimensional) process used in the temporal domain to compress frequency-

modulated radar pulses, the deconvolving function describing the wavefronts is the conjugate of the spatially-reversed hologram-to-image plane impulse response. Given that the corresponding free space impulse response is an even function, the deconvolving factor is again as described by eq. 3.8.

The numerical technique most widely used in microwave , acoustic and seismic holographic reconstruction processes avoids the convolution operation by Fourier transformation of the focussed hologram data.[35,87,94,95,102] This technique implements eq. 3.14, and is obviously best used when either software or hardware fast Fourier transform (FFT) processors are available.

The choice of reconstruction technique depends on the format of the hologram data (which may be complex, real bipolar or monopolar(biased) real data) as well as the degree to which the paraxial approximation simulates the holographic process. Most early work in microwave holography relied on coherent optical reconstruction.[6,7,14,17,18,20,24,31,32,88] The inherent limitations of film in reproducing hologram data produces imagery possibly accompanied by obscuring background fields generated by the other terms in the transmission hologram.(eq. 3.5) Quite apart from image obscuration, the hologram scaling process necessary to implement convenient optical processing is nearly always incomplete; that is, the hologram scaling factor is less than the ratio of microwave and optical wavelengths. This results in longitudinal image distortion. An exception is found in synthetic aperture radar (S.A.R.), since the significantly greater apertures synthesised usually permit convenient and faithful optical reconstruction of the reduced-scale quasi-holograms generated by this technique. Despite the inherent depth distortion, a certain operational inflexibility and some delay in (chemical) processing of the reduced-scale transmission holograms, optical reconstruction of images from microwave holograms does have the considerable advantages of quasi-instantaneous reconstruction due to

parallel processing. Variations in hologram aperture make sensibly no difference to the image formation time, a property which is certainly not possessed by digital computer-based reconstruction algorithms since these are usually implemented by sequential processing.

3.3.3 The Optical Reconstruction Process

This section uses the pertinent results from the analysis, presented in Appendix I, of the optical reconstruction process applied to reduced scale microwave hologram transparencies.

The image reconstruction procedure need only be based on the manipulation of the complex hologram $h_c(A,B)$ formed by interaction of the object wave A and the reference wave B (eq. 3.7) but practical considerations dictate that this complex function cannot be simply represented by the field emerging from a transmission hologram illuminated by plane wave coherent radiation. A constant bias is added to the real bipolar component of this complex hologram and a reduced scale analogue transparency prepared. This has a transmittance T(x',y'):

$$T \propto (\text{constant bias}) + AB^* + A^*B \quad \text{---------- 3.15}$$

T has transmission values in the range zero to unity. The hologram so prepared has K^{-1} of the linear dimensions of the original mapping aperture, that is:

$$x = Kx', \text{ and } y = Ky' \quad \text{---------- 3.16}$$

Fig. 3.2 shows the main features of the optical processor. The optical scale reduction stage uses two lenses and was included to allow plane wave illumination of the hologram transparencies, additional scaling of the hologram and ready access to the hologram transform plane without disturbing any optical components. The overall reduction factor, including the initial photographic stage and optical processor action, led to an effective K-value of 350. The plane wave reconstruction wavefront was chosen for experimental convenience in checking image longitudinal position.

The field emerging from the hologram is assumed to be:

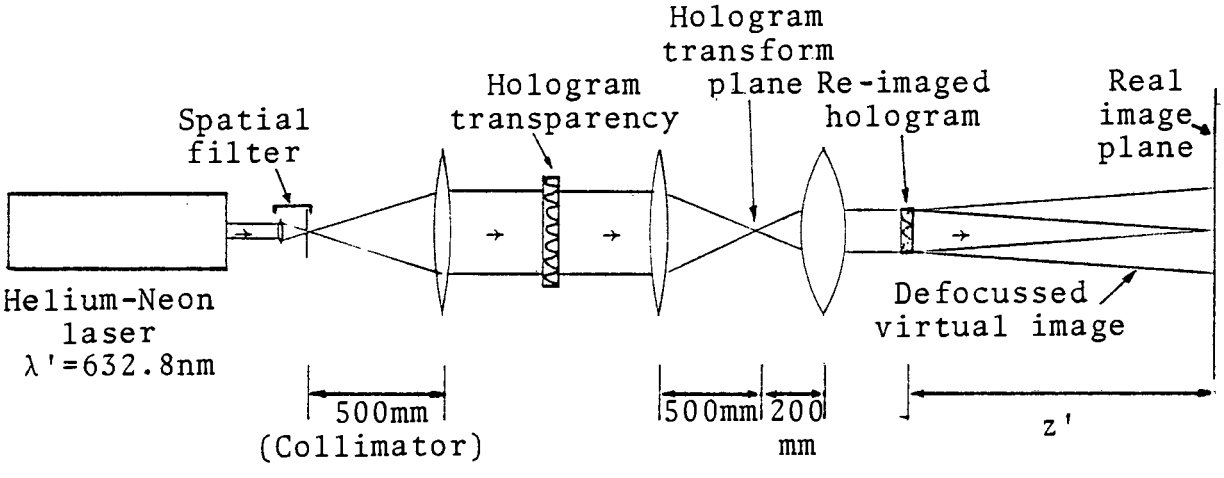

Fig. 3.2 The optical reconstruction processor

$$\psi(x',y') \propto T(x',y'), \text{ to within a complex constant.} \qquad \text{---------- 3.17}$$

The emergent field component which is a reduced scale version of the original complex hologram AB^* forms a virtual image behind the hologram. The field analogous to the component A^*B forms a real image, focussed beyond the hologram. Thus:

$$\psi_r(r,s) = T_r(r,s) \otimes e^{j\frac{k'}{2z'}(r^2+s^2)} \qquad \text{---------- 3.18}$$

where the image plane coordinates are (r,s), $k' = \frac{2\pi}{\lambda'}$, λ' = 632.8nm and z' is the image focal distance measured from the plane of the reduced and re-imaged hologram. The subscript r denotes the real image component. The paraxial approximation is valid in this process. The virtual and real image terms are found equidistant z' from the hologram. From the focussing condition:

$$z' = \frac{k'z}{kK^2} = \frac{\lambda z}{\lambda' K^2} \qquad \text{---------- 3.19}$$

The longitudinal position of image and object plane are simply related using plane wave reconstruction. For the prototype system:

$$\frac{z'}{z} = \frac{\lambda}{\lambda' K^2} = .39 \qquad \text{---------- 3.20}$$

In the focal plane z', the real image distribution is:

$$\psi_r(r,s) = e^{j\frac{k'}{2z'}(r^2+s^2)} . (A^*(\frac{z\lambda r}{Kz'\lambda'}, \frac{z\lambda s}{Kz'\lambda'}) . e^{-j\frac{k}{2z}(r^2+s^2)} . (\frac{z^2\lambda^2}{K^2 z'^2 \lambda'^2}) \otimes$$

$$\text{sinc}(\frac{X'}{2}(pK+\frac{k'r}{z'})) . \text{sinc}(\frac{Y'}{2}(pK+\frac{k's}{z'}))) \qquad \text{------- 3.21}$$

That eq. 3.21 represents a conjugated reflectance term is of little consequence if the image is regarded as the intensity of this field. The image is laterally scaled by a factor M_{lat} where:

$$M_{lat} = \frac{Kz'\lambda'}{z\lambda} = \frac{1}{K} \qquad \text{---------- 3.22}$$

The relationship between image and object distances has been taken from eq. 3.19. The sinc() terms on the extreme right hand side of eq. 3.21 represent the image (r,s) plane impulse response, and the resolution in this plane according to the Raleigh criterion is:

$$\Delta r = \frac{Kz'\lambda'}{z\lambda} . \frac{\lambda z}{X} = M_{lat} . \frac{\lambda z}{X} \qquad \text{---------- 3.23}$$

Likewise, the s-axis resolution is just:

$$\Delta s = M_{lat} \cdot \frac{\lambda z}{Y} .$$

X and Y represent the original (that is, microwave domain) hologram aperture dimensions. The resolution is seen to be fixed in the hologram recording stage by the aperture available in that domain. The image is in addition displaced an amount $M_{lat} \cdot \frac{pz}{k}$ in both r and s axes as a result of the offset reference wave synthesised in the recording process.

In the prototype system, the microwave wavelength was λ, and equal to 30.3mm, and the optical reconstruction wavelength λ' was smaller by a factor of 48000. The scale reduction factor K was only 350 and this implies significant longitudinal image distortion. This is, however, acceptable in the quasi-planar object geometry considered here.

3.3.4 Longitudinal Image Resolution in Paraxial Processing

The longitudinal or depth resolution available in the image reconstructed from a full-scale microwave hologram using paraxial region processing is found by examining the effect of small focal length perturbations on the lateral impulse response. Applying eq. 3.9, the image field amplitude in a plane z'' from the hologram is:

$$I'(u',v') = \iiiint_{xyuv} A(u,v) . e^{j\frac{k}{2z}(u^2+v^2)} . e^{j\frac{k}{2z}(x^2+y^2)} . e^{j\frac{k}{2z}(u^2+v^2)} . e^{-j\frac{k}{z}(ux+vy)} . e^{-j\frac{k}{2z''}(u'^2+v'^2)} . e^{j\frac{k}{z''}(u'x+v'y)} . e^{jp(x+y)} . e^{-j\frac{k}{2z''}(x^2+y^2)} . dudvdxdy \quad \text{---- 3.24}$$

The image distance in the reconstructed image is defined as:

$$z'' = z(1+\Delta), \ \Delta << 1 \quad \text{---------- 3.25}$$

Supposing a point scatterer at u_o in the object plane leads to a modified impulse response in the image plane u' axis:

$$\int_x e^{j\frac{k\Delta x^2}{2z}} . e^{-j\frac{k}{z}(u-(1-\Delta)u'-\frac{pz}{k})x} . dx \quad \text{---------- 3.26}$$

Integration is performed over the x-axis dimension L of the

microwave array. This integral (eq. 3.26) has the form of an even function of x. The image maximum will , consequently, be symmetric about the point u', where:

$$u' \quad -(\frac{pz}{k}-u_o)/(1-\Delta) \simeq (u_o-\frac{pz}{k}).(1+\Delta) \quad \text{---------- 3.27}$$

The image detail is, according to eq. 3.27, magnified an amount $(1+\Delta)$ for image distances $z''>z$ and similarly demagnified if $z''<z$. The locus of image detail, thus, in the region of the focal plane, lies on a straight line joining the aperture centre and the detail itself. (This result will be invoked in the examination of longitudinal image resolution in other object environments.)

Sutton[87] finds that the maximum value of eq. 3.26 drops to -3dB of its focussed value (that is, for $z'' = z$), when the peak value of the argument of the first term is $\pi/4$ radians; hence:

$$\Delta = \frac{\lambda z}{L^2}$$

The z-axis image half-power points are thus:

$$z\pm = z/(1\mp\frac{\lambda z}{L^2}) \quad \text{---------- 3.28}$$

and the z-axis resolution is approximately Δz, where:

$$\Delta z = (\lambda z^2/L^2) \quad \text{---------- 3.29}$$

The longitudinal and lateral image resolutions are equal if the paraxial approximation is valid at a distance z equal to the aperture dimension L.

The prototype system has a maximum aperture (in the horizontal axis) of 686.8mm, λ = 30.3mm and if z is 1 metre, then the longitudinal resolution is 128mm or 13% of the object distance. At twice this object distance, the longitudinal resolution is 523mm or 26% of the range. In contrast, lateral resolution is a constant fraction of the range.(eq. 3.12) High range resolution is not a striking feature of microwave holographic imaging systems using monofrequency techniques. As the range increases, the range resolution becomes worse and in the limit of far-field operation no range "clues" are present in either hologram or image. The situation is rather better in the quasi-holographic S.A.R. system.[77] As an example, a system aperture of 180m at an X-band wavelength equal to that used in the

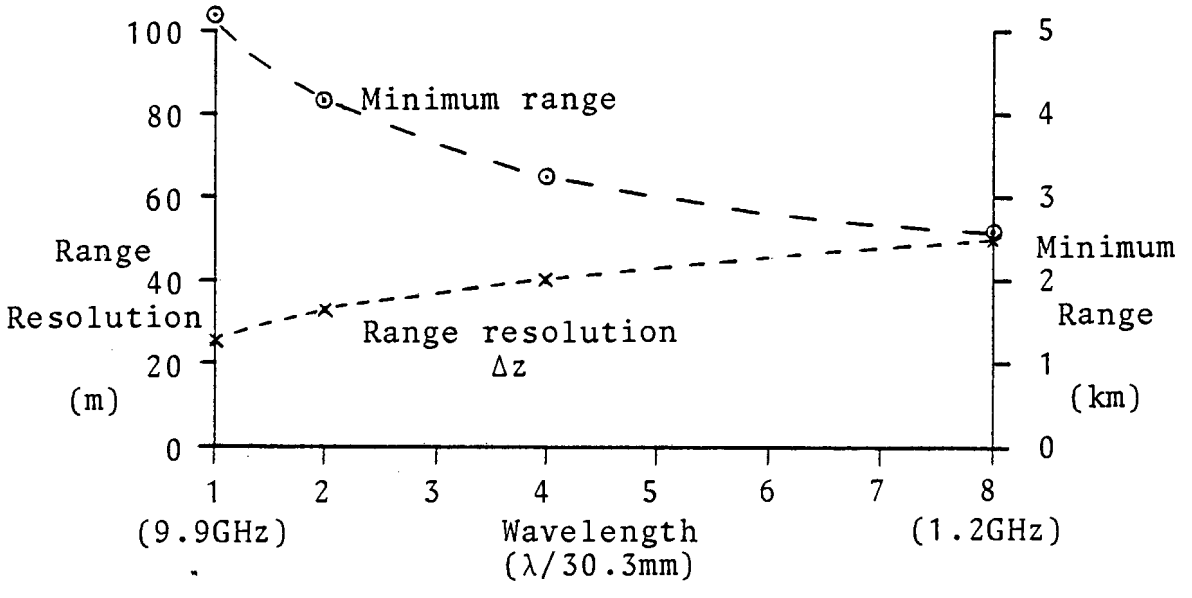

Fig. 3.3 On the dependence of range resolution on wavelength for a fixed aperture

prototype laboratory system is possible. At the minimum range for which the paraxial approximation is valid, and taking into account the effective wavelength reduction due to the go-and-return mode used in S.A.R., the range resolution is 25m. This represents a much more useful fraction of range than that obtained in most microwave holographic systems. One group [77] has exploited this property in the examination of object motion effects on S.A.R. imagery. The technique resolved ambiguity in the direction of propagation of ocean wave trains.

Reducing wavelength while keeping effective aperture constant is not a useful method for improving range resolution. This parameter, for a constant 180m aperture, over a 8:1 ratio of wavelengths shows only 2:1 improvement in absolute (that is, spatial) resolution. (Fig. 3.3) The improvement in the relative range resolution is just 4:1. In each case, range resolution was optimised in the sense that the paraxial minimum range was evaluated; the range resolution is worse (greater) at longer ranges.

3.4 Image Plane Distortion in Paraxial Processing

Wells[34] has described the holographic implementation of the orthogonal axis synthetic aperture system as "conic holography". The term refers to the synthetic aperture system's equivalence to a system of two orthogonal linear arrays of sensors (transmit and receive), mechanically focussed at a constant range, and each rotated about one axis to define an object region. (Fig. 3.4) Given that the arrays are sensibly isotropic normal to their long axes, the position of the beam maximum gain region is the intersection of the hyberbolae defining each array's planar object field maximum gain "strip".

The monofrequency holographic synthetic aperture system may be conceptually equated with a continuous wave phased array system, given a static object environment. The holographic and phased array systems differ only in the implementation

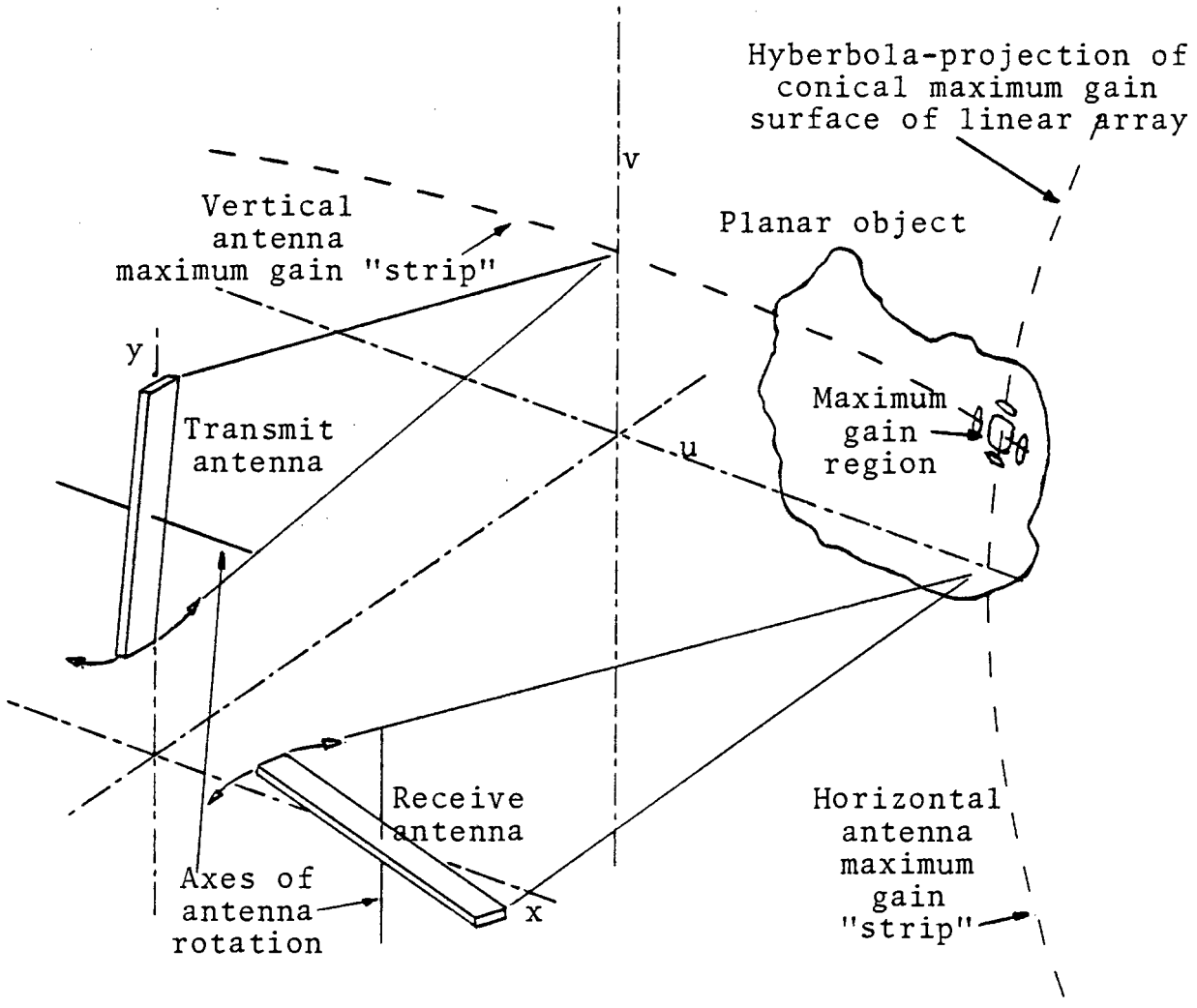

Fig. 3.4 A mechanically scanned "conic" imaging system

of the beam-forming process. In holography, only one sensor pair may be activated at any one time for reasons of signal identifiability, and the post-detection signal "complex weighting and integration" technique of reconstruction (eq. 3.10) is analogous to the hardware implementation of the same signal weighting and coherent summation which defines a given object region in both transmission and reception.

Wells considers the differences between holograms produced by "areal" and "conic" holography, the first referring to filled-aperture sensor array techniques. (Chp.1) The holograms are identical for objects in which the paraxial approximation is valid, and as a result the simple consecutive and separable convolution reconstruction process is applicable to either mode of recording.

Outside the paraxial region, any comparison between "areal" and "conic" holograms is of little utility, since the optimum reconstruction processes are significantly different. The reconstruction process applicable to "conic" holography has the advantage of separability, albeit with a more complicated algorithm than the paraxial one, but still potentially implemented in less time than that needed for the reconstruction of the "areal" hologram.[34]

The aim of this section is to develop practical limits to the application of the paraxial reconstruction process, and to investigate, using the prototype system as the example, the relative degradation of system impulse response arising from (a) the paraxial approximation and (b) the intrinsic hyberbolic impulse response loci implied by this process. To this end, only one axis of the equivalent phased array system need be considered. Limitations imposed in one axis may be inferred in the other.

The vertical phased array in Fig. 3.5 is focussed at a range z, by including a set of parabolic complex weights. This analogue of the paraxial reconstruction process generates a hyberbolic beam trajectory in the object plane, and the impulse

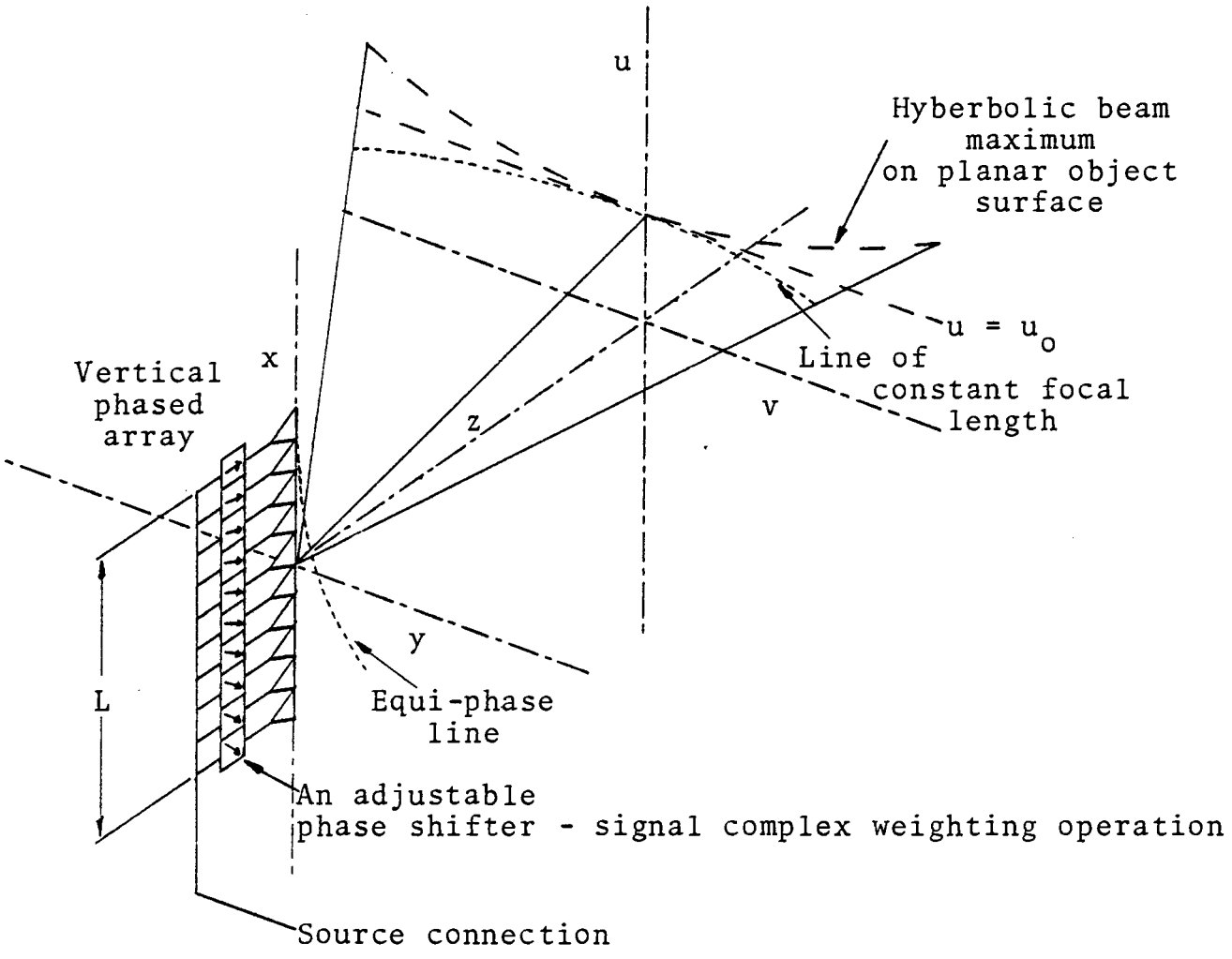

Fig. 3.5 Phased array analogy of the paraxial reconstruction process

response is a function not only of range and the u-axis co-ordinate, but also of the orthogonal axis coordinate. The impulse response is degraded in three ways. Firstly, the paraxial processor is only approximate and secondly, the constant focal length implies u-axis defocussing if imaging is attempted at large (v,z) plane angles. Thirdly, the beam maximum locus is an hyberbola on a planar object region. Taking the last statement, it has been shown (eq. 3.27) that the beam maximum lies along a straight line joining origin and object point. The beam locus is given by:

$$u^2/u_o^2 - v^2/z^2 = 1 \quad \text{---------- 3.30}$$

where u_o is the u-axis intercept for v=0. Hence:

$$u = u_o(1 + v^2/2z^2 - v^4/8z^4 + ...) \quad \text{-------- 3.31}$$

The Taylor series expansion has been used here. It is reasonable to require u to be within a fraction $\propto$ of a beamwidth from u_o for a range of v-axis values not exceeding u_o; u_o is the largest value of interest in the u-axis, and is determined by the paraxial approximation and allowable impulse response degradation. Thus the u-axis error is limited to:

$$u_o v^2/2z^2 \leq \propto .\lambda z/L \quad \text{---------- 3.32}$$

The aperture dimension is L, and the beamwidth is taken as $\lambda z/L$. Hence:

$$v \leq (\propto .\frac{2\lambda z^3}{u_o L})^{\frac{1}{2}} \quad \text{---------- 3.33}$$

If a (square) object area u_o x u_o is considered, and if v is smaller than u_o, then the hyberbolic distortion is taken as significant.

Considering the second cause of impulse response distortion due to defocussing, the field at $(u_o,0,z)$ due to the phased array is accurately expressed as :

$$F(u_o,0,z) = \int_{array} (\text{array weights}).e^{jk((x-u_o)^2+z^2)^{\frac{1}{2}}}.dx \quad \text{---- 3.34}$$

The array has been assumed to be continuous.

$$k((x-u_o)^2+z^2)^{\frac{1}{2}} = kz(1 + (x-u_o)^2/2z^2 - (x-u_o)^4/8z^4 + ...) \quad \text{---- 3.35}$$

The first term on the right hand side of eq. 3.35 is constant and the second term is the common second power paraxial

approximation. The quartic term must be kept sufficiently small so as not to degrade the impulse response. Requiring this term to be less than $\pi/8$ radians (peak value), following a "far-field" type of argument, is unnecessarily restrictive; depending on the criterion chosen for impulse response degradation, simulation suggests that peak quartic term values between π and 2π radians are possible, although impulse response degradation is rapid after this figure.

Simulation using the aperture and wavelength dimensions of the prototype system, covering the useful range of 0.75 to 2 metres, has revealed that phase errors from the quartic (and higher) terms of π radians caused sidelobe levels to rise from approximately -14dB (residual non-apodised value) to -6dB using a point scatterer object. In addition, the impulse response maximum was in error in its location by one quarter to one half the spatial resolution, and suffered 1-2 dB gain loss. The increase in sidelobe level was considered to be more limiting than the loss in spatial resolution. From eq. 3.35:

$$u_o \lesssim (\phi_{max} \cdot \frac{4\lambda z^3}{\pi})^{\frac{1}{4}} - \frac{L}{2} \qquad \text{3.36}$$

The peak phase error (ϕ_{max}) is taken as π radians. Combining the restrictions on u_o (eq. 3.36) and v (eq. 3.33) (Fig. 3.6) the conclusion is reached that, in the range of useful object distances accessible to the experimental system, the paraxial assumption is more likely to degrade imagery than the hyberbolic impulse response locus. The effect of the varying range from array to object position has been ignored for the sake of mathematical tractability in the preceding analysis.

Fig. 3.6 Paraxial and Hyberbolic Limits

Dimensions are in metres.

λ = 30.3mm $\quad \alpha$ = 1

L = 0.6868 $\quad \phi_{max} = \pi$ radians

z	u_o	v_{max}
0.75	0.13	0.53
1.00	0.25	0.59
1.50	0.46	0.80
2.00	0.65	1.04
2.50	0.83	1.29

The preceding conclusion has been checked by a simulation which describes the phase of the object wave exactly and re-

constructs the supposed hologram by a constant focal length paraxial process. Given an arbitrary point (u_o, v_o, z) in the object plane, and using the paraxial process for reconstruction of the complex hologram results in an image u'-axis distribution along a line parallel to the (x-axis) array:

$$F_{v_o}(u') = \int_{array} e^{jk((x-u_o)^2+(y-v_o)^2+z^2)^{\frac{1}{2}}} . e^{-j\frac{k}{2z}(u'-x)^2} . dx \quad \text{---------- 3.37}$$

The array and hologram plane variables are (x,y), and the image axis is u'. If the hologram plane y-axis is coincident with the centroid of the array, then $(y-v_o)$ is replaceable by just v_o in eq. 3.37. This provision allows the largest object displacement v_o, since v_o will, in general, be of either sign, and this requires that the arrays cross as close as to their centres as is possible. This compact geometry has been used with the experimental prototype system in its final form.

The image reconstruction process of eq. 3.37 has been simulated for a range of operational focal lengths and offsets v_o. In every case, the effect of the increase of the distance to object point by the orthogonal axis offset v_o was investigated for a range of v_o not exceeding u_o. The simulation result, based on:

$$F_{v_o}(u') = \int_{array} e^{jk((x-u_o)^2+(v_o^2+z^2))^{\frac{1}{2}}} . e^{-j\frac{k}{2z}(u'-x)^2} . dx \quad \text{---------- 3.38}$$

is exemplified in Fig. 3.7. Here, a range of 1 metre is assumed and a point scatterer object position $(u_o, 0, 1)$ initially used. (u_o = 360mm) This corresponds to about 4.8 radians peak phase error in the paraxial approximation for v_o = 0.(eq. 3.35)

The image lateral resolution is initially 55mm(measured between -3dB points, and about 25% more than that indicated by simple theory), and is degraded to 90mm if the object is moved laterally, keeping u_o constant, but changing v_o from zero to 400mm. The image maximum is, however, degraded only 1dB and shifted -25mm, which is less than one half the expected spatial resolution. The image shift for v_o = 0 is due to the paraxial reconstruction process.

Object orthogonal axis offset

Image u'-axis (metres)	v_o=0	.1	.15	.2	.25	.3	.35	.4 (metres)
.410	17	15	15	14	14	13	12	12
.405								
.400	12	12	13	13	14	13	13	12
.395								
.390	7	8	8	9	9	11	12	12
.385								
.380	5	5	5	6	6	7	8	9
.375								
.370	4	4	4	4	4	4	5	6
.365								
.360	+ 3	3	3	3	3	3	+3	4
.355	2	+ 2	+3	+3	+3	+3	3	+3
.350	1	1	2	2	2	3	3	3
.345	0	1	1	1	2	2	2	3
.340	0	0	1	1	1	2	2	2
.335	x 0	0	0	0	0	1	2	2
.330	0	x 0	x0	0	0	0	1	2
.325	0	0	0	x0	x0	0	1	1
.320	1	0	0	0	0	x0	0	1
.315	2	1	1	1	0	0	x0	x1
.310	+ 3	+ 3	2	2	1	1	1	1

← Object position

Note: (a) Values given in table are in dB below u'-axis maximum for $v_o = 0$.

(b) Point object range is 1 metre.

(c) Point object u-axis position is at u_o = 360mm.

(d) Maximum u'-axis image amplitude is traced by x's.

(e) The u'-axis -3dB response point is traced by +'s.

Fig. 3.7 Vertical Impulse Response Modulation by Orthogonal Axis Offset

It would appear from this and other simulations corresponding to smaller paraxial phase errors that a peak phase error of π leads to imagery whose detail is not noticeably degraded by the inherent hyberbolic distortion of "conic" holography when the paraxial reconstruction process is indiscriminately applied. Thus, the resolution degradation due to reconstruction processor mismatch is relatively worse (for the prototype system) than the inherent hyberbolic distortion caused also by the same processor.

It is also noteworthy that the positions of the image maxima indicated in Fig. 3.7 contract with increasing v-axis offset; this is in accordance with the equivalent phased array model of Fig. 3.5, since the image plane contours corresponding to equal processor weights are presumed horizontal in the paraxial reconstruction process, whereas the equivalent object plane beam maximum traces a hyberbolic trajectory. This results in a characteristic "pincushion" distortion of the image.

3.5 Hologram Formation and Reconstruction outside the Paraxial Region

3.5.1 Theoretical Description

The simple paraxial reconstruction method has been seen to be ultimately limited by impulse response distortion, leading to impaired resolution and errors in image plane geometry. The paraxial reconstruction processor can also restrict system field of view unnecessarily when array sampling is considered. Using the phased array analogy again, the application of paraxial theory without regard to accuracy in the prediction of beam maxima of a discrete element array, having antennae at one half (free space) wavelength spacing, would indicate subsidiary grating lobe flanking the main lobe. In reality, such an array exhibits only a single lobe beam pattern. More effective use can be made of the available aperture by employing a more accurate description of the impulse response of

the region between hologram mapping plane and object plane in the design of the "backpropagation function.

The technique[87] is nearly "exact" in respect of wavefront phase description, but neglects the apodising effects of the varying propagation path lengths between object detail and array elements and the non-isotropic nature of real antennae. A minor constraint easily met in practical systems sets a near-field limit outside the antenna reactive region.[103]

The total phase shift from a transmitting antenna to a receiving antenna via a reflecting region dudv on the object A(u,v) is, from eq. 3.1 and Fig. 3.1:

$$px + py + k((u-x)^2+v^2+z^2)^{\frac{1}{2}} + k((v-y)^2+u^2+z^2)^{\frac{1}{2}} \quad \text{---------- 3.39}$$

The complex hologram is:

$$h_c(x,y) = e^{jp(x+y)} \iint_{uv} A(u,v).e^{jk((u-x)^2+v^2+z^2)^{\frac{1}{2}}}.e^{jk((v-y)^2+u^2+z^2)^{\frac{1}{2}}}.dudv \quad 3.40$$

This form of the (complex) hologram from "conic" holography is rather different to that which would be generated by a system having an areal receiver aperture equal to the projected array dimensions (Fig. 3.1) and with illumination provided by an isotropic source. In such a case, the complex hologram would be:

$$h_{spherical}(x,y) = e^{jp(x+y)}.A(x,y).e^{jk(x^2+y^2+z^2)^{\frac{1}{2}}} \otimes e^{jk(x^2+y^2+z^2)^{\frac{1}{2}}} \quad \text{--- 3.41}$$

Clearly, the equivalent areal aperture-plus-illuminator concept valid under the paraxial approximation cannot be carried over to a wider field of view system. Wells[34] indicates that image reconstruction in this region from holograms generated by "conic" systems is, despite the increased complication of eq. 3.40 compared to eq. 3.4, still potentially faster than the image reconstruction from an "areal" hologram. He finds that the complex "conic" hologram separates into two multiplicative factors, which, if not independent as in paraxial imagery, still allow sequential row-and-column operations.

In paraxial holography, the image data obtained by one axis deconvolution of the hologram data assumes constant focal

length across the orthogonal image plane. In conic holography, however, and assuming a rectangularly sampled planar object geometry, the impulse response distortion and hyberbolic error is defeated by adjusting the deconvolving factor focal length for orthogonal axis position. The required image reconstruction operation is, using the "backpropagator" notion:

$$I(u',v') = \iint_{xy} h_c(x,y).e^{-jk((u'-x)^2+v'^2+z^2)^{\frac{1}{2}}}.e^{-jk((v'-y)^2+u'^2+z^2)^{\frac{1}{2}}}.dxdy \quad 3.42$$

This may be implemented by two sequential convolutions operating on orthogonal axis data:

$$\text{(a)}\quad I'(u',v') = h_c(u',v') \otimes e^{-jk(u'^2+(v'^2+z^2))^{\frac{1}{2}}}\Big|_{v'=\text{constant}} \quad \text{------} \quad 3.43$$

The second convolution generates the final image from the intermediate array:

$$\text{(b)}\quad I(u',v') = I'(u',v') \otimes e^{-jk(v'^2+(u'^2+z^2))^{\frac{1}{2}}}\Big|_{u'=\text{constant}} \quad \text{------} \quad 3.44$$

In effect, if the deconvolving factor is envisaged as the generator of a (uniaxial) sequence of intermediate image values from a data row in the hologram, then that factor is modified according to the position of the image row in the orthogonal axis. The image is completed by a similar sequence of operations in the orthogonal axis using column data.

3.5.2 Image Lateral Resolution

The hologram mapping and image reconstruction process may be viewed as spatial-frequency domain operations.[87]

$$H(f_x,f_y) = A(f_x,f_y).Q(f_x,f_y) \quad \text{----------} \quad 3.45$$

The (upper case) H,A,Q refer to transformations of hologram, object and "propagator" respectively. If eq. 3.45 is rewritten in short form notation as H = A.Q, then the corresponding image reconstruction operation is clearly:

$$I = H.Q^{-1} \quad \text{----------} \quad 3.46$$

where $Q^{-1} = Q^*/|Q|^2$. The image reconstruction operation is thus rewritten as:

$$I = \frac{(A.Q).Q^{-1}}{|Q|^2} \quad \text{---------- 3.47}$$

The bracketed term represents the spectrum of the (measured) complex hologram. If the approximation is made that the propagator amplitude spectrum is constant or nearly so, then eq. 3.47 is equivalent to eq. 3.42, since:

$$F^{-1}(Q^*(f_x,f_y)) = q^*(-x,-y,z) = q^*(x,y,z) \quad \text{------ 3.48}$$

The backpropagator q is an even function of x and y. Drawing an analogy with temporal domain pulse compression techniques, the image reconstruction operation is very close to matched filtering. The resolution offered by the process is taken as the inverse of the spatial frequency extent (occupancy) of either propagator or backpropagator. The (x-axis) deconvolving factor is from eq. 3.47:

$$e^{-jk(x^2+y^2+z^2)^{\frac{1}{2}}} \quad \text{---------- 3.49}$$

The spatial frequency extent of this function is estimated by the stationary phase technique:[103]

$$\text{Bandwidth (cycles/metre)} = \frac{1}{2\pi} \cdot \frac{d}{dx}(q(x))\Big|_{x=\pm\frac{X}{2}} \quad \text{--- 3.50}$$

The aperture dimensions are X and Y in x and y axes respectively. The resolution is taken as the reciprocal of the bandwidth: (eq. 3.50)

$$\delta x = \frac{\lambda}{X}(z^2+\frac{X^2}{4}+y^2)^{\frac{1}{2}} \quad \text{---------- 3.51}$$

$$\text{Similarly } \delta y = \frac{\lambda}{Y}(z^2+\frac{Y^2}{4}+x^2)^{\frac{1}{2}} \quad \text{---------- 3.52}$$

Using the same argument, the paraxial approximation suggests propagator bandwidth of $X/\lambda z$ in the x-axis. Hence resolution in the x-axis is confirmed as:

$$\delta x = \frac{\lambda z}{X}, \text{ and } \delta y = \frac{\lambda z}{Y} \quad \text{---------- 3.53}$$

The resolution available using the extra-paraxial processor of eq. 3.42 reduces to the above (eq. 3.53) forms in the limit of longer object distances z.

That the lateral resolution in the image plane is not constant over the plane can be taken as indicative of the adjustment to the deconvolving factor needed to maintain beam focus over an assumed plane object region. The linear resolution is worst at the edges of the object plane. Described in spatial

frequency terms, the hologram formation and subsequent image reconstruction processes are linear, and the overall impulse response should be an invariant function of image plane position. However, eq. 3.45 does not explicitly include a term which describes the finite hologram aperture available and which convolves the propagator spectrum , since this term has been assumed to be sufficiently narrow not to modify the propagator spectrum. The spatial domain backpropagation deconvolution approach matches propagator and backpropagator wavefronts (having regard for their relative directions) and ignores aperture dimensions. As a result, the impulse response and hence the spatial resolution vary over the image plane.

3.6 The Sampled Hologram

The assumption has been made up to this point that the hologram is a continuous recording. Practical microwave holograms, however, are nearly always discrete data recordings, and a digital computer-based image reconstruction process can in any event only incorporate a finite number of sampled field values.

The prototype system had two orthogonal arrays each comprising two 10 element subarrays functionally combined with directional couplers. Antenna spacing was 20.2mm in each axis, and although the arrays were broken at their centres to accommodate directional couplers and their cross-over, the antennae were fitted to a constant pitch. The gap in array centres is not considered here, as its effect on the imaging process does not contribute to the elucidation of the sampling process.

An approximate spatial frequency domain analysis is appropriate to determine the limits of object range and lateral extent (offset) imposed by the constant spatial frequency sampling interval. The spectra are approximate in the sense that amplitude characteristics are of secondary concern, and the limits of "instantaneous" (that is , local) spatial frequency are taken as the field bandwidth. A feature of the orthogonal

axis imaging system is the possibility of synthesising a plane reference wave which may make an arbitrary angle with the array plane by adjusting the antennae spacing. This offset reference wave mode is most useful in image reconstruction systems where the hologram data is real, so that spatial separation of the desired and potentially interfering image and other terms may be achieved. From eq. 3.5, the hologram resulting from the interference of object wave A and reference wave B is:

$$h(A,B) = |A|^2 + |B|^2 + A^*B + AB^* \quad \text{---------- 3.54}$$

In a reduced-scale optical reconstruction mode, the limitations of monopolar real hologram transmittance mean that all 4 terms of eq. 3.54 will be present in the field emerging from the hologram, although only the third (or fourth) is required , in principle, to recover the original object wave and hence the original object scene. A digital reconstruction system can, however handle real bipolar or complex data, and the spatial separation requirements can be relaxed or even ignored, as the background "clutter" producing terms in eq. 3.54 are then absent. A computer-based reconstruction system has therefore access to a potentially larger object region.

The object regions accessible without ambiguity are dependent on the process chosen for reconstructing the hologram data. This data, in turn, can be in one of three categories:

(a) Complex data corresponding to the object wave or its conjugate;(eq. 3.7)

(b) Real bipolar data corresponding to a component of the object wave;(eq. 3.6)

(c) Monopolar real data corresponding to an analogue of eq. 3.54.

The first two data representations are the usual (but not necessary) preserve of computer-based reconstruction. The last (c) is commonly used in optical reconstruction. Complex data has been recorded on film for optical reconstruction as so-called "kinoforms" [107] but the process is neither simple or common.

The sampling process is viewed here as an overlay or multiplication of the supposed continuous hologram by a two-dimensional square sampling grid. The equivalent spatial frequency domain representation convolves the continuous field and sampling grid spectra. Real, virtual and "background" fields will be spatially distinct in the image plane if their spectra do not overlap. The accessible object regions are divided according to the form of the hologram data. The Nyquist sampling criterion determines the allowable spectral occupancy.
Case 1: (Fig. 3.8) Given antenna spacing Δ in both axes, the permissible spatial frequency limits are just $\pm 1/2\Delta$ in each axis, and maximum object wave bandwidth is $1/\Delta$.
Case 2: (Fig. 3.9) Less spectral occupancy is available as the overlapping conjugate spectra of a real bipolar data hologram have been separated by introducing a spatial carrier frequency $1/4\Delta$ in both axes. Maximum object wave bandwidth is $1/2\Delta$ in both axes.
Case 3: (Fig. 3.10)The first term $|A|^2$ in eq. 3.54 corresponds to a spectral "patch" twice the width of the object wave spectrum, and has the form of the autocorrelation function of the spectrum of A. In addition, the reference term $|B|^2$ is clustered around the sampling harmonics. The available holo-bandwidth is more restricted than in either previous case, and is just $1/4\Delta$ in both axes. The separation of spectral regions leading to real and virtual image terms has been accomplished by the introduction of a spatial carrier at a frequency of $3/8\Delta$.

Image lateral resolution tends to be at a premium in microwave holographic imaging systems, and the above three cases are examined to find the largest object region accessible, as a function of both range and the reconstruction technique. It will be shown that the paraxial reconstruction process does not always allow efficient use of system aperture.

Case 1 (a) Non-offset point object
For a point scatterer object at a range z from the crossed orthogonal array system, the complex x-axis field is:

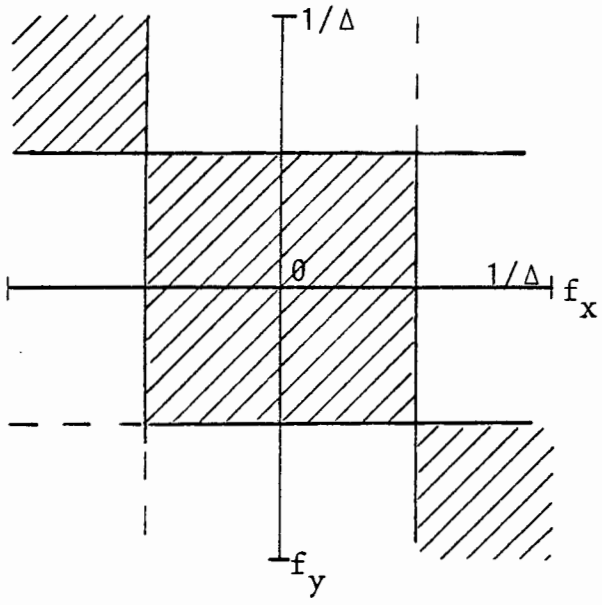

Fig. 3.8

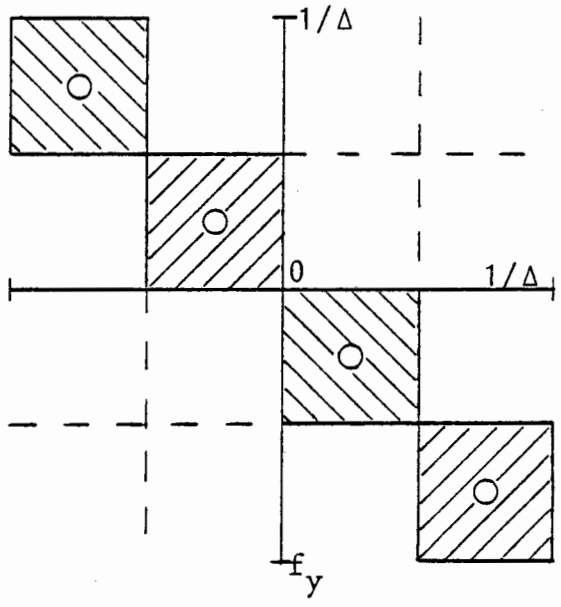

Fig. 3.9

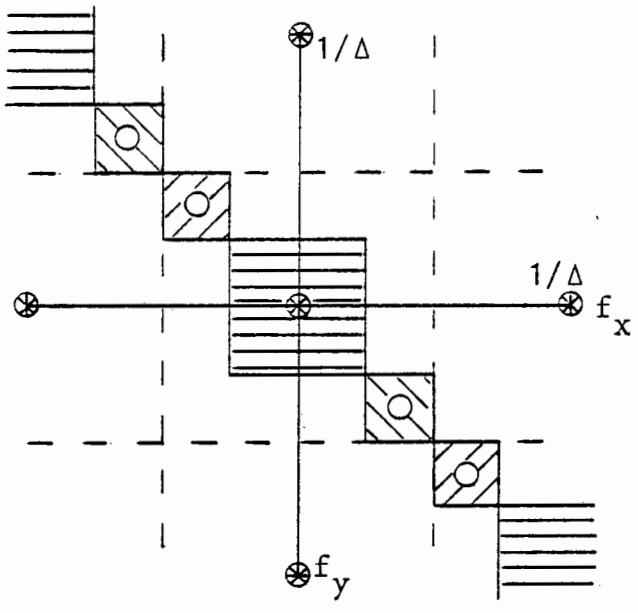

Fig. 3.10

= Virtual image

= Real image

= Background field

○ = Carrier term

⊗ = Reference term

Figs. 3.8-3.10 Spectral allocation for hologram data formats

$$h(x) = e^{jk(x^2+z^2)^{\frac{1}{2}}} \quad \text{---------- 3.55}$$

The object position in the (u,v,z) coordinate system is (0,0,z), and the maximum array dimension in the x-axis is $\frac{X}{2}$. In the prototype system, the x and y array dimensions were X = 686.8mm and Y = 585.8mm respectively. The maximum recorded spatial frequency is:

$$|f_x|_{max} = \frac{x}{\lambda(x^2+z^2)^{\frac{1}{2}}} \ (m^{-1}) \quad \text{(x is taken at maximum value.)}$$

$$\leq 1/2\Delta \quad \text{---------- 3.56}$$

Thus $$z \geq X(\Delta^2/\lambda^2 - \tfrac{1}{4})^{\frac{1}{2}} \quad \text{---------- 3.57}$$

In the practical system, assuming zero object offset, the minimum range values are:

z_{min} = .304m in the x-axis, and similarly,
z_{min} = .258m in the y-axis.

In comparison, the paraxial approximation (applied without regard to considerations of its accuracy) would suggest an x-axis field:

$$h(x) = e^{j\frac{kx^2}{2z}} \quad \text{---------- 3.58}$$

The corresponding minimum range is:

$$z_{min} = \frac{X\Delta}{\lambda} = .46m \text{ in the x-axis.}$$

(b) Offset point object

From eq. 3.40, the object field due to a point object at (u,v,z) is:

$$h(x,y) = e^{jk((u-x)^2+v^2+z^2)^{\frac{1}{2}}} . e^{jk((v-y)^2+u^2+z^2)^{\frac{1}{2}}} \quad \text{---------- 3.59}$$

Using a stationary phase approximation, the maximum offset possible in the object plane is:

$$u_{max} = 1.134(v^2+z^2)^{\frac{1}{2}} - \frac{X}{2}, \text{ and similarly:}$$
$$v_{max} = 1.134(u^2+z^2)^{\frac{1}{2}} - \frac{Y}{2} \quad \text{---------- 3.60}$$

A feature of eq. 3.60 is the increase in permissible object offset with orthogonal axis offset, due to the reduction in wavefront dispersion. A conservative limit is found when the orthogonal axis offset is zero. The longer (in this case, x-axis) aperture limits the maximum object offset at a given range, as shown in Fig. 3.11. This shows that the use of the

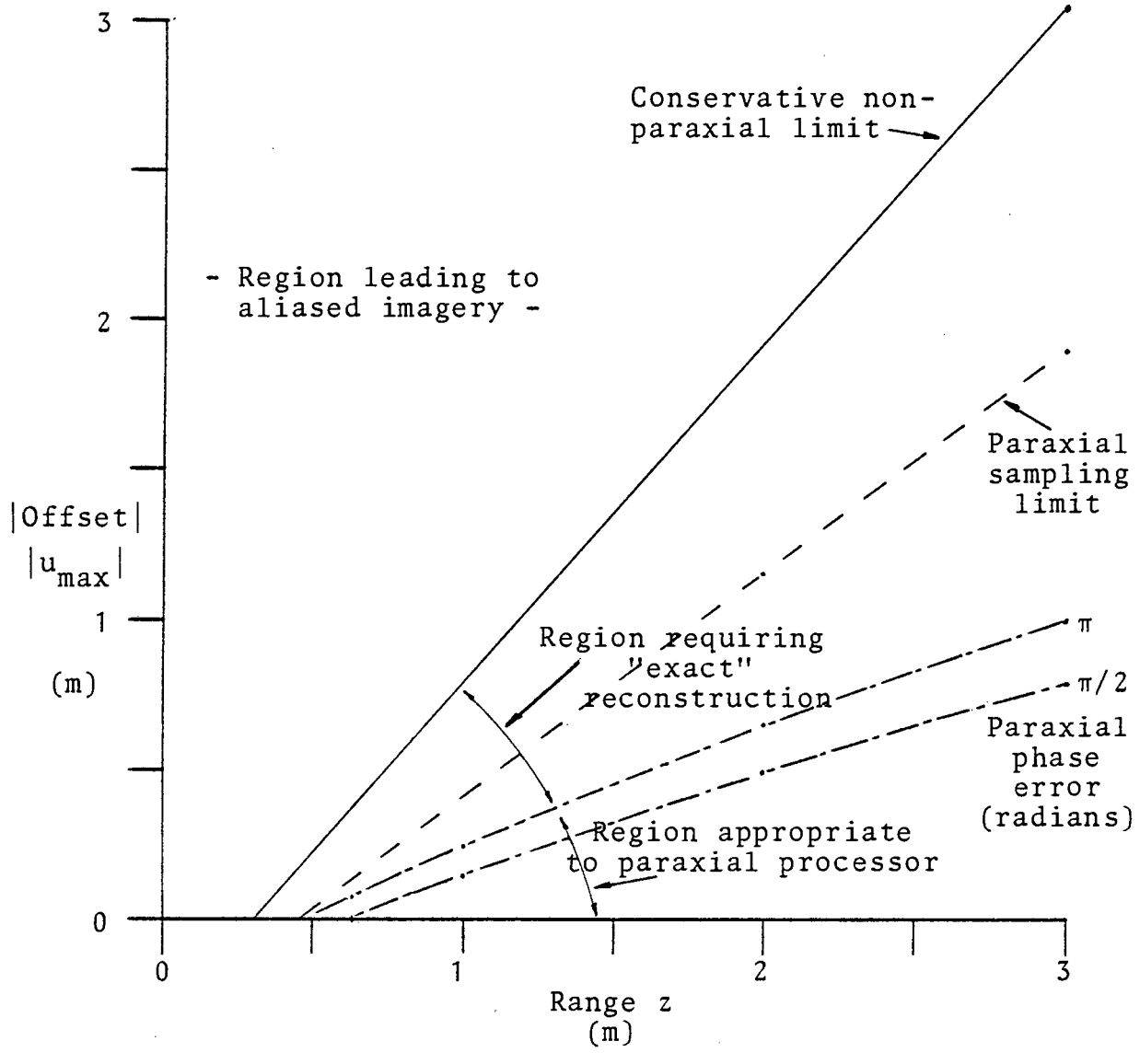

Fig. 3.11 Forbidden object regions and processor requirements (complex data hologram)

paraxial processor, when constrained by defocussing limitations will not lead to aliased imagery, although the accessible object region is restricted both in minimum range and in maximum offset compared to the region available to the more exact technique. (sec. 3.5) The absolute value of offset is plotted and the forbidden regions are indicated. The paraxial limits for $\pi/2$ and π peak phase errors are derived from eq. 3.36. The ranges used in Fig. 3.11 exceed the practical maxima of the prototype system. The use of the paraxial processor is also restricted by the Nyquist criterion in its own terms; for an x-axis field:

$$h(x) = e^{j\frac{k}{2z}(u-x)^2} \qquad \text{3.61}$$

Applying the Nyquist criterion, the maximum x-axis offset is:

$$u_{max} = \frac{\lambda z}{2\Delta} - \frac{X}{2} \qquad \text{3.62}$$

Case 2 The exploitable object wave bandwidth of a real bipolar data hologram is half that of the previous case. Using the approach leading to eq. 3.57 and assuming no object offset and the use of the "exact" processor:

$$z_{min} = .85m$$

The minimum range derived from the paraxial approximation is, following eq. 3.58:

$$z_{min} = .92m$$

A conservative value for the maximum u-axis object offset and assuming the "exact" processor is:

$$u_{max} = .405z - \frac{X}{2} \qquad \text{3.63}$$

The Nyquist criterion applied to the paraxial processor leads to a more restricted offset:

$$u_{max} = .375z - \frac{X}{2} \qquad \text{3.64}$$

The limitations on the minimum range and maximum offset of the point scatterer object using the two processing techniques, and including also the offsets leading to $\pi/2$ and π peak phase error in the paraxial approximation are summarised in Fig. 3.12. The penalty exacted for complete image component separation is a severe limitation of the system's field of view compared with that obtained in Fig. 3.11. The

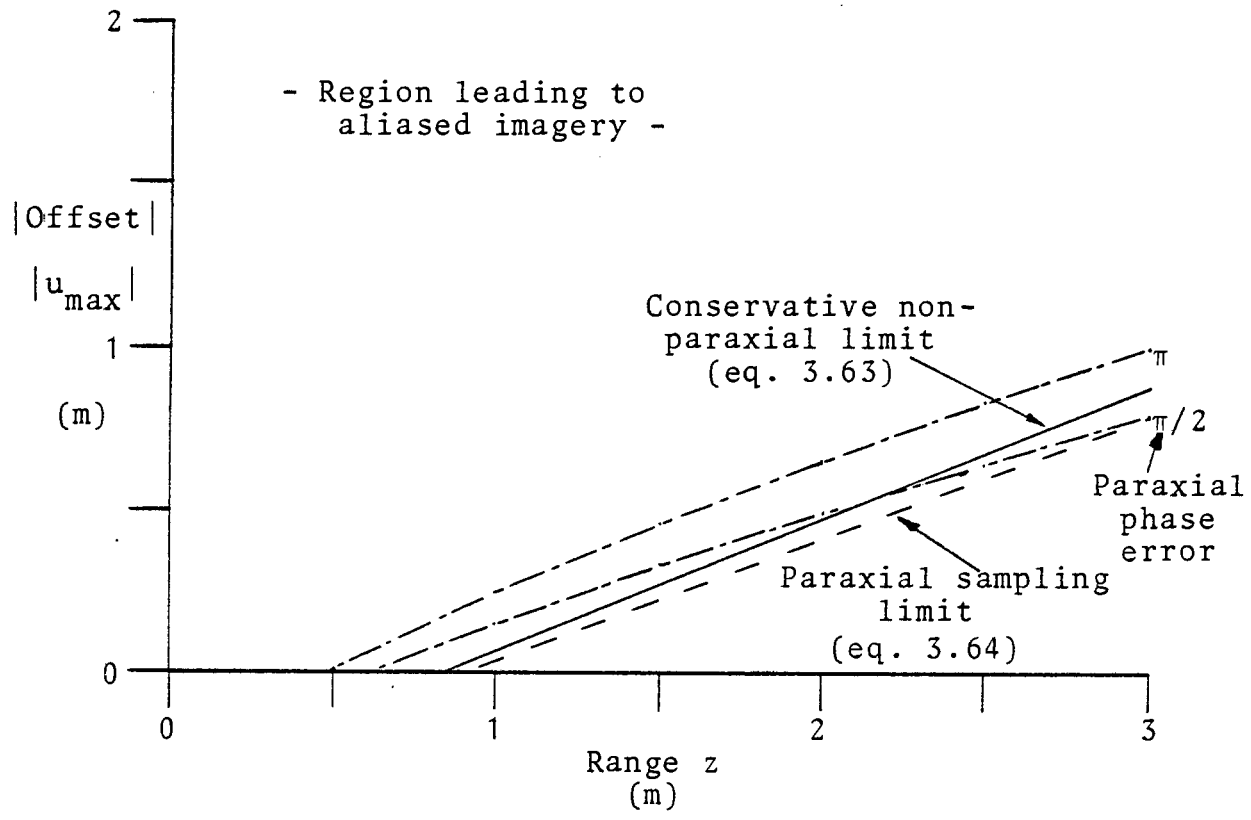

Fig. 3.12 Object region accessibility using real bipolar data

simple paraxial processor is, however, applicable almost to the edge of this field of view.

It is in addition necessary to shift the spectra of the conjugate image fields to avoid overlap, as indicated in Fig. 3.9. The offset can be generated by appropriate antenna spacing, or, if this is not a free parameter, by including a known phase shift from antenna to antenna of both arrays. The required reference field is:

$$B(x,y) = e^{j\frac{2\pi(x+y)}{4\Delta}} \qquad \text{3.65}$$

This function has spatial frequency $1/4\Delta(m^{-1})$. From eq. 3.4, the reference field is:

$$B(x,y) = e^{-jp(x+y)} \qquad \text{3.66}$$

The propagation constant of the waveguide array distributor is :

$$p = 2\pi/\lambda_g$$

Hence $\lambda_g = 4\Delta$. This value of λ_g implies operation rather close to the cut-off frequency of the waveguide, if $\Delta = 20.2$mm, and an alternative approach establishes the incremental phase shifts $p\Delta x$ and $p\Delta y$ in the two arrays by including phase shift elements in the path between distributor and antenna aperture. In this example, $-\pi/2$ radians incremental phase shift would be required, using the prototype system parameters.

Case 3 Monopolar real data holograms require spatial separation of real, virtual and background image components and only half the bandwidth available in Case 2 can be exploited. Applied to the prototype system, the paraxial approximation is adequately accurate throughout the useful object region, so that limitations on object offset derived by both "exact" and paraxial approaches are very similar. The minimum object range, for no object offset, is:

$$z_{min} = 1.84\text{m}$$

The Nyquist criterion limits either axis offset:

$$u_{max} = .188z - \frac{X}{2}\text{ , and similarly}$$

$$v_{max} = .188z - \frac{Y}{2} \qquad \text{3.67}$$

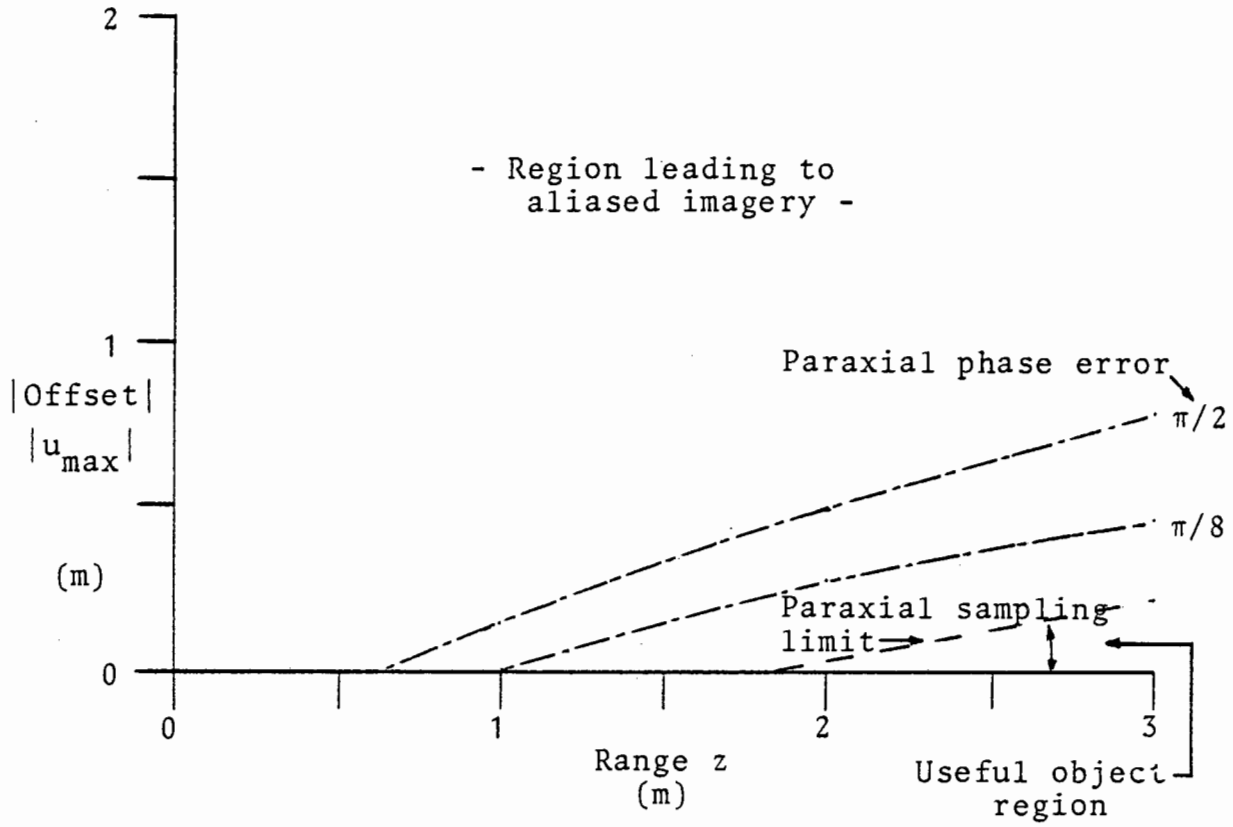

Fig. 3.13 Object region accessibility using monopolar real data hologram

simple paraxial processor is, however, applicable almost to the edge of this field of view.

It is in addition necessary to shift the spectra of the conjugate image fields to avoid overlap, as indicated in Fig. 3.9. The offset can be generated by appropriate antenna spacing, or, if this is not a free parameter, by including a known phase shift from antenna to antenna of both arrays. The required reference field is:

$$B(x,y) = e^{j\frac{2\pi(x+y)}{4\Delta}} \qquad \text{3.65}$$

This function has spatial frequency $1/4\Delta(m^{-1})$. From eq. 3.4, the reference field is:

$$B(x,y) = e^{-jp(x+y)} \qquad \text{3.66}$$

The propagation constant of the waveguide array distributor is :

$$p = 2\pi/\lambda_g$$

Hence $\lambda_g = 4\Delta$. This value of λ_g implies operation rather close to the cut-off frequency of the waveguide, if $\Delta = 20.2$mm, and an alternative approach establishes the incremental phase shifts $p\Delta x$ and $p\Delta y$ in the two arrays by including phase shift elements in the path between distributor and antenna aperture. In this example, $-\pi/2$ radians incremental phase shift would be required, using the prototype system parameters.

Case 3 Monopolar real data holograms require spatial separation of real, virtual and background image components and only half the bandwidth available in Case 2 can be exploited. Applied to the prototype system, the paraxial approximation is adequately accurate throughout the useful object region, so that limitations on object offset derived by both "exact" and paraxial approaches are very similar. The minimum object range, for no object offset, is:

$$z_{min} = 1.84\text{m}$$

The Nyquist criterion limits either axis offset:

$$u_{max} = .188z - \frac{X}{2}\text{ , and similarly}$$

$$v_{max} = .188z - \frac{Y}{2} \qquad \text{3.67}$$

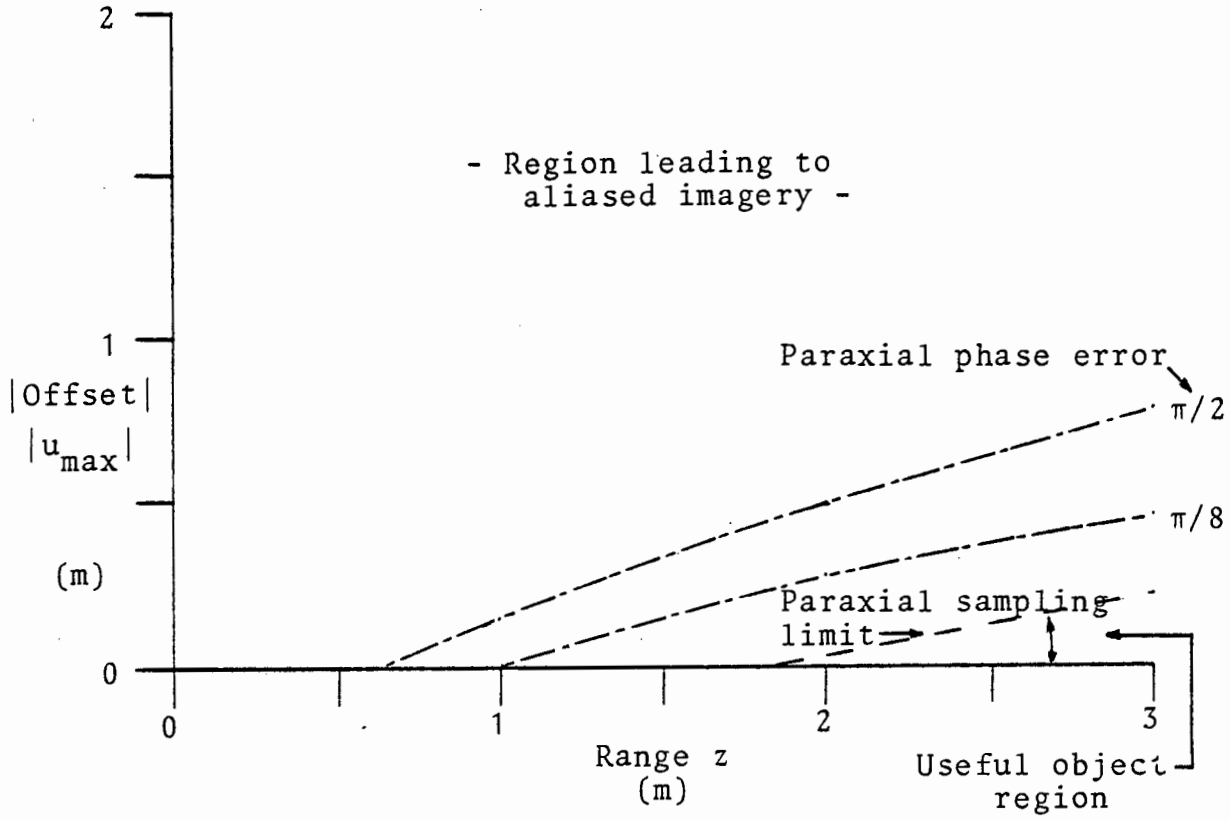

Fig. 3.13 Object region accessibility using monopolar real data hologram

The paraxial processor is in this case limited by sampling, rather than by accuracy, considerations. (Fig. 3.13) The spatial frequency carrier can be implemented by reference wave manipulation in a similar manner to the previous example. In terms of the prototype system, the provisions of Fig. 3.13 result in a severely limited system. The minimum range alone was close to the practical limit, and even at a range of 3 metres, the accessible object region is less than four beam-widths (-3dB points) wide.

3.7 Paraxial Simulation of Holograms from the Orthogonal Array System

In this section, the paraxial field description is used exclusively to simulate the orthogonal array system. A 400 point hologram is generated by two 20 element arrays, with unit antenna spacing presumed in each case. The system wavelength was varied, keeping antenna spacing constant, to demonstrate a range of synthesised offset reference wave formats. In all examples, the point scatterer object has been placed at the centre of the projected aperture at the position (10.5,10.5).

3.7.1 Offset Reference Wave

The wavelength is given as a fraction of the antenna interval. If the wavelength is $(1+\delta)$ units, then the reference wave makes an angle α with the array axes, where: (Fig. 3.14)

$$\alpha = \arcsin(\delta) \qquad \text{---------- 3.68}$$

Equal antenna spacing in both transmit and receive axes means that the reference wave subtends equal angles with both axes. The reference wave is described:

$$B(x,y) = e^{-j\frac{2\pi(x+y)\tan\alpha}{\lambda}} \qquad \text{---------- 3.69}$$

The reference wave spatial frequency in one axis is just the reciprocal of the system wavelength, measured in units of antenna spacing. The resultant spatial offset of the zone plate centre for the simple point scatterer object, is, in

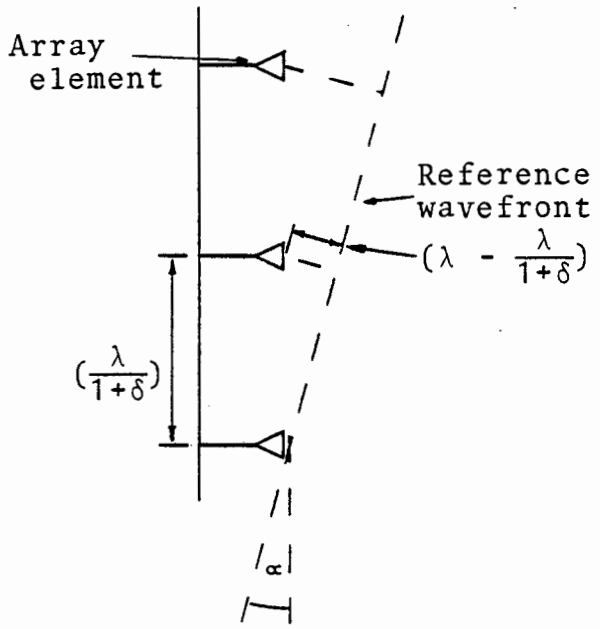

Fig. 3.14 Synthetic reference wave

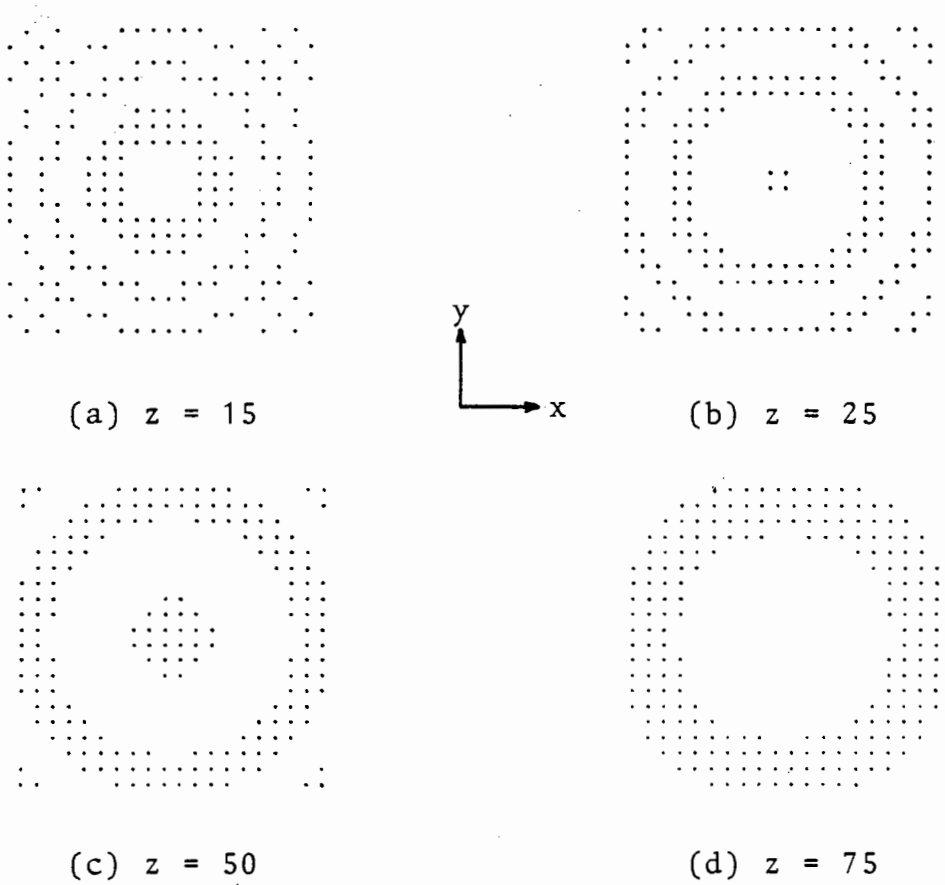

Fig. 3.15 "Zone plate hologram" series with increasing range

the x-axis:

$$\text{Zone plate centre shift} = z\tan\alpha \quad \text{---------- 3.70}$$

3.7.2 Examples from Simulation

A series of 4 examples exhibit diminishing hologram spectral occupancy with increasing object range. The wavelength is taken as equal to the antenna spacing. From eq. 3.68, $\alpha = 0$, and the reference wave is coplanar with the hologram aperture. There is no shift of zone plate centre.(eq. 3:70) The array coordinate system has the result of antenna (1,1) measurement at left bottom. The hologram is presented as a "hard-limited" version of a bipolar real data gathering process. (Figs. 3.15 (a) to (d)) The spectral diagram (Fig. 3.16) shows only the hologram of Fig. 3.15(a) to be undersampled, although all 4 holograms have coincident real and virtual image spectra.

The hologram bandwidth is taken as $\frac{L}{\lambda z}$, from eq. 3.54, where both x and y axis have an aperture of $L = 19$ units, and $\lambda = 1$ unit. For the purposes of image reconstruction, a hologram is considered aliased if it is impossible to perform spectral bandlimiting without reducing the spectral extent beyond that determined by the continuous version of the same hologram. Reduction of the spectral occupancy to avoid aliasing reduces resolution potential in the image.

Increasing the wavelength by 11% of the antenna interval generates a synthetic reference wave, not planar with the array aperture as in the previous cases, but at 6.3^{o} to both axes. The zone plate centre (Fig. 3.17) is consequently shifted $z\tan\alpha = 8.3$ units in both axes. The hologram spectrum (Fig. 3.18) shows incomplete separation of real and virtual image terms, so that image spatial separation is also not complete. The reconstruction process (Fig. 3.19) supports this result; the real image is chosen here for reconstruction using plane wave illumination and this image maximum lies near a corner of the extended virtual image background. Calculation shows the real image to be centred about (18.8,18.8,75).

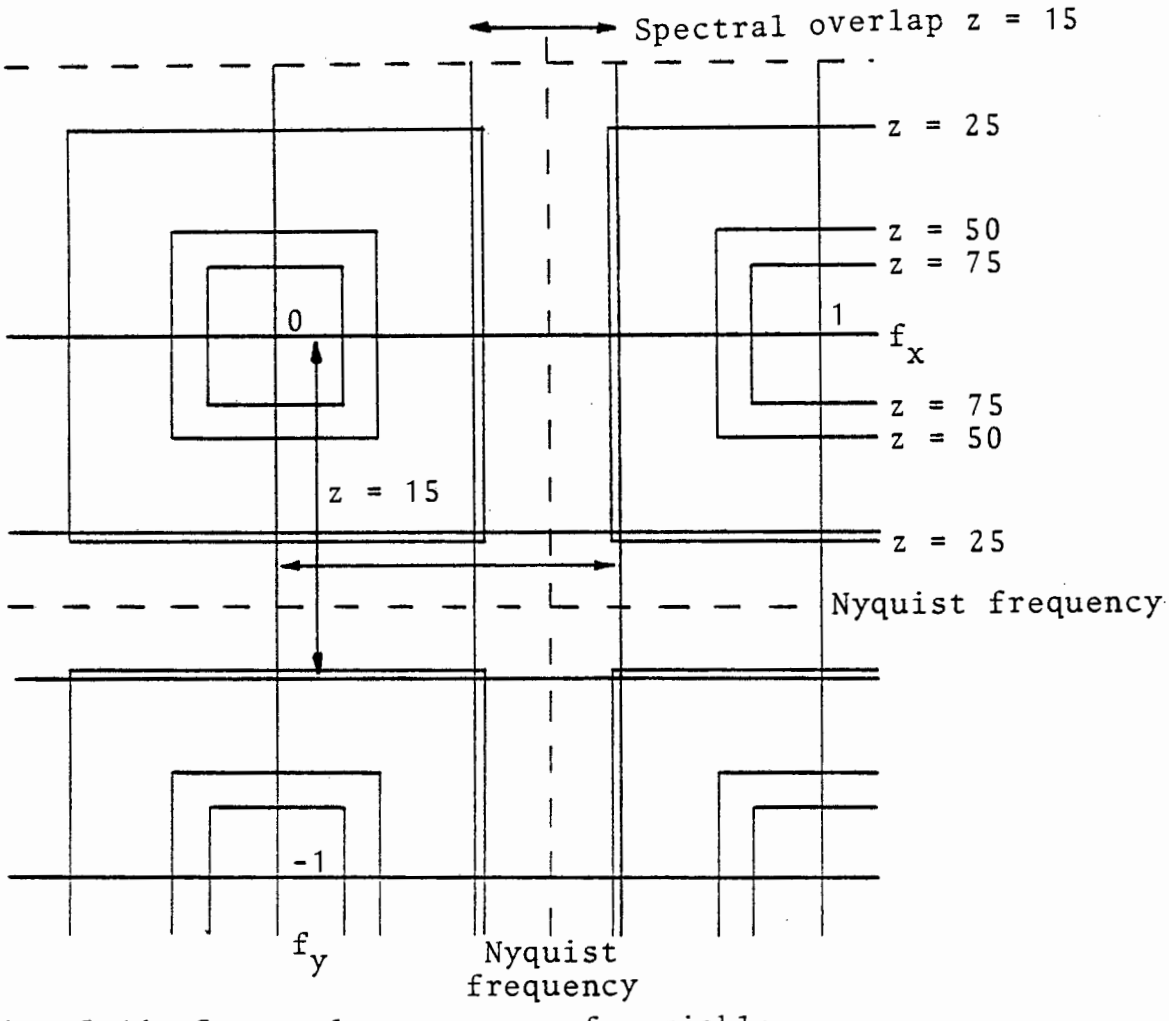

Fig. 3.16 Spectral occupancy of variable range holograms

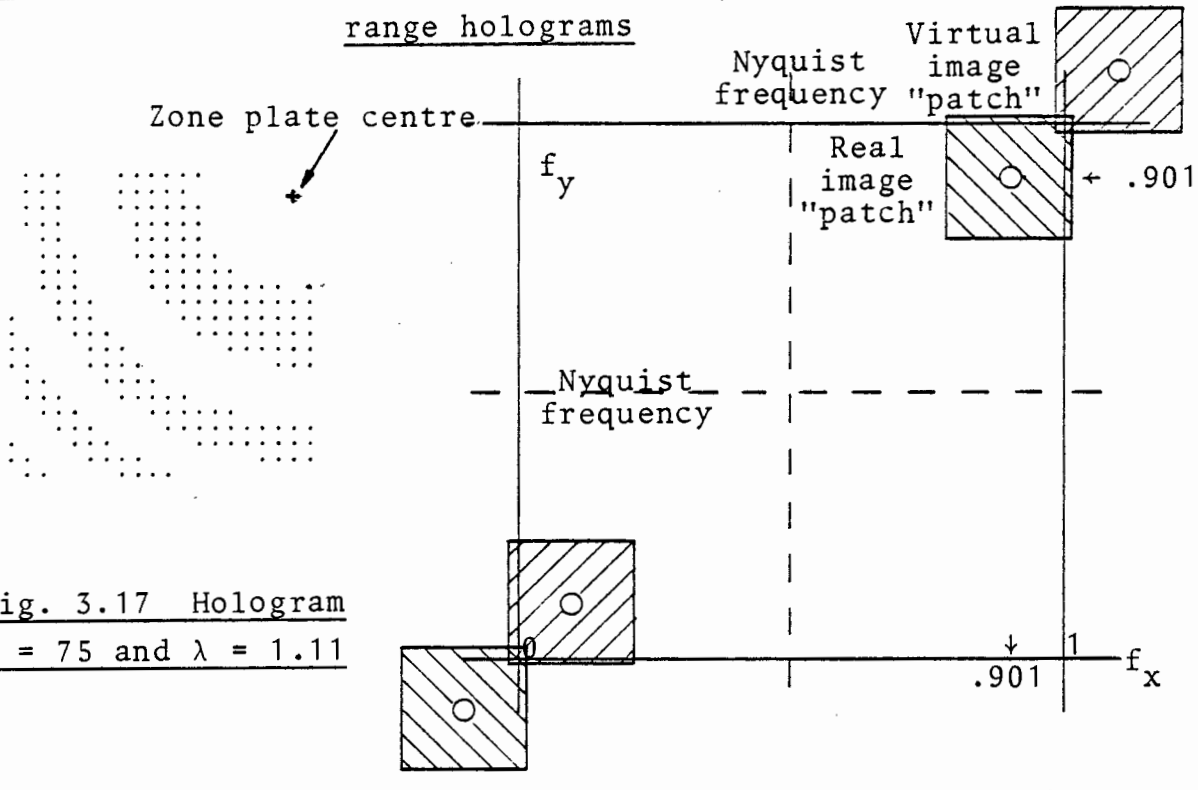

Fig. 3.17 Hologram z = 75 and λ = 1.11

Fig. 3.18 Spectrum of hologram of Fig. 3.17 shows "patches" leading to real and virtual images

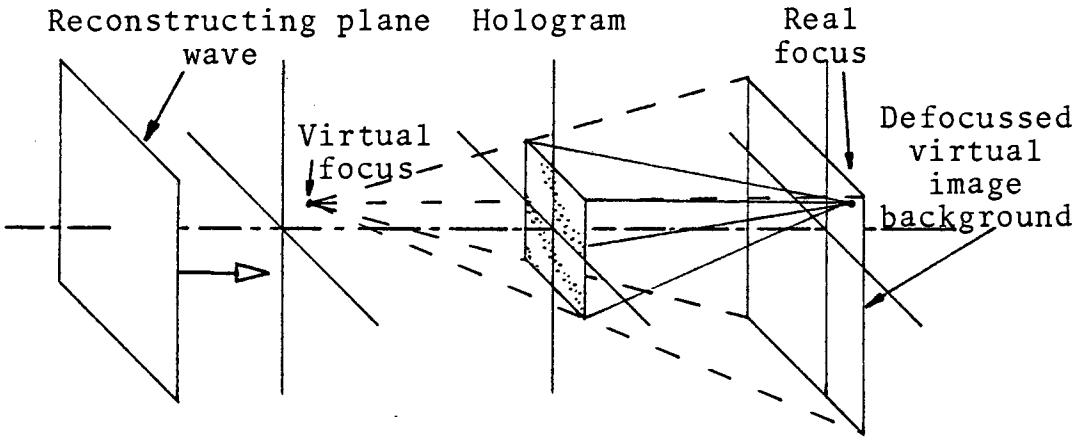

Fig. 3.19 Reconstruction of Fig. 3.17 by optical analogy

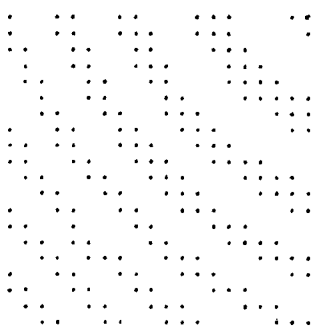

Fig. 3.20 Hologram
z = 75 and λ = 1.25

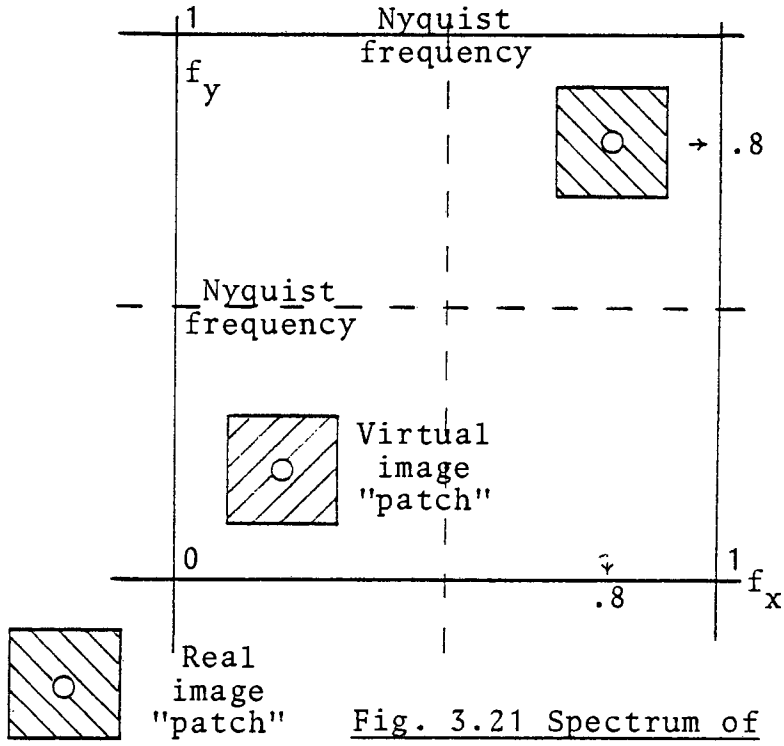

Fig. 3.21 Spectrum of hologram of Fig. 3.20

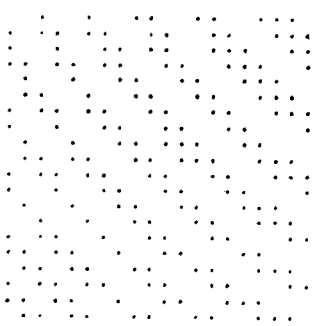

Fig. 3.22 Hologram
z = 75 and λ = 1.35

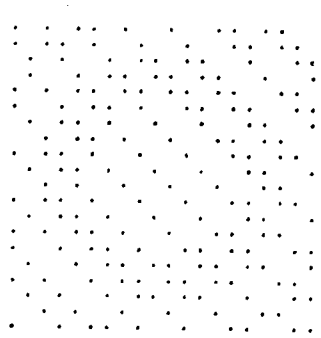

Fig. 3.23 Hologram
z = 75 and λ = 1.50

A further wavelength increase to 1.25 antenna units establishes spatial separation of the two image components. With λ = 1.25 units, the reference wave angle α = 14.5°, and the image is offset 19.4 units in both axes. The zone plate centre is thus 9.9 units beyond the top right-hand corner of the aperture. (Figs. 3.20 and 3.21) Further increases of wavelength (to λ = 1.35 and 1.5 units) develop larger offsets of the zone plate centre, as shown by the increase in perceived hologram spatial frequencies.(Figs. 3.22 and 3.23) Even in the latter case, the hologram is not aliased.

The image repeats at intervals of:

$$\text{Image period} = \frac{\lambda z}{\Delta} \qquad (3.71)$$

(Δ = 1 in this simulation.) In the example of Fig. 3.23, the image period is 112.5 units, and the offset due to the reference wave is not so large that an aliased image maximum is indicated on the hologram as an apparent zone plate centre towards the bottom left corner.

3.7.3 Reduction of Wavelength below Unity

If the system wavelength is reduced and made less than the antenna interval, the synthesised reference wave subtends an included angle whose sign changes.(eq. 3.68) An example for which λ = .8 units and z = 25 units is given in Fig. 3.24. The point scatterer object is centrally located at the position (10.5,10.5,25) as before. The hologram spectrum (Fig. 3.25) reveals that, although the hologram has been adequately sampled, the separation of real and virtual image components is not complete, an observation which is in accord with the fact that the zone plate centre is visible on the hologram.

An extreme example of hologram aliasing (Fig. 3.26) arises for an antenna spacing of many wavelengths. Here, the wavelength is only 10% of the antenna interval, and according to eq. 3.71 the image period is 7.5 units. The hologram reveals subsidiary maxima clustered around the central maximum and having just this spacing. The object is again a point scatterer

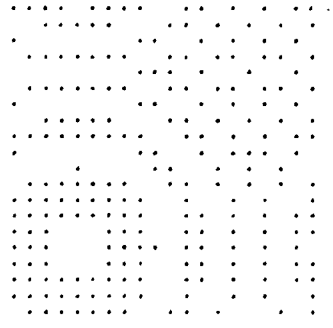

Fig. 3.24 Hologram
z = 25 and λ = 0.80

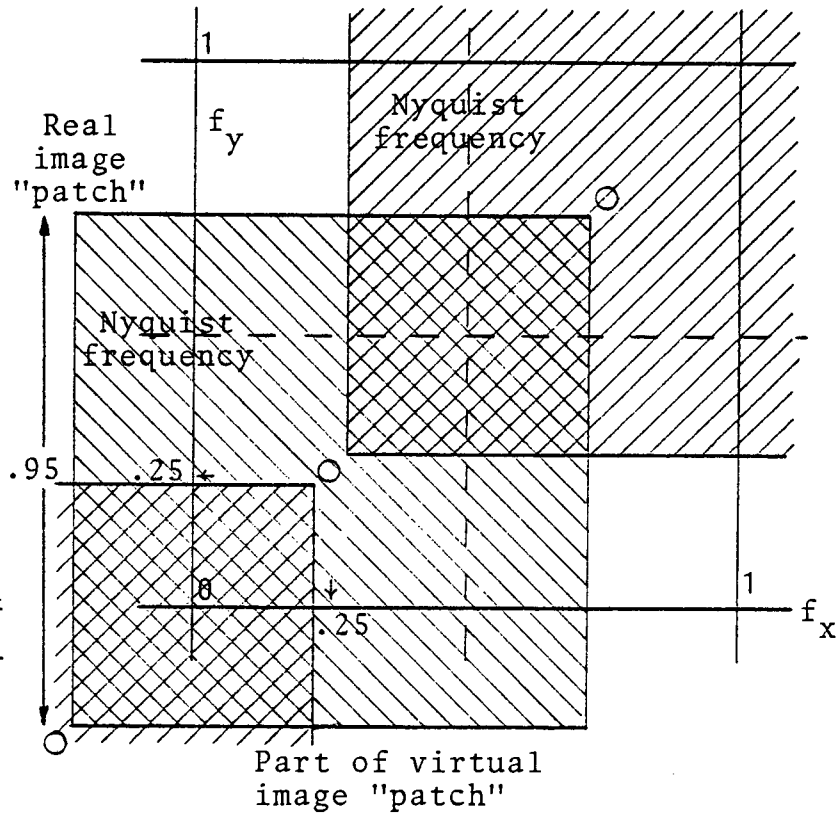

Fig. 3.25 Spectrum of hologram of Fig. 3.24; zone plate centre offset has reversed

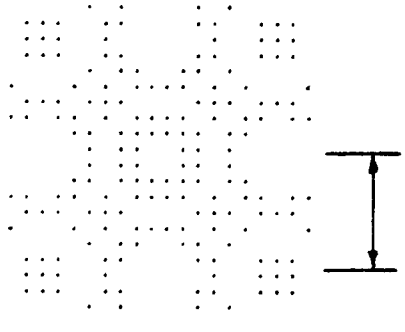

Fig. 3.26 Hologram with severe aliasing
z = 75 and λ = 0.10

and is located at (10.5,10.5,75)

3.8 Conclusion

The theoretical analysis of an elegant implementation of an inertialess microwave holographic imaging system has been presented.

The paraxial Fresnel region of operation utilises a simple reconstruction process, but the limited spatial resolution generally available in microwave images prepared by holographic techniques encourages the exploitation of object regions for which the paraxial reconstruction process is not suited. In these regions, a more exact description of the mapping process leads to a reconstruction process in which the orthogonal array geometry has inherent advantages compared with equivalent apertures formed by areal arrays.

Maximum accessibility of the object region is obtained if the hologram data is in complex form, which implies a complicated hardware signal processor. In such cases where this hardware complexity is not possible, it is feasible to manipulate the reference wave synthesised by the mapping operation so as to ensure spatial separation of wanted and unwanted image fields, although this done at the expense of limiting object region accessibility.

CHAPTER 4

Optical Image Reconstruction

4.1 Equivalent System Description

A series of preliminary tests of the holographic system used simple objects and a coherent optical reconstruction system in every case. There was appreciable direct coupling between transmitting and receiving arrays and large, smooth metal objects were used to ensure that the structure of the measured hologram was dominated by the specular reflection from such objects.

The form of the image distribution using a selection of planar, cylindrical and spherical conducting objects depends both on the description of the object surface and on the holographic mapping system. Subject to the validity of the paraxial approximation the orthogonal array system has been shown equivalent to a system having a receiving aperture whose area is equal to the projection of the transmitting and receiving arrays, and a single illuminating quasi-isotropic transmitting element situated at the point of intersection of the two arrays. (Fig. 3.1, [34-37])

The quasi-isotropic illuminator is common in microwave holography [14,17,18,20] since it allows a wide and predictable object region coverage with simple hardware and requires, as a result, little space both in the plane of the hologram aperture and in the direction normal to this plane. Other microwave holographic systems employ planar wavefront illumination, and these systems nearly always synthesise such a wavefront using some variant of the simultaneously scanned transmitter-receiver technique. [22-26,32] Such techniques extend into two dimensions the one-dimensional quasi-holographic S.A.R. concept. [46,49]

4.2 Specularly Reflecting Objects

The image reconstruction process operating on any hologram, whether derivative of electromagnetic or mechanical radiation, is directed towards the re-establishment of the original object wave. In some cases, the progress of this object wave is followed on a purely numerical basis, but a reduced scale analogue of the object wave is created in the optical reconstruction technique. If some á priori knowledge of the likely distance between hologram and object plane is available, then following the object wave's progress back to that plane derives an image distribution. In the case of specularly reflecting objects, the object wave appears to have originated at a significantly greater distance from the hologram mapping plane and behind the object.

4.2.1 Extended Planar Objects

The object is assumed to be uniform over a u-axis dimension u_o, and coplanar with the antenna arrays. The object distance is z. The reflected field on the object in the u-axis is: (Fig. 4.1)

$$A'(u) = e^{j\frac{k}{2z}(u^2)} . \text{rect}(\frac{u}{u_o}) \quad \text{---------- 4.1}$$

where the function $\text{rect}(\frac{u}{u_o}) = 1$ for $|u| \leq \frac{u_o}{2}$

$= 0$ for $|u| > \frac{u_o}{2}$ -------- 4.2

The field A'(u) propagates from object to array plane and appears to originated in a plane z behind the planar object and 2z from the array plane. As a result, an image reconstruction operation will, if maximum image intensity is any criterion, assume that the object represents the reflection from a point scatterer 2z from the arrays.

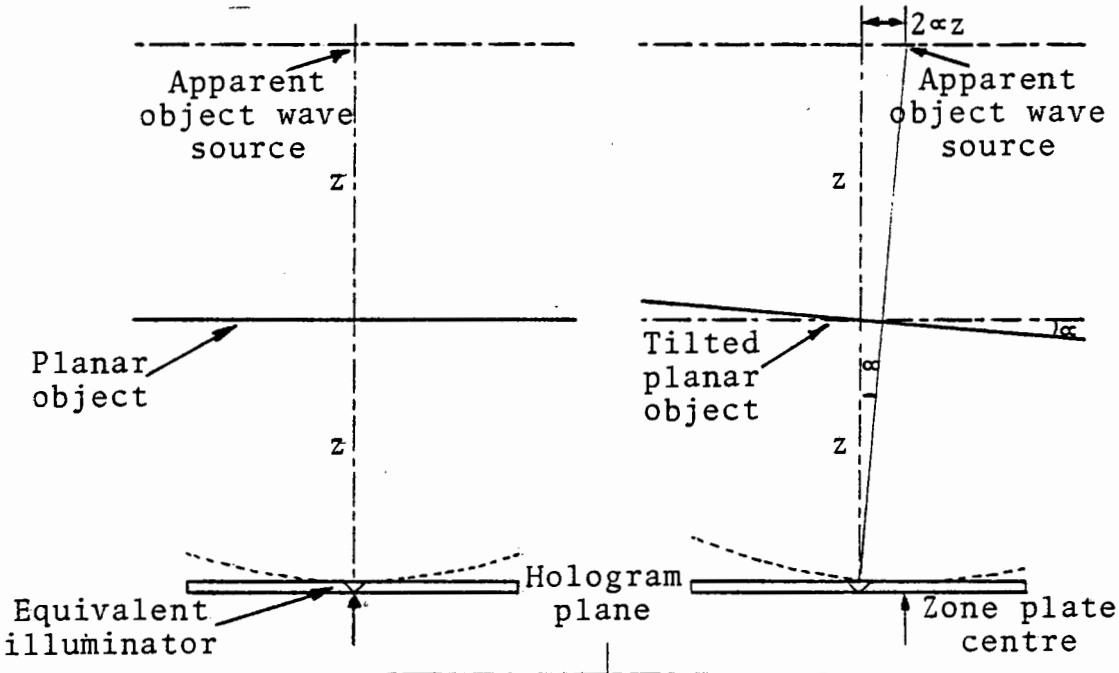

Fig. 4.1 Extended planar object

Fig. 4.2 Tilted planar object

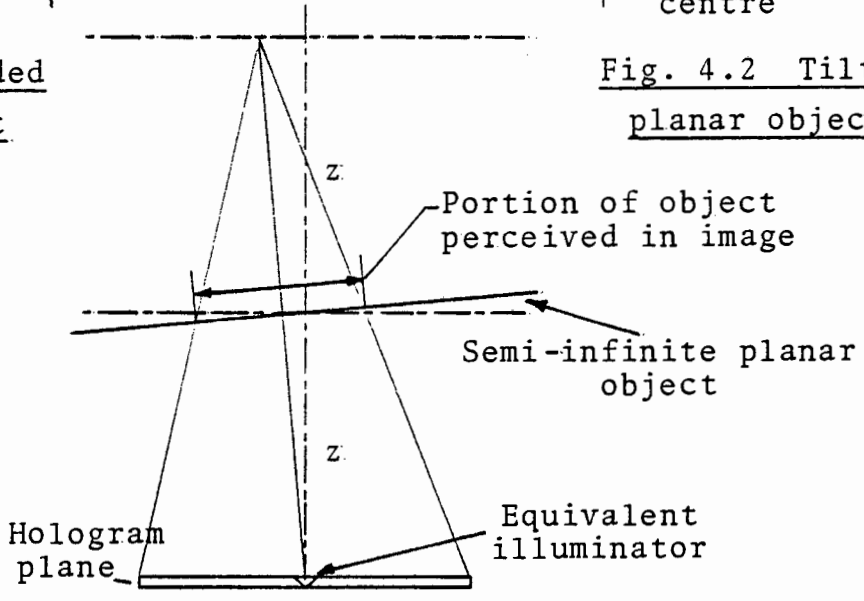

Fig. 4.3 Limiting image dimension

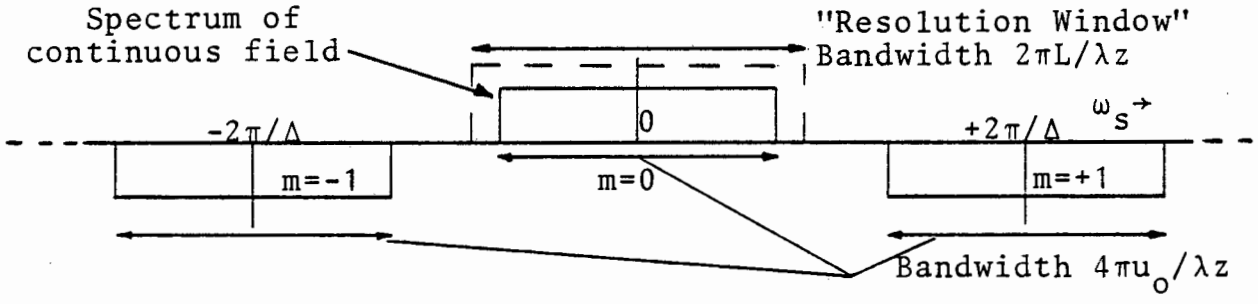

Fig. 4.4 Image spectrum of regularly sampled object

4.2.2 Tilted Planar Object

An object tilt may be represented, for small angles α, as a graded complex reflection coefficient multiplying the object dimension projected on to the (u,v) plane. (Fig. 4.2) The reflected field in the u-axis is:

$$A'(u) = e^{j\frac{k}{2z}(u^2)} \cdot e^{j2ku\alpha} \cdot \mathrm{rect}(\frac{u}{u_o})$$

$$= e^{-j\frac{k}{2z}(4\alpha^2 z^2)} \cdot e^{j\frac{k}{2z}(u+2\alpha z)^2} \cdot \mathrm{rect}(\frac{u}{u_o}) \quad \text{---------- 4.3}$$

This is within a complex constant of the field apparently originating from a point z behind the object, and laterally offset $2\alpha z$ from the (projected) illuminator position.

4.2.3 Far-field Imaging

If a planar object is of suitably restricted extent in both axes, the illuminating function can be regarded as sensibly flat. From eq. 3.12, the image amplitude I(u',v') of an object A(u,v) is:

$$I(u',v') = e^{-j\frac{k}{2z}(u'^2+v'^2)} \cdot (A(u',v') \cdot e^{j\frac{k}{z}(u'^2+v'^2)} \otimes \mathrm{sinc}(\frac{kL}{2z}(u'+\frac{pz}{k})) \cdot \mathrm{sinc}(\frac{kL}{2z}(v'+\frac{pz}{k}))) \quad \text{---------- 4.4}$$

A non-reducing reconstruction mode is assumed for the sake of clarity, although the result is equally applicable to optical reconstruction techniques. If the object dimensions are such that a peak phase deviation of $\pi/8$ radians in the third term of eq. 4.4 is not exceeded, then the object finds the array at twice the (object) far-field distance. This occurs if: $\frac{kM^2}{4z} = \frac{\pi}{8}$. The largest object width is taken as M. The reference wave is assumed to be coplanar with the arrays; hence p = 0. Thus $z > \frac{4M^2}{\lambda}$. In this case eq. 4.4 reduces to:

$$I(u',v') = e^{-j\frac{k}{2z}(u'^2+v'^2)} \cdot (A(u',v') \otimes \mathrm{sinc}(\frac{kLu'}{2z}) \cdot \mathrm{sinc}(\frac{kLv'}{2z}))$$

If the field intensity characterises the image:

$$|I(u',v')|^2 = (A(u',v') \otimes \mathrm{sinc}(\frac{kLu'}{2z}).\mathrm{sinc}(\frac{kLv'}{2z}))^2, \quad \text{----- 4.5}$$

since a planar object implies real A(u,v). The image is a replica of the object, although it is limited in spatial resolution in the normal manner. An example of this imaging mode is shown by Farhat and Guard.[14] The object used was a rectangular flat copper plate.

4.2.4 Limiting Image Dimension

A simple geometrical optics consideration of the image distribution obtained with a semi-infinite planar object (Fig. 4.3) suggests that the image will not exceed one-half the array dimension in length. This conclusion is also supported by eq. 4.4. Assuming that the object extent is unlimited, then the last two terms (that is, the impulse response) of eq. 4.4 can be regarded as imposing an upper limit on the spatial frequency bandwidth of the preceding two terms. The analysis is simplified by working in only one dimension, and by ignoring (a) the offset implied in the impulse response terms (since in the prototype system the reference wave was coplanar with the array aperture, so that p = 0), and (b) the first term of eq. 4.4 ,(since this term disappears when image intensity is calculated). Accordingly, the third term's spatial frequency extent is limited by the rectangular spatial filter $\mathrm{rect}(\frac{\omega z \lambda}{2\pi L})$, where:

$$F(\mathrm{sinc}(\frac{kLu'}{2z})) = C.\mathrm{rect}(\frac{\omega z \lambda}{2\pi L}) \quad \text{---------- 4.6}$$

F indicates the spatial frequency transformation operation, C is a constant, ω is the spatial frequency variable (in radians per metre) and the x-axis aperture dimension is L. The spatial frequency bandwidth of the third term of eq. 4.4 is derived by stationary phase techniques. (eq. 3.50-3.54) A maximum image plane dimension u' corresponds as a result

to a maximum spatial frequency $\frac{4\pi u'}{\pi\lambda}$ radians per metre. Hence, from eq. 4.6 the maximum u'-value is:

$$\frac{4\pi u'}{\lambda z} < \frac{\pi L}{\lambda z}, \qquad \text{4.7}$$

and the largest u'-axis image spread is just L/2. An example of a long thin wire imaged in this manner by real-aperture microwave holography is shown in [14].

4.2.5 Cylindrical Objects

For the purposes of accounting for specular reflection, cylindrical objects can be represented with a complex reflectance indicating curvature in one axis. If a long cylinder has its axis of symmetry aligned with the u-axis, then the approximate reflected field in a plane tangent to the cylinder is:

$$A'(u,v) = e^{j\frac{k}{2z}(u^2+v^2)} . e^{j\frac{k}{2f}(v^2)} \qquad \text{4.8}$$

The reflected field appears to have originated, at least in the u-axis, from a point z behind the plane tangent to the cylinder surface facing the array antennae and in the v-axis, from a point $\frac{f}{1+f/z}$ behind the same plane. The cylinder radius of curvature is 2f. Images of cylinders using the paraboidal illumination wavefront synthesised by the orthogonal array system thus exhibit different object wave focal lengths in orthogonal axes. The result is also applicable if the cylindrical long axis lies at another angle in the (u,v) object plane.

4.2.6 Spherical Objects

Extending the description of the cylindrical reflectance leads to the approximate field A'(u,v) reflected from a sphere and measured in a plane tangent to the sphere:

$$A(u.v) = e^{j\frac{k}{2z}(u^2+v^2)} . e^{j\frac{k}{2f}(u^2+v^2)} \qquad \text{4.9}$$

The reflected field appears to have originated from a

single point scatterer $\frac{f}{1+f/z}$ behind the tangent plane. The radius of curvature of the sphere is 2f, and it is taken as positive, but a portion of a spherical surface object seen as concave from the array will have f a negative quantity.

The analogies between the behaviour of optical components and the much larger specular objects considered here have been of some value in checking the operation of the prototype orthogonal array holographic imaging system. Simple geometrical optics theory is adequate to describe the salient aspects of the expected imagery.

4.2.7 Specular Effects with Regularly Spaced Objects

Two point scatterer objects spaced Δ apart can be rendered as two distinct images if their separation is sufficiently large. The analysis is again based on the description of the reconstructed image (eq. 4.4), but for the sake of clarity, only one image u'-axis is considered, and the non-offset reference wave mode (p = 0) used in the prototype system is assumed. The object is represented as:

$$A(u) = \delta(u \pm n\Delta/2), \text{ where } n = 1 \quad \text{---------- 4.10}$$

Hence the image u'-axis field is just:

$$I(u') = e^{j\frac{k}{z}(\Delta^2)} \cdot (\mathrm{sinc}(\tfrac{kL}{2z}(u' \pm \Delta u))) \quad \text{---------- 4.11}$$

The image has two cophasal distributions which are replicas of the impulse response. The object is resolved if the spacing Δ is somewhat in excess of the Raleigh resolution limit of $\frac{\lambda z}{L}$, since this limit does assume the use of incoherent radiation.

It might appear that a large regularly spaced object would be free of specular effects, but an example indicates the opposite. The regular object array is described:(|n| is odd.)

$$A(u) = \delta(u \pm \tfrac{n\Delta}{2}) . \mathrm{rect}(\tfrac{u}{u_o}), \text{ where } u_o \text{ is the total}$$

object width. The corresponding image amplitude is:

$$I(u') = \delta(u' \pm \frac{n\Delta}{2}) . e^{j\frac{k}{z}(u'^2)} . \text{rect}(\frac{u}{u_o}) \otimes \text{sinc}(\frac{kLu'}{2z}) \quad \text{------- 4.12}$$

The assumptions made in sec. 4.2.3 are also made here. The restrictions on object spacing (Δ) and number ($n+1$) are best examined from the domain of the image spatial frequency spectrum. (Fig. 4.4) The convolution operation in eq. 4.12 becomes, in this domain, a rectangular "window" $2\pi(\frac{L}{\lambda z})$ radians per metre in bandwidth. (eq. 4.6) The first three terms of eq. 4.12 represent a parabolic wavefront of total width u_o sampled at an interval Δ, and has a spectrum proportional to:

$$\text{rect}(\frac{\omega\lambda z}{4\pi u_o}) \otimes (-1)^m . \delta(\omega \pm \frac{2\pi m}{\Delta}) \quad \text{------------------ 4.13}$$

where $|m|$ takes zero and integral values. The convolution operation copies the spectrum of the continuous field $\exp(\frac{k}{z}u'^2)$ with centres at multiples of $\frac{2\pi}{\Delta}$ radians/metre. (Fig. 4.4)

If object spacing is so small that only the spectrum of the continuous field is preserved by the resolution "window" of the system, then no image periodicity is apparent, and object length u_o should not exceed $L/2$, by eq. 4.7. If, on the other hand, u_0 is sufficiently small so that the system resolution "window" is much larger than $2\pi(\frac{2u_o}{\lambda z})$, then image periodicity will begin to be apparent when:

$$\frac{2\pi}{\Delta} < 2(\frac{L}{2\lambda z})$$

This implies that the object spacing must satisfy:

$$\Delta > 2(\frac{\lambda z}{L}) \quad \text{---------- 4.14}$$

This value is just twice the Raleigh (incoherent) resolution limit. An approximate limit to the total number of object points $n+1$ which can be imaged is derived by assuming that only one sideband pair need to be included within the resolution window. (Fig. 4.5) On this basis. the maximum object length is:

$$u_o = \frac{L}{4}$$

The minimum object spacing is:

$$\Delta = 4(\frac{\lambda z}{L})$$

The total number of points that can be imaged is thus:

$$n+1 = \frac{u_o}{\Delta_o} = \frac{L^2}{16\lambda z} \qquad \text{4.15}$$

From eq. 3.54, the spatial bandwidth occupied by a field L in extent and originating z from the array is $\frac{L}{\lambda z}$. Hence eq. 4.15 suggests that the total number of points that can be imaged when these are assembled into a regular array is a fraction of the system aperture-bandwidth product, a result which is completely analogous to the operation of the linear FM-pulse compression process [65] used in the temporal domain.

4.3 Examples of Reconstructed Images

4.3.1 Hologram Transparency Preparation

The images considered in this chapter have all been reconstructed from hologram transparencies prepared from data photographed from a storage oscilloscope screen. A signal component (I or Q) of the complex received signal (Fig. 2.3) modulated the z-axis (brightness modulation axis) of a storage oscilloscope, while the position of the transmitting and receiving array element pair active at a given time was represented in x-y mode on the screen. No attempt was made to preserve data dynamic range, and following popular practice, "hard-limited" binary holograms were used. The data was manually transferred to an accurate scale grid representing the projected aperture in use at the time, and reduced photographically. Including the reduction in the optical reconstruction processor, the overall dimensions of the hologram were reduced by a factor K, where K = 350. Further details of the optical reconstruction process are given in Appendix I.

4.3.2 Image Analysis

The optical reconstruction processor used in this thesis is shown in Fig. 3.2. The plane wave illumination format implies a simple and direct relationship between object (mapping) domain and image domain distances (focal lengths). Image distributions were recorded directly in their respective focal planes, using a standard camera with lens removed as a convenient film holder and timer. The images are characterised by a dominant zero-order central distribution representing the "background" terms of eq. 3.5. and a two-dimensional spatial harmonic structure of the hologram sampling grid. The (required) real and diffused virtual image distributions accompany the zero-order background and all sampling harmonics. All measurements have been made using the real image component accompanying one of the first-order sampling maxima, as the image plane extent of these is significantly less that that of the zero-order terms. (sec. 3.6)

The hologram reduction factor (350) is much less than the wavelength ratio (about 48 000) of respective microwave mapping and optical reconstruction domains, so that the reduced transparencies are characterised by many sampling grid maxima, and the paraxial description is completely adequate over many such maxima in the optical domain. (Appendix I) Image analysis is made using optical transparency magnification, and the periodic sampling and image structure served as an invariant scale for the purpose of predicting object (mapping) domain detail. This procedure takes the fractional image offset in the reconstructed image, and knowing the paraxially-approximate repetition interval in the object (mapping) domain, compares the product of the two with the measured position of corresponding object detail. (Appendix I) The only linear measurement required in the optical domain is that of focal length z'. Given the known scale factors, the object

domain distance (focal length) z is:

$$z = 2.56\, z' \qquad (4.16)$$

4.3.3 2 x 1 Array and Planar Object

An early deployment of the microwave arrays had two vertical transmitting and one horizontal receiving arrays. The object was a simple rectangular mesh plane, with a mesh period much less than the system lateral resolution and as a result treated as a planar conducting object. The array and object geometry are presented from the point of view of an observer facing the microwave radiating elements. The vertical array offset was caused by the waveguide directional coupler used in this plane. The horizontal array was 20mm further from the object than the transmit array, but in view of the characteristically extended depth resolution (sec. 3.3.4) did not limit performance. (Fig. 4.5)

A bright image maximum (indicated in Fig. 4.5 (c)) is found at $z' = 395$mm. The mesh object was parallel to the hologram and at 480mm range. The image focal length $z' = 395$mm corresponds, using eq. 4.16, to a mapping domain object wave focal length $z = 1010$mm. This value is within 5% of twice the planar object range, and so illustrates the simple theory of sec. 4.2.1. The real image has been reconstructed and presented from the same aspect as in the mapping stage, so as to aid the geometrical elucidation of the image plane measurements. In the crude hologram (Fig. 4.5 (b)), the contours of equal relative phase suggest clearly an image to the left of the aperture. An image maximum appears to the left of the defocussed first order component (Fig. 4.5(c)) and has essentially no vertical offset. The horizontal offset is measured as 18% of the image repetition interval. From the paraxial

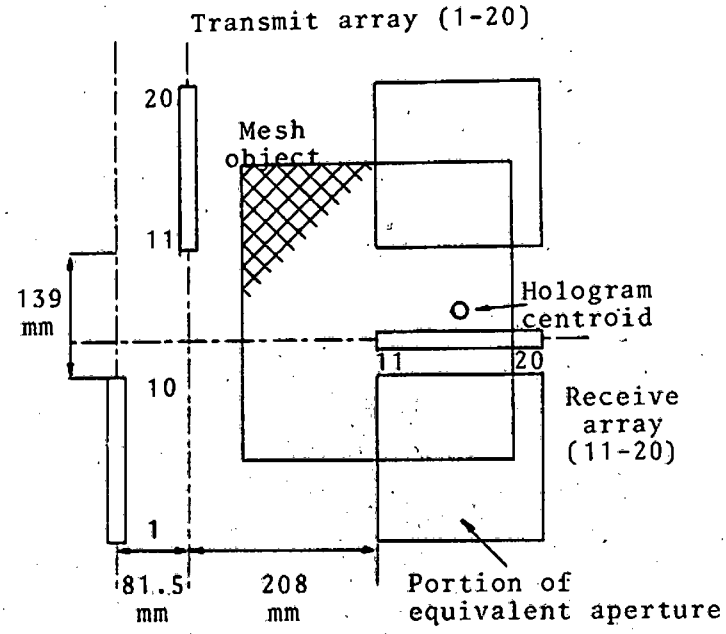

All subarrays 181.8mm overall aperture

Fig. 4.5(a) Hologram recording system and object geometry

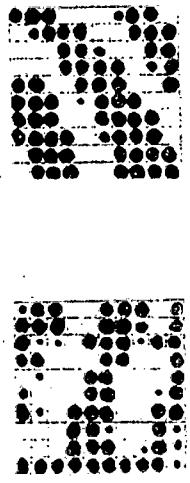

Fig. 4.5(b) Hologram

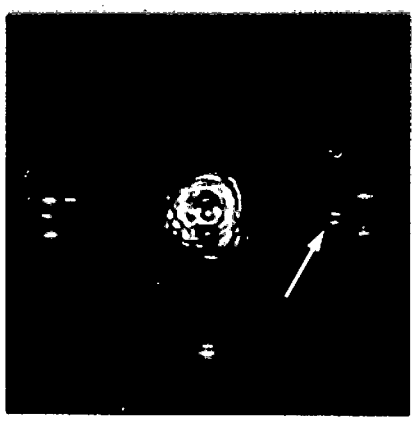

- Image is indicated by white arrow -

Fig. 4.5(c) Optical image found at z' = 395mm

reconstruction theory (Appendix I), the supposed (microwave array) mapping stage image repetition interval should be: $\frac{\lambda z}{\Delta x}$ = 1.52m. (The antenna interval Δx = 20.2mm, and microwave wavelength λ = 30.3mm.) The expected mapping stage offset is thus 18% of 1.52m, or 268mm. From Fig. 4.5(a), the illuminator is 380mm left of the hologram centroid, and according to the theory of sec. 4.2.1, the object wave origin is likewise expected 380mm left of the hologram centroid. The error in position of this object wave origin inferred from the image and more directly from Fig. 4.5(a) is 112mm, but this is within the spatial resolution of this axis (170mm) calculated at the same range.

The image vertical position is very close to the horizontal axis. The mesh object, being parallel to the hologram aperture, causes the object wave origin to lie close to the centroid of the projected aperture. (Fig. 4.5(a)) The error in this axis is only 2% of the image repetition interval.

If the notion of an equivalent point illuminator at the intersection of the orthogonal (subarray) axes is strictly followed, then the system should be regarded as having two such illuminators horizontally spaced 81.5mm. However, the typical horizontal axis resolution (combined with the complicated "sidelobe" structure of the impulse response) did not justify such elaboration.

4.3.4 2 x 1 Array and Cylindrical Object

A cylindrical object was aligned with the transmitting array axis (Fig. 4.6(a)) and tilted in the plane normal to the array at an angle of 9.6m Rads. The cylinder portion opposite antenna 20 was closer to the hologram plane than lower antennae.

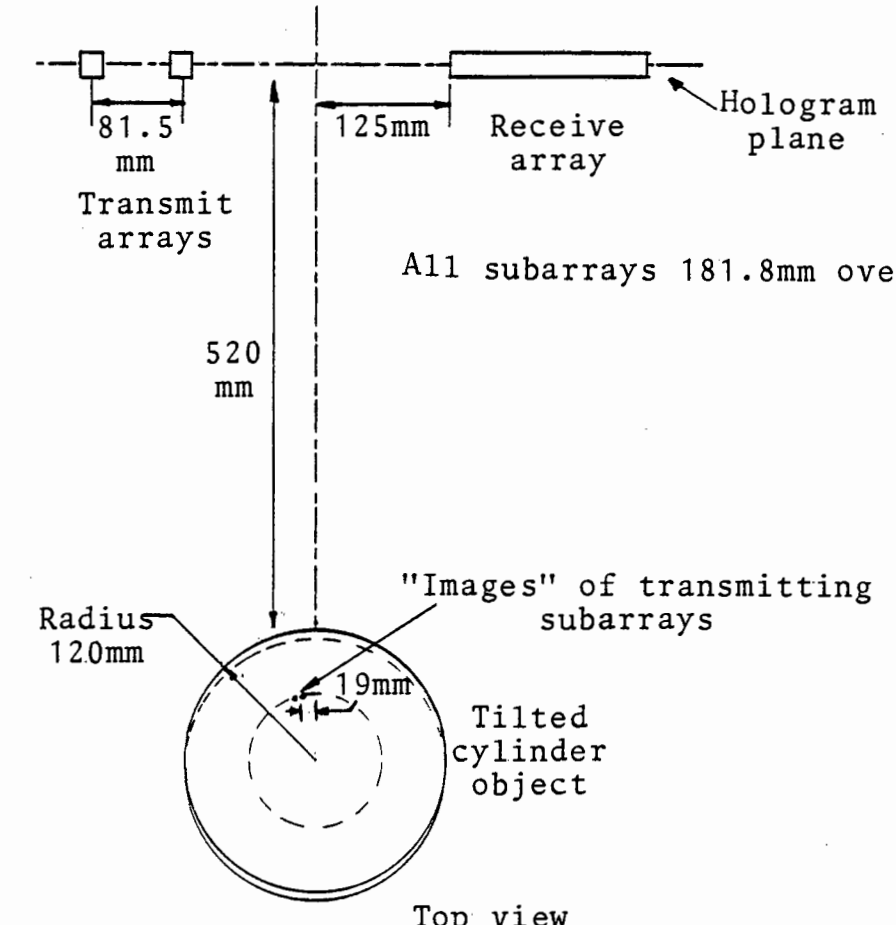

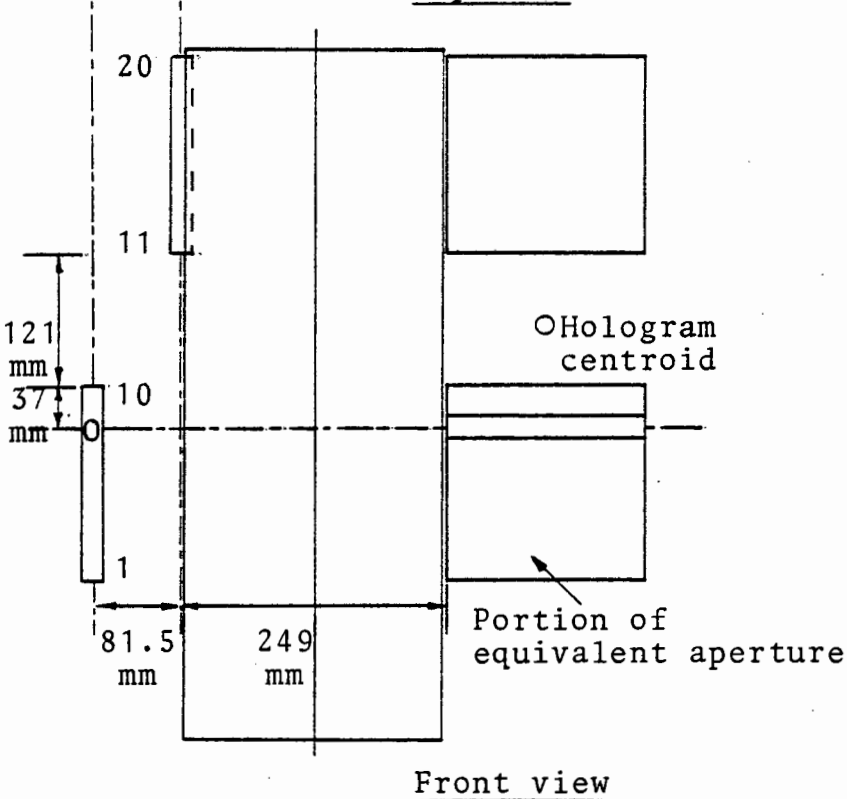

Fig. 4.6(b)
Hologram

Fig. 4.6(a) Hologram recording system and object geometry

- Image components are indicated by white arrows -

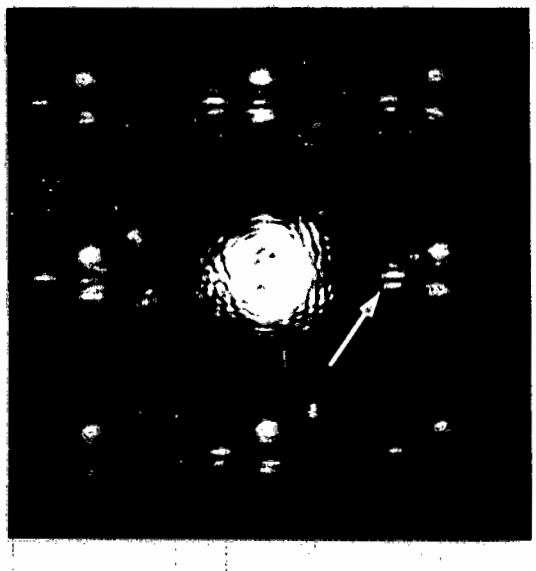

Fig. 4.6(c) Image found at z' = 400mm

Fig. 4.6(d) Image found at z' = 200mm

A bright specular image maximum is found at z' = 400m (Fig. 4.6(c)) and corresponds to a (microwave) mapping domain range z = 1023mm, using eq. 4.16. The fractional image offset in the horizontal axis is 26%, (391mm in the mapping domain, using the paraxially based reasoning of Appendix 1), and the vertical offset (-2.6%) corresponds to -39mm in the mapping plane. The cylindrical object tilt of 9.6m Rads. causes the object wave origin apparently found in this plane to be raised 10mm. From Fig. 4.6 (a) and the theory of sec. 4.2.2, the illuminator at 0 would be 98mm below the hologram centroid and the object wave origin is calculated as 10mm higher or -5.7% of the image repetition interval. It is significant that both object geometry and optical image predict maxima below the hologram centroid.

The theoretical distance to the focal plane corresponding to the cylinder scattering line (taken here as half the cylinder radius below the object surface, from sec. 4.2.5) is z' = 200mm. The image is characterised by two separate components horizontally offset by 27% of the image repetition interval, corresponding to 204mm in the mapping plane. From Fig. 4.6(a), the scattering centre will lie in the direction of the vertical array as seen from the cylinder centre. The expected scatterer offset is thus 235mm from the hologram centroid; the error is only 31mm compared to the horizontal axis resolution of 97mm at the half intensity points. The horizontal axis resolution for Fig. 4.6(d) is 78mm (referred to the mapping domain), which does show that the scattering centre is correctly resolved. The locus of the (horizontal) image with increasing range beyond the focal point was shown (sec. 3.3.4) to be a straight line joining hologram centroid and object. The same fractional image offset at both z'=200mm (27%) and z'=400mm(26%) is confirmed in this example.

The lateral offset of the two transmit subarrays (81.5mm) is not important in this example since the cylindrical surface acts to demagnify the "images" of the individual subarrays, such that their separation is negligible. However, the differing path lengths do introduce a phase discontinuity in the object wave recording causing a shift of the impulse response structure within the overall "sinc" envelope. This effect is considered in Appendix 1.

4.3.5 2 x 2 Array and Convex Object

An image characteristic of a point reflector and obtained using a large (900mm) diameter searchlight reflector (414mm focal length) presenting its convex surface to the microwave arrays tends to confirm the equivalent illuminator-and-areal-aperture model in the expanded holographic system. (Fig. 4.7)
The apparent object wave origin is derived from eq. 4.9, and the expected hologram to image maximum range is $z = 1106$mm. referred to the mapping domain. The optically reconstructed image (Fig. 4.7 (c)) is found at $z' = 450$mm, corresponding to $z = 1150$mm in the mapping domain. The range difference to the two apparent sources, developed by the lateral offset of the vertical subarrays, induces only 0.1 radians relative object wave phase shift. The demagnifying effect of the convex surface results in only 10mm lateral (receive array axis) separation of the two apparent sources, and being almost cophasal, they are not resolved at this range.

4.3.6 An Image series using the 2 x 2 Array

A rigid planar aluminium sheet (450 x 535mm) has been

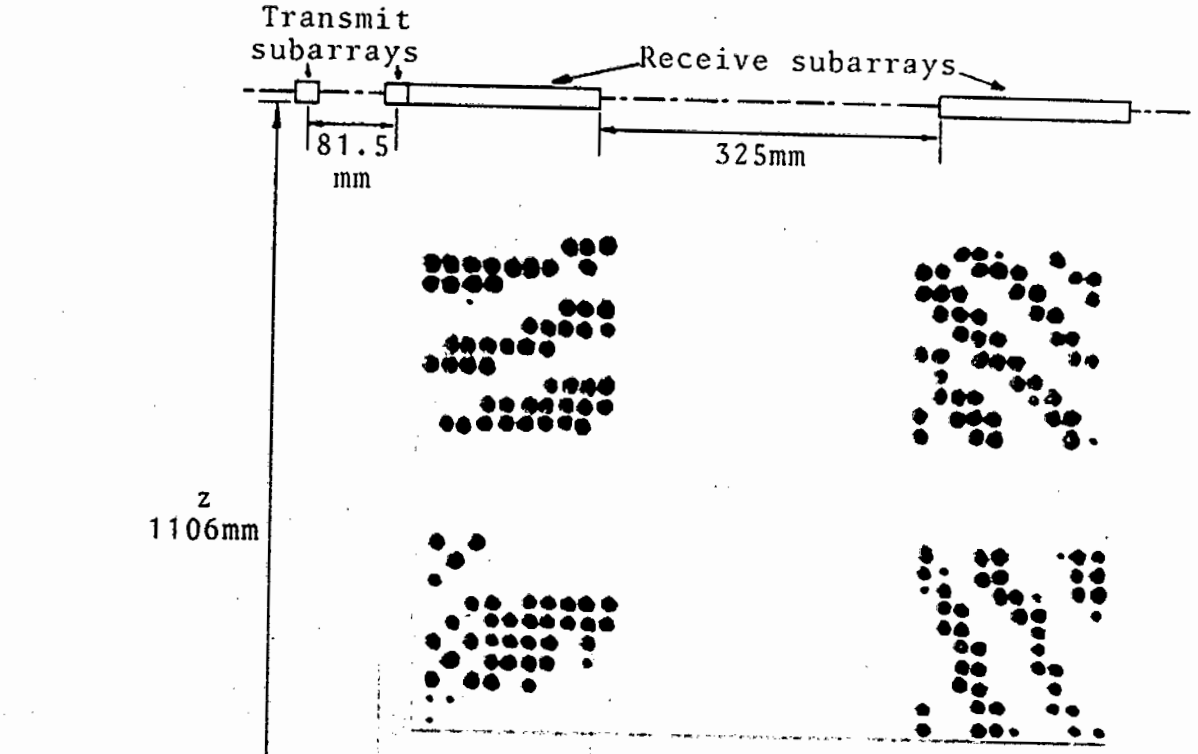

Fig. 4.7(b) Hologram

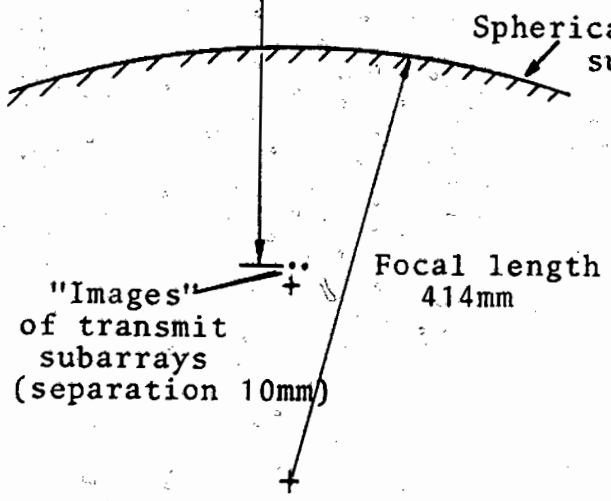

Fig. 4.7(a) Hologram recording system and object geometry

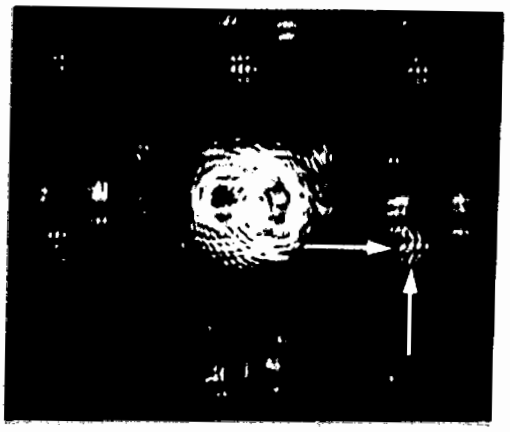

Fig. 4.7(c) Image found at z' = 450mm

Fig. 4.7 Imaging a convex object using the full 2 x 2 array

used to check the image plane trajectory of the object wave origin as the sheet rotated throught 38^{o} (in 2^{o} increments) from -26^{o} to $+12^{o}$, relative to a plane parallel to and at a range of 673mm from the hologram aperture. (Fig. 4.8) A series of 20 images is given in Fig. 4.8 (c) and the initial and final holograms of the set clearly suggest by their contours that the image maximum has migrated across the aperture from right (-26^{o}) to left ($+12^{o}$). (Fig. 4.8 (d)) The trajectory of the specular image maximum increases with object angle (Fig. 4.8 (e)), but is sensibly constant in the vertical axis. The axis of rotation made an angle of 1.6^{o} with the vertical (transmit) axis such that the object wave origin appeared higher than the equivalent system illuminator. (sec. 4.2.2) Fitting a straight line to the data of Fig. 4.8 (e) predicts zero image effect for an angle of -13^{o}. Applying previous reasoning, this prediction is in error by only 32mm, which is about 30% less than the image lateral resolution at this range (referred to the mapping domain), and taking into account the interrupted horizontal aperture. The slope of the linear fit to the data of Fig. 4.8 (e) is 1.1% of the image repetition interval per 1^{o} of object aspect change, and corresponds to 0.93^{o} of apparent planar object aspect change per 1^{o}. Significantly, the image trajectory predicts smaller, more conservative offsets than those controlled experimentally. Referring to Fig. 4.8 (b), the $+12^{o}$ object position would seem to predict 660mm specular image offset from the hologram centroid, in contrast to 480mm from the optically reconstructed image, referred to the mapping domain.

This lack of accuracy is attributable to violation of

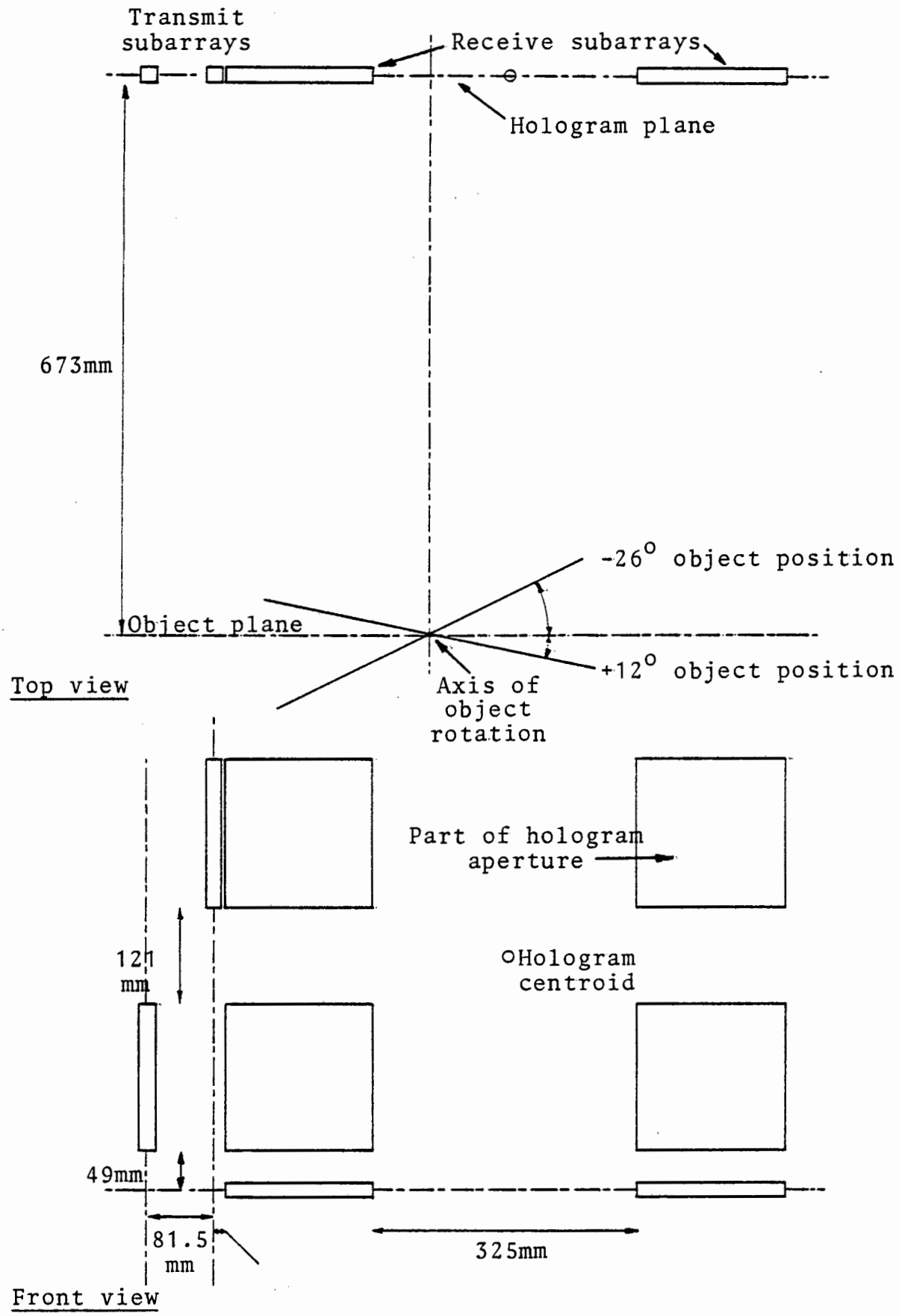

Figs. 4.8(a) and (b) Hologram recording system and variable angle object geometry

- Images are indicated by white arrows -

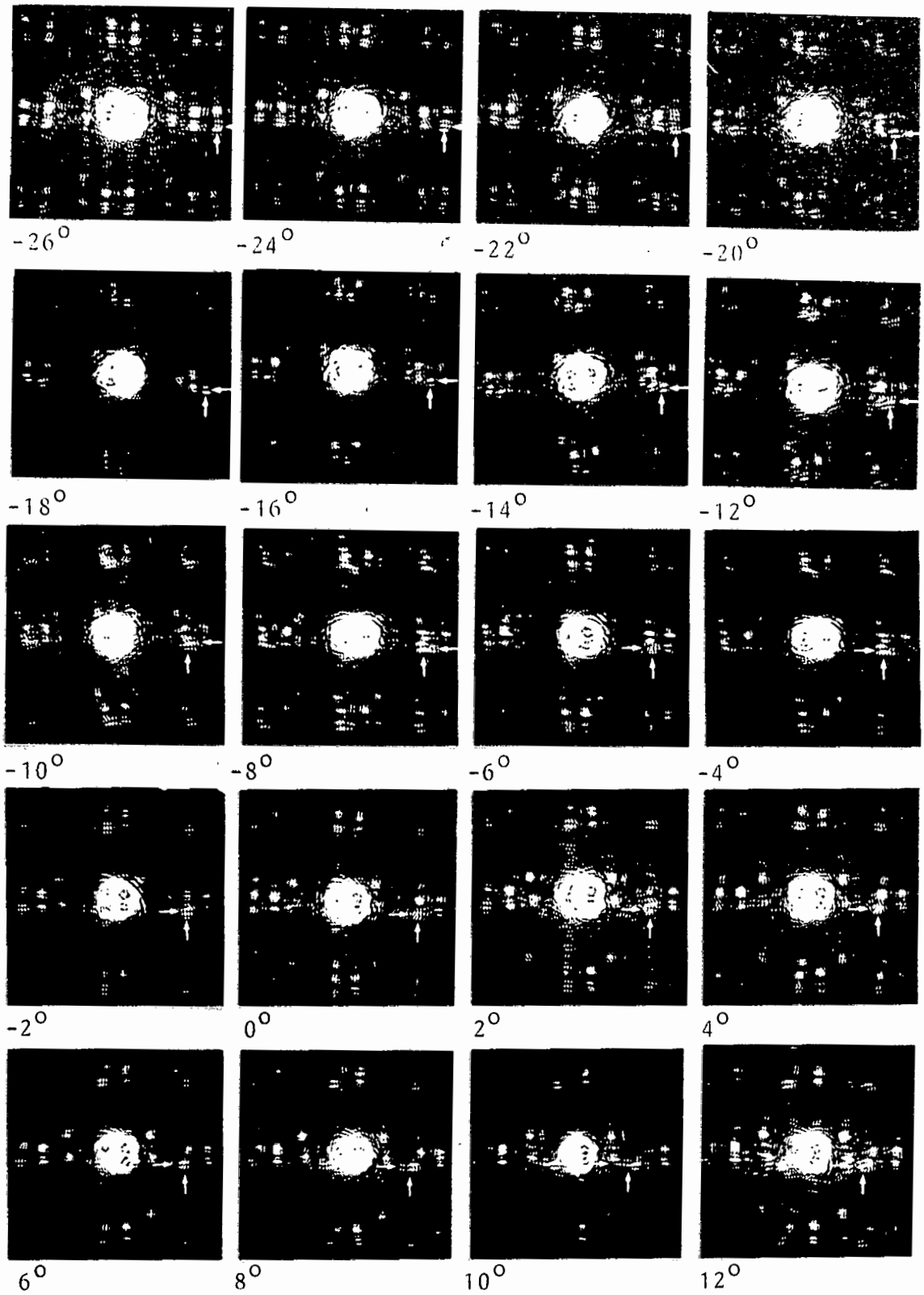

Fig. 4.8(c) Image series for 38° range of object aspect

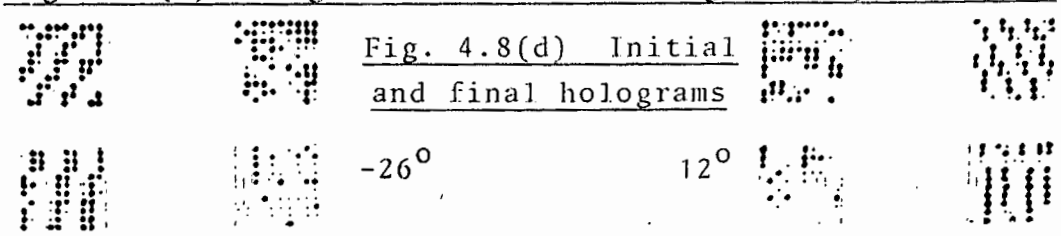

Fig. 4.8(d) Initial and final holograms

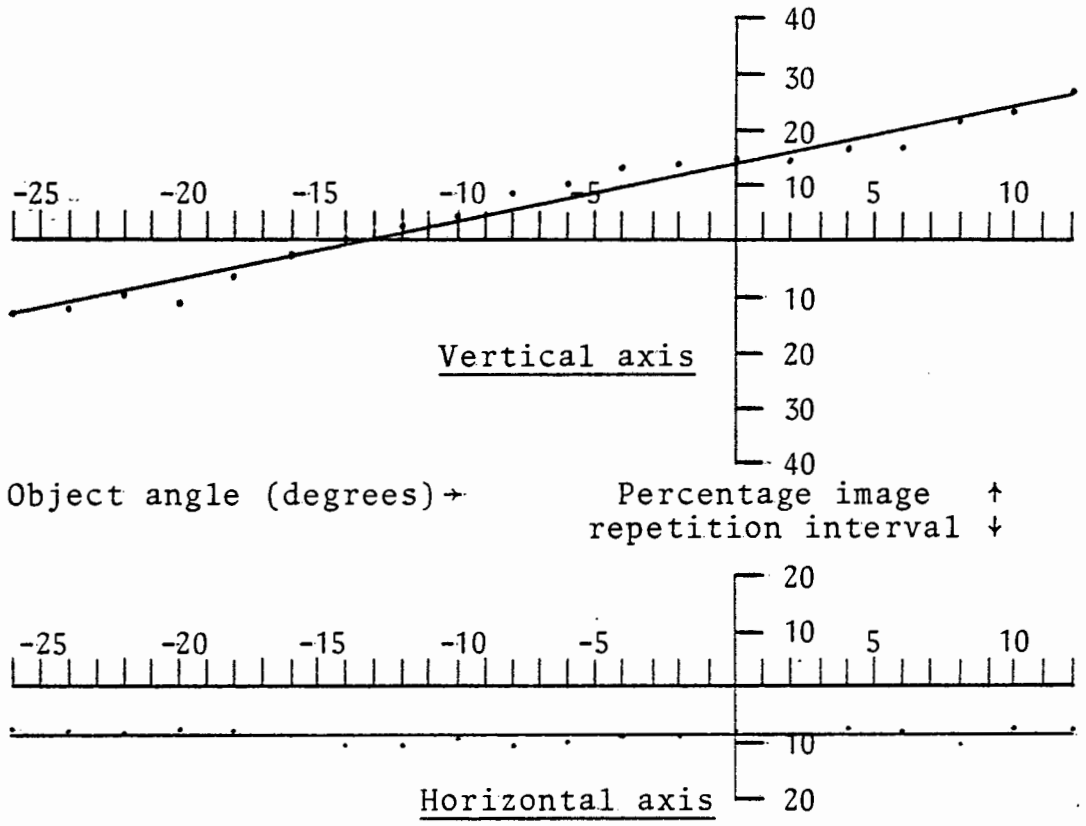

Fig. 4.8(e) Linear fit to image centre positions for 38^{o} range of object angle

the Fresnel paraxial approximation at larger angles. (sec. 3.4) The optical reconstruction system has a maximum width between centre and largest unambiguous image position of 3.3mm in this particular example, and the paraxial approximation is entirely adequate to about three times this distance. (Appendix I) In the mapping domain, however, the same criterion is only valid to an offset of 400mm, and the resulting misapplication of the optical processor results in characteristically conservative image offsets. A single-axis simulation of the $+12^{o}$ object geometry using paraxial reconstruction predicted 425mm image maximum offset, or just 55mm different from that value inferred from the optical image. The same simulation at the other extreme object position (-26^{o}) showed agreement to within 40mm. The paraxial approximation violation tends to produce a hologram which has less fringes, or equivalently, given a point scatterer object, the phase of the wave front recorded in the hologram plane is less dispersive than that of the (assumed) paraboloid. The nature of the reconstruction process is such that the reconstructing field fits the object field best when the paraxial reconstructing wavefront is of relatively longer focal length and has less offset.

CHAPTER 5

Computer-assisted Image Reconstruction

5.1 Introduction

The inclusion of a digital computer in the two step holographic imaging process facilitates the rapid manipulation of both hologram data and image. Additionally, the known systematic limitations of the mapping stage can be corrected. If a two channel receiver is used to generate complex hologram data from I and Q (Fig.2.3) components, then phase and amplitude errors of the elements of the transmitting and receiving arrays can be compensated, and the unwanted data arising from the direct coupling between these two arrays can be removed.

Accurate complex data representation may improve image contrast, since the desired image need not be overlaid by the (defocussed) conjugate image distribution and/or the fields arising from the necessary inclusion of a bias term in the optical analogue hologram. This is not to dismiss optical reconstruction as unworthy of consideration, since it has the significant advantage of parallel processing, continuous output, and negligible delay, once the hologram has been prepared. As an example, the doubling of aperture dimensions in a holographic system relying on optical reconstruction would not affect image formation time, but the image computation time in a serial processor might be drastically increased, as the data handled would be quadrupled, and probably more image plane points would be desirable.

The reconstruction procedure applicable to synthetic aperture radar (SAR) is of comparable complexity, but only quite recently have dedicated digital systems been designed for practical imaging; not the least of the problems involved is the very high data rate, quoted in one spaceborne imaging system as approaching 100Mbits/second.[105]

There are optical analogue techniques available whereby the hologram emergent field represents substantially the original object wave unaccompanied by other terms. An early technique [106] is essentially a two-dimensional coherent optical implementation of a single-sideband processor and combines two holograms mapped by an orthogonal reference wave pair. A more elegant approach [107] uses the principle of the (stepped) Fresnel lens. Both appear to require some skill and possible delay in preparation.

A computer-based reconstruction technique lends itself to the exploitation of image planes where the scaled optical impulse response differs from that of the mapping stage. Such a technique is explored in the latter part of this chapter as a variant of the planar object imaging system. The limitations on lateral resolution imposed by the Fourier transform relationship between image impulse response and hologram aperture occupancy can be alleviated by recourse to more recent spectral estimation algorithms [108], developed for time series analysis, but equally applicable in two-dimensional form in the spatial domain. These techniques appear to offer substantially better resolution and are less sensitive to the effects of additive data noise than techniques such as superdirectivity. [109-111]

As well as conventional digital reconstruction from complex data, a hybrid technique is also used in sec. 5.6, wherein the potentially obscuring cross-coupling field is removed and image contrast improved in an optical reconstruction system. A synthetic offset reference wave is added to the hologram data after the recording stage, and the result used to regenerate the phase-only (binary) optical hologram transparency.

5.2 The Geometry of the Microwave Hologram Mapping System

In the interests of reliability, the array hardware was transferred to a rigid support with subarrays accurately aligned in their respective axes and fitted to a regular grid. The arrays were also accurately coplanar, and were arranged with axes crossing near the centroid of the equivalent hologram aperture to maximise the system pointing accuracy with the paraxial reconstruction processor. (Figs 5.1 and 5.2; sec. 3.4)

5.3 Subtractive Field Techniques in Microwave Holography

Wavefront subtraction has been variously suggested to improve microwave holographic imagery. That routinely used in this work generated a complex difference hologram from two recordings. The object was only introduced in the latter stage. If the field arising from the direct transmission between active elements (a "cross-coupled" field) can be regarded as leading to an unwanted image component, then the subtraction procedure is similar to that proposed by Kujoory and Farhat [47], except that their subtraction operation was carried out analogously and the image optically reconstructed from a double exposed hologram. Their process relies on film linearity, generates low-level intermodulation products, and allows only low modulation depth and consequently a poor ratio of image to zero order distribution intensity.

By contrast, the computer-based subtraction is trivially and speedily accomplished with either real or complex date. For effective removal of the cross-coupled component, the linearity condition must be extended to the mapping stage. No interaction between cross-coupling and object field is permissible, but the hologram-object geometry mitigates against this possibility in practice.

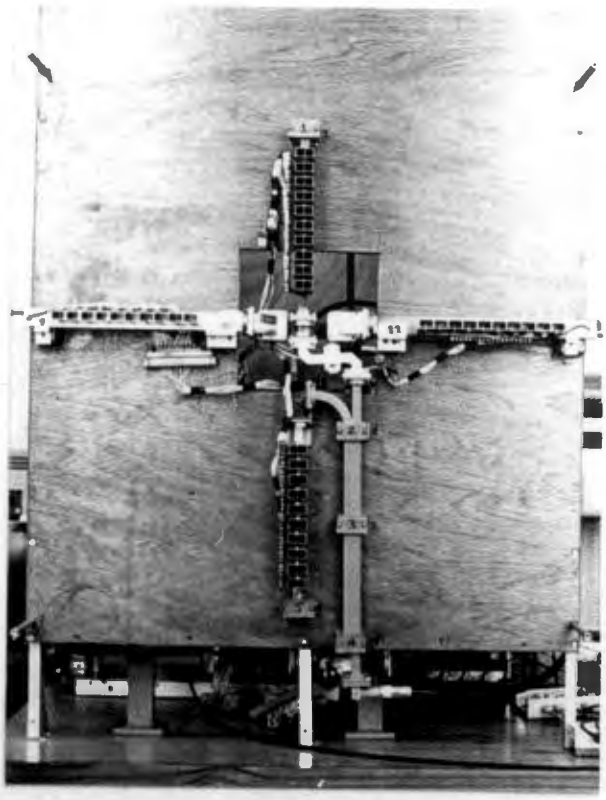

Fig. 5.1 Front view of array elements

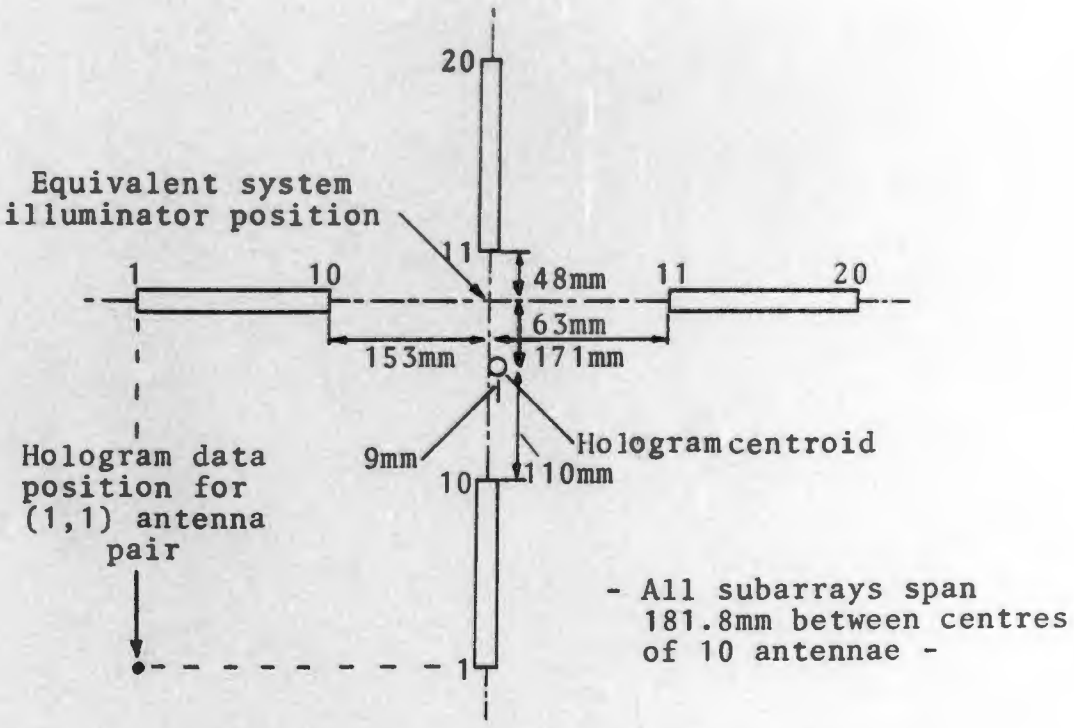

Fig. 5.2 Crossed array dimensions

The enhancing of bottom surface reflections in the presence of much larger top surface returns has been subtractively performed in the holographic ice surveying system (HISS) [45], and the imaging of blockage effects in aperture antennae has been facilitated by removing from the holographically mapped data the field predicted for the undisturbed aperture. [53]

5.4 Generating an Offset Reference Wave

The crossed array geometry optimises the object region available to the paraxial processor (sec. 3.4), whether this is implemented by computation or optically but objects close to the (projected) intersection point of the arrays (Figs. 5.1 and 5.2) tend to lead to images obscured by the central zero order background and periodic distributions produced by the sampled hologram structure. The periodic image property is, however, a valuable feature in retrieving image lateral dimensions, and an interim reconstruction scheme added an offset reference wave to create a binary hologram. (The array design was based on the slotted wall resonant waveguide distributor, and the reference wave function accordingly was coplanar with the plane of the transmitting and receiving elements; see sec. 2.3) Data corresponding to orthogonal components of the received field found with and without object were converted to polar form and an incremental phase shift of 4.2 radians per element added to the complex hologram (enhanced by the subtraction process) in both vertical (transmit) and horizontal (receive) axes. Taking one component of this, and hardlimiting produced a binary reduced-format transmission hologram.

From the theory of sec. 3.7, the reference wave subtends an angle of 45^{o} with the array plane, and, from eq. 3.70 the image lateral offset, referred to the mapping domain,

becomes just the object range z. In the reduced scale optical image, the image offset becomes $\frac{z}{K}$ in each axis, using eq. 3.21. (K is the overall hologram reduction factor) The image repetition interval is, from Appendix I, just $\frac{1}{K}(\frac{\lambda z}{\Delta x})$, where the element spacing Δx (in both x and y axes) is 2/3 of the microwave wavelength. In the optical image, the deliberate offset is thus 2/3 of the image repetition interval.

The orthogonal receiver I and Q outputs were sampled sequentially by a single analogue-to-digital converter for the first 400 antenna pair intervals after the (1,1) pair epoch. Total data gathered amounted to 1600 samples, from which a 400-point complex hologram was calculated wherein the object wave phase was unambiguously resolved in the range -90^{o} to $+270^{o}$. (This was a range of 360^{o}) All hologram data was gathered in two separate one second intervals.

5.5 Examples of Optically Reconstructed Images

5.5.1 A Rectangular Planar Object

A large rectangular planar object, placed approximately coplanar with the array plane at a range of 765mm resulted in an offset image maximum (Fig. 5.3(a)) at a focal length $z' = 594$mm in the optical reconstruction processor. The corresponding mapping plane dimension $z = 1.52$m is very close to twice the real object distance expected of such an object. (sec. 4.2.1) The superior image contrast possible with the synthesised reference wave manipulated after the recording operation can be assessed by comparison with the same image plane derived from a non-offset reference hologram. (Fig. 5.3(b)) Here, the image maximum corresponding to the apparent object wave origin is superimposed on the central zero order and sampling structure distributions and is by

- Images are indicated by arrows or in outline -

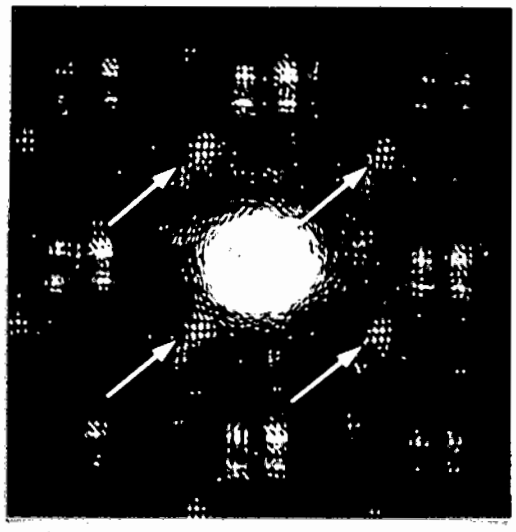

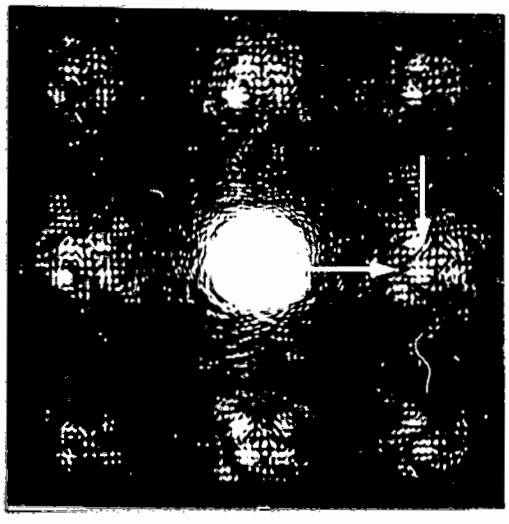

Figs. 5.3(a) and (b) Specular image component from planar object (Reference wave is offset in left image)

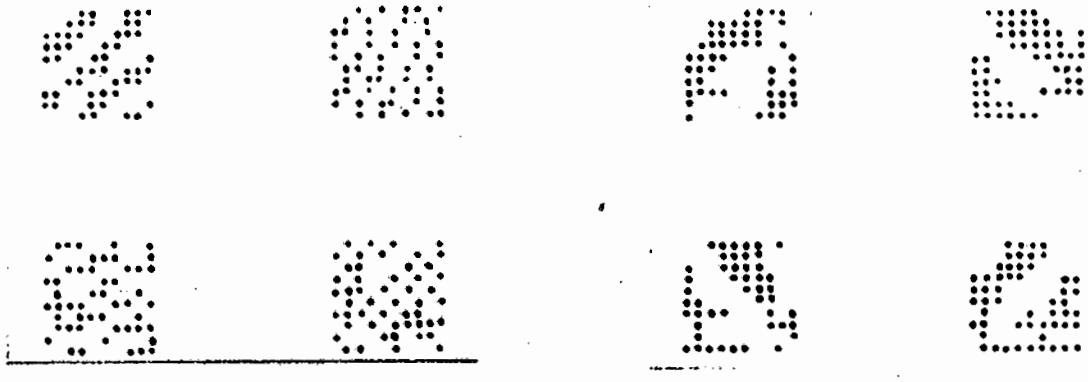

Figs. 5.3(c) and (d) Offset(left) and non-offset holograms

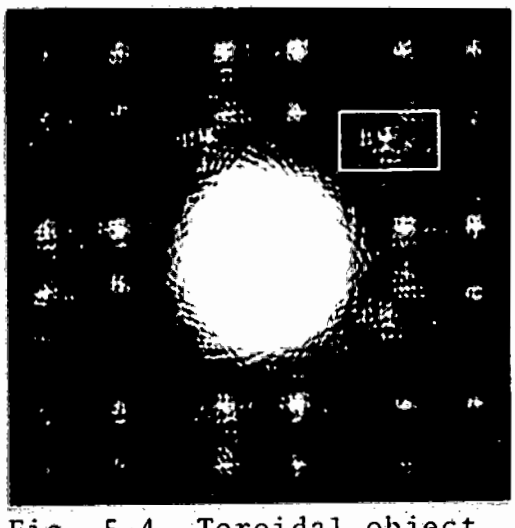

Fig. 5.4 Toroidal object Note central bright region

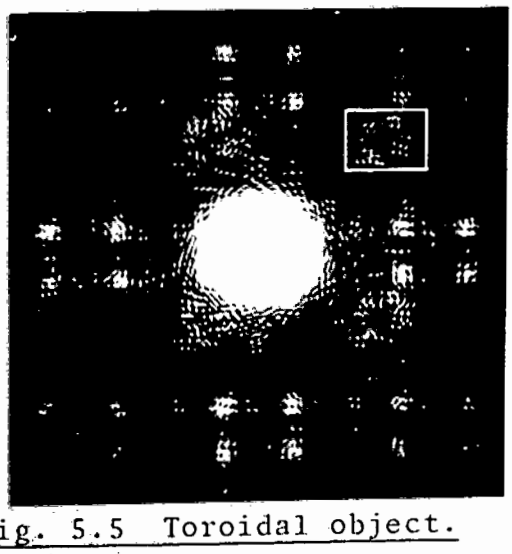

Fig. 5.5 Toroidal object. Internal reflections have been suppressed here

no means obvious. The respective offset and non-offset holograms (Figs. 5.3(c) and 5.3(d)) are mirror images of those used in the reconstruction process, but it is evident that in the former the lowest spatial frequencies, indicating the direction of the image maximum, are to the top and right, in contrast to the symmetrical appearance of the non-offset hologram.

Measured image lateral offset as a fraction of repetition interval is 67% horizontally and 65% vertically. 67% is introduced deliberately in both axes, and the measured object tilt of 19 mRadians accounts for -1.3% offset in the vertical aspect. (Fig. 5.3(a);sec 4.2.2)

5.5.2 A Toroidal Object

A circular image is obtained using an ordinary car inner tube, covered with metal foil. The image is found at $z' = 2.82$mm, corresponding to 36mm more than the object range of 690mm to the nearest surface, when referred to the mapping domain. The minor diameter of the torus (140mm) would suggest a focal length of 35mm for this surface. The torus major diameter was 360mm and that estimated from the image is slightly conservative (308mm), since the object is close to the paraxial minimum range.

The appearance of a bright central region within the fainter extended circular image is evidence of internal torus reflections and is not due to any "ghost imagery"[112] generated by the thresholding operations necessary to derive the binary hologram. The result of a similar experiment (Fig. 5.5), performed using the same object but with an inner circumferential lining of microwave absorptive material, demonstrates the removal of the central image component and provides a rather more distinct image of the torus. The circular image is broadened by the extended impulse re-

ponse of the system. The estimated object diameter of 300mm from Fig. 5.5 is also conservative. The position of the image centre is correct to within the calculated lateral resolution at this range.

5.5.3 A Regularly Corrugated Object

An image of a tilted corrugated object (Figs. 5.6(a) and 5.6(b)) shows marked specular character. The measured image focal length of $z' = 720$mm is translated as $z = 1.67$m in the mapping stage. This figure is intermediate between twice the object range limits of 670mm and 1.05m and the vertical fractional offset indicates an apparent object wave origin at an angle of 16.3^{o} below the equivalent quasi-isotropic illuminator, allowing for the deliberate vertical axis offset. The horizontal image offset is negligible since the corrugations are parallel to the hologram plane.

The combination of superficial wavelength and amplitude leads to near-normal incidence reflection for a calculated depression of 16.7^{o}, and the incremental distance to neighbouring components of the corrugation is one wavelength at this depression angle. The corrugations in this angular region reflect cophasal components as from a sampled plane. The calculated depth resolution at this range (about 400mm is indicated from eq. 3.29) is insufficient to resolve the individual strips contributing to the specular effect.

Rotating the same object such that the corrugations are in the plane of the array (Fig. 5.7(a), yields a fainter image (Fig. 5.7(b)) at a reduced focal length $z' = 410$mm, corresponding to $z = 962$mm. The observed image behaviour larger focal lengths was such that the image was of superficial detail, since the image is characteristically focussed in the vertical axis, but horizontally extended. The corrected vertical image offset of -19.3% of the

- Images are indicated by arrows or in outline -

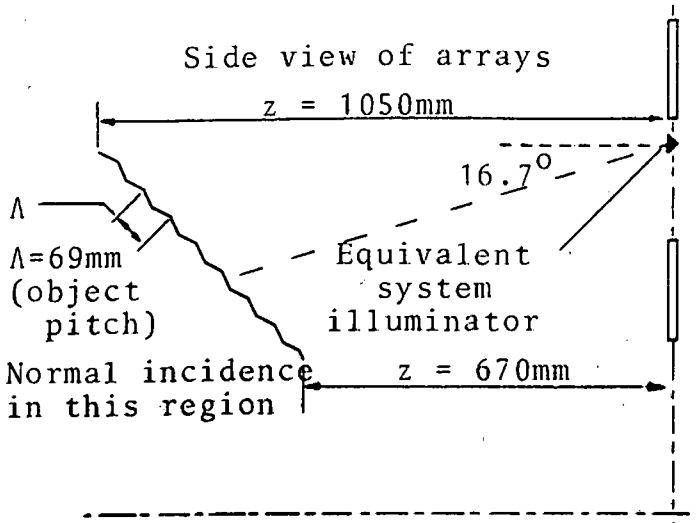

Fig. 5.6(a) Tilted object

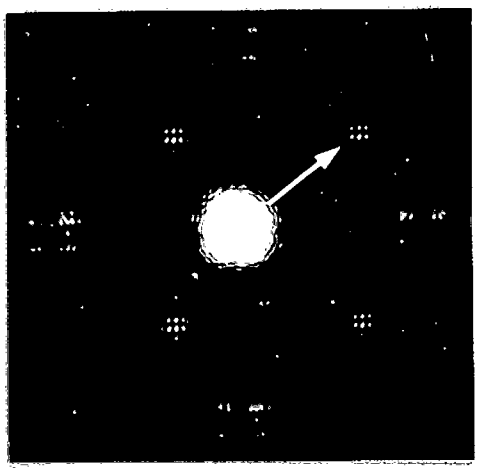

Fig. 5.6(b) Specular image

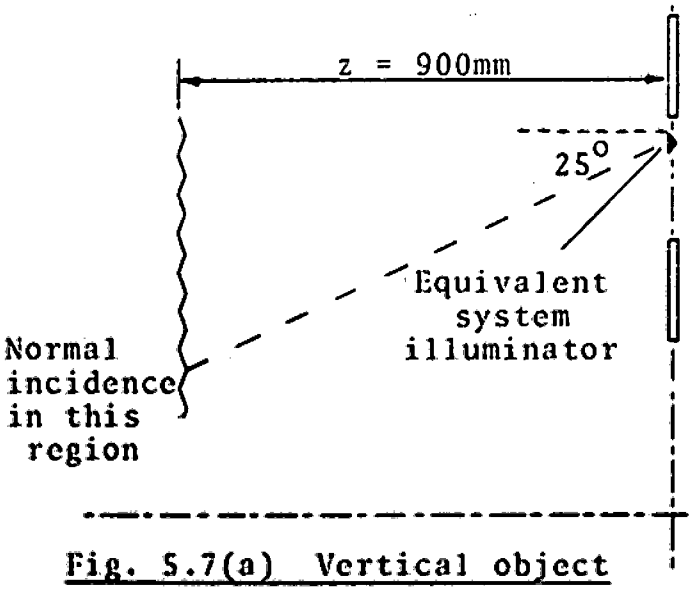

Fig. 5.7(a) Vertical object

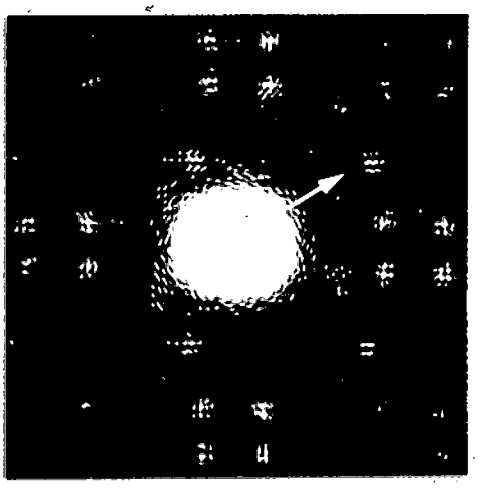

Fig. 5.7(b) Extended image

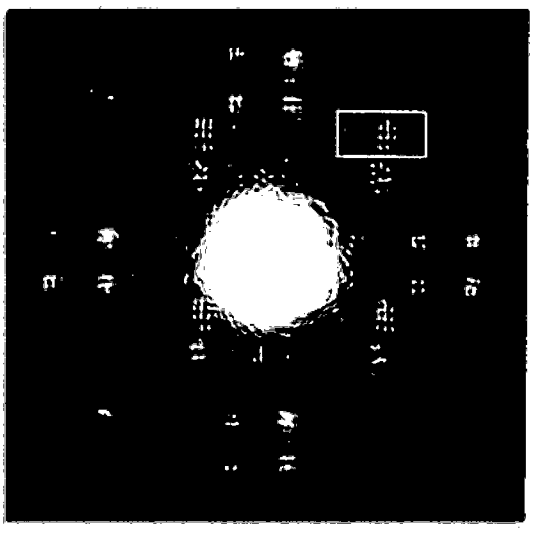

Fig. 5.8 Vertical cylinder object

repetition interval predicts a return from a region 19.5° below the equivalent illuminator. (Fig. 5.7(a)) Including the known vertical angular offset of the object, an object corrugation is expected to present normal incidence at a depression angle of 25°. The conservative image offset estimate is characteristic of the paraxial processor when used at excessive offsets. (sec. 3.4)

5.5.4 A Cylindrical Object

An extended image provides further evidence of the equivalent linear scatterer behaviour of a cylindrical object. (Fig. 5.8; sec. 4.2.5) The image is close to and slightly above a line from the image centroid and at 45° to the horizontal axis. A component below the highest proved to behave as a conjugate or defocussed virtual image with changing focal length in the optical processor.

The lateral image dimension is essentially that of the system impulse response in this axis, and the measured spacing of the three interrupted vertical lines is that expected at the calculated range z = 937mm in the mapping stage. (Appendix I).

The image centroid is found at 73.3% of the repetition interval in the vertical axis. Allowing for the deliberate offset of 67%, that remaining is very closely that expected of a cylinder whose centre is in line with the equivalent illuminator (Fig. 5.2) and consequently somewhat above the hologram centroid. The cylinder long axis was parallel to the mapping plane.

Vertical fractional extent of the real image component (23%) corresponds to an object dimension of 325mm or 66mm more than that measured. The object length is thus not accurately determinable given the complicated impulse response of the vertical axis which tends to extend

perceived lengths, and the conservative estimates produced by the paraxial reconstruction system.

5.6 Examples of Digitally Reconstructed Images

In this section a series of digitally reconstructed images using complex data holograms tends to confirm the object specular behaviour deduced from optically reconstructed images. The same set of objects as that used in the first section have been used again here. The paraxial reconstruction process was implemented as a direct deconvolution operation on the phase of the complex hologram, according to eq. 3.8, and, in contrast to the real image displayed in the optical system, the virtual image was computed here. The reference wave synthesised by the antenna commutation sequence is coplanar with the arrays, and hence the hologram represents essentially object wave data. No offset reference wave is necessary in this reconstruction mode. (sec. 3.6) The (subtractive) crosscoupled suppression scheme was used routinely.

The stratagem determining image dimensions as fractions of the repetition interval is unnecessary, and in the images to be presented the image plane left bottom corner was close to the (1.1) antenna coordinates (Fig. 5.2) and is presented from the point of view of an observer facing the array. The image field is quantised into ten levels, symbolically represented according to Fig. 5.9(c), and scaling was used to fill most of this range.

5.6.1 A Rectangular Planar Object

An apparent paraboidal object wave origin is imaged at z=1.9m, behind a large rectangular plane 950mm from and coplanar with the hologram aperture. (Fig. 5.9(a);sec. 4.2.1)

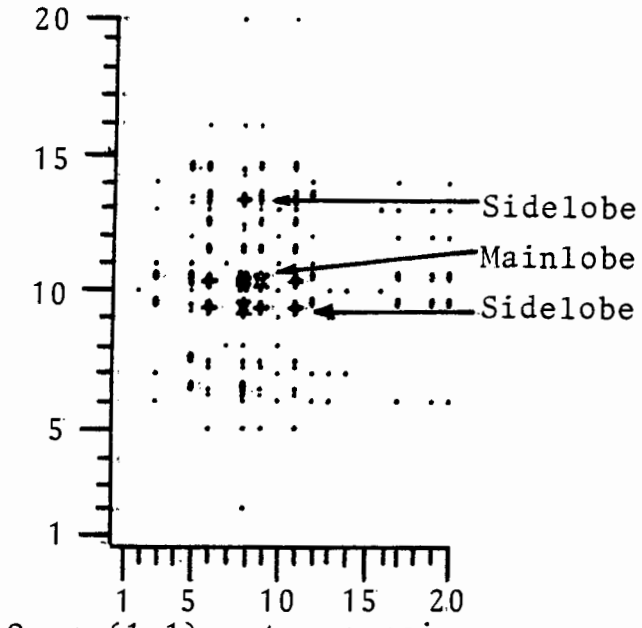

Fig. 5.9(a) Specular image component from planar object

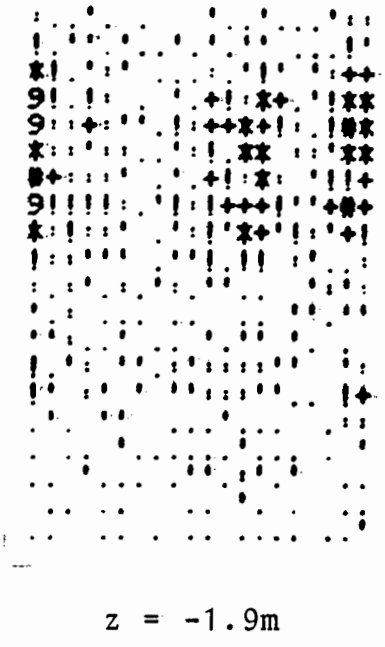

Fig. 5.9(b) Image found in complementary focal plane

Fig. 5.9(c) List of image quantisation levels with respective symbols

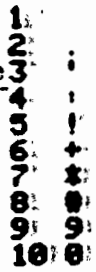

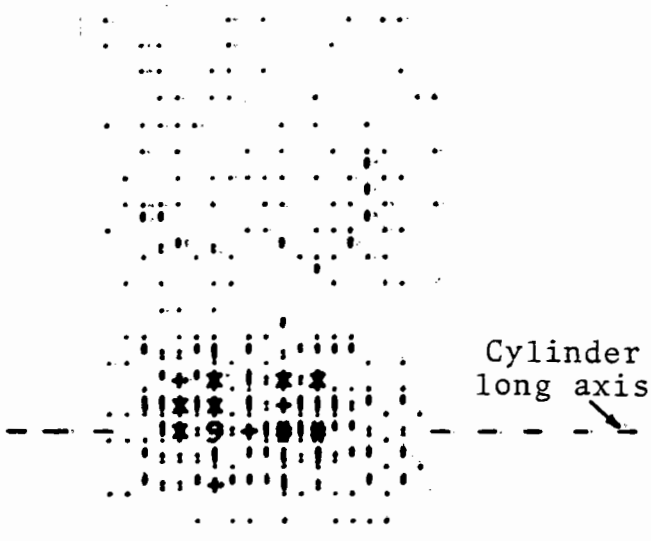

Fig. 5.10(a) Image of cylinder found at z = 1m

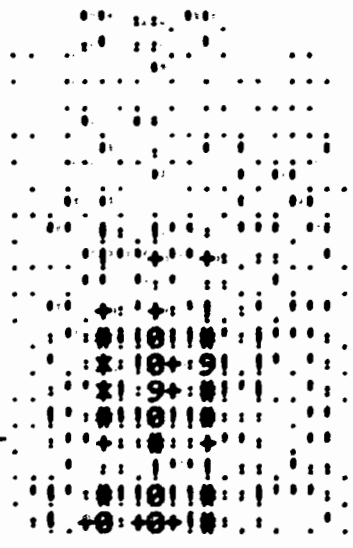

Fig. 5.10(b) Image component found at z = 2m

The maximum intensity point is found 8.5 units right and 9.5 units above the origin, and the image field is computed at 40.4mm (twice the antenna interval Δx) increments in both lateral axes. The image maximum position is in error by only -30mm in the vertical axis and essentially correct in its horizontal position. The first sidelobe pair of the image is spaced 222mm in the horizontal axis, and from the calculated angular distribution in Appendix I, closely approximates the diffraction-limited copy of the quasi-isotropic illuminator supposed at the array intersection.

A lower amplitude dispersed distribution is obtained if reconstruction is attempted in a plane corresponding to that of the real image in an optical system. (Fig. 5.9(b)) The image amplitude has been amplified 8 times relative to that of Fig. 5.9(a) and shows no additional focussed term (up to the second display level) which might have been expected had serious orthogonality error been present in the reference channel of the microwave mixer. The orthogonality error is estimated as less than 5^{o}, using the simple theory of Appendix II. For the apparent point scatterer of Fig. 5.9(a), the approximate ratio of virtual image amplitude to that evaluated in the plane corresponding to the real image is, from the same theory, $\frac{2XY}{\lambda z}$, for a continuous hologram aperture XY in area. In the practical system, the conjugate background to the focussed (and optically produced) real image is characterised by four separate "patches" (as an example, see Fig. 5.6(b)). Ascribing the continuous aperture ratio to the practical system in these regions indicates about 7% relative amplitude, whereas Fig. 5.9(b) has dispersed regions up to 11% relative amplitude.

5.6.2 A Horizontal Cylindrical Object

An image of a thin cylinder, parallel to the horizontal array and with the scattering centre estimated at z = 1m from the array, is impulse response limited in the vertical direction and horizontally extended. (Fig. 5.10(a)) The estimated centre of the image is within 10mm of its correct position. At double this range, the image is compressed horizontally and vertically extended. The first sidelobe pair spacing is, from Fig. 5.10(b), 242mm and compares favourably with the calculated value 257mm. The range axis focal separation in orthogonal axis is similar to that observed in Fig. 4.6.

The same object tilted in the plane of the array exhibits similar separation at the same range values, but the structure of the impulse response and its array axial dependence diminish image recognizability in this case (Figs. 5.11(a) and 5.11(b)), although the two components do appear to subtend complementary angles.

5.6.3 A Toroidal Object

The image of a toroidal object is perturbed by the impulse response of the system, but there is evidence of an extended quasi-circular scatterer. (Fig. 5.12) The horizontal and vertical diameters are estimated at 320mm and 283mm respectively and the image aspect ratio has here been corrected to remove perceived distortion tolerable in point-like and extended linear images. The more subtle modulation of the image radius according to the aspect of the equivalent illuminator relative to the object is not appreciable. The image dimension is somewhat less than the 360mm diameter of the scattering circle, but is comparable to the optically reconstructed image of the identical object under the conditions obtaining in Fig. 5.5.

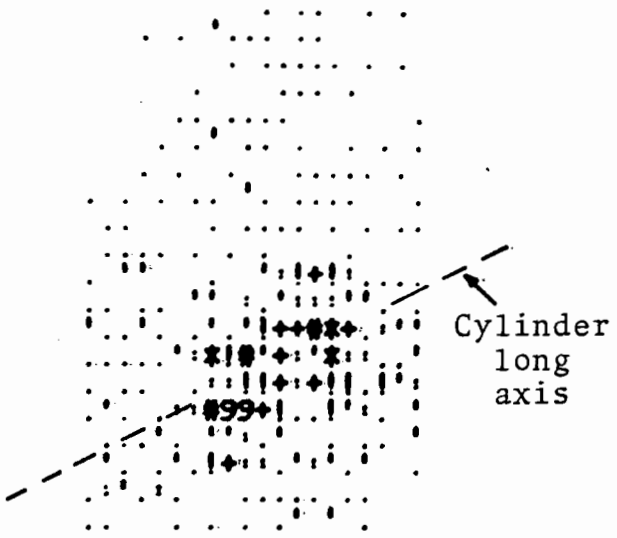

Fig. 5.11(a) Image of inclined cylinder found at z = 1m

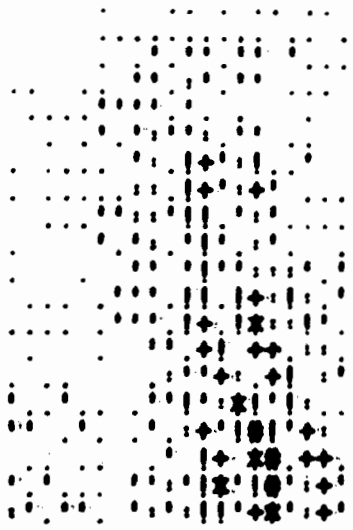

Fig. 5.11(b) Image component at double range; z = 2m

Fig. 5.12 Image of toroidal object

Fig. 5.13 Image of spherical object

5.6.4 Spherical Object

A single spherical object shows evidence of some impulse response distortion (asymmetry) attributable to the much lower reflected field amplitude and subsequent poorer signal-to-noise ratio (Fig. 5.13), but is comparable as a point scatterer at z = 1.1m with the form of the specular image component obtained from a large planar object. (Fig. 5.9(a))

5.7 A Range-Plane Imaging System

This section describes a variant of the planar imaging system which sacrifices an image dimension to obtain azimuthal and enhanced range resolution. The procedure is designated "range-plane" imaging. The imaging system is shown in Fig. 5.14, and the enhanced range resolution arises from the grazing intersection of the (assumed) planar object region and the extended focal axis structure of the equivalent vertical axis beam, since the object plane is constrained to be considerably below the array projected aperture. The geometry considered here has an object plane parallel to the horizontal as this configuration is probably most useful experimentally.

Range resolution is achieved in a rather different way to both the holographic depth probe (HISS) of Iizuka et al.[42-45] and Karg's implicit pulse domain technique.[2,3] The former had two coaxial (rather than two orthogonal) arrays, and the intersection of the "fan beams" of transmitting and receiving arrays is a compact function of range. That the beam focal regions intersect at an included angle which is itself a function of range, yields a range-varying depth resolution. Karg's holographic imaging system is capable of two-dimensional imagery with most impressive and constant

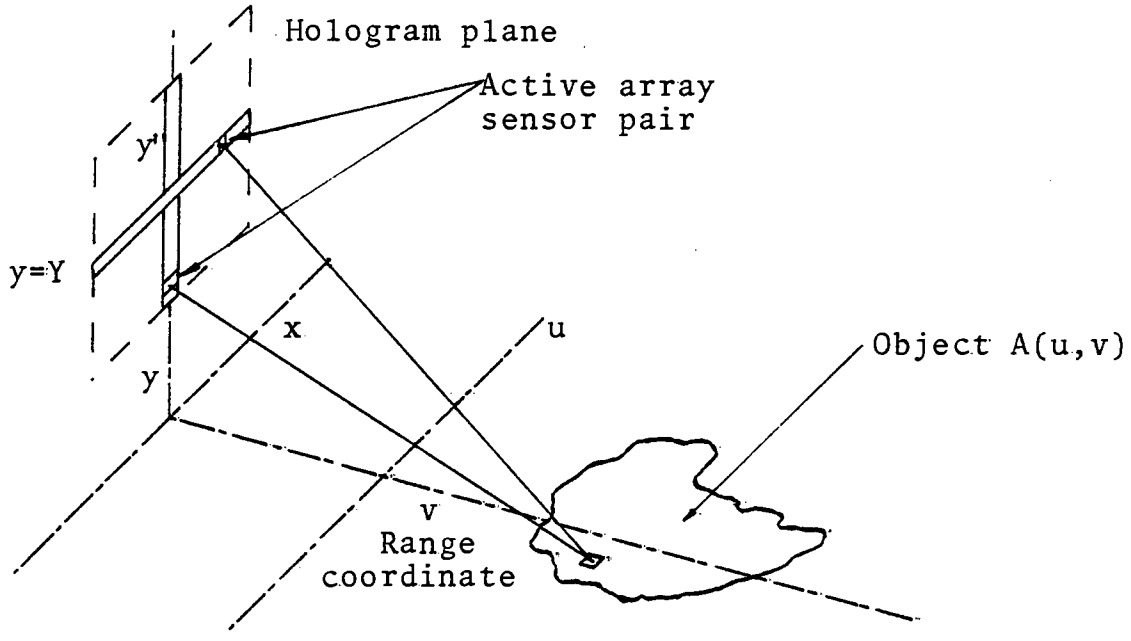

Fig. 5.14 Range-plane imaging geometry

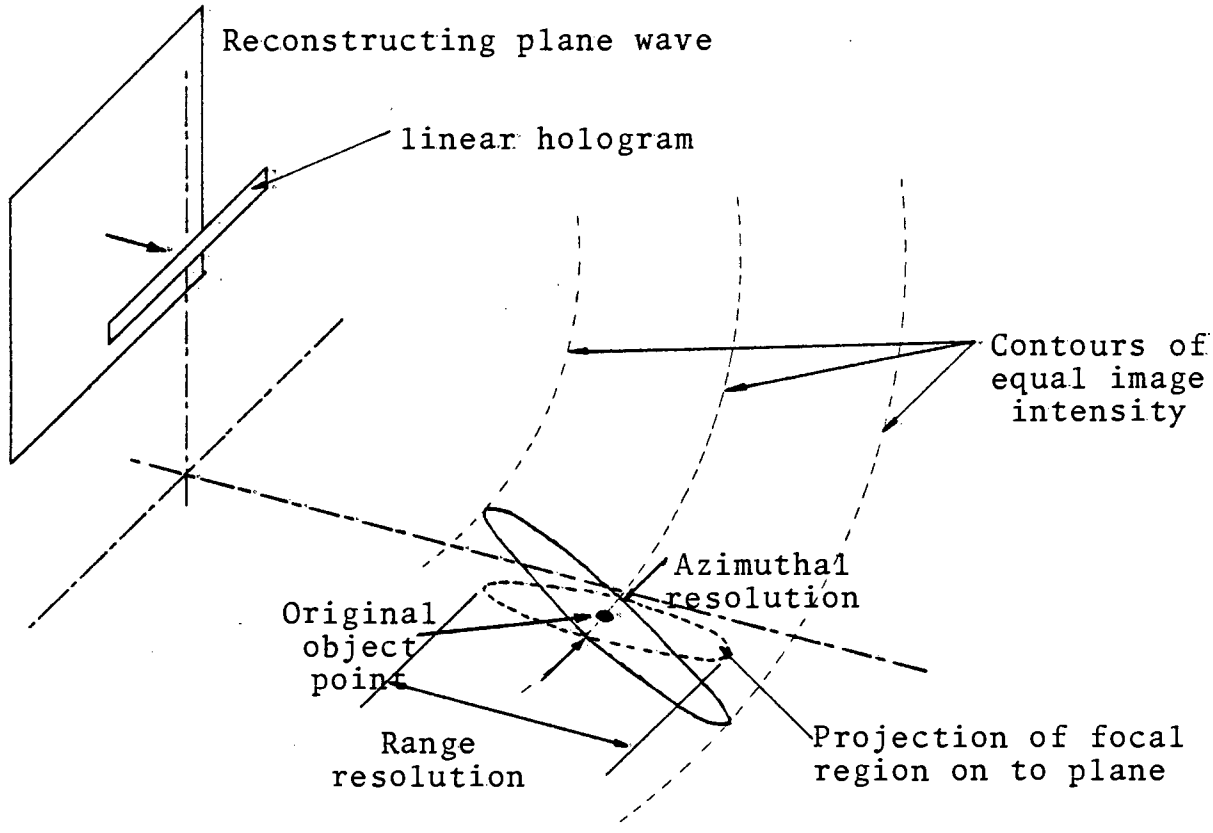

Fig. 5.15 Range-plane imaging by a single linear array

range resolution by using wide bandwidth, but it is felt that in at lease one application (the laboratory instrumentation of a variable focal length microwave probe for the wave-wave interaction process is proposed in Chp. 1 and discussed in Chp. 6) the monofrequency system may be preferred. In most static imaging techniques, the extension of the imaging system's bandwidth (in a temporal sense) generally improves the recognizability of the image.[2] The monofrequency system does, however, have the advantage of simpler processing.

The geometry considered in this section does require á priori knowledge of the vertical position of the object plane, but even this can be obtained given a single object at known range as a calibration point.

5.7.1 Theory of Range-Plane Imaging

The analysis is confined to static, planar object distributions. The array intersection point (Figs. 5.1 and 5.2) is at a height Y above the mapping plane coordinate system, and the arrays are envisaged as "looking down" at the object plane. (Fig. 5.14) If the object region is static during the hologram data acquisition interval, and if the vertical antennae are assumed to be commutated more rapidly than the horizontal antennae, then the system is similar to that used in synthetic aperture radar (S.A.R.), where a platform (aircraft or satellite) transports a coherent pulsed radar at constant speed past the object plane.[49,64]

In S.A.R., range discrimination is achieved naturally by the temporal ordering of the scattered signals, but useful range resolution in a laboratory continuous wave holographic system requires a second mapping region coordinate, and knowledge of the height of the object plane.

It should be noted that mapping of an extended plane object does not intrinsically require field measurements to be made in two dimensions, since in principle holographic mapping is able to collapse two object dimensions into a one-dimensional linear record. The geometry of reconstruction of such a linear (complex) hologram is suggested in Fig. 5.15. The hologram is considered to be illuminated from behind by a plane wave, representing the original reference wave in the practical system. The dotted area on the object plane suggests the action of the reconstruction process. In most laboratory microwave holographic systems the range resolution is sufficiently poor not to warrant serious consideration of this mode, but as the scale of the imaging system increases, so does the range resolution become a more useful specification. (sec. 3.3.4)

In Fig. 5.14 the complex field measured in the hologram mapping using all combination of transmitting and receiving elements, and assuming that the chosen element spacing leads to an equivalent coplanar synthetic reference wave, is:

$$h_c(x,y') = \iint_{A(u,v)} A(u,v).e^{jk(u^2+y^2+v^2)^{\frac{1}{2}}}.e^{jk((u-x)^2+Y^2+v^2)^{\frac{1}{2}}}.dudv \qquad \text{---------- 5.1}$$

The variable $y = y' + Y$, $dy = dy'$, and Y is the height of the transmitting and receiving array intersection point above the chosen (u,v) object plane. Both exponents of eq. 5.1 are functions of the object plane coordinate system, and this complicates the image reconstruction operation. The required image I(u'v') is strictly reconstructed from the complex hologram $h_c(x,y')$ using the "backpropagator" approach [26,87]:

$$I(u',v') = \iint_{xy'} h_c(x,y').e^{-jk(u'^2+y^2+v'^2)^{\frac{1}{2}}}.e^{-jk((u-x)^2+Y^2+v'^2)^{\frac{1}{2}}}.dxdy' \qquad \text{---------- 5.2}$$

This repeats the reconstruction procedure of eq. 3.42. The image plane is specified by the (u',v') coordinate system, where v' is a coordinate in the range direction normal to the hologram projected aperture. Direct evaluation of eq. 5.2 poses a sizeable calculation problem; given only a 20 x 20 array of complex data comprising the hologram and calculating a similarly sized image array requires that the backpropagation function be calculated as 400 complex data for each of 400 proposed output plane points. This direct calculation has been performed as a check on an approximate method[38], and even using Fortran 5 execution on a terminal system, routinely took between 1 and 2 minutes while using Basic took over an hour. Since this investigation was of an exploratory nature, and as the geometry was not envisaged in the original system design, some sacrifice of image positional accuracy was felt worthwhile in order to force separability on to the reconstruction algorithm and consequently improve image computation time.

5.7.2 Approximate Reconstruction Procedure

The image reconstruction procedure (eq. 5.2) can be simplified if the maximum azimuthal image plane dimension is such that azimuthal dependence can be neglected in one exponent of eq. 5.2. The approximate reconstruction procedure is:

$$I(u',v') = \iint_{xy'} h_c(x,y') . e^{-jk(y^2+v'^2)^{\frac{1}{2}}} . e^{-jk((u'-x)^2+Y^2+v'^2)^{\frac{1}{2}}} . \; dxdy' \quad \text{---------- 5.3}$$

The approximate procedure can be viewed as a two-step process producing a final image I from an intermediate field I', where:

$$I'(x,v') = \int_{y'} h_c(x,y') . e^{-jk(y^2+v'^2)^{\frac{1}{2}}} . dy' \quad \text{---------- 5.4}$$

and

$$I(u',v') = \int_{x} I'(x,v') . e^{-jk((u'-x)^2+(Y^2+v'^2))^{\frac{1}{2}}} . dx \quad \text{---- 5.5}$$

The intermediate field produced by the first integration (eq. 5.4) can be regarded as a range-ordered sequence of fields sampled at only one position in a plane normal to v' and coplanar with the hologram mapping aperture. (Fig. 5.16) If eq. 5.4 is rewritten as:

$$I''(x,w) = \int_{y'} h_c(x,y').e^{-jk((y-w)^2+v'^2)^{\frac{1}{2}}}.dy \quad \text{---------- 5.6}$$

then eq. 5.6 describes a procedure which generates an intermediate field I'' using hologram column (y-axis) data, assuming a constant range v', and performing a deconvolution operation in the vertical (w-axis) direction. The procedure of eq. 5.4 generated a series of fields I'', range-ordered, but only sampled at the single point w=0. This point is coincident with the (known) position of the object plane. The range-plane object is thus treated as an assembly of range-ordered strips at a constant distance below the hologram array intersection point.

The image is (approximately) determined by the second operation (eq. 5.5) which acts on the intermediate field I' row data by operating on that data with a function which is adjusted for image u'-axis offset in the normal manner, but is also adjusted for the range (v'-axis) assigned that I' row data by the initial operation. (eq. 5.4) The complete range-plane reconstruction process is thus equal in complexity (and hence in execution time) to the separable paraxial imaging process of eq. 3.8, when both are implemented by direct deconvolution, except that a single line only of azimuth (u'-axis) data is calculated at a given range v', but many such v'-axis azimuth samples constitute a planar image. A simpler second stage process has also been used:

$$I(u',v') = \int_{x} I'(x,v').e^{-jk((u'-x)^2/2v')}.dx \quad \text{---------- 5.7}$$

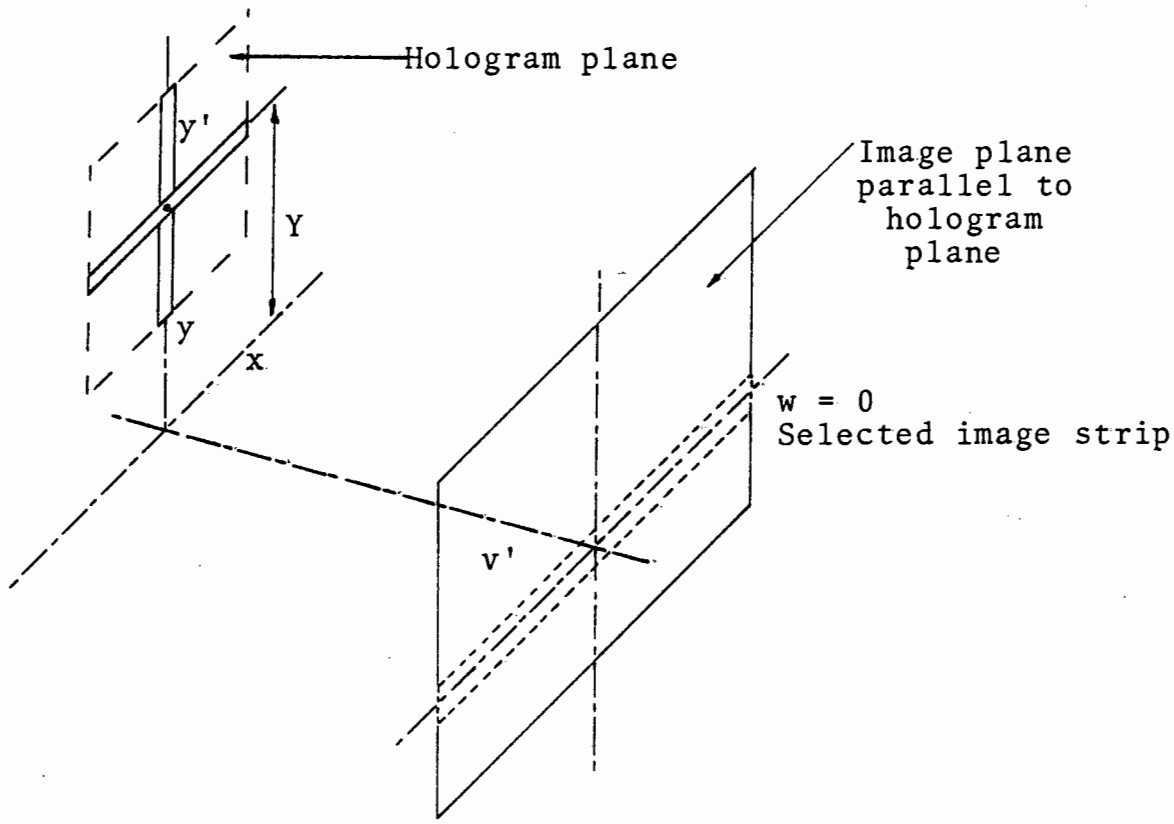

Fig. 5.16 On the approximate reconstruction procedure

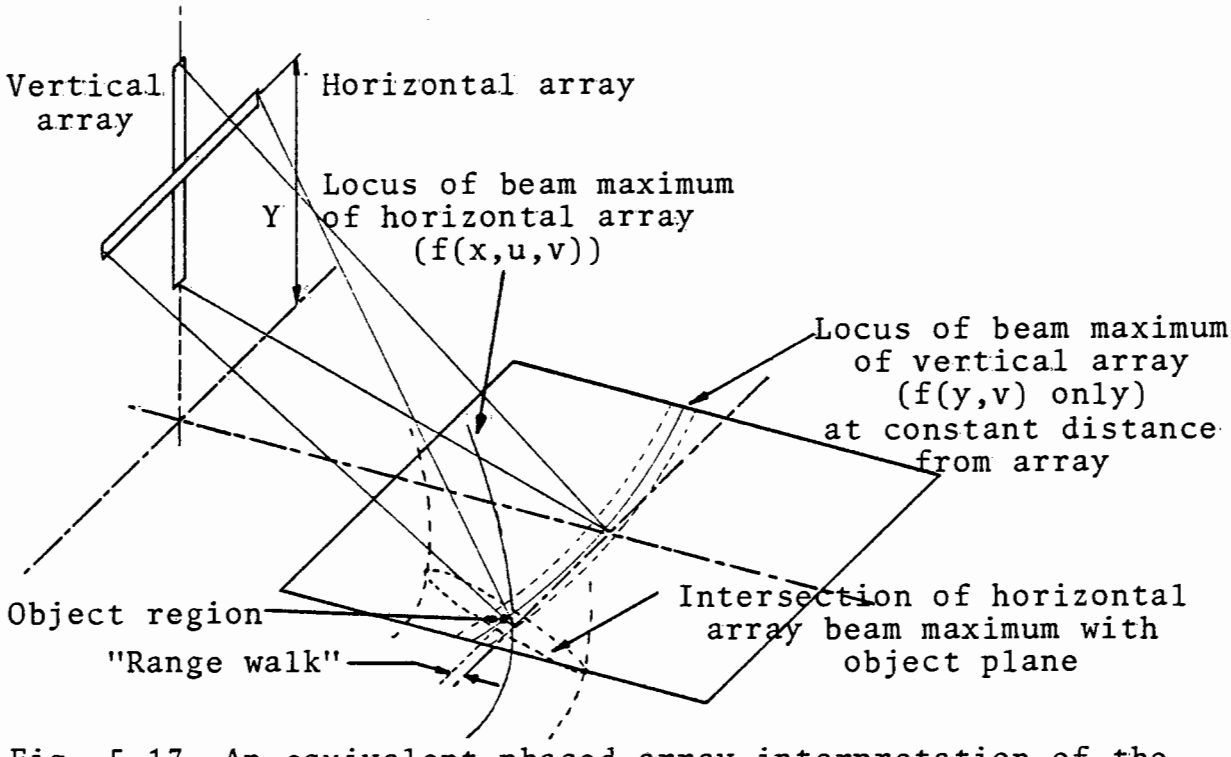

Fig. 5.17 An equivalent phased array interpretation of the approximate imaging process

This is based on the paraxial reconstruction process. (sec. 3.3.1)

The approximate reconstruction procedure (eq. 5.3) is also supported by the equivalent phased-array view of the imaging process. (Fig. 5.17) The intersection of the vertical (y-axis) and horizontal (x-axis) beam maxima defines the location of the particular object region point as a function of the separate array complex weighting operations. The price paid for the simplification of the reconstruction algorithm as separable operations on each axis's data is a range error or "walk" coupled to azimuthal object offset (u-axis), and a "gain error" (of less importance) arising from the lack of exact registration of the two beam maxima at other than object positions directly in line with the array intersection point. The latter error is easily corrected in a digital reconstruction process.

The hologram data comprised a 20 x 20 array of complex field values. The algorithm, which implemented eq. 5.3 as a direct integration in a Basic program, generated an intermediate (complex) array by calculating first the approximate vertical "backpropagator" and applying this to the hologram data, according to eq. 5.4. The image was completed by implementing eq. 5.5, or, in some preliminary cases, the simpler version in eq. 5.7. The azimuthal (u'-axis) spread of the image was 19 units of 60.6mm, or 576mm on each side of the projected aperture.

5.7.3 Demonstrating the Range-Plane Imaging Mode

The initial demonstrations of this range-plane imaging mode were made using only the vertical array of antennae and replacing the horizontal array functionally by a single horn antenna. The object chosen was a narrow cylindrical bar which was laid across the object region parallel to the

u-axis and at a known distance below the horizontal array. The object range was varied from .4 to 1.2 metres and the reconstruction operation was confined to the evaluation of a series of vertical sections through the suspected object plane. The height-range sections for the first and last experiments are shown. (Fig. 5.18)

In all 8 cases, the image estimate of range was within the inherent 50mm resolution of the displayed data, assuming that the object's distance below the array centre was accurately known. The vertical beam cross-section did not vary much in the focal region along a line joining array centre and focal point, so that the range resolution could be estimated by projection onto the object plane. (sec. 3.3.4) For an object range 0.4m, and using the extra-paraxial theory of sec. 3.5.2, the vertical resolution (-3dB points) is approximately δy:

Vertical resolution $= \dfrac{\lambda (v^2+(Y+L_y/2)^2)^{\frac{1}{2}}}{L_y}$, where L_y=585.8mm, λ=30.3mm, and Y=606mm. $^{-3dB}$

The angle between array centre, focal point, and object plane ie:

$\alpha = \arctan(Y/v) = 50^{o}$, whence range resolution Δv is:

$\Delta v = \delta y . \cot\alpha = 44$mm. (The display increment was 50mm.)

The linear hologram or one-dimensional data array represented measured complex field values in polar form. Image fidelity was improved by subtracting the field measured in absence of the bar object from that found in its presence. (sec. 5.3) The image was found using:

$$I(w,v') = \int_{y'} h_c(y') . e^{-jk((w-y)^2+v'^2)^{\frac{1}{2}}} . dy' \quad \text{---------- 5.8}$$

The variable w is an image plane variable parallel to y. (Fig. 5.16) Image amplitude is displayed as one of ten possible levels, and follows the format used in the first part of this chapter. (Fig. 5.9(c))

List of image quantisation levels with respective symbols (Fig. 5.9(c))

1 .
2 :
3 :
4 :
5 !
6 +
7 *
8 #
9 9
10 0

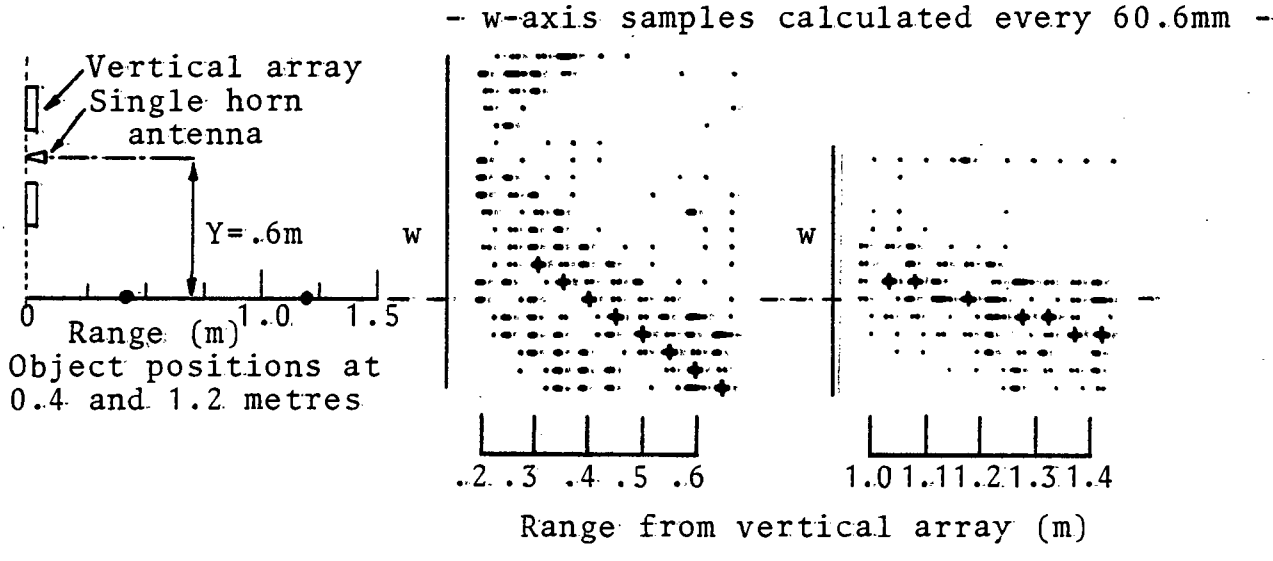

Fig. 5.18 Height-range image sections with a single array

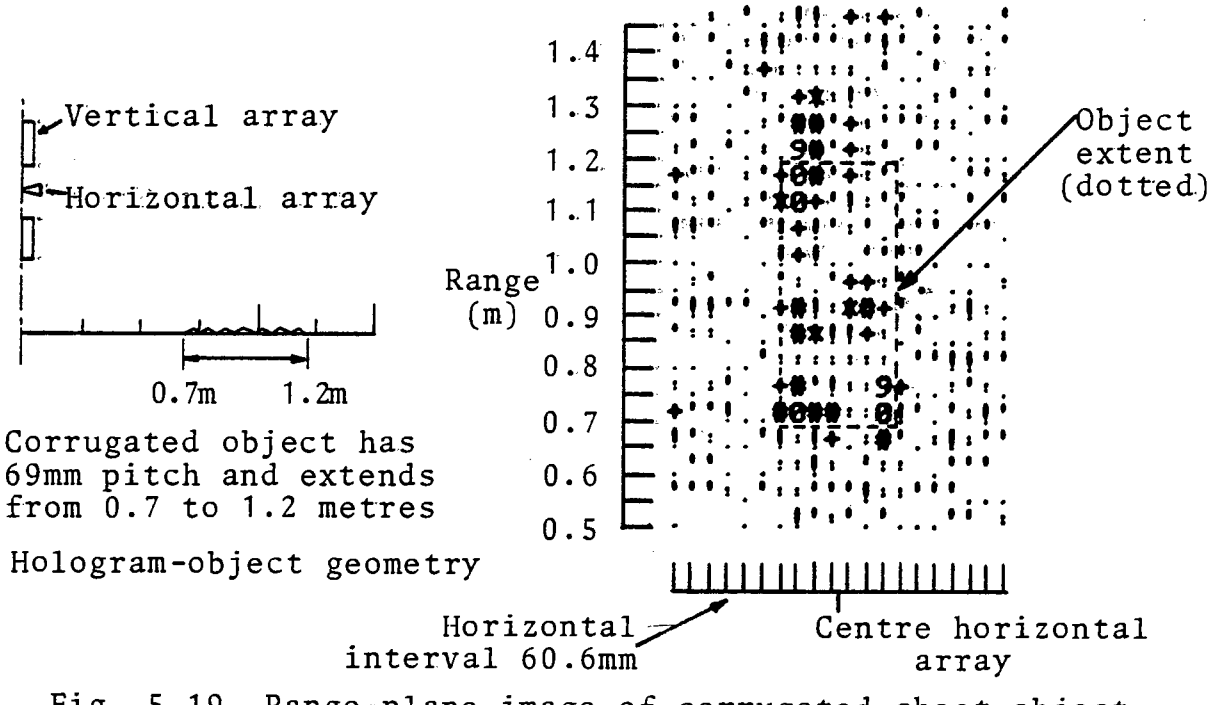

Fig. 5.19 Range-plane image of corrugated sheet object

An early implementation of the range-plane imaging system was undertaken using the paraxially-approximate second stage reconstruction process. (eq. 5.7) One example of imagery using both antenna arrays and this reconstruction process resulted from a triangularly corrugated metal sheet object. The corrugation wavelength was 69mm, and the crests were parallel to the u-axis. The sheet was 400mm wide and extended from 700mm to 1.2m in the range (v) axis. The image has been presented from the point of view of an observer stationed at the array intersection point, and looking outwards and downwards.

The image structure is complicated by sidelobes arising from the interrupted array geometry, but has an extended maximum around range 1.2m and also at 700mm. The latter is probably due to the return from leading edge of the object; the former may similarly be from the far edge but is significant that the Bragg mode of reflection could enhance the return from this region. Given 69mm pitch and 30.3mm wavelength, a Bragg reflection maximum should occur for: $\cos\theta = 2\lambda/\Lambda$, where Λ is corrugation pitch and λ is wavelength; Incident beam and object included angle=arccos (2.30.3/69) $=28.6^{o}$. (118) This angle is found at a range v, where: $v=Y\cot(28.6^{o})=1.13m$. This estimated range to the Bragg interaction region is close to the image maximum in Fig. 5.19. The horizontal image structure is extended as a result of the specular reflection from the object.

The same reconstruction process was used to track the u-axis position of a simulated point object at constant range v from the arrays. (Fig. 5.20)

The object, a 150mm diameter metal sphere, was initially at a range of 880mm and closely aligned with the horizontal array centre. As in previous experiments, the complex data represents the difference hologram. The image maximum is

- Horizontal image interval is 60.0mm -

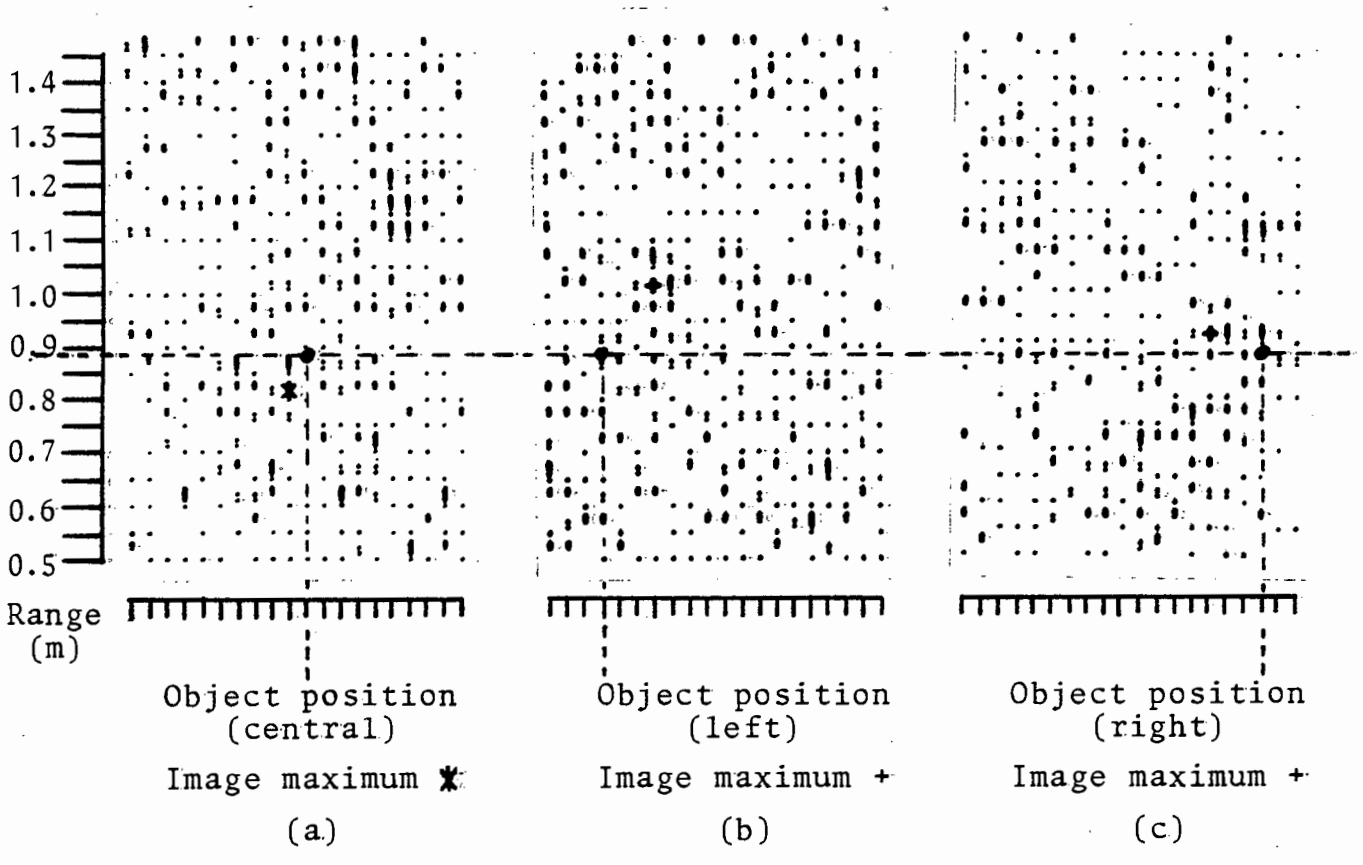

Fig. 5.20 Range walk effect using a simulated point scatterer

within 60.6mm of the correct position and to the left, and has no more than 80mm range error.

By contrast, moving the same object 7 display units (424mm) to the left (Fig. 5.20(b)) and right (Fig. 5.20(c)) results in slightly reduced image amplitude (86%), but the image position is severely misrepresented. The object positions inferred from the images are conservative and the range errors (averaging 150mm) are reminiscent of the similar "range-walk" effect encountered in S.A.R. imagery.[105]

Demonstration of Hologram Averaging

The demonstration of the range-plane imaging mode revealed that below a certain object wave amplitude (it is understood that the difference hologram mode has been used in all experiments) the noise introduced into the complex data destroyed the correspondence between image and object detail. This noise arose mainly in the receiver mixers, and uncorrelated additive noise from this source was converted into phase and amplitude noise in the polar data representation.

The object used in Fig. 5.20 was placed at a range of 1.29m from the arrays, and in a known object plane. Object positions were in line with the horizontal array centre, and a point 182mm to the right. (3 display units) In Fig. 5.21(a), the image maximum has only 13mm range error, and is aximuthally 30mm left of the correct position, which is about one-half the lateral resolution of a filled array. Moving the object results in image Fig. 5.21(b), and a reduction in object wave amplitude has destroyed the image. There is a component at the correct position, but ambiguous components abound.

The image fidelity has been improved by the simple expedient of recording several (8) object fields, as difference

- Horizontal image interval is 60.6mm -

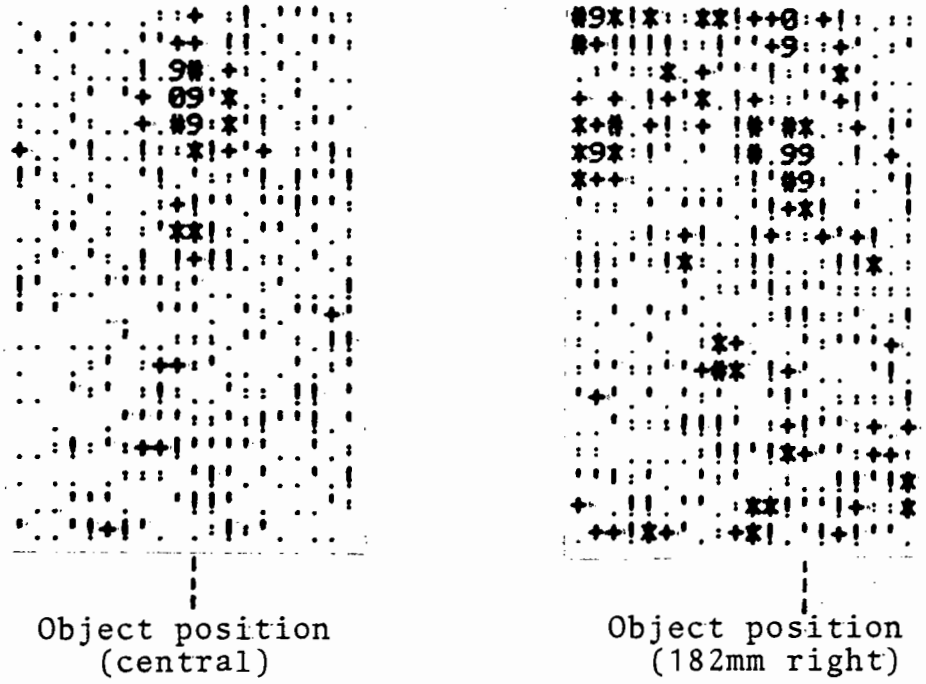

Figs. 5.21(a) and (b) Threshold of single-field hologram imaging

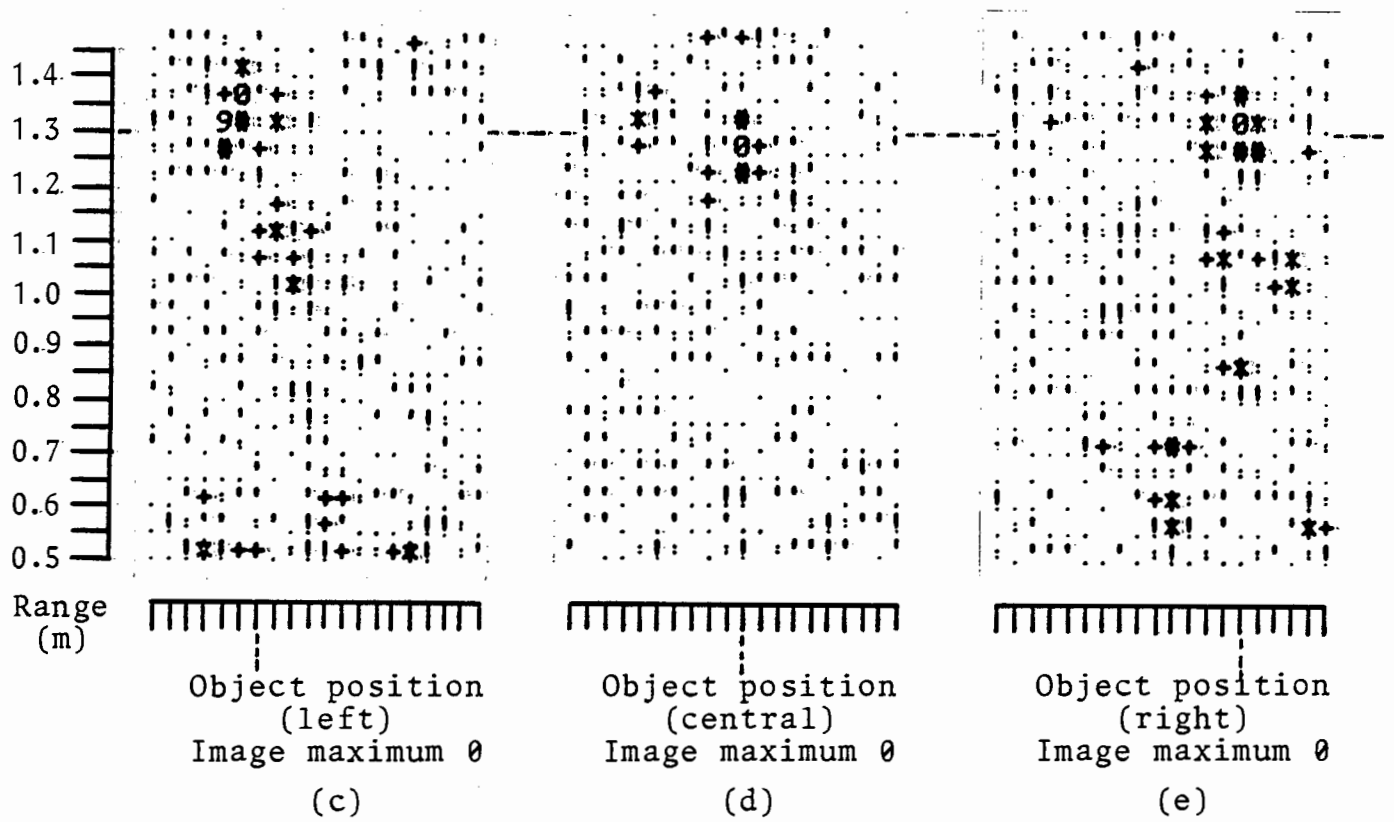

Figs. 5.21(c)-(e) The effect of averaged holograms

holograms, and averaging by vector addition. Such images, reconstructed from averaged holograms, are given in Fig. 5.21(c)-(e). The object positions, at a constant range of 1.29m, were central and 250mm left and right of this point. The "range-walk" phenomenon has been greatly reduced since the reconstruction process used here is that of eq. 5.3. The "range-walk" amounts to 38mm; using the equivalent phased array notion of Fig. 5.17 indicates 24mm. The estimated object offsets from the images are 333mm (left) and 242mm (right) and this error is not worse than the 67mm azimuthal resolution at this range. The curvature of the image trajectory at constant range of the object, but with varying lateral offset is opposite (that is, convex with respect to the array) to that indicated in Fig. 5.17. In this equivalent phased array description, the concave object region beam maximum is a contour of equal processor weight, and larger aximuthal offsets are accessed by longer (rather than shorter) vertical array processor focal lengths. In this respect, reasoning is similar to that advanced in sec. 3.4 to explain hyberbolic image plane distortion.

A cylindrical object, laid parallel to the x-axis was successfully imaged by the multiple field averaging technique at a range of 1.9m. (Fig. 5.22) As in previous demonstrations, y-axis position was assumed known, and the reconstruction process was that of eq. 5.3. The image azimuth extent is, at 670mm, very close to the true object length of 620mm, but the theory of sec. 4.2.4 suggests that the limiting image dimension of one-half the array aperture in that axis is apparently extended by the horizontal axis impulse response distribution. The range is accurately represented to within two display units (100mm). At this range, some care must be taken in estimating the effective scattering centre of the cylinder, as every 1mm error in y-axis position influences the image range by -2.8mm.

- Horizontal image interval is 60.6mm -

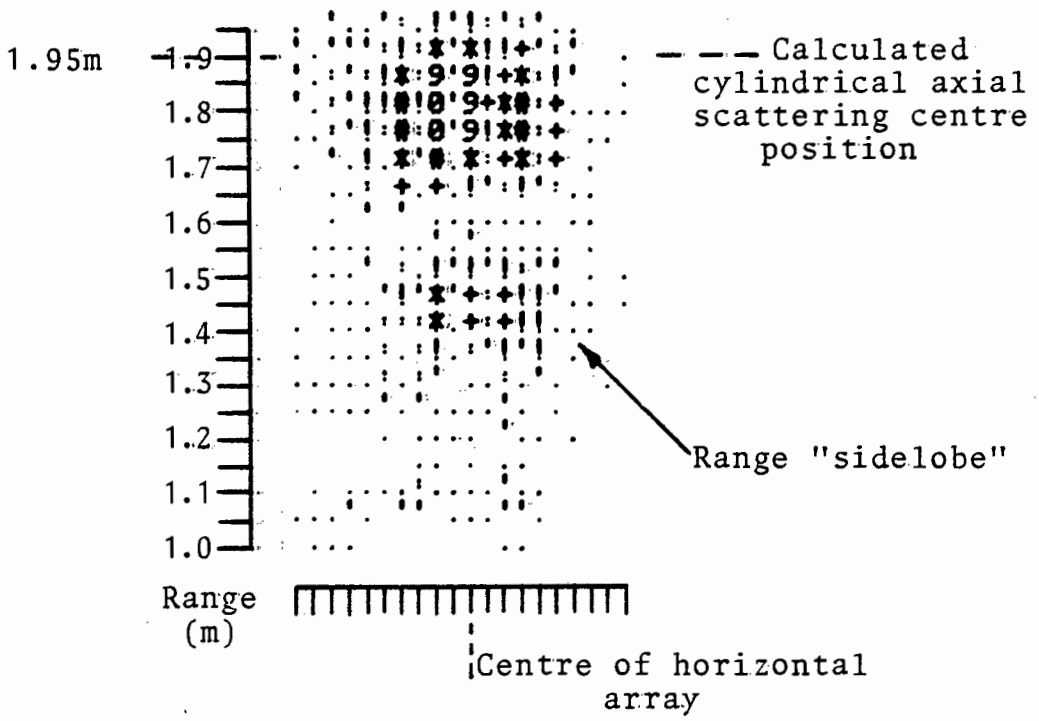

Fig. 5.22 Range-plane image of cylinder at long range

5.7.4 Simulation of the Exact Reconstruction Process

A direct deconvolution check of the range-plane imaging mode using a point object and with Fortran 5 translation of the reconstruction procedure of eq. 5.2 has been performed by Pare [38] as a continuation of an undergraduate project. The images were generated using both synthetic and measured data, and the former assumed array geometry indentical to that of the prototype experimental system.

9 images (Fig. 5.23(a)-(i)) reveal that there is sensibly no error in the location of the image maxima, although the point object offset of 303mm left and right of the horizontal array centre at the lowest range simulated (581mm) would have produced at least 74mm range error (according to the equivalent phased array approach of Fig. 5.17) had the simpler approximate reconstruction process of eq. 5.3 been followed. The images have been presented as if the object plane were viewed facing the array elements, and the side-lobe structure surrounding the image maxima is a function of the aperture antennae distribution rather than an inherent feature of the technique.

The small errors in maxima position (not worse than 1 unit of 40.4mm) have been traced to an integer rounding operation which has generated the image in a plane 5% higher than the object plane. As a result, all image dimensions are slightly conservative, which is in agreement with the operation of the equivalent phased array of Fig. 5.17.

An example of the reconstruction of experimental data by the process is given in Fig. 5.24(a). Image orientation is as for other images from measured data. The object was the 150mm metal sphere used in previous studies. Hologram data was captured using the local Varian V-77 minicomputer and stored on punched paper tape. The Univac Fortran 5 system

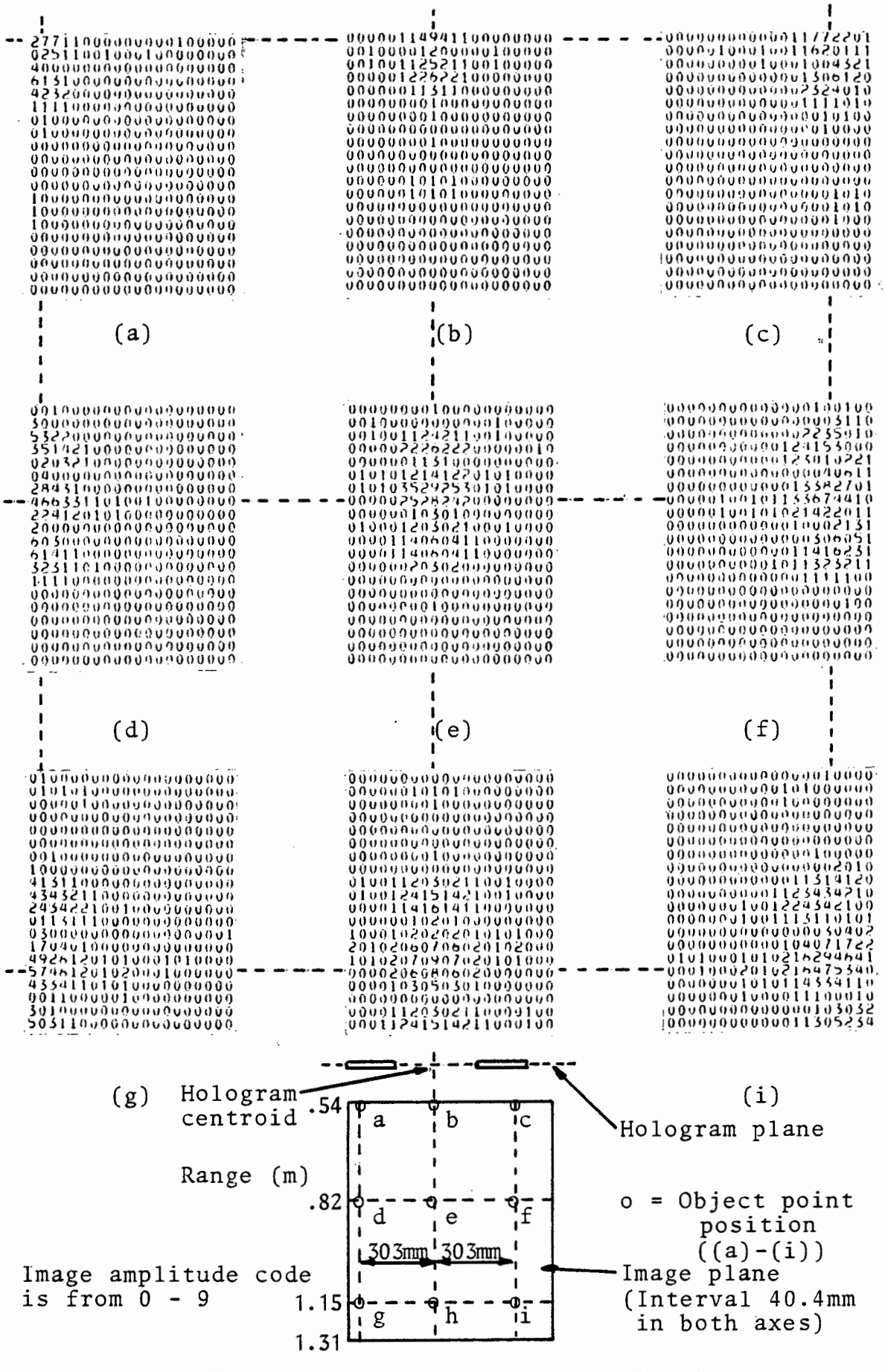

Fig. 5.23 A simulation of the range-plane imaging process

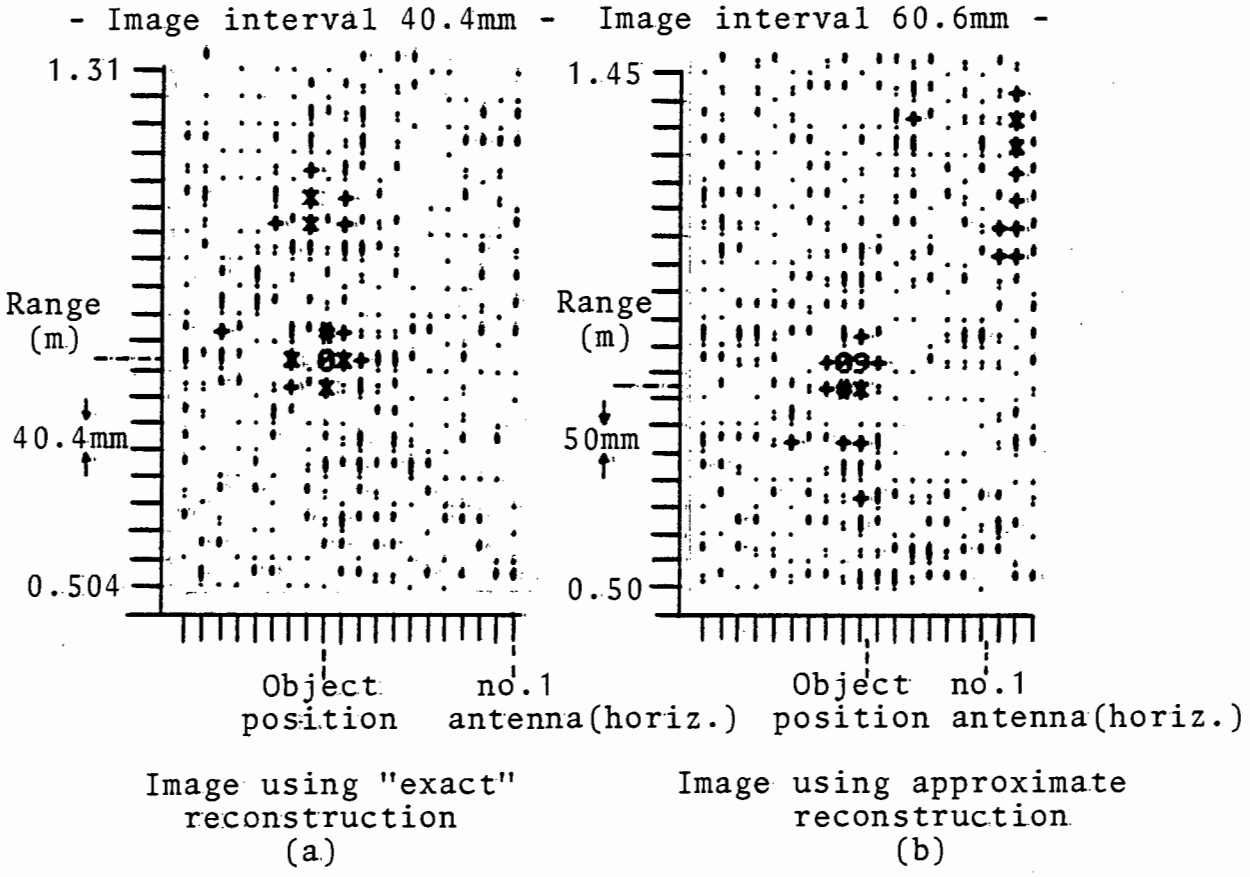

Fig. 5.24 Images using exact and approximate reconstruction

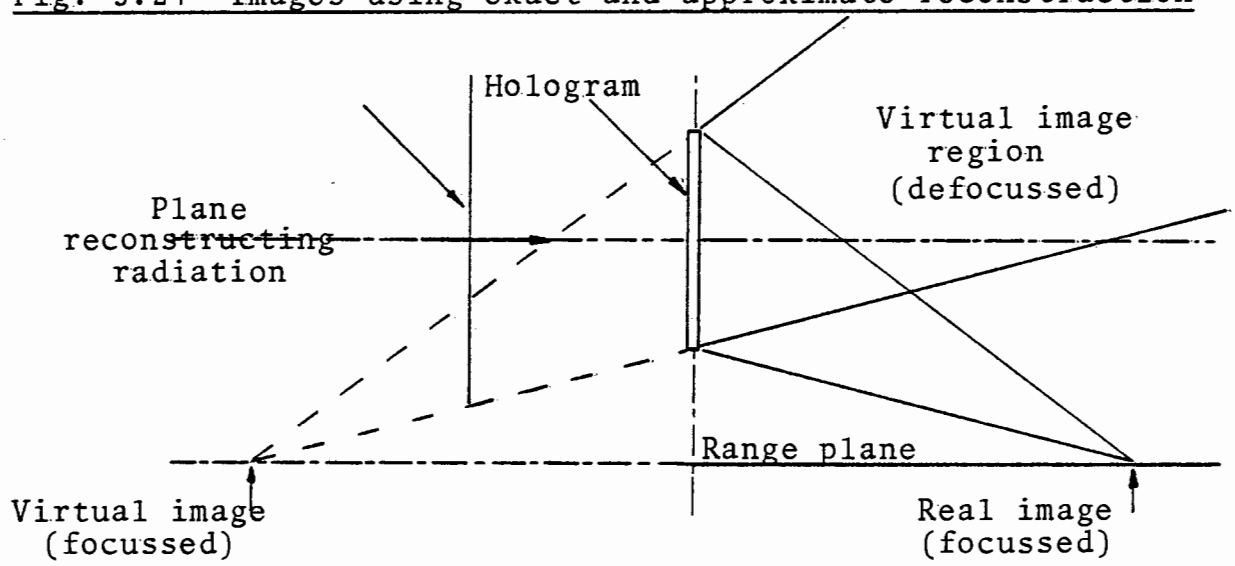

Fig. 5.25 Imaging in the presence of conjugate data - an optical analogue

was used for reconstruction, and this process was that of eq. 5.2. The image displays essentially no azimuthal error and has an estimated 13mm range error only. It is noteworthy that the measured range resolution of two display units (81mm) is close to that indicated by the simple theory of sec. 5.7.3.

An image processed according to the simpler approximate algorithm of eq. 5.3 is given in Fig. 5.24(b) and uses the data identical to Fig. 5.24(a). The object range is indicated as 875mm, which is accurate to well within the range resolution, while the azimuthal error in image maximum position is about 40mm - no significant error arises from the use of the approximate algorithm in this case.

The execution of the exact reconstruction procedure (eq. 5.2) with either synthetic or measured data took between 1 and 2 minutes. The use of the approximate algorithm (eq. 5.3) suggested in this chapter would reduce this time by a factor of 10, based both on comparative measurements of the program execution time run in Basic and Fortran 5 languages, and on the relative number of multiplication operations required in each algorithm, and a 6 to 12 second reconstruction time would be close to "real-time" processing.

5.7.5 Array Systematic Errors

A notable difference between the image derived from synthetic and measured holograms is the persistent "clutter" in the latter, even when appreciable data averaging has reduced the effects of random amplitude and phase errors. This discrepancy is attributed to the lack of systematic error correction. There is no reason why these could not be corrected in an operational system, and in this case, the multiple field averaging process may be valuable where object velocity is negligible over the total averaging time.

A practical advantage of the geometry used in this section would allow imaging in the presence of conjugate hologram components generated by various hardware tolerances. (Appendix 11) If the reconstruction process is regarded as equivalent to plane (reference) wave illumination of the complex perturbed hologram, then the defocussed conjugate image field will not intersect the wanted image plane. (Fig. 5.25) This analogy with optical practice is imperfect, since the backpropagation function peculiar to the extra-paraxial geometry does not mimic the "natural" impulse response function of free space.

5.7.6 Object Region Accessibility

The range-plane imaging system appears to violate the object and range relationships determined by available aperture and antenna spacing. No problem has been experienced with an object offset Y of 600mm at only 400mm range, although Fig. 3.11 appears to forbid this. The range-plane imaging system has a fixed object plane vertical offset and the aliased imagery arising from sampling violations can be suppressed by displaying only a finite positive sample of the image range dimension. The situation is similar to that found in a phased array antenna with element spacing greater than $\lambda/2$; the element spacing used in the prototype holographic system was $2\lambda/3$. The "grating lobe" maximum appearing above the normal to the vertical array does not intercept the object range-plane if the primary beam is focussed below this normal. Fig. 5.18 is a vertical axis section of the focussed beam and does show a subsidiary maximum at an angle of opposite sign such that no interference is experienced in an image plane parallel to the object and below the vertical array.

5.7.7 Conclusion

It has proved possible to retrieve specular image components of simple object scenes with satisfactory accuracy in lateral and longitudinal axes. The "self-cluttering" of images from more complex objects due to the high impulse response sidelobe level is not inherent to the crossed array configuration and could be remedied in an operational system. The accessible object region need not be as conservative as that indicated in Fig. 3.13, as real and conjugate image overlap is acceptable given adequate contrast of the two components.

A hybrid reconstruction system offers a continuous optical image output if a simple computer is attached to the hologram mapping system. This generates a binary hologram in which an offset reference wave is incorporated after the mapping process, and could also control antenna commutation, compensate known systematic errors and cancel expected and unwanted background data, such as the cross-soupled signals routinely suppressed in this latter series of demonstrations.

The unambiguous knowledge of received signal phase is a prerequisite for reference wave manipulation, since the á posteriori processing retrieves the original object wavefront from a complex data recording. In this manner, both hardware specification (which is most accurately implemented by an element spacing leading to an equivalent coplanar reference wavefront) and image recognizability requirements (which suggest an offset reference mode) can be satisfied. The binary hologram is suitable for photographic reduction and recording in the conventional manner, but a much faster reconstruction process is feasible using an electro-optical modulator array. [21]

A variant of the planar field imaging system exchanges one object coordinate for an improved, finite, but range-varying depth resolution property. The format is comparable with that exploited by S.A.R., albeit as a continuous wave technique, and the offset object confers considerable tolerance of those errors tending to introduce image components which might perturb a more conventional constant range planar image. The format is geometrically most suited to computed image reconstruction, and an approximate technique greatly reduces the time necessary for reconstruction by an order of magnitude.

CHAPTER 6

Imaging in the Presence of Object Motion

6.1 Introduction and Motivation

The continuous wave nature of the object illumination in microwave holographic imaging systems tends to confine applications of the technique to the laboratory scale, and aperture to object ranges of less than one to a few tens of metres are typical.

This limitation is not inherent or unique to microwave holography, but is imposed by the finite dynamic range and stability of the detection system as the field scattered by the object and holographically recorded must be measured in the presence of a residuum of detector noise, drift and background fields coupled from the illuminating source. Pulsed radar imaging systems, whether coherent or incoherent, exploit the temporal separation of illuminator and scattered signals, and thus need not be range-limited by coupled field components. In practice, a subtractive technique enhanced the continuous wave holographic system's range performance since the close proximity of some transmit and receive elements necessitated this.(sec.5.3)

At this stage however, holography does not, with very few exceptions[32], appear to compete directly with pulsed imaging techniques such as synthetic aperture radar(SAR) as a coherent mapping tool. SAR has demonstrated impressively the quasi-holographic spatial pulse compression mode, albeit in one dimension only.[49,64,65,75,81,96] It has been applied with success to a vast range of imaging and remote sensing tasks. These have not been confined to the evaluation of static object environments, and a very significant and useful SAR application has recently emerged with the demonstrated imaging of some dynamic features of the ocean surface, as diverse as swells, ice conditions, the interaction of sub-surface topography and superficial relief, small scale surface

viscosity modulation by oil slicks and the faint wakes of ships.[68,71,77-79,82,83] The dynamic characteristics of the water surface interact with the coherent SAR mapping operation to produce additional image artifacts subtly hidden from real aperture incoherent imaging systems.

An accurate characterisation of the scattering of electromagnetic radiation from the ocean surface is extremely complicated[81,83,115], and much effort has been expended also in the modelling of the effect of the aperture synthesis procedure and to glean more hydrodynamic information from the resulting image.[68,69,72-74,80,114]

The evaluation of the interaction of electromagnetic and water waves is usually performed under controlled artificial conditions using laboratory wind/wave tanks. Those electromagnetic microwave transducers currently employed include real-aperture focussed doppler probes[70,85] and short range FM radars[78] and occupy frequencies in the 1-20GHz range.

It is the object of this section to highlight the operation of a microwave holographic wave probe. It would appear, given the current and anticipated future application of SAR as a major remote sensing tool[76], to be advantageous to duplicate a small scale version for laboratory instrumentation, where the narrow-band spectral characteristics are retained while an image has both azimuthal and range spatial resolution sufficient to delineate features of the wave tank "sea".

Microwave holography is uniquely capable of image linear resolution which is independent of signal temporal bandwidth and inertialess aperture synthesis procedures seem to offer data collection times compatible with the dynamics of the observed quantity.

It is felt to be important for the maturity and utility of the microwave holographic technique that the quality and range of observable features be minimally constrained by instrumentation artifacts.

The effects of certain deterministic object motions on the overall image impulse response are derived and compared with the corresponding modifications incurred by SAR sensors. The aim is the specification of a practical imaging mode using orthogonal arrays and holographic field mapping, duplicating as closely as possible the formation of SAR imagery, but on a smaller scale.

6.2 Aperture Synthesis in Microwave Holography and SAR

An orthogonal array aperture synthesis holographic system and a pulsed, coherent SAR system have similar features when used to image objects lying in a plane normal to the array axes. (Figs. 6.1 and 6.2) The holographic system, having N transmit elements and M receive elements orthogonally arranged, can develop an MN-element areal aperture by controlling transmitting and receiving operation in any (even random) order, provided that all element pairs are used, but common usage and convenience usually dictate that an element of one array axis is combined with a rapid sequential addressing of the elements of the orthogonal array. It is even possible that the elements of the latter array be simultaneously active, if the hardware implementation is suitable.[31,32] (Chp. 7) If the horizontal axis elements (1 to N) are switched at a constant rate (this affords equal signal averaging times at each position), then the situation approaches closely that found commonly in SAR, where a common coherent transmitter and receiver are transported at a known velocity V_h above and to the side of the object plane. (Fig. 6.2) The transmitter is regularly pulsed and the phase history of the received signal is measured during the time that a particular object point is illuminated.[49,64,65] The reflected signals from objects at different ranges using the SAR system are naturally time-ordered, but continuous wave microwave holographic systems require a second (in this case, vertical) axis in order to define different range intervals. It is possible to suppose single-axis holographic

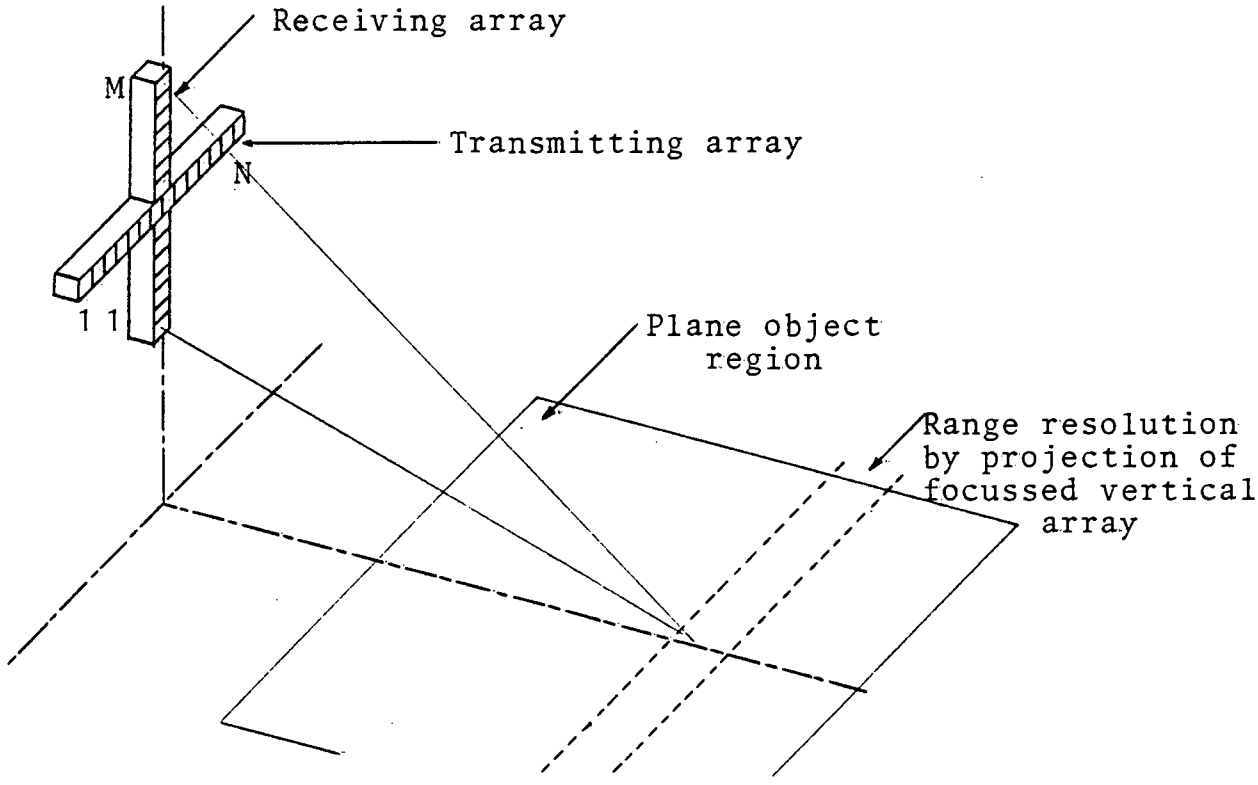

Fig. 6.1 Microwave holographic geometry

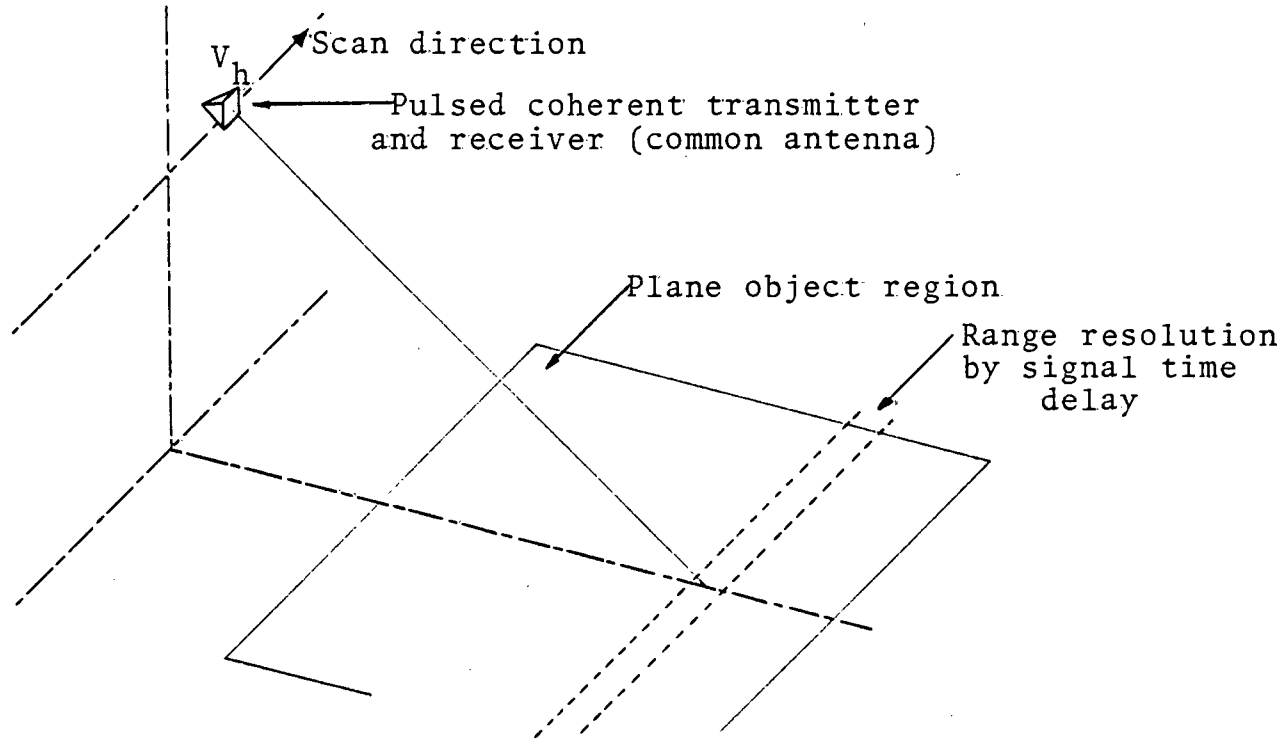

Fig. 6.2 Synthetic aperture radar geometry

systems, but the limited range resolution available in laboratory scale systems does not recommend practical deployment.(Chp.5) The range intervals are thus produced essentially by the projection of the focussed vertical axis beam on the object plane.

A significant difference between the two systems is the relative motion of transmitting and receiving elements in the holographic interpretation, which is absent in SAR. There does not yet appear to be a pure holographic, two axis interpretation of the SAR system with equivalent illumination mode and, in addition, capable of implementation as an inertialess system.

However, the differences in equivalent illumination function between the two systems would only be apparent in comparison of images of specularly reflecting surfaces, since SAR has an equivalent plane wave illuminator and the orthogonal axis imaging system a point illuminator.(sec.4.1) Tomiyasu[74] states relationships linking scan vector, illumination vector and object normal which prohibit specular surface reflections so that this difference need not be material. This difference is not important if imaging of extended rough surfaces is attempted.[104]

It is also convenient if the sequential measurements of the reflected field by a discrete element array can be equated with the measurements obtained by a single element scanned over the equivalent aperture at a constant velocity. The vertical array of Fig.6.1 is replaced by a single focussed array illuminator, and the paraxial approximations commonly made in both microwave holography and SAR are assumed. The vertical array is assumed to be composed of simultaneously-addressable elements, a provision which is in fact compatible with an elegant hardware implementation, and no consideration of sequential field sampling in this axis need be made.

The field f(x) scattered by a point object is measured over an aperture X in a total time T seconds.(Figs.6.3 and 6.4) The spatial smoothing of f(x) introduced by the finite aperture of each individual array element is ignored, as the effect is both common to discrete and continuous models, and did not compromise the measurement of the (bandlimited) fields in the practical system. Field measurements are made at N places, Δx apart, and temporally sampled at intervals of Δt seconds.($\Delta t = \frac{\Delta x}{V_h}$) Each measurement is temporally averaged over a fraction b of the commutation interval Δt. The dimensionless parameter b varies with system configuration, and in the case of the prototype system, b = 0.25. The receiver was operated on a sequential I and Q component measurement schedule, with additional time allowed for analogue computation in the interval Δt. If hardware symmetry in a two-channel receiver were guaranteed, or if a single receiver with SSB processing were used(Chp.7), then b could approach unity. The measured field is thus:

$$f(V_h t) \otimes \text{rect}\left(\frac{V_h t}{b\Delta x}\right) \cdot \sum_T \delta\left(t - \frac{n\Delta x}{V_h}\right) \quad \text{---------- 6.1}$$

The continuous measurement as indicated by Fig.6.4 would result in just:

$$f(V_h t) \quad \text{---------- 6.2}$$

Considering the paraxially-approximate field scattered by a point object, the results of the two measurements are similar, but for a spectral overlay due to the finite integration time, and a periodic spectral structure arising from the regularly spaced field samples. The field spectra are given in Fig.6.5. The apodising effect of the spectral overlay is not serious, since it cannot, as a real function, influence image position, but only influences the sidelobe structure. The Nyquist sampling criterion requires that a frequency f_N is not exceeded:

$$2\pi f_N = \frac{\pi V_h}{\Delta x} \text{ rads./sec.} \quad \text{---------- 6.3}$$

Subject to the above conditions, the simple constant velocity scan adequately describes the operation of the discrete element system.

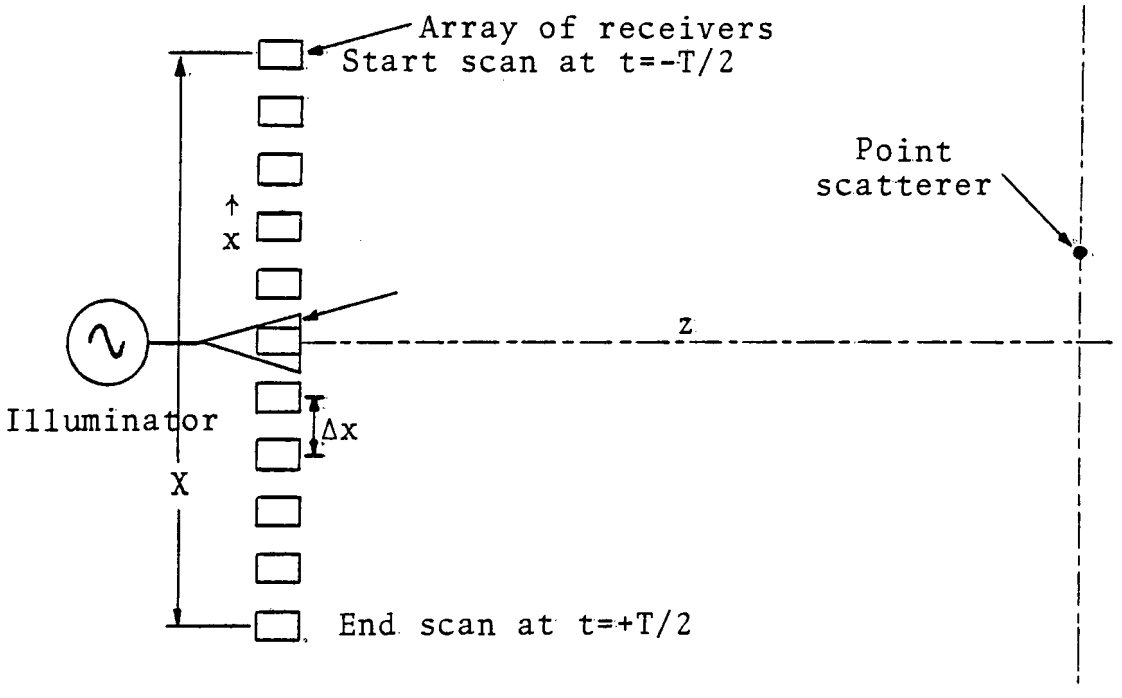

Fig. 6.3 Spatially sampled field measurement

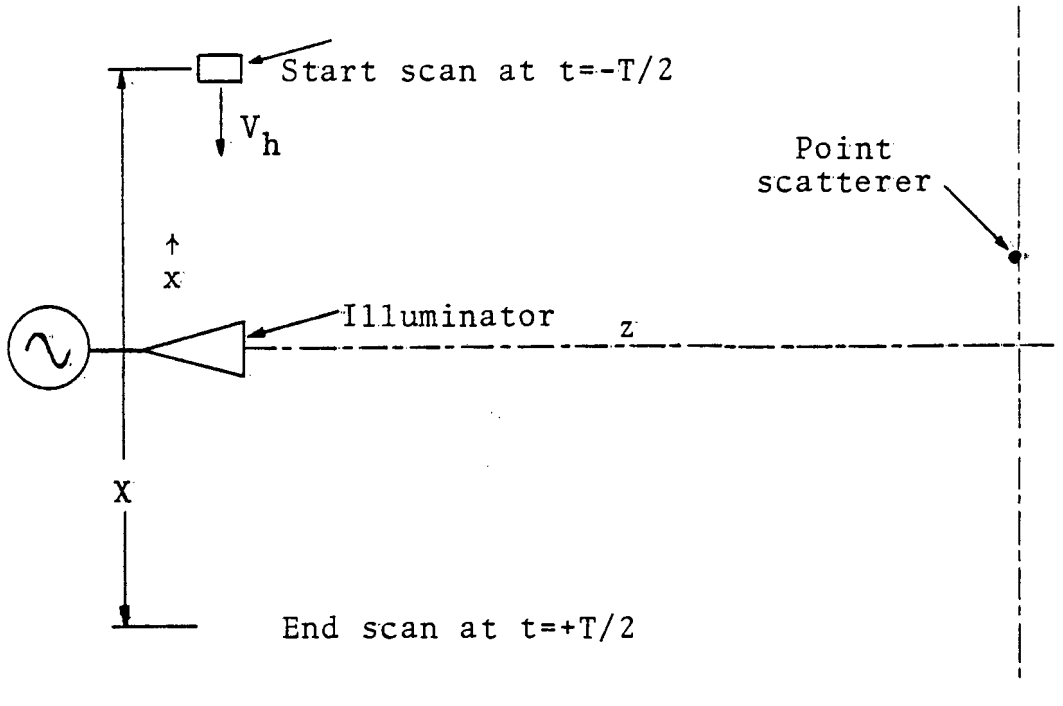

Fig. 6.4 Continuous field measurement

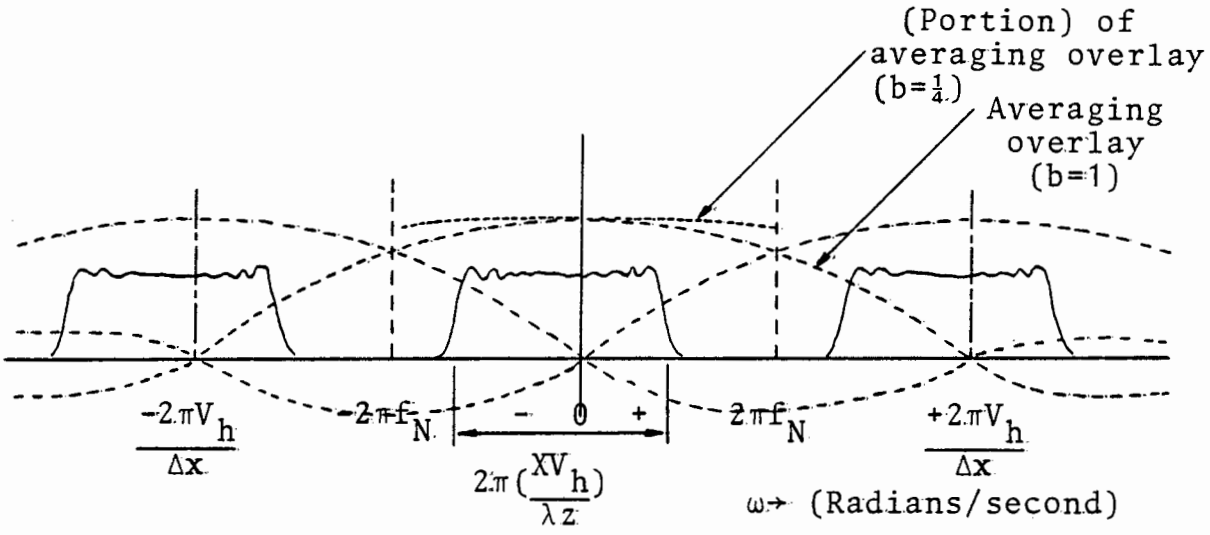

Fig. 6.5(a) Spectrum of sampled field measurement

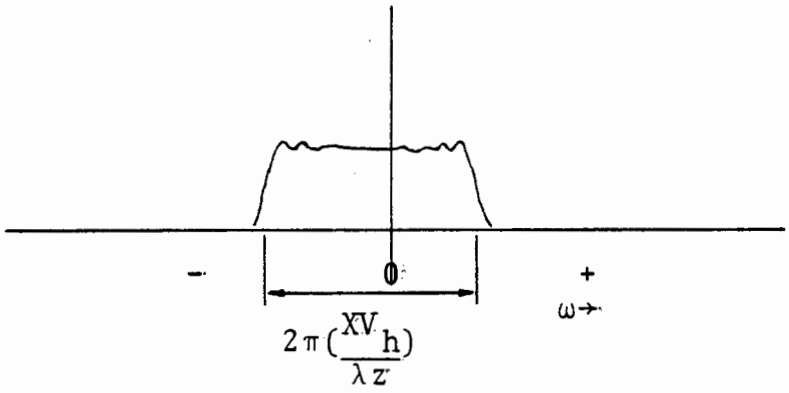

Fig. 6.5(b) Spectrum of continuous field measurement

6.3 Impulse Response in the Presence of Object Motion

6.3.1 Imaging with a continuously scanned array

The effects of object motion on the system impulse response are examined for a point scatterer object moving with arbitrary velocity and acceleration. The array is considered to be scanned in one axis, while the data aquisition in the orthogonal array is assumed to be completed in parallel within one step. This provision produces an imaging mode similar to SAR and is quite compatible with anticipated hardware implementation. An analysis of the motion-induced image artifacts in a system having sequential antenna sampling in both axes, (which was used in the prototype hardware), does not appear to have any advantages compared to the simpler stratagem considered here.[116]

The paraxial Fresnel region of operation implies field separability and allows the orthogonal array to be replaced by an equivalent linear illuminator. (Fig.6.6) Using the notion of a constant velocity receiver scan, the path lengths from illuminator to object and from object to the instantaneous receiver position are respectively:

$$z_1(t) = (z_o^2(t) + y_o^2(t) + x_o^2(t))^{\frac{1}{2}} \quad \text{---------- 6.4}$$

and $$z_2(t) = (z_o^2(t) + y_o^2(t) + (x_o(t) - V_h t)^2)^{\frac{1}{2}} \quad \text{---------- 6.5}$$

and the complex reflected field over the aperture is:

$$f(x_o, y_o, z_o, t) = e^{jk(z_1(t) + z_2(t))} \quad \text{---------- 6.6}$$

The scan is completed in T seconds, and develops an aperture dimension X, where:

$$X = V_h T \quad \text{---------- 6.7}$$

In order to gain some insight into the relative effects of different axial motions, eqs.6.4 and 6.5 are expanded as a Maclaurin series about the point t=0, and linear and quadratic terms are retained, following the reasoning of Raney in [114]. These terms correspond to image offset and defocus respectively, and represent, in turn, the more important image perturbations. Object motion is taken in 3

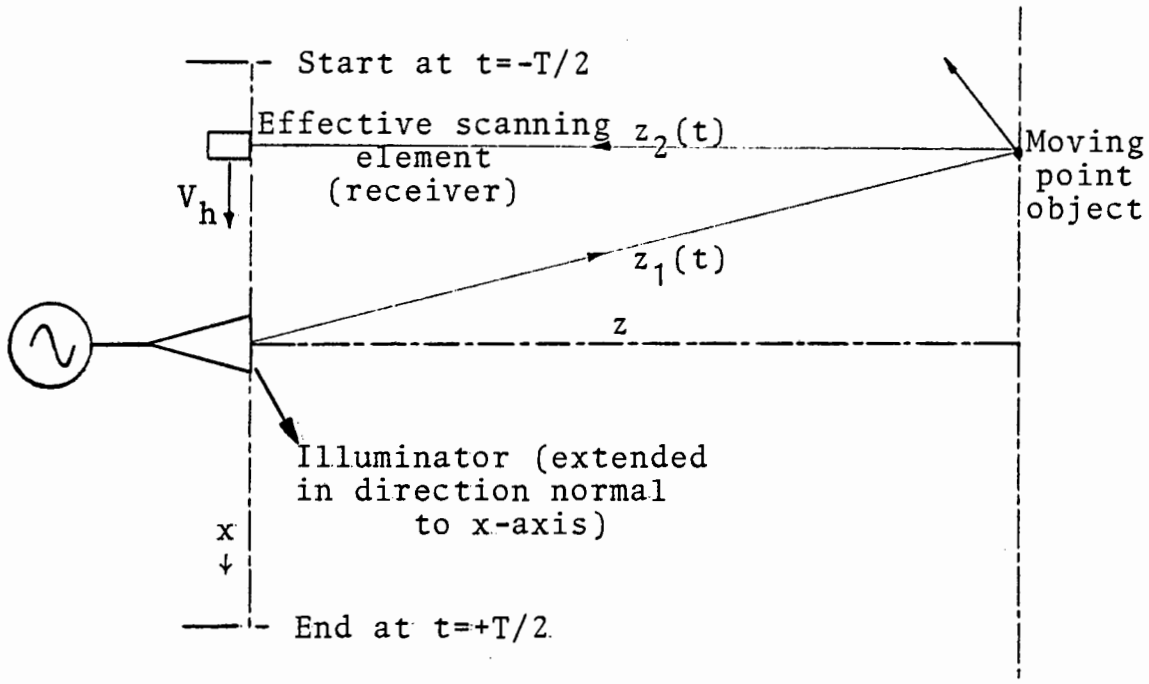

Fig. 6.6 On imaging a moving object

axes, as:

$$x_o(t) = x_o + V_x t + \tfrac{1}{2}a_x t^2$$
$$y_o(t) = y_o + V_y t + \tfrac{1}{2}a_y t^2$$
$$z_o(t) = z_o + V_z t + \tfrac{1}{2}a_z t^2 \quad \text{---------- 6.8}$$

The approximate total path length is:

$$z_1(t)+ z_2(t)= 2z' + \frac{(2z_oV_z+x_o(2V_x-V_h)+2y_oV_y)t}{z'} +$$

$$\frac{(x_oa_x+y_oa_y+z_oa_z)t^2}{z'} + \frac{(2V_z^2+2V_y^2+V_x^2+(V_x-V_h)^2)t^2}{2z'} -$$

$$\frac{(z_oV_z+x_oV_x+y_oV_y)^2\,t^2}{2z'^3} - \frac{(z_oV_z+x_o(V_x-V_h)+y_oV_y)^2\,t^2}{2z'^3} \quad \text{------ 6.9}$$

where $z' = (z_o^2 + x_o^2 + y_o^2)^{\frac{1}{2}}$ ---------- 6.10

A further simplification results if object position at t=0 is confined to the immediate vicinity of the z-axis; that is, if $x_o=y_o=0$. This assumption is always acceptable in SAR processing, since it is in the nature of this technique to produce an along-track data record whose physical extent far exceeds that ground swath illuminated at a given time. It is thus unnecessary to account for other than symmetrical object-aperture geometries in SAR, and indeed one reported digital processor discards imagery within one half illuminated ground swath at the origin and end of the data record.[105] Such a provision is usually unacceptable in microwave holography, since spatial resolution is almost always sufficiently coarse not to warrant further restriction by illumination modification. However, the approximation is made to extract the dominant motional artifacts, and to suggest an experimental geometry.

From eq.6.10, the field phase is $\phi(t)$, where:

$$\phi(t)= 2kz_o + 2kV_z t + \frac{k(2V_y^2+V_x^2+(V_x-V_h)^2+2z_oa_z)t^2}{2z_o} \quad \text{--------- 6.11}$$

If the terms in V_x^2 contribute much less than π radians phase, they can be ignored, and time-invariant terms in eq.6.11 are also of no consequence. Hence:

$$\phi(t)= 2kV_z t + \frac{k(2V_y^2+V_h^2-2V_xV_h+2z_oa_z)t^2}{2z_o} \quad \text{---------- 6.12}$$

6.3.2 Imaging Static Objects

The reconstruction process appropriate under the paraxial approximation is, from sec.3.3.1:

$$F(\beta) = \int_{-T/2}^{+T/2} e^{j\phi(t)} \cdot e^{-j\frac{kV_h^2}{2z_o}(\beta-t)^2} \cdot dt \quad \text{---------- 6.13}$$

The image plane variable x' is:

$$x' = \beta V_h \quad \text{---------- 6.14}$$

A point object, stationary at position $(0,0,z_o)$ leads to a system azimuthal impulse response:

$$F(\beta) \propto \operatorname{sinc}\left(\frac{kV_h^2 \beta T}{2z_o}\right) \quad \text{---------- 6.15}$$

This function has a half-intensity width of approximately:

$$\beta_{-3dB} = \frac{\lambda z_o}{TV_h^2} \text{ seconds} \quad \text{---------- 6.16}$$

This corresponds to the conventional form of the spatial resolution x'_{-3dB}: (eq.6.7)

$$x'_{-3dB} = \beta_{-3dB} \cdot V_h = \frac{\lambda z_o}{X} \quad \text{---------- 6.17}$$

6.3.3 Radial Object Velocity

From eq.6.12 only radial velocity component V_z leads to image shift, and other velocity and acceleration components tend to defocus the image. The reconstruction process of eq.6.13 will generate an image centred about β_{max}, where:

$$\beta_{max} = \frac{-2z_o V_z}{V_h^2}, \text{ and the image spatial shift is:}$$

$$x'_{max} = \frac{-2z_o V_z}{V_h} \quad \text{---------- 6.18}$$

Compared with the equivalent situation in SAR,[69,73,74,114] the holographic process develops twice the offset, since there is relative motion between illuminator and scanning element, and the SAR system has better resolution by a factor of two, when the systems are compared on the basis of equal wavelength, range and aperture dimensions. The foregoing analysis would appear to allow unrestricted radial velocity, but the spectral shift implicit in eq.6.12 must not violate

the Nyquist criterion (eq.6.3) nor cause image radial shift outside the range resolution (depth of focus) of the orthogonal illuminator axis, which is assumed to have been focussed at range z_o.

A more complete expansion of eq.6.6 admitting only radial motion finds a cubic range term. The allowable cubic phase error depends on the acceptable extent of impulse response degradation in terms of peak gain loss and sidelobe suppression, but an upper limit of about one radian is suggested by Harger.[64] Assuming peak error of $\pi/4$ radians:

$$V_z < \frac{2z_o^2 V_h \lambda}{X^3} \qquad \text{6.19}$$

The total radial object motion is $V_z T$, and from eq.6.7:

$$V_z T < \frac{2\lambda z_o^2}{X^2} \qquad \text{6.20}$$

The paraxial region range resolution is , from eq.3.29:

$$\Delta z = \frac{\lambda z_o^2}{X^2}$$

The restriction is analogous to SAR[114], with the difference that the latter has range resolution defined by pulse width. The holographic interpretation using an orthogonal axis array, simultaneously addressed, defines range resolution, and factors such as object motion which influence azimuthal focal length can be monitored by reference to focal length in the orthogonal axis.

Quite apart from radial motion within the depth of focus, the radial velocity component must not cause image aliasing due to excessive spectral shift. From eq.6.12, the radial velocity frequency shift is $\omega = 2kV_z$. Referring to eq.6.3 and Fig.6.5, the Nyquist criterion requires:

$$2kV_z + \frac{\pi V_h^2 T}{\lambda z_o} < \frac{\pi V_h}{X} \qquad \text{6.21}$$

Maximum radial object displacement is $V_z T$, where:

$$V_z T < \frac{\lambda X}{4\Delta x} - \frac{X^2}{4z}$$

In the limit of long ranges:

$$V_z T < \frac{\lambda X}{4\Delta x} = \frac{\lambda}{4}(N-1) \quad \text{---------- 6.22}$$

N is the number of antennae (35 including the gap in the array in the prototype system) in the azimuthal axis. The restriction of eq.6.22 proves more conservative than that of eq.6.20 at ranges exceeding 2 metres. Such ranges were not exceeded in the prototype system.

6.3.4 Azimuthal Object Velocity

The peak quadratic phase error in eq.6.12 must not exceed π radians, if defocussing is not to diminish image intensity by more than 3dB. Assuming the reconstruction process of eq.6.13 is used, with reconstruction attempted at range z_o, then from eq.6.12:

$$\frac{k}{2z_o}(-2V_x V_h + 2V_y^2 + 2z_o a_z)\, t^2 < \pi$$

The largest value of t is T/2, and total azimuthal object motion is $V_x T$. If $V_y = a_z = 0$:

$$V_x T < \frac{-2\lambda z_o}{X} \quad \text{---------- 6.23}$$

The object must not move by more than twice the lateral resolution during the aperture formation time. This motion could be compensated by adding a term to the reconstruction process which cancels the quadratic dependence of eq.6.13. The effective reconstruction focal length or range would then become z_o', where:

$$z_o' = z_o + \frac{2V_x z_o}{V_h} \quad \text{---------- 6.24}$$

Eq.6.24 assumes that V_x is much smaller than V_h. The range offset required for correct focussing is of the same form as that developed as azimuthal offset by radial motion. (eq.6.18) A velocity component V_x of the same sign as V_h will reduce hologram spatial frequency range, and this is attributable to a reflection from a longer object range.

6.3.5 Elevation Object Velocity

If both azimuthal (x-axis) velocity and radial (z-axis) acceleration are suppressed, then applying previous reasoning (eq.6.23) leads to:

$$V_y T < (2z_o\lambda)^{\frac{1}{2}} \quad \text{---------- 6.25}$$

A second, more restrictive, limit on allowable y-axis displacement during the horizontal (x-axis) aperture formation time T is imposed by the vertical (y-axis) array illumination(Fig.6.6) This illumination is extended an amount Δz in the range axis,(eq.3.29) and will have a -3dB resolution in the vertical axis of $\lambda z_o/X$, assuming that both arrays have equal lengths. The vertical aperture is taken to be formed by parallel(that is, simultaneous) operation of all array elements during the time allocated to one horizontal axis element, and if no vertical axis defocussing is allowable, then object displacement in this axis must not exceed $\lambda z_o/X$. In the ranges used in the prototype system,(z_o=0.4 to 2metres), the last criterion dominates allowable y-axis object displacement. Other object motions do not perturb the vertical axis imaging operation, since the criteria derived in the slower horizontal axis operation are governed by aperture formation times T at least N(N is the number of horizontal array elements) times larger than that of the vertical array.

6.3.6 Radial Acceleration

Radial acceleration is the only significant component of object acceleration, and leads to image defocussing.(eq.6.12) If radial acceleration is a major contributor to eq.6.12, then the aperture formation time must be less than T, where:

$$T < \left(\frac{2\lambda}{a_z}\right)^{\frac{1}{2}} \quad \text{---------- 6.26}$$

Given the same allowable peak phase error, an identical limitation applies in SAR imaging.[79,114]

6.3.7 Comparison with SAR Imaging

Raney's SAR analysis[114] is extended to include motion in the plane normal to that common to aperture and object, as has been done in eq.6.9 here. Under the conditions leading to eq.6.11, and assuming the geometry of Fig.6.6, but with simultaneous scanning of illuminator and receiver, the returned field phase becomes:

$$\phi(t) = 2kV_z t + \frac{k((V_h-V_x)^2+z_o a_z+V_y^2)t^2}{z_o} \qquad \text{6.27}$$

The appropriate SAR reconstruction operation is, assuming range as z_o:

$$F(\beta) = \int_{-T/2}^{+T/2} e^{j\phi(t)} \cdot e^{-jkV_h^2(\beta-t)^2/z_o} \cdot dt \qquad \text{6.28}$$

The differences between the motional image artifacts found in SAR and holography are those of scale.

The azimuth (x-axis) image offset due to radial velocity is of similar sign but half the value found in eq.6.18, and the maximum allowable radial motion $V_z T$ will increase with diminishing range as the pulse-width determined range resolution in SAR is degraded at shorter ranges.[83] The maximum allowable SAR azimuthal velocity V_x is one half the holographic value, but overall motion is still twice the azimuthal resolution, since this is superior to that found in the microwave holographic system by a factor of two. Both y-axis velocity V_y and radial acceleration a_z are subject to the same limitations in the two imaging systems.

6.4 A Practical Microwave Holographic Wave Probe

An implementation of the orthogonal axis microwave holographic system as an instrumentation tool in a laboratory wavetank should be capable of variable incidence angle illumination, and for the purposes of avoiding motional effects in cross-section measurements, be capable of forming the required aperture in a selected time.

The geometry of Fig.6.1 is suited to this task, as the experimental parameters of variable incidence angle and varying azimuthal offset can be simply implemented by using the "range-plane" imaging régime of Chp.5. Some demands are made of the polar patterns of transmitting and receiving elements, particularly at shorter ranges, but a secondary advantage of the arrangement is the freedom from image defects due to certain hardware errors which tend to introduce a defocussed conjugate image overlay on more conventional coplanar object-hologram aperture geometries. The radiation patterns of the individual elements need only approximate the "cosec^2" pattern often specified in SAR[103], as the effect of varying illumination field strength with increasing range is easily compensated in a numerically-based reconstruction process.

To demonstrate the effect of varying incidence angle, and to include the possibility of object azimuthal offset, x- and z-axis motions simulate , as an example, part of a wave swell moving in the object "range-plane". Vertical (y-axis) motion is neglected. A very similar situation has been studied by Elachi and Brown[69] and assumed the use of the SAR sensor. (Fig.6.7)

A modified paraxial approximation is used to describe the scattered field, and the illuminator-object-receiver distance expanded as a function of both time and azimuthal position including no more than second order terms. The projection of the focussed vertical array illumination function on the object plane is taken to determine both range and range resolution, against which motional defocussing of azimuthal data can be compared. The respective illuminator-object and object-receiver distances are:

$$z_1(t) = (z^2(t) + y^2 + x^2(t))^{\frac{1}{2}} \qquad \text{6.29}$$

and $$z_2(t) = (z^2(t) + y^2 + (V_h t - x(t))^2)^{\frac{1}{2}} \qquad \text{6.30}$$

where

$$x(t) = x + V_x t + \tfrac{1}{2} a_x t^2$$

and $$z(t) = z + V_z t + \tfrac{1}{2} a_z t^2 \qquad \text{6.31}$$

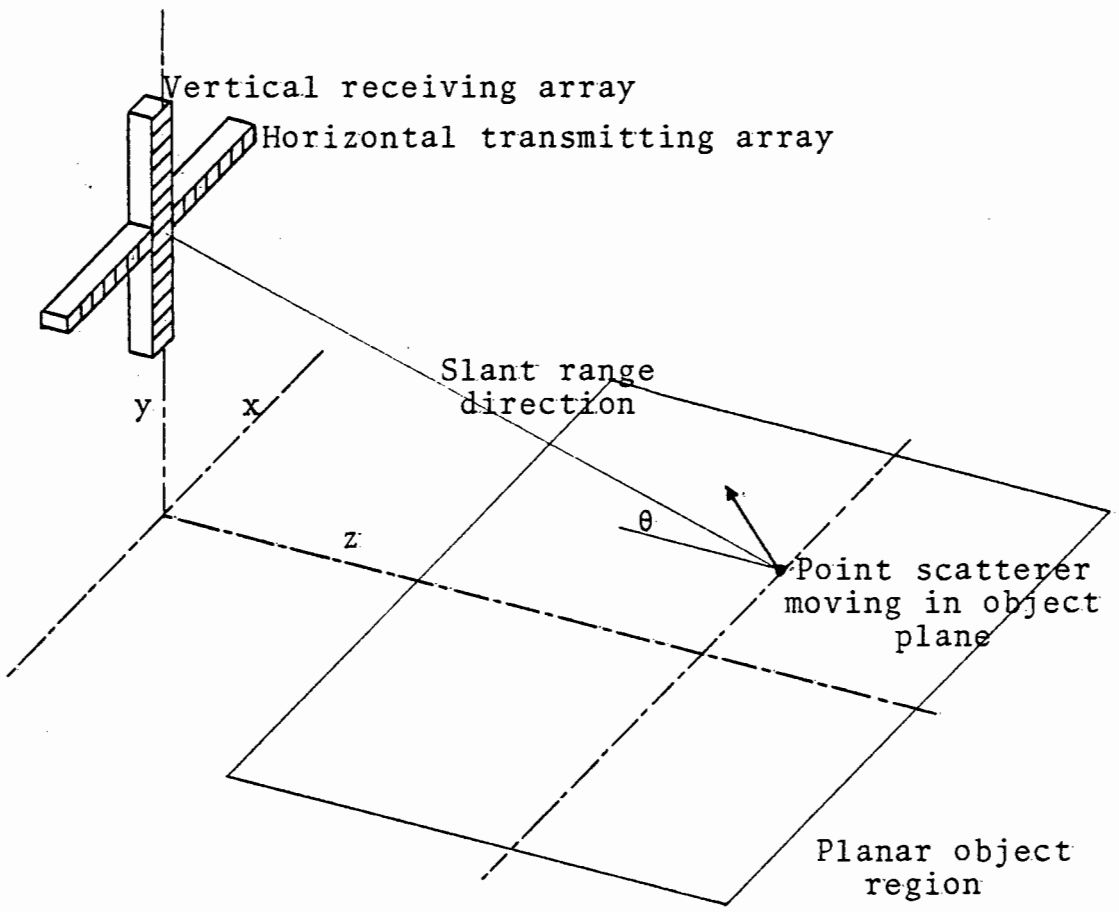

Fig. 6.7 A practical microwave holographic wave probe geometry

$$z_1(t)+ z_2(t)= 2z' + 2V_z\cos\theta t + \frac{x^2}{z'} + \frac{x}{z'}(2V_x-V_h)t +$$

$$(\frac{V_z^2\sin^2\theta}{z'} + a_z\cos\theta + \frac{V_h^2}{2z'} - \frac{V_hV_x}{z'} + \frac{V_x^2}{z'})t^2 \quad \text{---------- 6.32}$$

The slant range $z' = (z^2 + y^2)^{\frac{1}{2}}$, and depression angle $\theta = \sin^{-1}(y/z')$. The incidence angle is $\pi/2-\theta$ radians. Terms which are not functions of time are disregarded for reconstruction purposes. Following eq.6.13, the azimuthal reconstruction, assuming no á priori knowledge of object motion is:

$$F(\beta) = \int_{-T/2}^{+T/2} e^{jk(z_1(t)+ z_2(t))} \cdot e^{\frac{-jkV_h^2}{2z_o}(\beta-t)^2} .dt \quad \text{------- 6.33}$$

The maximum image amplitude is "delayed" an amount β_{max}, where:

$$\beta_{max} = \frac{-2z'V_z\cos\theta}{V_h^2} - \frac{x}{V_h^2}(2V_x-V_h) \quad \text{---------- 6.34}$$

The image maximum is centred about x'_{max}:

$$x'_{max} = x - \frac{2xV_x}{V_h} - \frac{2z'V_z\cos\theta}{V_h} \quad \text{---------- 6.35}$$

Both range and azimuth velocity components contribute to azimuthal error in image position, although the magnitudes of such errors reduce as the scan velocity is increased. The apparent radial velocity is the V_z component resolved in the slant range direction, although the magnitude of the offset is compensated by the slant range, since $z'\cos\theta = z$. An azimuthal image positional error arises only if the object is offset.

A fundamental property of both coherent pulsed and continuous wave aperture synthesis procedures is the ambiguous relationship of radial velocity and azimuthal offset(eq.6.35), such that observed image offsets are attributable to either or both parameters. This property is reminiscent of coupling between range and range rate in linear-FM pulsed radars.[65] Zero vertical (y-axis) object motion has been supposed, but the range-plane velocity component normal to the slant range direction introduces a term similar to V_y in eq.6.12. To avoid image defocussing on this account:

$$V_z\sin\theta < \frac{(2z\lambda)^{\frac{1}{2}}}{T} \quad \text{---------- 6.36}$$

It is necessary that radial motion does not exceed twice the range resolution. The range resolution is principally determined by the vertical array illumination function, and assuming the paraxial field description, would not be less than:

$$\Delta z = \frac{\lambda z \cot\theta}{Y} \qquad \text{6.37}$$

The vertical aperture dimension is here taken as Y. Eq.6.36 can be ignored if:

$$\frac{(\lambda z)^{\frac{1}{2}}}{Y} > \frac{\sec\theta}{1.42} \qquad \text{6.38}$$

For the range of θ encountered in SAR imaging ($\theta = 70^{o}$ to grazing incidence), the right hand side of eq.6.38 will not greatly exceed unity, and can be viewed as a requirement for operation outside the far-field region of the mapping aperture, if no defocussing due to the component of V_z resolved into the slant range direction is wanted. However, within this region, allowable z-axis object displacement is in any case limited by the illuminator function in the normal manner. (eq.6.20)

Following eq.6.23, x-axis motion is limited during the aperture formation time T to:

$$V_x T < \frac{2\lambda z'}{X}$$

If object motion is confined to uniform velocity in x- and z-axes, then the x-axis component modulates the apparent focal length, and for small V_x the change is:

$$\Delta z' = \frac{2V_x z'}{V_h} \qquad \text{6.39}$$

The arrangement of Fig.6.7 allows the recovery, from either hologram data or a completely specified image, of the sign and magnitude of object azimuthal velocity, since eq.6.39 represents the dominant focal length modification. Image refocussing techniques implemented by optical processors have been reported in the SAR literature.[77] A microwave array geometry admitting significant object velocity in the direction normal to slant range and azimuth axes would thus be rather less useful, since the relevant focal length modulation term is ambiguously represented in sign. (eq.6.12)

6.5 Manipulation of Scan Format

Several authors have drawn attention to the differences in imagery produced by synthetic aperture radars(SAR) and real aperture radars (usually referred to as SLAR).[76,78,81] The latter can be regarded as a limiting case of the former in which the spatial sampling has been carried out at very high velocity. A direct comparison of imagery from the two techniques is complicated by differing wavelengths, pulse lengths and aperture dimensions of competing systems.

A result which is trivially obtained but nevertheless of considerable importance arises from the foregoing analyses. Object motions have diminishing influence on the image impulse response as the scan velocity V_h is increased.

A lower aperture formation time can be specified below which motional influences lead to image offsets and change of focal lengths less than the spatial resolution in any axis. It would thus appear that a microwave holographic reduced scale implementation of the SAR technique could be operated with varying aperture formation times T to simulate both SAR and, effectively, SLAR at a common wavelength and with equal aspect and spatial resolution of the same controlled object environment.

The incentive is the separation of image detail due purely to hydrodynamic modulation of the regional water cross-section, an effect "relatively well understood"[81], and that detail apparently introduced by the relative motion of scanning element, and the linear, accelerated, and cyclic motions of the water surface. As an example, scan modulation could be used to test a SAR image formation model wherein a surface of uniform cross-section which has a periodic particulate velocity profile, leads to image domain contrast and periodicity.[68,72]

That there exists a need for such clarification is evident from the remarks of Alpers et al.[81], recommending radar oceanographic research objectives:

"The most promising avenues of research can be presently accomplished through collaborative efforts involving radio scientists and engineers on the one hand and oceanographers, geophysicists, and hydrodynamicists on the other. There is a great need for experiments involving aircraft equipped with SAR, SLAR, and two-frequency scatterometers flown in coordination with carefully planned surface-truth measurements. The latter has been overlooked in the past and merits much attention in the future.

It is strongly recommended that wave tank and tower experiments be conducted to develop and test models of hydrodynamic and electro-magnetic modulation of the ocean surface microstructure by long waves. Measurements of the dependence of these modulations on the windspeed and wavelength of the microwaves are needed to determine optimum radar-system wavelengths. Tower experiments can be coordinated with remote measurements using simultaneously-operating microwave systems to define the interaction of short waves and long waves and their interaction with electro-magnetic waves.

Research on radar-ocean interaction should have priority over the search for the applications of these radar systems to new oceanographic features with wave or wave-like patterns."

6.6 Moving Object Imaging

6.6.1 Experimental Procedure

Some simple observations of a controlled wave tank surface were made to illustrate the application of a holographic wave probe. The non-dispersive gravity wave régime was selected to simulate the analytically tractable situation of an object of limited extent travelling at known velocity. Water wavelengths substantially in excess of the system linear resolution were required for meaningful imagery. Both requirements pointed to a shallow water wave, with mean water depth much less than a wavelength. This was fortunately logistically convenient. The tank was equipped with an

electrically driven, variable stroke and rate paddle, which was shielded from system view by a mesh screen and covering microwave absorptive material above water. At the other end, an angled screen trapped floating plastic balls, and formed an effective wave energy absorber.(Fig.6.8) This precaution prevented the development of a standing wave pattern in the tank, a situation which would have unnecessarily complicated image analysis.

The time taken to complete aperture formation (47.5mS and 950mS respectively for fast and slow array axes) denied a practical two-axis imaging system using the established hardware of the prototypical system in the face of wave crest speeds up to nearly 1m/S. The array circuitry was, however, flexible and commutation rates could be exchanged. Following the array-object deployment proposed in Chp.5,the vertical array was used with a fixed focal length and at the faster rate to define a "range-interval" on the water surface. The image series derived from time-ordered reconstructions of successive complete array scans was intended to produce a history of surface reflectivity in this interval.

The Nyquist sampling criterion of eq.6.3 restricts the maximum radial movement of an object crest during the formation time of an aperture. From eq.6.21:

$$V_z T < \frac{\lambda X}{4\Delta x} - \frac{X^2}{4z}$$

A typical crest speed was 670mm per second. Even in the limit of long ranges, the slower axis formation time T=950mS would result in over one half metre object movement, whereas less than half this is allowed by eq.6.21. The faster axis has a limit on object movement of about 32mm by the same criterion, and this is rather less than the range resolution found in static demonstrations of the "range-plane" imaging mode.

The test geometry(Fig.6.8) had therefore, the vertical array switched at the faster rate of 421Hz and performed a receive function. The horizontal array was functionally replaced by an isolated shunt switch and horn antenna assembly, so that the received signals simulated normal operation of the

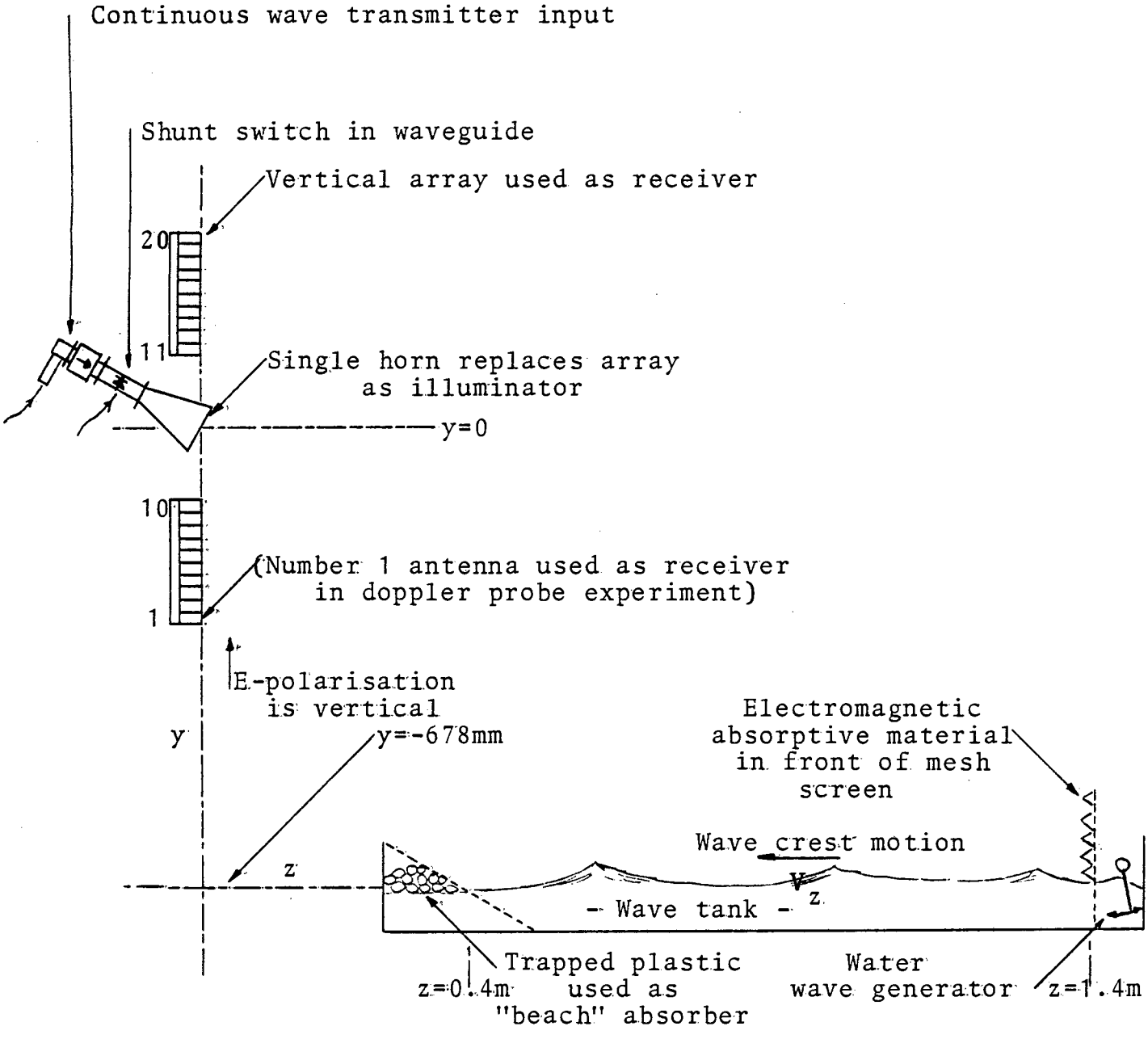

Fig. 6.8 Side view of vertical array and wave tank

orthogonal axis array mode. The non-availability of the second array restricted the scope of imaging processes by one dimension.

As an aid to image analysis, an optical photograph of the tank was taken looking along and down at the crest line. The camera and associated flash system were triggered by a radio remote controlled link as **the first of the series of** interrupt pulses signalling computer data acquisition became available.

6.6.2 Bragg mode reflection from Surface Ripples

An initial experiment used the simplest possible system for checking the feasibility of monitoring surface reflections. The single horn illuminator and the first receiver antenna simulated a sampled data doppler transceiver-with-sense. The vertical array was conventionally switched, but a software demodulator was used to extract I and Q data pairs from the data stream at positions 1,2,41,42,81,82,..... corresponding to a 21Hz sampling rate of a single receiver.

The radial velocity component of the paddle generated waves was too high for unaliased operation, and lower velocity short gravity waves were generated using a compressed air source. (Fig.6.9(a))Stroboscopically examined, the surface ripples appeared at a rate of 8.3Hz and had wavelengths in the range 25 to 35mm, leading to a phase velocity in the region of 0.25m/S. This value is intermediate between the phase velocity of supposed surface tension waves (0.11m/S) and deep water gravity waves (0.59m/S) at this wavelength, although the wavelength was too long for the former, and the water too shallow for the latter descriptions.[117]

The Bragg reflection mode was implicated as the I and Q components representing the complex received signal were routinely observed in space quadrature on an oscilloscope in the X-Y mode, and the periods of maximum signal return were characterised by sporadic circular patterns on the

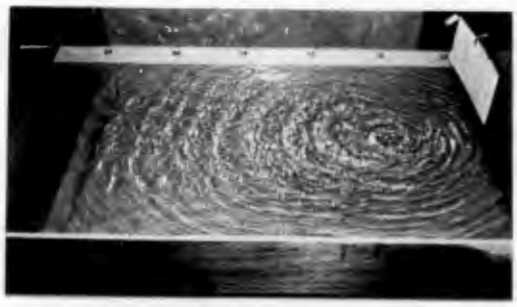

Fig. 6.9(a) Short gravity waves in tank
(Doppler probe left of tank)

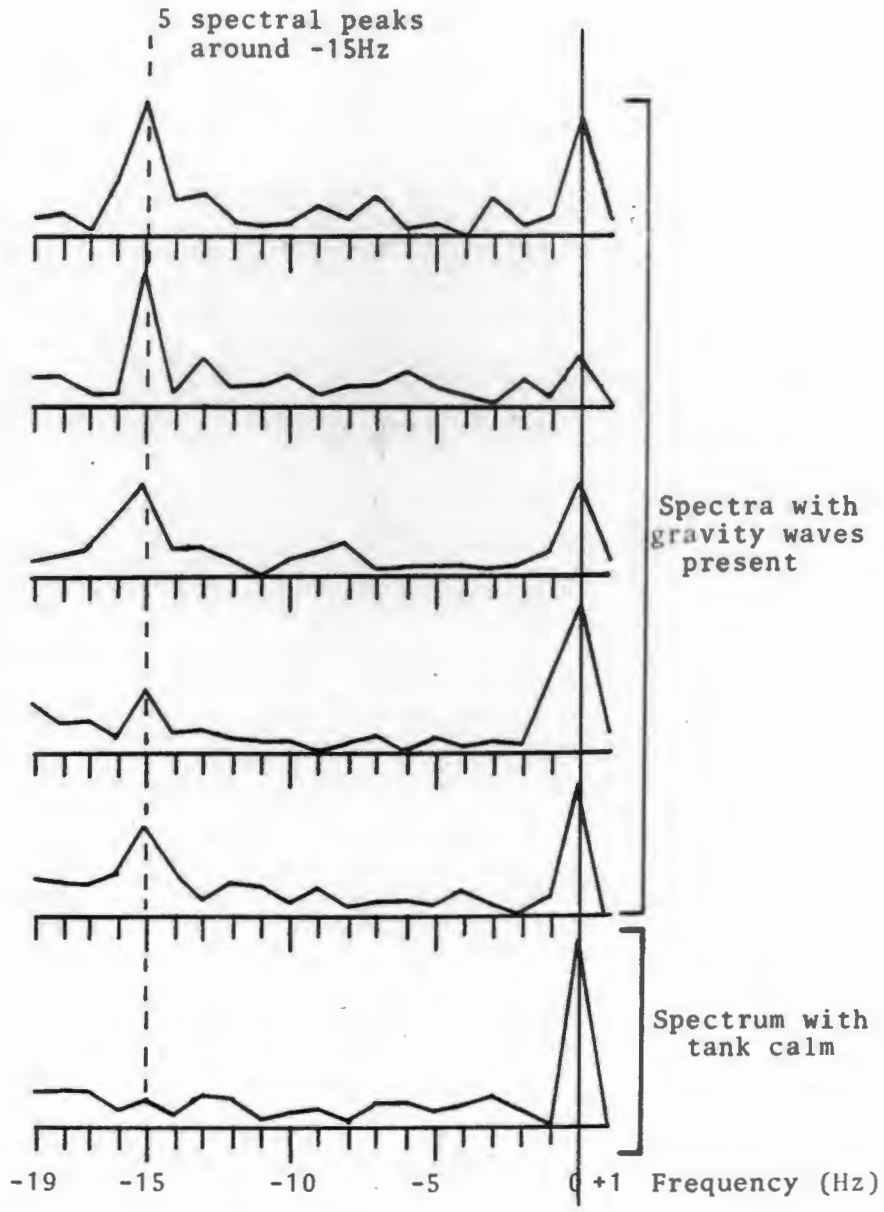

Fig. 6.9(b) Spectral series using doppler probe

screen, with an observed sense of rotation clearly linked to the sense of "wind" radial velocity. The observed ripple wavelength range also supports this conjecture.(118) Assuming a depression angle θ for the transmitting horn, and ϕ for the receiving antenna, the received doppler offset would be very close to:

$$f_d = \frac{V_z f_o}{c}(\cos\theta + \cos\phi)$$

The transmitted carrier frequency is f_o=9.9Ghz, c is the EM wave propagation velocity, and V_z is measured normal to the aperture.(Fig.6.9) The range from aperture to interaction area on the surface varies and is not retrievable by imaging procedures using only one antenna pair.

The data sampling rate was 21.1Hz so that unambiguous doppler determination was possible over a range -10.5Hz to +10.5Hz. Once the anticipated sign of doppler offset was known, a complex offset was added to the data, so that the doppler frequency range of Fig.6.9(b) is -19Hz to +1Hz. The spectra were obtained by applying a discrete Fourier Transform(DFT) to the complex, offset data.

$$F(f_d) = \sum_{n=1}^{21}(f_c(n\Delta t).e^{j\omega'\Delta t}).e^{-j\omega\Delta t}$$

The sample interval Δt is 47.5mS and f_c represents complex data. The offset intoduced is ω', and was equivalent to 9.5 Hz in Fig.6.9(b). Five spectra clearly show a peak at -15Hz, in contrast to a sixth spectrum of data taken with the tank in a calm state in which only components around zero frequency are present.

The spectral peaks at -15Hz indicate a radial velocity component of 0.23m/S, and the sign of the offset was correct- this was checked using a manually translated cooperative target (Appendix II) and the same DFT processing. The data record was of approximately 1 second length, and comprised 42 signal measurements, but the spectral resolution was in some cases determined more by the object stability than by record length, as the observed Bragg interaction intervals were often less than one second in duration.

The aliasing limitations of the processor in relation to the received signal offset did not allow unambiguous comparison of simultaneous positive and negative frequency spectra over a range exceeding ±15Hz about zero frequency. A fundamental limitation of the sequential processor is the appearance of conjugate spectral peaks (Appendix II) , and these would be here at a level of -31dB relative to the wanted spectrum.

The continuous wave doppler probe has demonstrated in microcosm a remote sensing technique much used in the determination of distant sea states.(81,115,119-121)

6.6.3 A Vertical Aperture Imaging System

The vertical (receiver) array and single horn illuminator were used to create a "range interval" on the water surface. The lack of a second aperture dimension removed the possibility of resolving object detail in the azimuthal axis. The array centre and illuminator are both positioned a distance Y above the object plane. The vertical aperture is of length Y' and is scanned at a rate V_vm/S in a time T seconds. (Fig.6.10) Thus:

$$Y' = V_v T \quad \text{----------} \quad 6.40$$

In the practical system, the array was in two sections, and the scanning proceeded directly from the last antenna of the bottom subarray to the first antenna of the top subarray. The effect of this discontinuity has been checked by simulation. The practical system also suggested that object motion be limited to one axis, z, since motional components in the x-axis would, in a single array system, lead to reduced image contrast. The depression angles ϕ, θ commonly used were in excess of those allowable under the paraxial approximation, and a modified two-variable expansion of the distances from object to source to array is used. The distance from object to illuminator is:

$$z_1(t) = (y^2 + z^2(t))^{\frac{1}{2}} \quad \text{----------} \quad 6.41$$

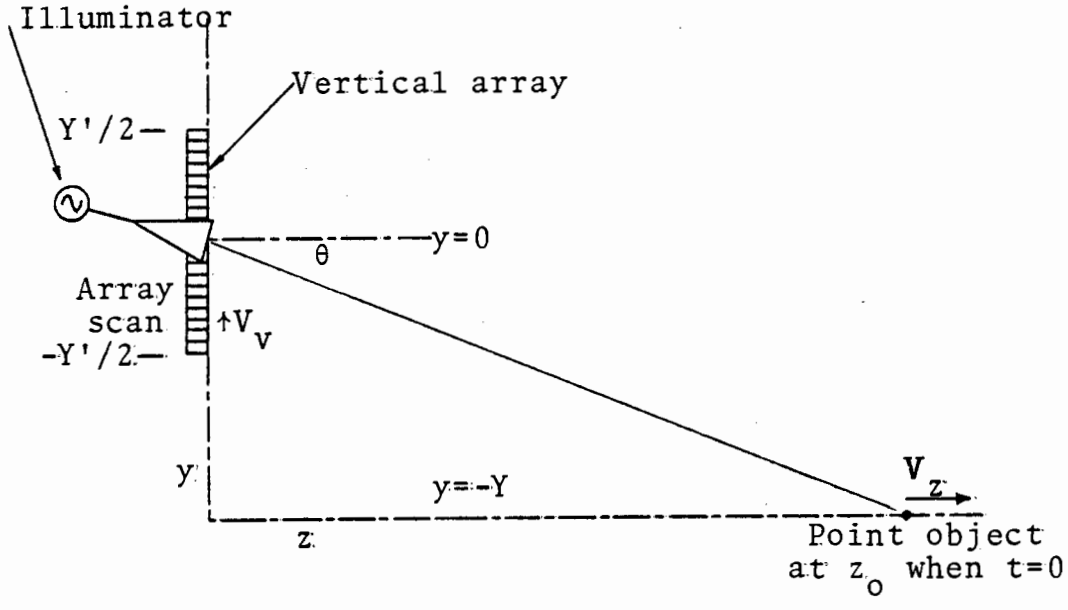

Fig. 6.10 A single vertical array and moving object

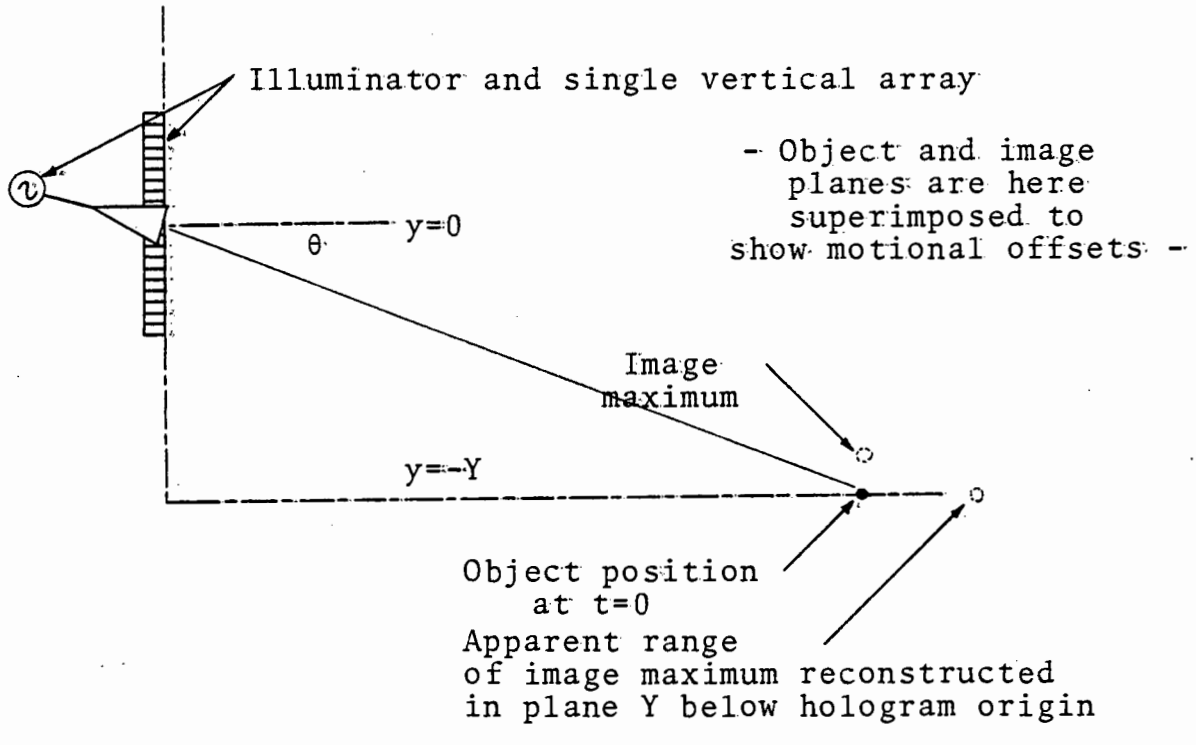

Fig. 6.11 On the image maximum shift

where: $$z(t) = z_o + V_z t \quad \text{---------- 6.42}$$

The distance from object to the scanning receiver is:

$$z_2(t) = ((y - V_y t)^2 + z^2(t))^{\frac{1}{2}} \quad \text{-------- 6.43}$$

The quantity $(z_1(t) + z_2(t))$ is expanded as a Taylor series of two variables about t=0 and y=-Y, whence:

$$z_1(t) + z_2(t) = 2V_z \cos\theta\, t + \frac{YV_y t}{z'} + \frac{V_z^2 \sin^2\theta\, t^2}{z'} + \frac{V_y^2 \cos^2\theta\, t^2}{2z'} \quad \text{-- 6.44}$$

Terms in (y+Y)t are ignored as reconstruction need only be performed about the point y = -Y, since no image detail is expected above or below this point in the case of static objects. The slant range z' is defined as:

$$z' = (z_o^2 + Y^2)^{\frac{1}{2}} \quad \text{---------- 6.45}$$

If the object velocity $V_z = 0$, then the significant terms in eq.6.44 become:

$$z_1(t) + z_2(t) = V_y \sin\theta\, t + \frac{V_y^2 \cos^2\theta\, t^2}{2z'} = y\sin\theta + \frac{y^2 \cos^2\theta}{2z'} \quad \text{---- 6.46}$$

This reduces to the paraxial form $y^2/2z'$ for small angles θ. Eq.6.46 suggests that a paraxial reconstruction operation assuming a backpropagation function whose phase is $y^2/2z''$ would generate an image with insufficient offset, and would be found at a distance $z'' = z'\sec^2\theta$, or in excess of the true distance. This behaviour has been noted in imagery generated by the paraxial optical reconstruction processes. (Chps.4 and 5) A reconstruction procedure suggested by eq.6.46 for image detail close to y = -Y is:

$$F(\beta) = \int_{-T/2}^{+T/2} e^{jk(z_1(t)+z_2(t))} \cdot e^{-jk((\frac{V_y^2 \cos^2\theta}{2z'})(t-\beta)^2 + V_y \sin\theta\,(t-\beta))} \cdot dt \quad 6.47$$

The impulse response near y = -Y in the y-axis for motionless objects is:

$$F(\beta) \propto \mathrm{sinc}(\frac{\pi V_y^2 \cos^2\theta\, T.\beta}{\lambda z}) \quad \text{---------- 6.48}$$

The spatial -3dB resolution is:

$$\beta_{-3dB} \cdot V_y = \frac{\lambda z'}{Y' \cos^2\theta} \quad \text{---------- 6.49}$$

The resolution is larger , or worse, than that expected of paraxial reconstruction, as the projected aperture is less than the physical aperture and the range is modulated by object offset. Including the effects of object motion(eq.6.44) and using the same reconstruction process, the y-axis position

of the image is apparently shifted an amount δy, where:

$$\delta y = \frac{-2V_z z'}{V_v \cos\theta} \qquad \text{6.50}$$

In the practical situation V_z was negative as the wave crest advanced towards the array, and the measured hologram data has apparently the characteristic of that hologram derived from a static object some distance above the water surface. If the reconstruction simply assumes $y = -Y$, then the locus of image maximum is such that the image will appear to have a longer range. The image detail reconstructed for $y = -Y$, as for static detail, thus corresponds to object detail at a closer range, if the object closes the array. (Fig.6.11)

The component of V_z normal to the slant range direction is $V_z \sin\theta$, and it modulates the apparent data focal length. From eq.6.44 the apparent focal length is z'', where:

$$\frac{V_z^2 \sin^2\theta t^2}{z'} + \frac{V_v^2 \cos^2\theta}{2z'} = \frac{V_v^2 \cos^2\theta}{2z''} \qquad \text{6.51}$$

$$z'' \doteq z' - \frac{2V_z^2}{V_v^2} \tan^2\theta z' \qquad \text{6.52}$$

In the practical system, $V_z = -0.67$m/S, $V_v = 7.65$m/S, z' was not less than 1m, and θ was not more than 45°, such that:

$$z'' = z' - 15\text{mm}$$

The total phase shift associated with the normal range component should not exceed π radians if re-focussing of the hologram data is to be avoided. Thus:

$$V_z T < (2\lambda z' \sin^2\theta)^{\frac{1}{2}} \qquad \text{6.53}$$

The aperture formation time was $T = 47.5$mS, and for the practical system, eq.6.53 required that V_z be less than 2.62m/S, which was easily satisfied. The maximum allowable V_z is also controlled by the Nyquist sampling criterion. From eq.6.21:

$$V_z T < \frac{\lambda Y'}{4\Delta y} - \frac{Y'^2}{4z_o}$$

The y-axis antenna spacing is Δy. Using typical experimental parameters, the maximum allowable V_z is 2.82m/S, again much larger than the observed value.

The range resolution of the system is essentially that of the y-axis impulse response function projected onto the orthogonal z-axis.(sec.5.7.3)

$$\text{Range resolution} = \frac{2\lambda z'}{Y' \sin 2\theta} \qquad \text{6.54}$$

A typical value for the practical system, assuming z_o = 1.4m, Y' = 677mm, λ = 30.3mm was 178mm, if the gap in the array centre is ignored. The modest object velocities encountered meant that reconstruction operations did not need to compensate for defocussing effects arisng from linear motion.

Influence of Commutation Sequence on Impulse Response

The foregoing analysis has assumed the existence of a finite, filled aperture scanned at uniform velocity V_v. The practical system had a gap in the array centre caused by the bulk of the microwave directional coupler combining the the subarray outputs.(Figs.5.1 and 5.2) The effect of this gap is documented in Appendix I . The axial impulse response has a regular oscillatory structure under an overall "sinc" envelope if the object is stationary with respect to the array. The impulse response of the vertical array imaging system varies with object velocity V_z, even if such velocity does not cause appreciable defocussing, as was the case here. The commutation sequence proceeded directly to the 11th antenna (the 21st in a regular sequence across the gap) from the 10th without allowing a scaled time delay. Both 182mm subarray apertures were switched in 23.75mS and accounted for an equivalent 7.65m/S scan velocity. A simulation of this situation for a range of object velocities V_z shows that the y-axis image offset is determined by ratio of object and scan velocities, according to eq.6.50, but that the position of peak response moves under the overall "sinc" envelope, rather after the manner of the impulse response changes caused by subarray combination phase errors. This effect has also been observed in experimental situations.

Reconstruction from Experimental Data

The reconstruction process assumed return from the mean surface level only $y = -Y$, and accounted for motional offsets in the vertical y-axis by extending the reconstruction focal length z until the image maximum straddled the mean surface level. Data was captured in the normal format, as 20 pairs of interlaced I and Q values every 47.5mS, and sufficient memory space was available for 60 such records, representing 2.85 seconds of continuous surface observation. A second series of just 20 I and Q data pairs corresponding to a return from a calm tank was used as a background reference and subtractively removed from every aperture data sequence before reconstruction. (sec. 5.3) Imaging was also attempted in the absence of tank contents but with wave generator operating, and spurious image components arising from this source were of negligible level. The image amplitude is taken as:

$$F(y') = \int_{-Y'/2}^{+Y'/2} f_c(y) . e^{-jk(y'^2+z^2)^{\frac{1}{2}}} . dy \quad \text{----- 6.55}$$

The measured data in complex form is denoted f_c, y' is the image coordinate system and z was increased from z_o until image maximum apparently coincided with the mean water level. A range of F(y') values were generated in this region.

The reconstruction, according to eq.6.55 from data simulating both stationary and moving objects is given in Fig.6.12. The impulse response in an observed object velocity range $\pm$0.1m/S about $V_z = -0.67$m/S is such that the peak response position indicates the range offset caused by object motion only. The projection of the image on to the range z-axis has negligibly affected the form of the impulse response and the maximum is only 0.5dB below the static object value. The value of z used in the reconstruction process of eq.6.55 thus represents solely the range modulation due to object velocity V_z, and the form of the impulse response, projecton to the z-axis, is not significantly affected by such velocity from the results of the simulation.

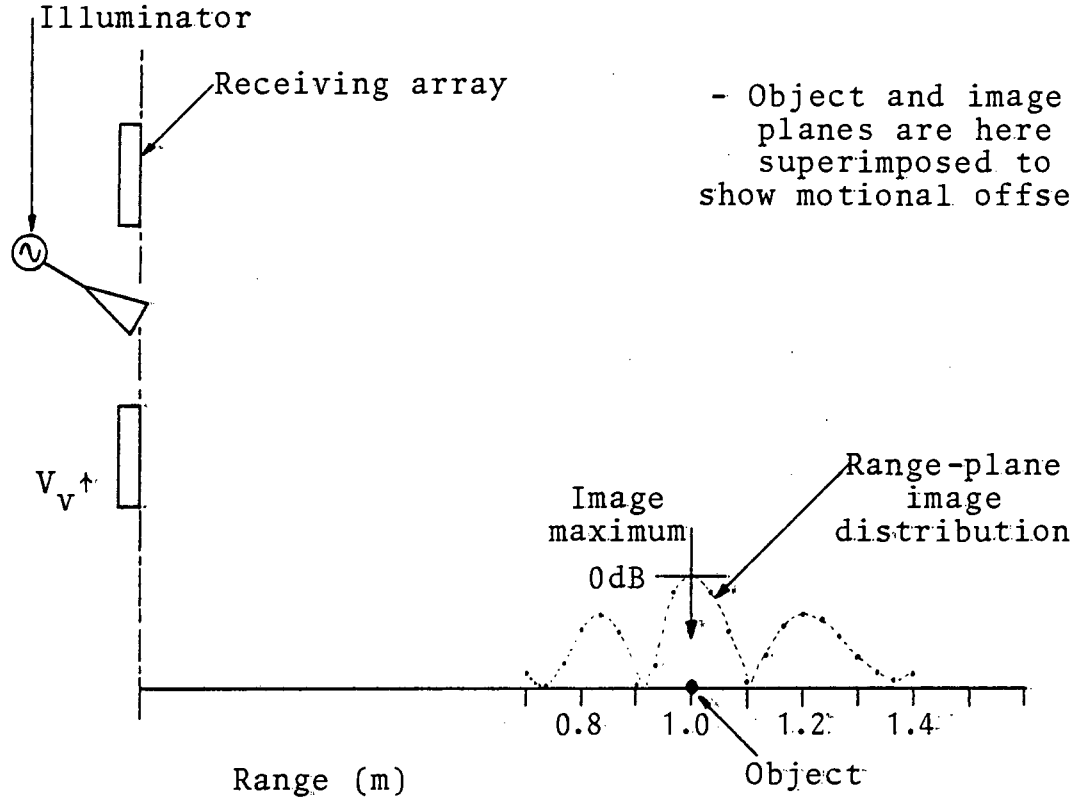

Fig. 6.12(a) Stationary object at z_o=1metre

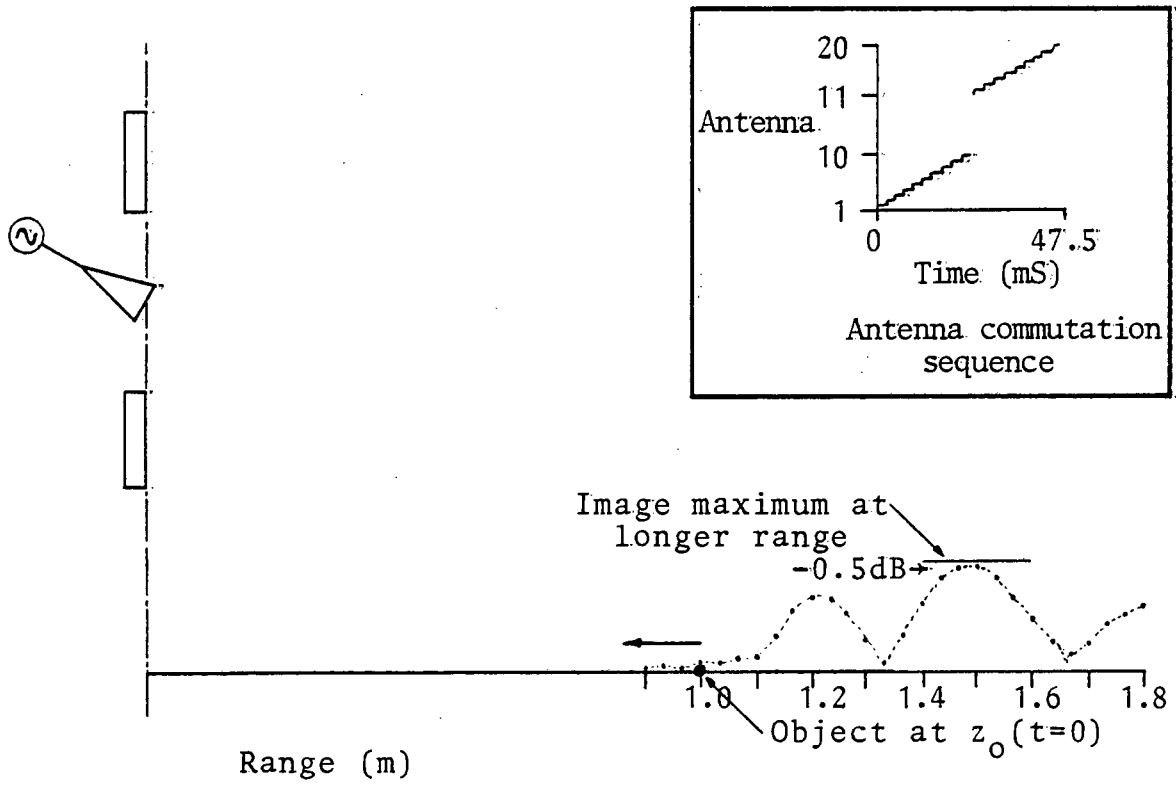

Fig. 6.12(b) Moving object at z_o=1metre for t=0

Comparison of a time-ordered image series with optical photographs of the same situation demonstrates the appearance of periodicity in the microwave image.(Fig.6.13) The image amplitude code is common to that used in Chp.5. The analysis is complicated by the repetitive and extended range sidelobes of the impulse response(Fig.6.12), but it is evident that crest and image maxima are aligned in the shortest wave period image.(Fig.6.13(a),(b),(c)) In Fig.6.13(a), a crest is visible at z_o = 1.3m, while a corresponding image maximum occurs 6 image records (0.285 seconds) after the start of data aquisition and photographic sampling. The measured crest velocity of 0.63m/S indicates that the crest is centred in the range "window" on the surface at z = 1.12m, but only data reconstructed using z = 1.4m in eq.6.55 shows correct y'-axis offset. This is confirmed by the simulation of Fig.6.12.

A single example of imagery reconstructed with z_o = 1m is given in Fig.6.13(f) and has evident periodicity, but the y'-axis maximum lies 3 units (182mm) too high, which is also in keeping with a negative radial velocity component. In Fig.6.13(e) the measured water wavelength is 750mm, and the range-shifted image peaks have overlapping leading and trailing sidelobes of successive maximum reflection regions which appears to double the perceived wave frequency. The maxima lead the crests by about 160mm in this example, which suggests that the position of maximum reflectance is also in the region of z = 1.1m and that maximum reflectance is related to the region of maximum wave slope; it is the region which subtends least angle between the slant range direction and wave surface.

The extended sidelobe structure does not encourage a more definite conclusion, but such a conjecture would be supported by a tilt modulation model of wave EM cross-section.[69, 76,82]. In the shorter wavelength cases, the region of maximum maximum tilt immediately preceeds the crest in the direction of wave advance, as the wave is close to breaking, while

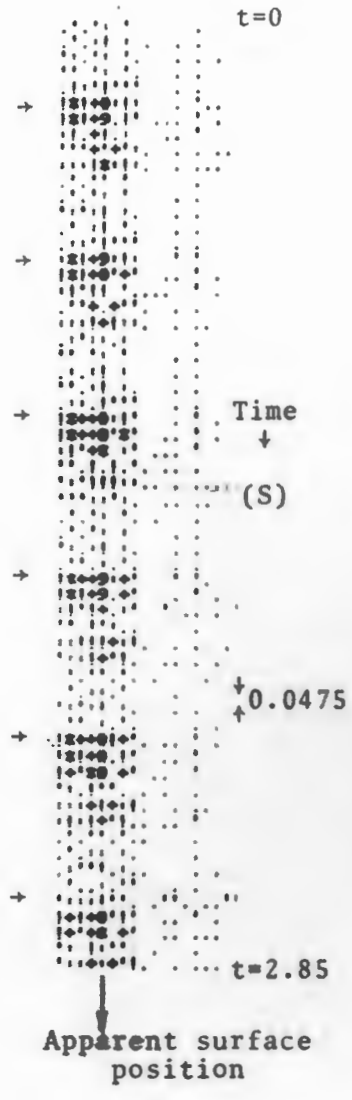

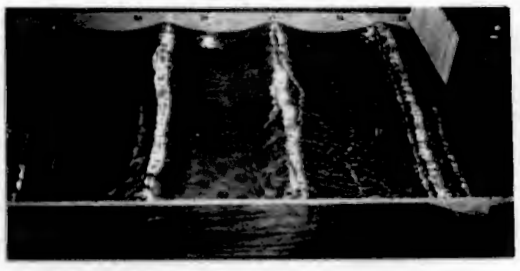

Fig. 6.13(a) Surface reflectivity history; reconstruction uses z=1.4 metres.(Left) Wave period was 467 mS. Photograph taken of tank at t=0 is given above.

- Arrows on images indicate independent wave period measurement - (Figs. 6.13(a)-(e))

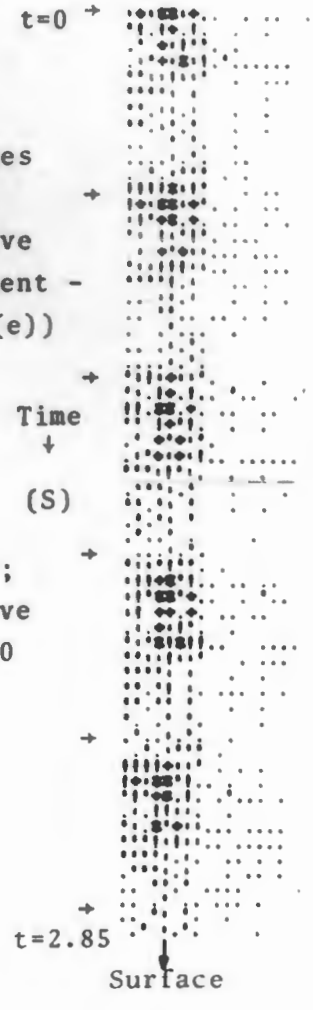

Fig. 6.13(b) Surface reflectivity history; reconstruction uses z=1.4metres.(Right) Wave period was 540mS. Photograph of tank at t=0 is given below.

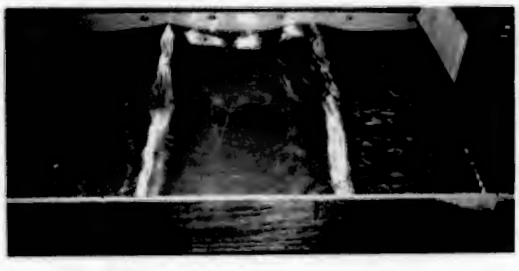

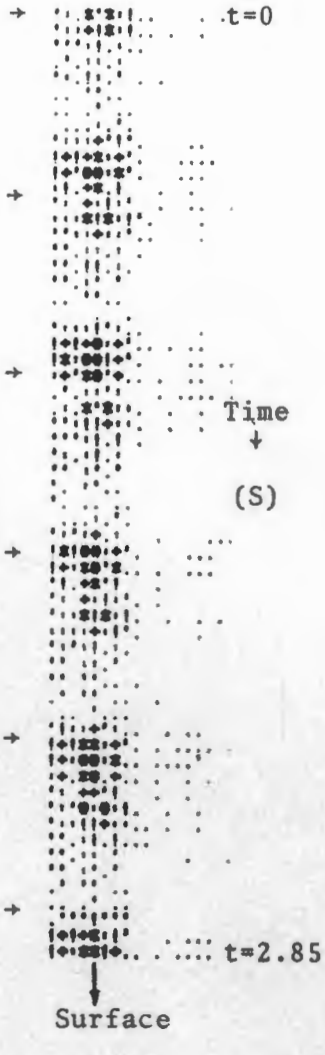

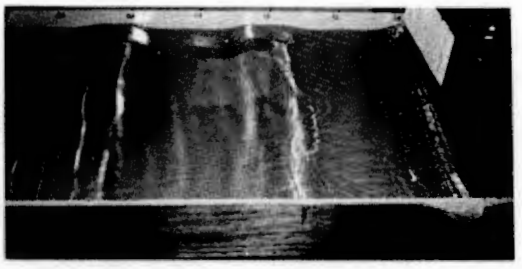

Fig. 6.13(c) Surface reflectivity history; reconstruction uses z=1.4 metres.(Left) Wave period was 546 mS. Photograph of tank at t=0 is given above.

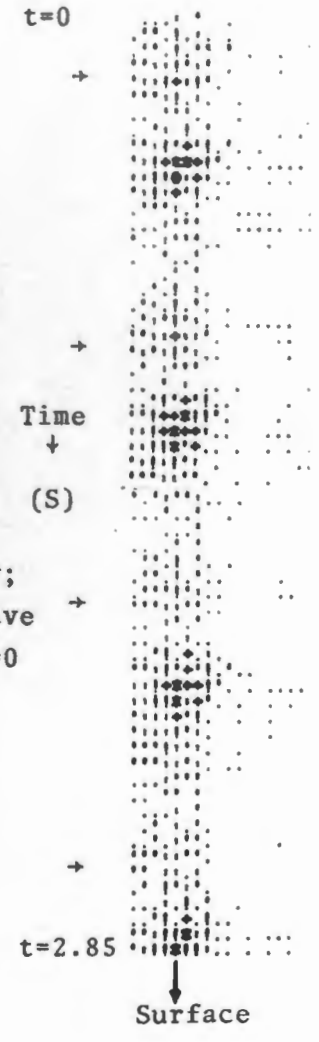

Fig. 6.13(d) Surface reflectivity history; reconstruction uses z=1.4metres.(Right) Wave period was 790mS. Photograph of tank at t=0 is given below.

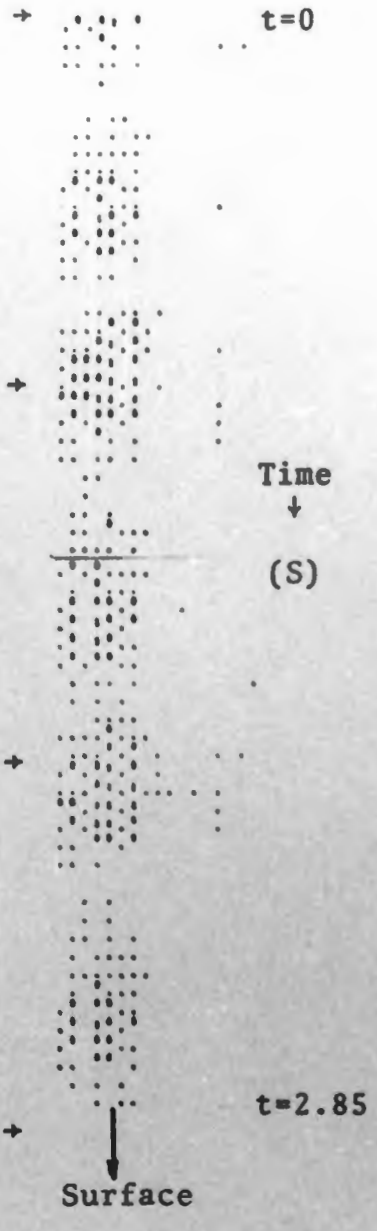

Fig. 6.13(e) Surface reflectivity history; reconstruction uses z=1.4 metres.(Left) Wave period was 980 mS. Photograph was taken of tank at t=0.(Above)

Fig. 6.13(f) A portion of the image reconstructed using z=1metre shows image maxima apparently lying 182mm above known surface position.(Right) Wave period was here 708mS.

CHAPTER 7

Conclusion

7.1 Confirming the Imaging Principle

The orthogonal axis array microwave holographic imaging principle has been demonstrated using the simplest biased real data format and optical reconstruction of reduced scale transmission holograms. No simple method was available in the initial stages to compensate for the superimposed cross-coupled data components, but the specular return from large planar and simply curved objects dominated the hologram data. The resulting images have confirmed the validity of the equivalent point illuminator and areal receive aperture model of the system in the paraxial Fresnel region, and have displayed both the anticipated spatial resolution and impulse response structure.

7.2 Simulation of an Offset Reference wave

The system incorporates an effective two channel receiver which allows the representation of essentially object wave data in complex amplitude and phase notation. Computer-assisted data capture has extended the system dynamic range by removing the unwanted cross-coupled, background and residual system offsets from the data using a two-pass experimental procedure.

Simulation of an offset reference wave field technique is a valuable feature since unwanted image plane components may be spatially separated from the desired distribution. This has been acheived by adjusting the object wave phase á posteriori, and recreating a biased real hologram as a reduced transparency in the normal manner. The optical reconstruction process implements a paraxial region reconstruction technique, and the orthogonal arrays were crossed close to

their centres to maximise the region accessible to this processor. The images have demonstrated improved fidelity and contrast using the offset reference mode and two-pass complex data assembly. The technique is felt to be more flexible when implemented by software means, since the antenna spacing need not be dictated by synthesis of the required reference wave, but more directly by system spatial resolution requirements and microwave hardware feasibility. In this respect, the extra microwave and lower frequency circuitry developed to measure I and Q received signal components has proved most worthwhile.

The two-pass subtractive technique removes all signal components common to both measured fields; such common components include not only unwanted cross-coupled and background signals but also system constant offsets such as those arising in the post-mixer preamplifier, commutation and synchronous detection stages. (Fig.2.3) As a result of this strategy, extreme care taken to reduce system offsets is not warranted, provided that the offsets do not change with time and that receiver linearity is assured. Despite its apparent complexity, the microwave system was simple to use and was also most reliable in operation. A period of about 20 minutes was allowed before every imaging session to allow the stabilisation of the klystron source and the travelling wave tube preamplifier. No attempt was made to trim system constant offsets, although these often exceeded single object field amplitude.

7.3 Numerical Reconstruction of Holograms

A numerically-based reconstruction process operating on complex hologram data provides maximum object region access with ideally no unwanted fields overlapping the required images.

A development of the planar imaging system leads to a geometry similar to that exploited by SAR, with the difference that range resolution is defined by the projection of the vertical

array beamforming process onto an object plane normal to the array aperture rather than by conventional pulsed technique. The two-pass subtractive hologram data assembly has been supplemented by multiple field averaging to improve image fidelity in situations where the return from low cross-section objects has been excessively corrupted by system noise. An advantage of the chosen geometry is the spatial separation from the desired image of unwanted components developed by certain mixer and following receiver errors. An approximate reconstruction algorithm has demonstrated tolerable image distortion while allowing a very significant reduction in time taken to compute the image field.

7.4 Imaging in the Presence of Object Motion

The similarity between the aperture synthesis process in SAR and the crossed array microwave holographic system considered in this thesis has been investigated with a view to using microwave holography as an instrumentation tool in the laboratory evaluation of the interaction between hydrodynamic and electromagnetic waves. SAR is a major remote sensing instrumentation technique applied to sea state measurement and a smaller, laboratory scale system duplicating the same imaging process as far as is possible is clearly required.

The sequential sensor commutation in orthogonal axes has been found undesirable, but a simple hardware configuration which allows simultaneous field measurements at all receiver array elements reduces the equivalent scanning procedure to only one axis. It is of some practical significance that the simplified hardware configuration also leads to a system closely copying the SAR imaging process without compromising its performance as a conventional imaging system in any way.

The following comments apply to a proposed microwave holographic imaging system to be used as a wave probe, and represents an extrapolation of prototypical hardware practice and a selection of techniques used in related instrumentation

and reported in the literature.

7.5 Hardware Adaptation for a Holographic Wave Probe

7.5.1 Wave Probe Specification

The orthogonal axis imaging system is seen to be capable of deployment as a mini-SAR instrumentation tool in the evaluation of the interaction of hydrodynamic and electromagnetic phenomena. In order that the action of SAR may be closely simulated, and to implement a flexible system, it is desirable that(a) the vertical array aperture be formed as fast as possible, preferably with the constituent elements sampled in parallel,

(b) the horizontal aperture be formed in a variable time, ranging from some minimum time in which object motion causes negligible impulse response distortion, and that the sequence of element switching be reversible,

(c) the received signal be processed and fully represented in complex format, giving maximum object region access with the appropriate reconstruction processor, and

(d) both arrays be of reliable and simple design.

7.5.2 Wave Probe Hardware

The most elegant implementation of (a) follows that used by Larson[31,32] and has an array of receiver mixers, instead of antennae only, whose reference inputs are derived from a sample of the transmitted signal. The reference field supplied to the mixers was in Larson's system offset in frequency(using a SSB generator) from that of the source and illuminator so that the post-mixer signal amplification was performed at a low intermediate frequency. The use of a mixer array, rather than a single mixer preceded by a microwave preamplifier compensating for the receive array multiplexing insertion loss, also has a beneficial effect on the dynamic range of the system.[103]

It is always convenient to process the received signal as a component offset in frequency from the reference field, since performance is severely compromised if transmitting and receiving antennae are merely turned on and signal detection made in the presence of the output residual offsets of the balanced mixer. For this reason, the current system "marked" both transmitting and receiving antennae with distinctive tones, although the simple shunt switches used in both arrays were fundamentally inefficient in converting incident source continuous wave power to power at a sideband frequency.

A more efficient design might use cross waveguide directional couplers with the short coupled waveguide radiators terminated by diode switches.(Fig.7.1) Even the simplest one diode switch backed by a short circuit plane one quarter waveguidelength distant has nearly 10dB improvement in conversion loss compared with the shunt transmission switches used in the prototype,(Appendix II), and operation of such an array with significant unmodulated signal leakage from other antennae need not compromise performance. This switch reflects essentially DSBSC modulated fields, and adding just one more diode can further improve insertion loss by implementing a SSB generator.[122] This device reflects an incident unmodulated field in 3 possible phase states, if the 3 possible short circuit planes are activated in a regular sequence. The sign of frequency offset is controlled by commutation sequence, and the magnitude of the offset is the commutation frequency divided by the number of possible phase states.[122-124]

The SSB device is probably best used to offset the reference frequency, however, since only one device is required and it will be easier to optimise conjugate sideband rejection in a single switch than attempt to do so for the number required in a practical transmitting array. A particularly compact implementation of the SSB generator uses a 4 port circulator. (Fig.7.2) A port is terminated by a two terminal reflection amplifier for the purposes of both boosting reference power

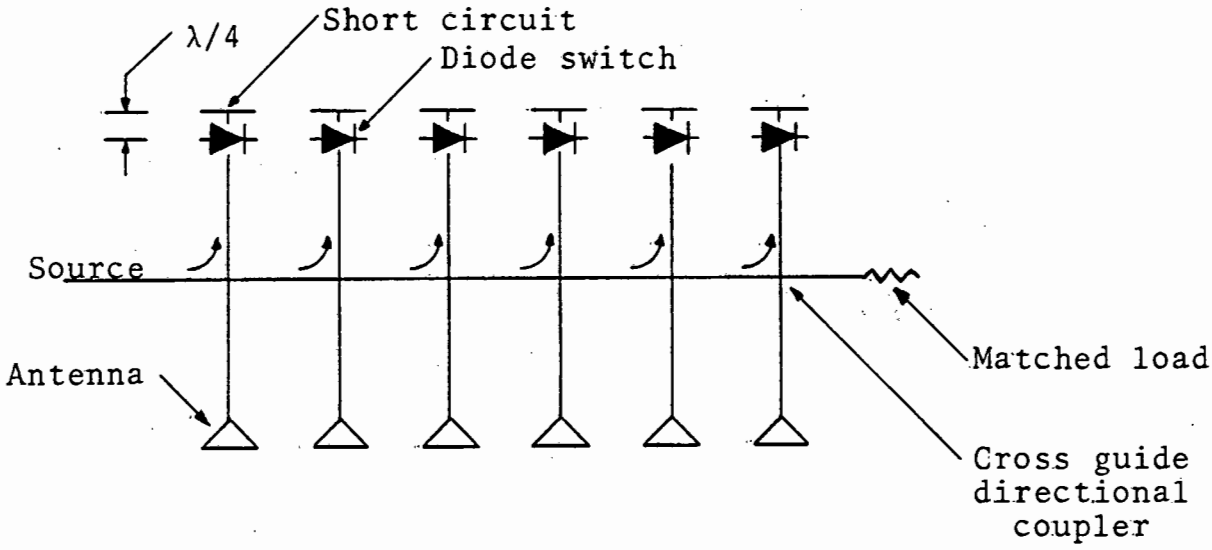

Fig. 7.1 A DSB mode cross coupled waveguide transmit array

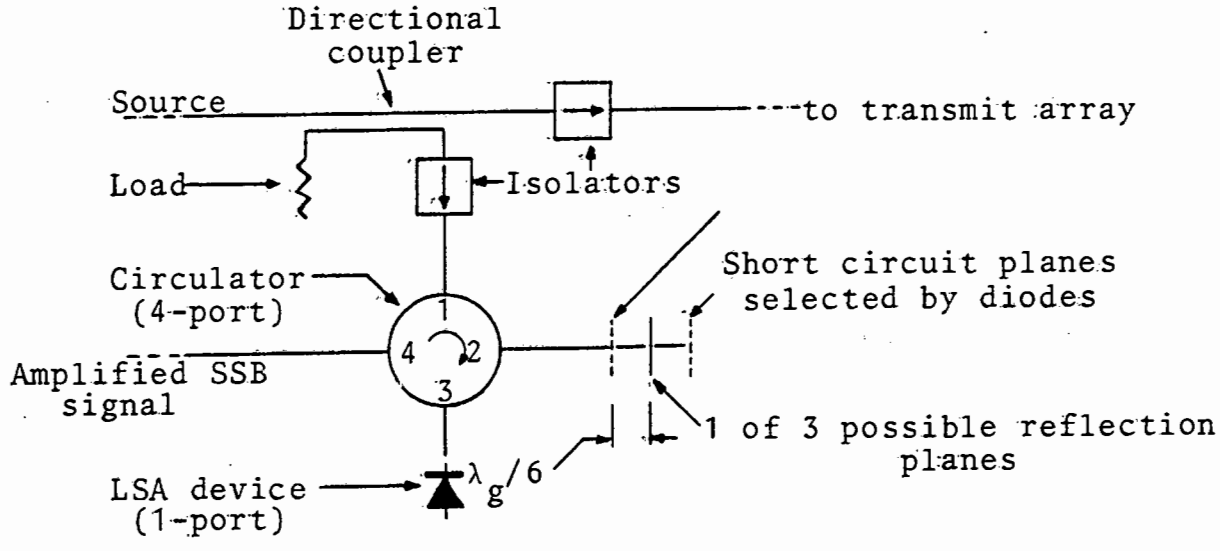

Fig. 7.2 A proposed SSB reference signal generator

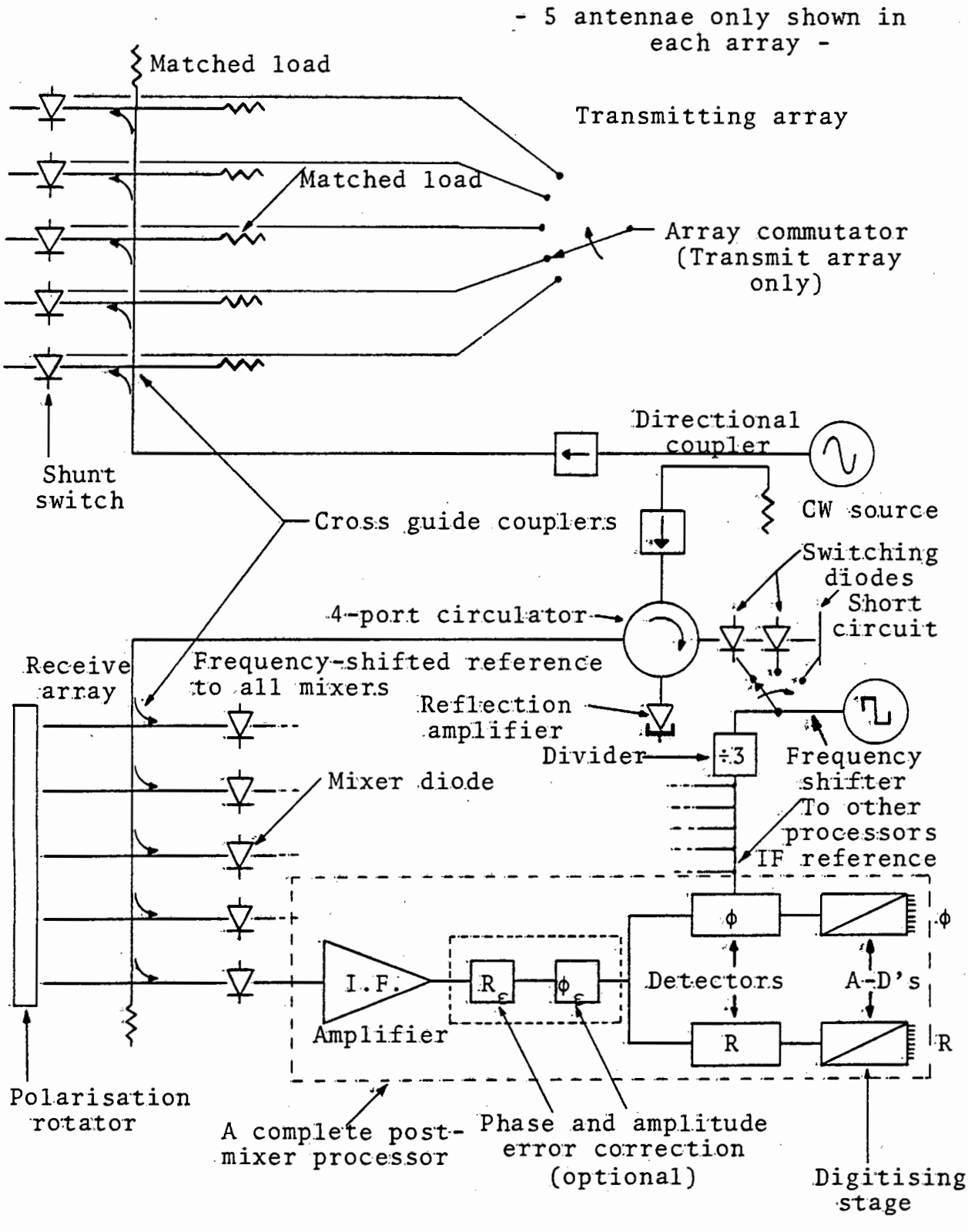

Fig. 7.3 Projected hardware for wave probe

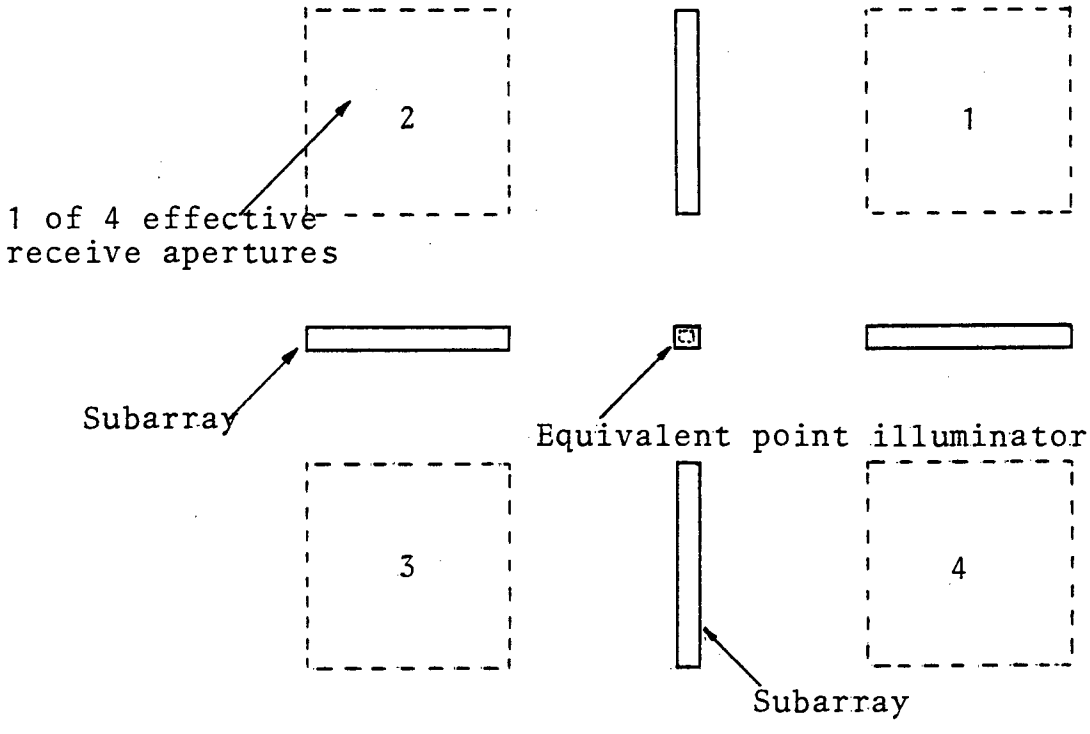

Fig. 7.4 On "multiple-look" imaging : incoherent combination of subarray functions

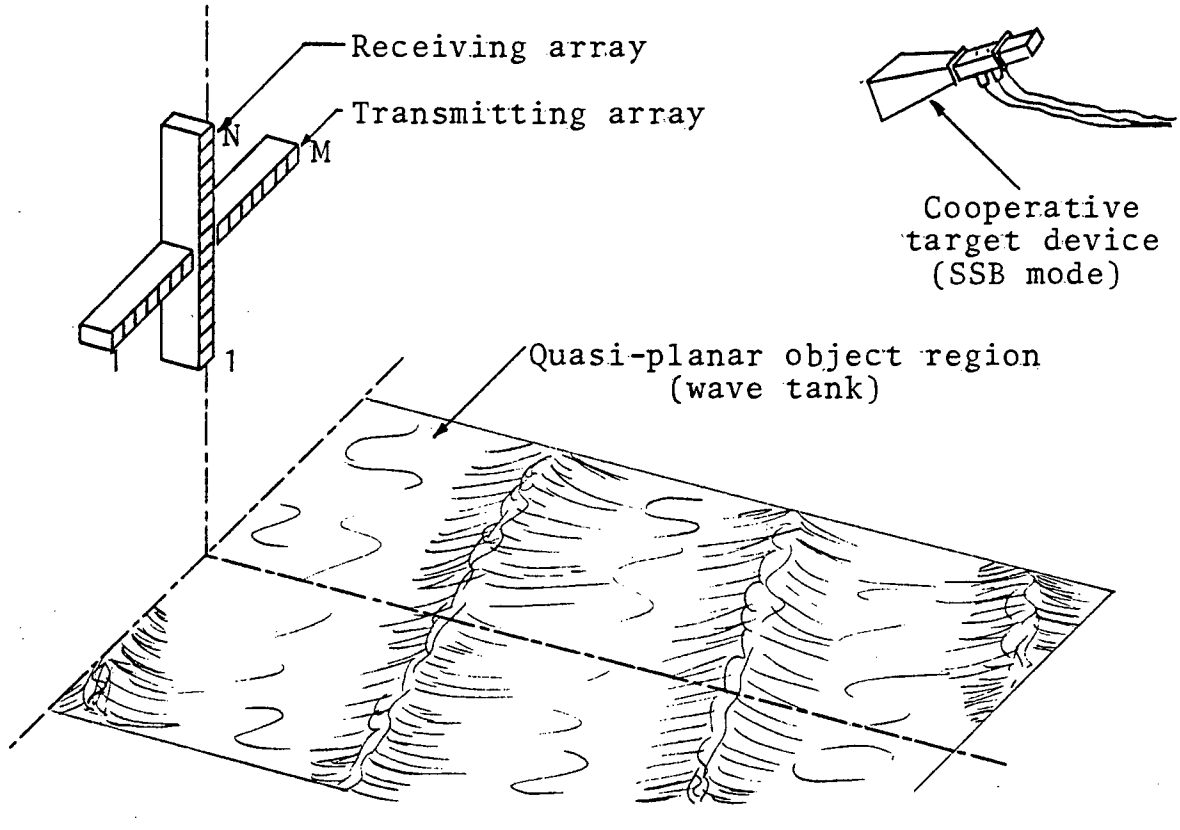

Fig. 7.5 Operational holographic wave probe geometry

7.5.3 Operational Calibration Procedure

A practical microwave holographic imaging system should incorporate some means of periodically compensating both unwanted signal components and systematic errors. This procedure is quite simply included in the crossed-array system. The two major imperfections of the system are the unwanted cross-coupled, background and electronic system offset components and the tolerances of the transmitting and receiving arrays which arise in the fabrication stage.

Both types of imperfections can be measured using a "co-operative target" device situated within the system field of view. (Fig.7.5) In order to distinguish the return from the cooperative target in the presence of obtrusive signals, the intermediate frequency reference signal used in the synchronous detection part of the suggested circuit (Fig.7.3) would be temporarily reduced in frequency, so that the obtrusive signals do not match the receiver processor. It is then a simple matter to switch the "cooperative target" device in a sequence direction and at a rate which affects the frequency of the scattered field and re-establishes the match to the receiver. If there are M transmitting and N receiving elements, M+N complex numbers describe the array systematic errors.

Establishing the contribution of the obtrusive signal components requires that the "cooperative target" be removed or rendered invisible to the system. If removal is either time-consuming or not acceptable, then the return from the device is largely and conveniently removed by operating the imaging system in the normal mode, with matching mixer offset and intermediate reference frequencies, and cycling the "cooperative target" through an integral number of complete phase state sequences during every transmitting antenna active epoch.

Both obtrusive signal fields and systematic errors could be held in reconstruction device memory, and applied to complex

measured data before image recovery was attempted. Two successive complete hologram field measurements could establish both sets of data, so that experimental use should be minimally interrupted. The error correction procedure can be automated easily and is no more complicated than the demonstrated data capture process.

REFERENCES

1. D.Gabor, "Holography 1948-1971", Proc.IEEE, vol.60,pp.655-668, June 1972.
2. R.Karg, "Experiments with a multifrequency microwave imaging system", NTZ, vol.30, pp.651-654, no.8, 1977.
3. R.Karg, "Multifrequency microwave holography", AEU, vol.31, pp.150-156, no.4, 1977.
4. N.H.Farhat, "A new imaging principle", Proc.IEEE, vol.64, pp.379-380, March 1976.
5. N.H.Farhat, T.Dzejov and E.Ledet, "Computer simulation of frequency swept imaging", Proc.IEEE, vol.64, pp.1453-1454, September 1976.
6. L.G.Gregoris and K.Iizuka, "Visualization of internal structure by microwave holography", Proc.IEEE, vol.58, pp.79-80, May 1970.
7. C.F.Augustine, C.Deutsch, D.Fritzler and E.Marom, "Microwave holography using liquid crystal area detectors", Proc.IEEE, vol.57, pp.1333-1334, July 1969.
8. W.M.Waters, "On the design of a large aperture radar for target imaging", IEEE Transactions on Aerospace and Electronic Systems, vol.AES-4, pp.886-892, November 1968.
9. R.F.Mueller, "Acoustic holography", Proc.IEEE, vol.59, p.1323, September 1971.
10. A.Macovski, "Ultrasonic imaging using arrays", Proc.IEEE, vol.67, pp.484-485, April 1979.
11. B.D.Steinberg, "Design approach for a high-resolution microwave imaging radio camera", Journal of the Franklin Institute, vol.296, pp.415-432, December 1973.
12. B.D.Steinberg et al., "First experimental results from the Valley Forge radio camera program", Proc.IEEE, vol.67, pp.1370-1371, September 1979.
13. Y.Aoki and A.Bovin, "Computer reconstruction of images from a microwave hologram", Proc.IEEE, vol.58, pp.821-822, May 1970.
14. N.H.Farhat and W.R.Guard, "Millimeter wave imaging of concealed weapons", Proc.IEEE, vol.59, pp.1383-1384, September 1971.
15. N.H.Farhat, W.R.Guard and A.H.Farhat, "Spiral scanning in long-wave holography", in "Acoustical Holography", Proceedings of the 4th International Symposium on Acoustical Holography, vol.4, pp.267-297, Plenum Press, 1972.

16. N.H.Farhat, "Quasi-real time microwave holography", Journal of the Franklin Institute, vol.296, pp.393-402, December 1973.
17. N.H.Farhat and W.R.Guard, "Holographic imaging at 70 Ghz", Proc.IEEE, vol.58, pp.1955-1956, December 1970.
18. G.Papi, V.Russo and S.Sottini, "Microwave holographic interferometry", IEEE Transactions on Antennas and Propagation, vol.AP-19, pp.740-746, November 1971.
19. N.H.Farhat and A.H.Farhat, "Double circular scanning in microwave holography", Proc.IEEE, vol.61, pp.509-510, April 1973.
20. G.Papi, V.Russo and S.Sottini, "Imaging by microwave holography through aberrating media", IEEE Transactions on Antennas and Propagation, vol.AP-24, pp.832-836, November 1976.
21. G.Tricoles and N.H.Farhat, "Microwave holography : application and techniques", Proc.IEEE, vol.65, pp.108-121, January 1977.
22. D.N.Swingler, "Simple double-resolution microwave holography", Proc.IEEE, vol.61, pp.1140-1141, August 1973.
23. C.S.Nilsen, "Double resolution microwave holography", M.Sc. Thesis, Department of Electrical Engineering, University of Cape Town, 1976.
24. D.N.Swingler and C.S.Nilsen, "Double resolution microwave holography : the resolving power of a laboratory system versus the Raleigh limit for a conventional hologram", Proc.IEEE, vol.63, p.1074, July 1975.
25. H.Shigesawa, K.Takiyama and O.Hirao, "Microwave holography by synthetic aperture", Proc.IEEE, pp.137-139, January 1972.
26. H.Shigesawa, K.Takiyama and M.Nishimura, "High-quality image reconstruction from double microwave holograms", IEEE Transactions on Microwave Theory and Techniques, vol.MTT-24, pp.529-531, August 1976.
27. D.N.Swingler, "Some new aspects of microwave holography", Ph.D. Thesis, Department of Electronic and Electrical Engineering, University of Sheffield, 1971.
28. R.D.Orme and A.P.Anderson, "High-resolution microwave holographic technique", Proc.IEE, vol.120, pp.401-406, April 1973.
29. Z.S.Boitsova, M.S.Krivolutskaya and V.M.Meshchankin, "Recording radio-holograms by the perturbed field method", Instruments and Experimental Technique(USA), vol.18, pp842-843, part2, 1976.

30. N.S.Kopeika, D.Even-zur and I.Fishbein, "Low-cost glow discharge tube microwave frequency sensor", Proc.IEEE, vol.64, pp.382-384, March 1976.
31. R.W.Larson , J.S.Zelenka and E.L.Johansen, "Microwave holography", Proc.IEEE, vol.59, pp.2162-2164, December 1969.
32. R.W.Larson, J.S.Zelenka and E.L.Johansen, "A microwave hologram radar system", IEEE Transactions on Aerospace and Electronic Systems, vol.AES-8, pp.208-216, March 1972.
33. R.E.Collin and F.J.Zucker, "Antenna theory", part2, chp.27, McGraw-Hill, 1969.
34. W.H.Wells, "Acoustical imaging with linear transducer arrays", in "Acoustical Holography", Proceedings of the 2nd. International Symposium on Acoustical Holography, vol.2, pp.87-103, Plenum Press, 1970.
35. R.A.Hayward, E.L.Rope, G.Tricoles and O.N.Yue,"Enhancement by non-coherent superposition of images formed with crossed, coherent arrays", in "Acoustical Holography", Proceedings of the 6th. International Symposium on Acoustical Holography, vol.6, pp.469-483, Plenum Press, 1975.
36. R.Pitman, "Microwave holography", B.Sc. Thesis, Department of Electrical Engineering, University of Cape Town, 1975.
37. C.S.Nilsen and D.N.Swingler, "Quasi-real-time microwave holography", Proc.IEEE, vol.65, pp.491-492, March 1977.
38. P.Pare, "Microwave holography", B.Sc.Thesis, Department of Electrical Engineering, University of Cape Town, 1979.
39. J.Nakayama, T.Miyashita, N.Akagi, H.Ogura, Y.Yoshida and T.Soma, "Imaging a two-dimensional target by means of hologram matrix - an ultrasound experiment", Proc.IEEE, vol.66, pp.1287-1289, October 1978.
40. J.Nakayama, U.Ogura and M.Fujiwara, "Multifrequency hologram matrix and its application to two-dimensional imaging", Proc.IEEE, vol.66, pp.1289-1290, October 1978.
41. H.Ogura and S.Fukoka, "Imaging of a two-dimensional target by means of hologram matrix", Proc.IEEE, vol.64, pp.364-366, March 1976.
42. H.Ogura and K.Iizuka, "Hologram matrix and its application to a novel radar", Proc.IEEE, vol.61, pp.1040-1041, July 1973.

43. K.Iizuka, H.Ogura, J.L.Yen, V.K.Nguyen and J.Weedmark, "Performance of a hologram matrix radar", Proc.IEEE, vol.62, pp.1718-1719, December 1974.
44. K.Iizuka, H.Ogura, J.L.Yen, V.K.Nguyen and J.Weedmark,"A hologram matrix radar", Proc.IEEE, vol.64, pp.1493-1504, October 1976.
45. K.Iizuka, "Subtractive HISS radar", Proc.IEEE, vol.65, pp.1081-1083, July 1977.
46. E.M.Leith, "Quasi-holographic techniques in the microwave region", Proc.IEEE, vol.59, pp.1305-1318, September 1971.
47. M.A.Kujoory and N.H.Farhat, "Microwave holographic subtraction for imaging of buried objects", Proc.IEEE, vol.66, pp.94-96, January 1978.
48. M.A.Kujoory and N.H.Farhat, "Electronic wavefront subtraction in longwave holography", Proc.IEEE, pp.1258-1260, August 1975.
49. W.M.Brown and L.J.Porcello, "An introduction to SAR", IEEE Spectrum, pp.52-62, September 1969.
50. O.V.Bazarskiy and Y.L.Khlyavich, "Holographic interferometry at microwave frequencies", Radio Eng. and Elec. Physics, vol.19, pp.111-113, March 1974.
51. G.Papi, V.Russo and S.Sottini, "Two-frequency microwave holographic interferometry", Proc.IEEE, pp.1004-1005, August 1972.
52. K.Haines and B.P.Hildebrand, "Contour generation by wavefront reconstruction", Physics Letters, vol.19, 15th September 1965.
53. A.P.Anderson, J.C.Bennet and P.A.McInnes, "Fourier-subtractive holographic imaging of microwave antenna apertures", Elec. Lett., vol.8, pp.277-278, 1st June 1972.
54. P.J.Napier and R.H.T.Bates, "Antenna-aperture distributions from holographic type of radiation pattern measurements", Proc.IEE, vol.120, pp.30-34, January 1973.
55. D.J.Thomsit, "Colour display of microwave fields", Electronics and Power, pp.408-412, June 1979.
56. J.C.Bennet, A.P.Anderson, P.A.McInnes and W.J.T.Whitaker, "Microwave holographic metrology of large reflector antennas", IEEE Transactions on Antennas and Propagation, vol.AP-24, pp.295-303, May 1976.

57. V.I.Turchin, N.M.Tseytlin and A.K.Chandaev, "Measurements of antenna patterns based on radiation from a source in the Fresnel zone, with the help of SHF holography and computer processing", Radio Eng. and Elec. Physics, vol.17, pp.527-536, May 1972.
58. G.Schmidt and A.Turianen, "The localisation of ionospheric irregularities by the holographic method", Journal of Geophysical Research, vol.80, pp.4313-4324, November 1975.
59. D.N.Swingler, "Holographic measurement of K-factor on line-of-sight microwave routes containing knife-edge obstacles", IEEE Transactions on Antennas and Propagation, vol.AP-25, pp.445-446, May 1977.
60. D.N.Swingler, "Microwave holography and the location of knife-edge obstacles on line-of-sight microwave routes", Transactions SAIEE, pp.257-270, November 1975.
61. J.A.Constant, "Microwave automatic vehicle identification (MAVI) system", IEEE Transactions on Vehicular Technology, vol.VT-23, pp.44-54, May 1974.
62. W.E.Kock, "Comments on "Hologram matrix and its application to a novel radar"", Proc.IEEE, vol.62, June 1974.
63. H.E.Lee, "Extension of synthetic aperture radar(SAR) technique to undersea applications", IEEE Journal on Oceanic Engineering, vol.OE-4, pp.60-63, April 1979.
64. R.O.Harger,"Synthetic aperture radar systems", Academic Press (New York and London), 1970.
65. A.W.Rihaczek, "Principles of high-resolution radar", McGraw-Hill, 1969.
66. J.H.Mims, "Synthetic aperture imaging with maneouvers", IEEE Transactions on Aerospace and Electronic Systems, vol.AES-8, pp.410-418, July 1972.
67. C.Elachi and D.D.Evans, "Effects of random phase changes on the formation of synthetic aperture radar imagery", IEEE Transactions on Antennas and Propagation, vol.AP-25, pp.149-153, January 1977.
68. T.R.Larson, L.I.Moskowitz and J.W.Wright, "A note on SAR imagery of the ocean", IEEE Transactions on Antennas and Propagation, vol.AP-24, pp.393-394, May 1976.

69. C.Elachi and W.E.Brown, "Models of radar imaging of the ocean surface waves", IEEE Transactions on Antennas and Propagation, vol.AP-25, pp.84-95, January 1977.
70. J.W.Wright, "Detection of ocean waves by microwave radar; the modulation of short gravity-capillary waves", Boundary Layer Meteorology, vol.13, pp.87-105, January 1978.(Special issue on radio oceanography)
71. C.Elachi, "Radar imaging of the ocean surface", Boundary Layer Meteorology, vol.13, pp.165-179, January 1978.
72. W.R.Alpers and C.L.Rufenbach, "The effect of orbital motions on synthetic aperture radar imagery of ocean waves", IEEE Transactions on Antennas and Propagation, vol.AP-27, pp.685-690, September 1979.
73. D.D.Evans, "A point target model for the SAR detection of ships and ice conditions during a swell", IEEE Transactions on Antennas and Propagation, vol.AP-27, pp.30-34, January 1979.
74. K.Tomiyasu, "Tutorial review of SAR with applications to imaging of the ocean surface", Proc.IEEE, vol.66, pp.563-583, May 1978.
75. E.D.R.Shearman, P.Bickerstaff and L.Fotiades, "Synthetic aperture skywave radar:techniques and first results", in "Radar, past, present and future", IEE publication, pp.414-421, October 1973.
76. R.K.Moore, "Active microwave sensing of the Earth's surface-a mini review", IEEE Transactions on Antennas and Propagation, vol.AP-26, pp.843-849. November 1978.
77. R.A.Schuchman and J.S.Zelenka, "Processing of ocean wave data from a synthetic aperture radar", Boundary Layer Meteorology, vol.13, pp.181-191, January 1978.
78. G.P.de Loor and H.W.Brunsveld van Hulten, "Microwave measurements over the North Sea", Boundary Layer Meteorology, vol.13, pp.119-131, January 1978.
79. O.H.Shemdin et al., "Comparison of "in situ" and remotely sensed ocean waves off Marineland,Florida", Boundary Layer Meteorology, vol.13, pp.193-202, January 1978.
80. F.I.Gonsalez et al., "Seasat synthetic aperture radar: ocean wave detection capabilities",Science, vol.204, pp.1418-1421, June 1979.

81. K.Hasselmann et al., "Radar measurements of wind and waves", Boundary Layer Meteorology, vol.13, pp.405-412, January 1978.
82. C.Elachi, "Wave patterns across the North Atlantic on September 28th, 1974 from airborne radar imagery", Journal of Geophysical Research, vol.81, pp.2655-2656, May 1976.
83. W.E.Brown, C.Elachi and T.W.Thomson, "Radar imaging of ocean surface patterns", Journal of Geophysical Research, vol.81, pp.2657-2667, May 1976.
84. K.Krishen, "Correlation of radar backscattering cross sections with ocean wave height and wind velocity", Journal of Geophysical Research,vol.76, pp.6528-6539, 1971.
85. W.J.Plant and J.W.Wright, "Growth and equilibrium of short gravity waves in a wind-wave tank", Journal of Fluid Mechanics, vol.82, pp.767-793, part4, 1977.
86. J.H.Ja, "Measurement of angles of arrival of waves by microwave holographic techniques", IEEE Transactions on Antennas and Propagation, vol.AP-23, pp.720-722, September 1975.
87. J.L.Sutton, "Underwater acoustic imaging", Proc.IEEE, vol.67, pp.554-566, April 1979.
88. M.Wu and N.H.Farhat, "Real-time optical reconstruction of microwave holograms", Proc.IEEE, vol.63, pp.1254-1255, August 1975.
89. R.E.Collin and F.J.Zucker, "Antenna theory", part 1, chp.14.8, McGraw-Hill, 1969.
90. C.Nilsen, "Analogue signal processing in a microwave imaging system", Research Review(UCT), vol.1, no.3, pp.7-9, June 1977.
91. R.J.King, "Microwave homodyne systems", IEE Electromagnetic series 3, Peregrinus Press, 1978.
92. A.R.Koelle and S.W.Depp, "Doppler radar with cooperative target measures to zero velocity and senses direction of motion", Proc.IEEE, vol.65, pp.492-493, March 1977.
93. A.R.Koelle, S.W.Depp and R.W.Freymann, "Short-range radio telemetry for electronic identification using modulated r.f. backscatter",Proc.IEEE, vol.63, pp.1260-1261, August 1975.

94. G.L.Fitzpatrick, "Seismic imaging by holography", Proc. IEEE, vol.67, pp.536-553, April 1979.
95. Y.Aoki, "Computer simulation of synthesising images by digital phased arrays", Proc.IEEE, vol.58, pp.1856-1858, November 1970.
96. L.J.Cutrona, W.E.Vivian, E.N.Leith and G.O.Hall, "A high-resolution combat surveillance system", IRE Transactions on Military Electronics, vol.MIL-5, pp.127-131, April 1961.
97. B.J.Levin, "Millimeter wave image conversion using a semiconductor image convertor", Proc.IEEE, vol.60, pp.496-498, March 1970.
98. A.P.Anderson, R.D.Orme and S.J.Mawani, "Direct microwave imaging with enhanced resolution", Elec.Lett., vol.9, pp.205-206, 17th May 1973.
99. I.I.Shchukin and Y.S.Obtemperanskiy, "The use of Fresnel lenses in radiointroscopy", Radio Eng. and Elec. Physics, vol.19, p.120, 1974.
100. A.P.Anderson, D.G.Jones, J.C.Bennet and S.J.Mawani, "Microwave remote sensing using a Fourier transform / spherical scanning technique", Radio and Electronic Engineer, vol.46, pp.555-559, November 1976.
101. A.S.Klyuchnikov, V.P.Sidorovich, A.F.Sidorkin and I.I. Shchukin, "Comparative evaluation of the radio images formed by a Fresnel lens and visualized by a scanning method and with the use of liquid crystal films", Radio Eng. and Elec. Physics, vol.19, p.164, July 1974.
102. Y.Aoki and S.Ishizuka, "Numerical image reconstruction from an off-axis sound-wave hologram", Proc.IEEE, vol.63, pp.735-736, April 1975.
103. M.I.Skolnik, "Radar handbook", McGraw-Hill, 1970.
104. R.L.Mitchell, "Models of extended targets and their coherent radar images", Proc.IEEE, vol.62, pp.754-762, June 1974.
105. A.B.E.Ellis, "Processing of SAR from a satellite",GEC Journal of Science and Technology, vol.45, pp.121-128, 1979.
106. M.G.Maginness, "Comment on nonoptical holography", Proc. IEEE, vol.55, pp.2050-2051, November 1967.

107. L.B.Lessin, P.M.Hirsch and J.A.Jordan, "The kinoform : a new wavefront reconstruction device", IBM Journal of Research and Development, vol.13, pp.150-155, March 1969.
108. D.G.Childers(Editor), "Modern Spectrum Analysis", IEEE Press, 1978.
109. R.N.Strickland, J.C.Bennet and A.P.Anderson, "Retrieval of diffraction-limited images from below threshold of recognition by superdirective data processing", IEEMOA, vol.2, pp.85-90, May 1978.
110. R.N.Strickland, A.P.Anderson and J.C.Bennet, "Resolution of sub-wavelength spaced scatterers by superdirective data processing simulating evanescent wave illumination",IEEMOA, vol.3, pp.37-42, March 1979.
111. A.P.Anderson and J.C.Bennet, "Feasibility of enhanced microwave resolution using a superdirective aperture", Proc.IEEE, vol.64, pp.376-378, March 1976.
112. B.D.Steinberg, "Hard-limiting in synthetic aperture signal processing", IEEE Transactions on Aerospace and Electronic Systems, vol.AES-11, pp.556-561, July 1975.
113. H.N.Kritikos and J.Shuie, "Microwave sensing from orbit", IEEE Specrum, pp.34-41, August 1979.
114. R.K.Raney, "Synthetic aperture imaging radar and moving targets", IEEE Transactions on Aerospace and Electronic Systems, vol.AES-7, pp.499-503, May 1971.
115. D.E.Barrick, "First-order theory and analysis of MF/HF/VHF scatter from the sea", IEEE Transactions on Antennas and Propagation, vol.AP-20, pp.2-10, January 1972.
116. C.Nilsen, "Microwave imaging in the presence of target motion", Research Review(UCT), vol.2, no.1, pp.18-20, February 1978.
117. I.G.Main, "Vibrations and waves in physics", chp.13, Cambridge University Press, 1978.
118. P.Beckmann and A.Spizzichino, "The scattering of EM waves from rough surfaces", chp.4, pp.34-69, Pergamon Press, 1963.
119. J.M.Headrick amd M.I.Skolnik, "Over the horizon radar in the HF band", Proc.IEEE, vol.62, pp.664-672, June 1974.

120. G.L.Tyler et al., "Second order scattering from the sea : ten-meter radar observations of the doppler continuum", Science, vol.177, pp.349-351, 28th July 1972.
121. D.E.Barrick, "HF radar oceanography-a review", Boundary Layer Meteorology, vol.13, pp.23-41, January 1978.
122. C.Nilsen, "A simple frequency translating target tracking device offering polarisation adaptability", Research Review (UCT), vol.1, no.7, pp.27-30, October 1977.
123. C.H.Grauling and B.D.Geller, "Broad-band frequency translator with -30dB suppression of spurious sidebands", IEEE Transactions on Microwave Theory and Techniques, vol.MTT-18, pp.651-652, September 1970.
124. R.D.Davies and J.D.Meindl, "Delay generated offset: a direction sensitive pulse-coherent doppler detection technique", IEEE Transactions on Aerospace and Electronic Systens, vol.AES-13, pp.430-433, July 1977.
125. B.Shieck, J.Köhler and W.Schilz, "A modulated subcarrier technique with instantaneous amplitude and phase information", IEEE Transactions on Instrumentation and Measurement, vol.IM-25, pp.128-131, June 1976.
126. H.A.Burger, "A dual polarised antenna system using a meanderline polariser". in IEEE AP-S International Symposium Digest, pp.55-58, May 1978.
127. J.Powers, J.Landry and G.Wade, "Computed reconstructions from phase-only and amplitude-only holograms", in "Acoustical Holography", Proceedings of the 2nd International Symposium on Acoustical Holography, vol. 2, pp.185-210, 1970.
128. D.H.Fargan and J.P.Newsome, "Application of dispersive networks in data-transmission receivers", Proc.IEE,vol.121, pp.237-243, April 1974.
129. J.A.Wiess, "A phenomenological theory for the Regia-Spencer phase shifter", Proc.IRE, pp.1130-1137, June 1959.
130. H.R.Phelan, "Spira-phase - a new , low-cost lightweight phased array", Microwave Journal, (in four parts, December 1976, January 1977, March 1977 and July 1977 issues.)
131. W.Swindell and H.H.Barrett, "Computerised tomography : taking sectional X-rays", Physics Today, pp.32-41, December 1977.

132. A.M.Cormack, "Representation of a function by its line integrals, with some radiological applications", Journal of Applied Physics, vol.34, pp.2722-2727, September 1963.
133. M.Ryle, "The new Cambridge radio telescope", Nature, vol.194, pp.517-518, 12th May 1962.
134. R.N.Bracewell and A.C.Riddle, "Inversion of fan-beam scans in radio-astronomy", The Astrophysical Journal, vol.150, pp.427-434, November 1967.
135. H.H.Barrett and W.Swindell, "Analog reconstruction methods for transaxial tomography", Proc.IEEE, vol.65, pp.89-107, January 1977.
136. A.Lindegsrd-Andersen and G.Thuesen, "Simplified highly efficient apparatus for photographic transaxial X-ray tomography", Journal of Scientific Instruments, vol.12, pp.924-926, 1979.
137. H.J.Scudder, "Introduction to computer-aided tomography", Proc.IEEE, vol.66, pp.628-637, June 1978.
138. H.K.Wickramsinghe and M.Hall, "Phase imaging with the scanning acoustic microscope", Elec. Lett., vol.12, pp.637-638, 25th November 1976.
139. K.A.Dines and R.J.Lytle, "Computerised geophysical tomography", Proc.IEEE, vol.66, pp.628-637, June 1978.

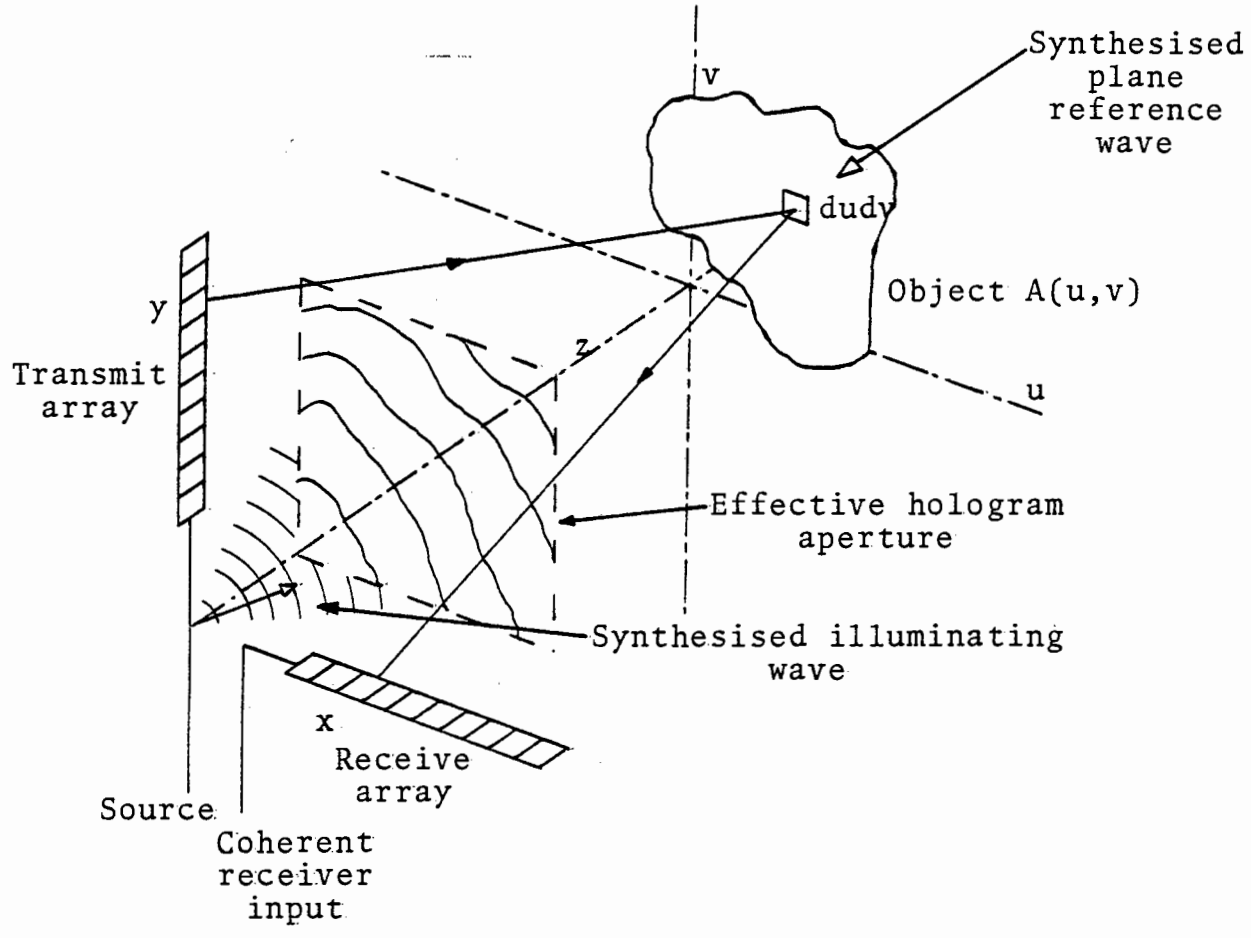

Fig. AI.1 Hologram recording system and object geometry

$$h(A,B) \propto |A+B|^2 = |A|^2 + |B|^2 + A^*B + AB^* \quad \text{---- AI.4}$$

A slightly more complex two diode mixer in a balanced configuration can be regarded as a multiplier, and the mixer output in this case becomes:

$$h(A,B) \propto A^*B + AB^* \quad \text{---------- AI.5}$$

Using the notation of eq.AI.3, the hologram is described:

$$h(A,B) \propto \cos(e^{jp(x+y)}.(A(x,y).e^{j\frac{k}{2z}(x^2+y^2)} \times e^{j\frac{k}{2z}(x^2+y^2)})) \quad \text{AI.6}$$

Conventionally, the original object wave is recovered by illuminating the hologram with the original reference wave B, and the following terms appear in the output field of the hologram:

$$I(A,B) \propto B(|A|^2 + |B|^2) + A^*B^2 + A|B|^2 \quad \text{------- AI.7}$$

If the last term, which represents a copy of the original object wave, is spatially separate from the other terms, the image will be a faithful reproduction of the original object to within the inherent limitations of spatial resolution and monochromatic illumination, since the planar reference wave B synthesised by the recording process is of constant amplitude (eq.AI.2)

The hologram recording as a photographic transparency usually requires a non-negative transmission in its simplest form. A constant or bias term must therefore be added to the hologram of eq.AI.6 to yield a suitable transparency analogue. It is common practice[14,16-21,24,127] in microwave holography to subject such a hologram to a hardlimiting process by electronic and/or photographic means in the exposure of the hologram transparency. This dynamic range compression process is found to lead to better image-to-background contrast, although shorter focal length defocussed image artifacts do arise from the limiting process. In the prototype system, the hologram was stored temporarily on a storage oscilloscope screen, and the highly non-linear threshold characteristic of this channel produced essentially the same limiting process. The process can also be regarded as a removal of amplitude information in the hologram of eq.AI.6, leaving regions of positive or negative component only. The correspondence

between these regions and AB^* hologram phase has lead to the term "phasigram" being applied to this technique.[17]

AI.1.2 Relationship with Areal Aperture Systems

The expression of the mixer input field in eq.AI.3 is completely equivalent to that field which would be measured over the aperture projected by the transmitting and receiving arrays with an illuminator positioned at the array point of intersection (0,0,0), and using as reference wave a plane wavefront $e^{-jp(x+y)}$ making an included angle $\propto$ with the array plane in both axes. The angle $\propto = \sin^{-1}(\lambda_g/\Delta x - 1)$, $p = 2\pi/\lambda_g$ the antenna interval is Δx. As a result, the hologram generated by the orthogonal array system has the same image resolution as that which would be displayed by the equivalent areal aperture system. The prototype system had $\Delta x = \lambda_g/2$ with alternate phase shifts of π radians incorporated in the design of the waveguide distributor in both axes and the reference wave was as a result both planar and coplanar with the orthogonal microwave arrays. (Appendix II)

AI.1.3 The Optical Reconstruction Process

The analogue transparency must be scaled to a size suitable for optical components. Supposing reduction by a factor K, (K>>1), then a point (x,y) in the original hologram is related to that in the scaled transparency h(x',y') by:

$$(x,y) = (Kx',Ky') \qquad \text{AI.8}$$

The reconstruction is accomplished by illuminating the hologram with a copy of the (scaled) reference wave; in the practical system this was coplanar with the array plane. The reconstruction system (Fig.AI.2) incorporated a demagnifying stage to provide both further hologram reduction and to establish a convenient spatial Fourier transform plane in which filters could be introduced without disturbing the other components. The spatial spectral purity of the laser radiation was conventionally established by a short focal length lens and 30μm

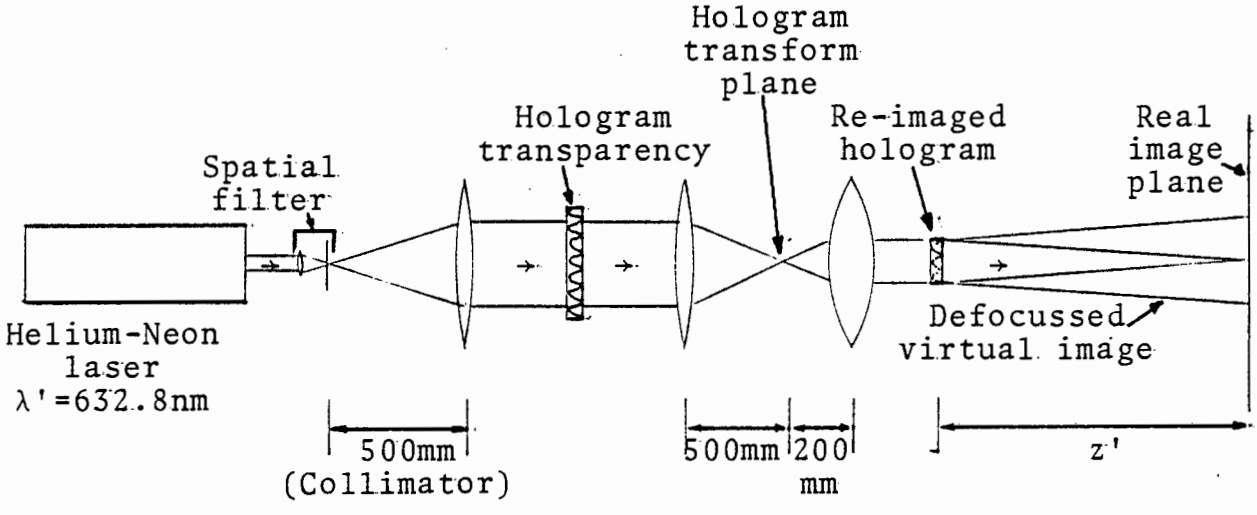

Fig. AI.2 The optical reconstruction processor

spatial filter with following collimator.

The significant fields emerging from the hologram transparency T(x',y') when this is illuminated by plane wave coherent light are (a) a reduced scale version of A^*B^2,

(b) a similar version of $A|B|^2$ and

(c) a constant background field, corresponding to the bias term. In a plane distant z' fron the reduced re-imaged hologram (Fig.AI.2), the field is:

$$\psi(r,s) \propto \int_{x'y'} T(x',y').e^{j\frac{k'}{2z'}((r-x')^2+(s-y')^2)}.dx'dy' \quad \text{----- AI.9}$$

where $k' = 2\pi/\lambda'$, $\lambda' = 632.8$nm and (r,s) is the optical image plane coordinate system. The term T(x',y') is within a complex constant of that indicated in eq.AI.6 and has also a bias term. The component of eq.AI.9 corresponding to the original field is $A|B|^2$ and is traced through the reconstruction process:

$$\psi_v(r,s) \propto \int_{x'y'} \int_{uv} A(u,v).e^{j\frac{k}{z}(u^2+v^2)}.e^{jx'(pK-\frac{ukK}{z}-\frac{rk'}{z'})}.$$
$$e^{jy'(pK-\frac{vkK}{z}-\frac{sk'}{z'})}.e^{j\frac{k'}{2z'}(r^2+s^2)}.$$
$$e^{j(x'^2+y'^2)(\frac{kK^2}{2z}+\frac{k'}{2z'})}.dudvdx'dy' \quad \text{- AI.10}$$

The focussing condition requires that the exponent of the last term of eq.AI.10 be set to zero, whence:

$$z' = -\frac{k'z}{kK^2} = -\frac{\lambda z}{\lambda' K^2} \quad \text{---------- A1.11}$$

The negative sign of z' indicates that the optical axis position of this field is on the laser side of the hologram, and it is interpreted as thus a virtual image. Substituting eq.AI.11 into eq.AI.10, and integrating over (x',y'), the limits being the scaled aperture dimensions X',Y', yields:

$$\psi_v(r,s) \propto \int_{u,v} A(u,v).e^{j\frac{k}{z}(u^2+v^2)}.e^{j\frac{k'}{2z'}(r^2+s^2)}.\text{sinc}\frac{X'}{2}(pK-\frac{ukK}{z}-\frac{rk'}{z'}).$$
$$\text{sinc}\frac{Y'}{2}(pK-\frac{vkK}{z}-\frac{sk'}{z'}).dudv \quad \text{-- AI.12}$$

The integration limit $X' = X/K$, and $Y' = Y/K$. ---------- AI.13

The constant of proportionality in eq.AI.12 absorbs a term equal to hologram area X'Y'.

$$\psi_v(r,s) \propto e^{j\frac{k'}{2z'}(r^2+s^2)} \{\int A(-\frac{rk'z}{z'kK}+\frac{pz}{k}, -\frac{sk'z}{z'kK}+\frac{pz}{k}) \cdot e^{jk((-\frac{rk'z}{z'kK}+\frac{pz}{k})^2+(-\frac{sk'z}{z'kK}+\frac{pz}{k})^2)} \otimes \mathrm{sinc}\frac{X'}{2}(\frac{rk'}{z'}) . \mathrm{sinc}\frac{Y'}{2}(\frac{sk'}{z'})\} \quad \text{AI.14}$$

If the smoothing effect of the sinc() terms is disregarded, then the virtual image is just:

$$\psi_v(r,s) \propto A(rK-\frac{pz}{k}, sK-\frac{pz}{k}) . e^{jk((rK-\frac{pz}{k})^2+(sK-\frac{pz}{k})^2)} \quad \text{AI.15}$$

The result of eq.AI.11 has been used here, and the leading term of eq.AI.14 has been ignored, since the measured or observed quantity is the image intensity $I_v(r,s)$, where:

$$I_v(r,s) = \psi_v^*(r,s) . \psi_v(r,s) = |\psi_v(r,s)|^2 \quad \text{AI.16}$$

The image is reduced in size by K (K>>1), shifted from the optical axis by the effect of the reference wave an amount pz/kK and is, in addition, phase-modulated. The virtual image is not useful for permanent recording, and the real image derived from the A^*B^2 term in the transmission hologram output is used instead; for this term the focussing criterion becomes:

$$z' = \frac{\lambda z}{\lambda' K^2} \quad \text{AI.17}$$

and the expression for real image amplitude is, again ignoring the sinc() smoothing terms:

$$\psi_r(r,s) \propto e^{j\frac{k'}{2z'}(r^2+s^2)} . A^*(rK-\frac{pz}{k}, sK-\frac{pz}{k}) . e^{-jk((rK-\frac{pz}{k})^2+(sK-\frac{pz}{k})^2)} \quad \text{AI.18}$$

The real image position is behind the hologram with respect to the reconstructing radiation. (Fig.AI.2)

AI.1.4 The Reconstructed Image Position

Both real and virtual images are offset an amount pz/kK in both r and s axes. This reflects the fact that in a continuous (as opposed to sampled) antennae array the synthetic reference wave makes an angle p/k radians with the axis, and the image offset in a non-reduced reconstruction would be pz/k if a

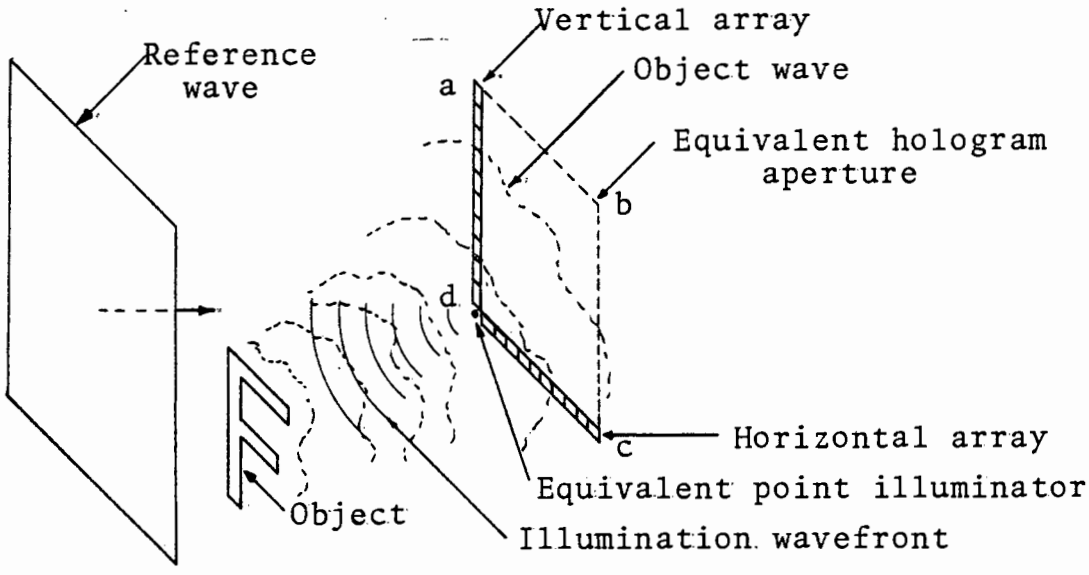

Fig. AI.3(a) The hologram formation stage

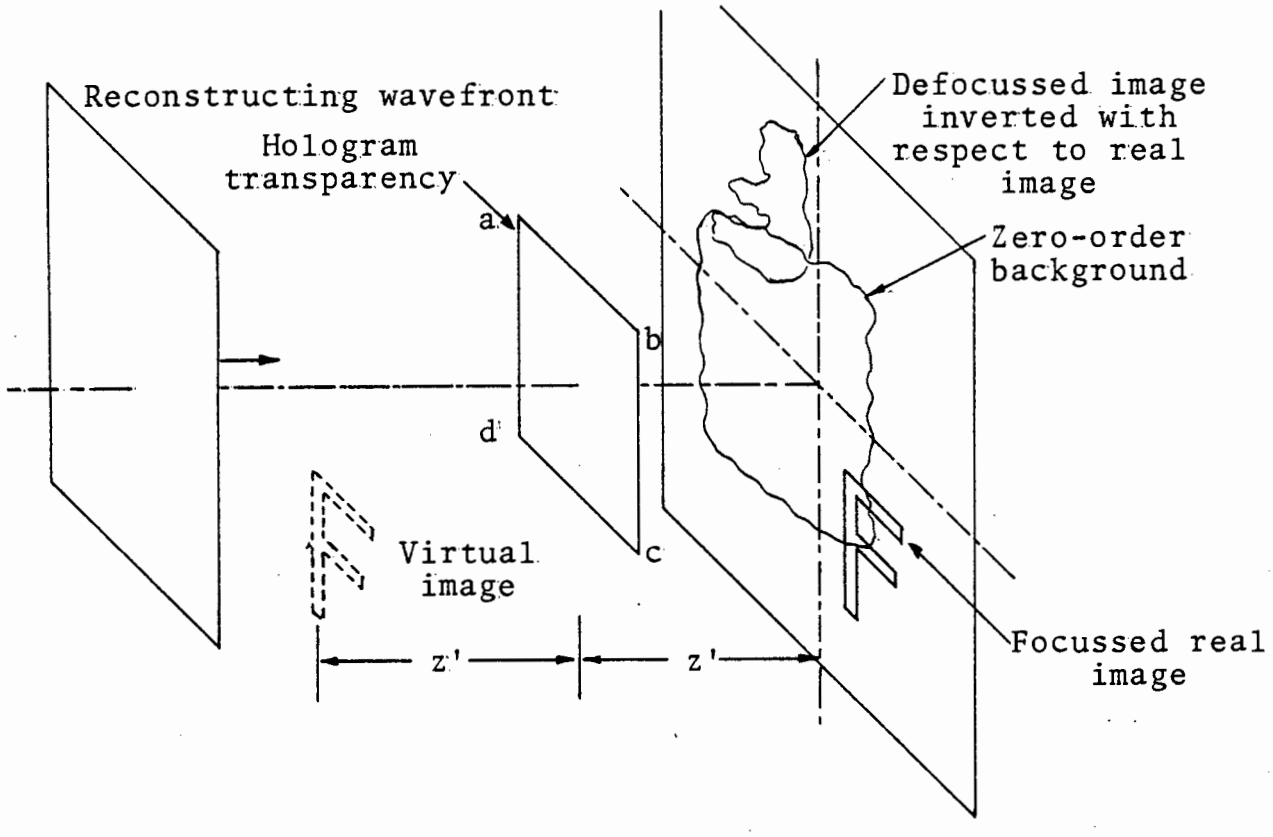

Fig. AI.3(b) On image position and orientation in holography

reconstructing wavefront coplanar with the hologram is supposed.

The hologram formation and reconstruction is sketched in Fig. AI.3. There need not always be one virtual and one real image since other combinations are possible by manipulating the focal length of the reconstructing radiation, but planar reference and reconstructing wavefronts are useful experimentally as direct z' estimates may be made without having first to compensate for additional system lenses. In digital reconstruction techniques, the use of the "backpropagator" notion can be viewed as leading to the derivation of the virtual image. The advantage of the digital reconstruction is the facility with which the propagation direction of the simulated illuminating radiation can be altered.

In Fig.AI.3(a), the formation stage of the hologram, the object F is seen as ∃ from the hologram aperture. The same is seen as a reconstructed virtual image, looking through the hologram towards the illuminating source in Fig.AI.3(b). By way of comparison, the real image, allowed to self-focus on a suitable screen z' beyond the hologram is seen as F. Both images are focussed below the hologram centre, but the virtual image will form a defocussed distribution above the focussed real image if the screen here has adequate vertical extent. The real image magnification from the original object plane to the reduced optical image is:

$$M_{lat} = \frac{z'kK}{zk'} = \frac{z'\lambda'K}{z\lambda} \qquad \text{AI.19}$$

From eq.AI.11, $z' = \lambda z/\lambda' K^2$, so that M_{lat} is just:

$$M_{lat} = \frac{1}{K}$$

The longitudinal image position is from the same equation:

$$z' = \frac{\lambda z}{\lambda' K^2}$$

In the prototype system K was, including the hologram re-imaging stage (Fig.AI.2), about 350, but the longitudinal image position was just 0.4 of that of the object. Had K been equal to the ratio of formation and reconstruction stage wavelengths λ/λ' (about 48000), then image proportions would have been in all three axes a similarly scaled version of those of

the object, but this provision would have resulted in unacceptably small transparencies.

The lateral image resolution is simply derived from eq.AI.14. The sinc() functions have in their respective axes a width at the half-intensity points given by:

$$\Delta r = \frac{\lambda' z'}{X'} \text{ , and } \Delta s = \frac{\lambda' z'}{Y'} .$$

Substituting for z' and X' and Y':

$$\Delta r = \frac{\lambda z}{XK} \text{ , and } s = \frac{\lambda z}{YK} \qquad \text{AI.20}$$

Provided that the reduced scale hologram aperture is fully used, the resolution of the optical image is seen to have been determined in the hologram mapping or formation stage.

It should be stressed that the image offset has been derived as though the orthogonal microwave antenna arrays were composed of continuous emitters and receptors. In a practical microwave system, only discrete antennae are feasible in an inertialess implementation and the system described in this thesis used a resonant waveguide distributor which ensured zero relative phase difference between elements.(Appendix II) The reference wave was accordingly coplanar with the hologram aperture and the terms A^*B and AB^* in eq.AI.5 corresponded to the object wave itself and its conjugate as a result, and their sum represented a component of the object wave.

AI.1.5 The Sampled Hologram

The preceding analysis has presumed continuous transmitting and receiving arrays, and consequently has considered the reconstruction of the field emerging from a continuous hologram. The reduced hologram is multiplied by a two-dimensional sampling grid to simulate the sampling process arising from discrete arrays of antennae. The sampled hologram is thus:

$$h_s(x',y') = \int_{x'} \int_{y'} T(x',y').\delta(x'-n\Delta x').\delta(y'-n\Delta y')dx'dy'$$

The sampling interval $\Delta x'$, $\Delta y'$ is:

$$\Delta x' = \Delta x/K, \quad \Delta y' = \Delta y/K,$$

where $\Delta x = \Delta y$ and represents the antenna interval in the

mapping stage. The prototype system had Δx = 20.2mm.(sec. AI.1.2) The sampling function can be decomposed by standard methods:

$$\delta(x'-n\Delta x') \propto \sum_n e^{j\frac{2\pi n x'}{\Delta x'}}$$, where n takes integral values. Similarly:

$$\delta(y'-n\Delta y') \propto \sum_n e^{j\frac{2\pi n y'}{\Delta y'}}$$.

The inclusion of the sampling function generates a multiplicity of equally spaces optical image orders; the image amplitude $\psi_v(r,s)$ becomes :

$$\psi_v(r,s) \propto \int_{u,v} A(u,v) . e^{j\frac{k}{z}(u^2+v^2)} . e^{j\frac{k'}{2z'}(r^2+s^2)} . \operatorname{sinc}\frac{X'}{2}\left(\pm\frac{2\pi n}{\Delta x'}+pK-\frac{ukK}{z}-\frac{rk'}{z'}\right) . \operatorname{sinc}\frac{Y'}{2}\left(\pm\frac{2\pi n}{\Delta x'}+pK-\frac{vkK}{z}-\frac{sk'}{z'}\right) dudv \quad \text{---------- AI.21}$$

The virtual image is identical to that of eq.AI.12, but in addition is repeated at intervals in the (r,s) plane, where:

$$\frac{2\pi n}{k\Delta x'} = \frac{r_n k' z}{z' k K} - \frac{pz}{k}$$, such that r_n is:

$$r_n = n.\frac{\lambda z}{\Delta x}.\frac{1}{K} - \frac{pz}{k}.\frac{1}{K} \quad \text{---------- AI.22}$$

The intervals between successive images is just $\frac{\lambda z}{\Delta x}.\frac{1}{K}$. This corresponds to a reduced (by K) version of the image spacing in the full-size hologram reconstruction, assuming that the paraxial approximation is valid at the angles suggested by eq.AI.22. That the paraxial approximation is not always valid at this offset in the non-reduced image is apparent from sec. 3.6 , but the reduction process generates a hologram wherein the sampling interval $\Delta x'$ is many wavelengths (about 91) long, rather than just two thirds of a wavelength long as in the microwave system, and hence the paraxial approximation is applicable over a much wider portion of the optical image field. Given a hologram of width X', and an image plane offset r, then the error in assuming paraxial wavefront description is no worse than ignoring the next term in the Taylor series field expansion, or:

$$\varepsilon(r,s) = e^{j\frac{k'}{8z'^3}(r-x')^4}$$.

This term should have a maximum value not in excess of π radians for the exponent. (sec.3.4)

Hence: $r < (4z'^3\lambda')^{\frac{1}{4}} - \frac{X'}{2}$, and as the least z' value encountered was about 200mm, the minimum value of r under which the paraxial approximation is still valid is 11mm. By way of comparison, the image will repeat at intervals of only 2.1mm at this range. The paraxial approximation is thus valid and adequately accurate over distances much larger than the optical image repetition interval, and thus over the lowest and brightest image order. The consequence is that the image impulse response and image location accuracy are wholly determined by the accuracy of the paraxial approximation in the (microwave) formation stage.

The spatial extent of the individual data samples comprising the binary reduced hologram is of little importance, since only the amplitudes of the higher image orders are then in question. Given an optical image, knowledge of the optical focal length z', the scaling factor K, the formation and reconstruction wavelength ratio λ/λ' and a measurement of the ratio of image offset from the optical axis to image repetition interval in the (r,s) plane will determine the original object geometry, and no image order higher then the first (n=1) is required for this purpose.

AI.2 Confidence Testing of the Imaging System

The imaging operation is not considered complete with the retrieval of the optical component. An assessment of the success of the overall imaging operation should be based on the original object geometry, taking into account the object orientation and the nature of its interaction with coherent microwave illumination.

The object geometry was simply deduced using the sampled hologram-image pair to advantage. An initial direct measurement of image focal distance z', taken between the plane in which the reduced re-imaged hologram was found and the plane in which the "sharpest" image appeared.(Fig.AI.2) The corresponding object domain focal distance (range) is a simple function of reduction factor K (about 350) and the wavelength

ratio λ/λ'. (about 48000)(eq.AI.17) The image lateral offsets can in principle be multiplied by K and compared with the object domain dimensions (eq.AI.19), but the small size of this image (the image repetition interval is at most a few millimetres) suggests the use of magnifying components to examine its detail. Rather than attempt to measure overall image magnification produced on the optical bench and the following printing stages, the image offsets are taken as fractions of the image repetition interval, a ratio which is invariant with respect to image size.

The predicted object lateral offset is taken as the same fraction of the paraxially-equivalent object domain repetition interval $\frac{\lambda z}{\Delta x}$. (eq.AI.22) That this quantity corresponds to an object-array plane angle far outside the paraxial approximation's region of validity is not important provided that the approximation adequately describes the region common to object and array plane.

In practice, the image was directly recorded at original scale on Kodak Tri-X panchromatic film. (35mm, 400ASA) The film holder was a conventional SLR camera operated without lens, and depending on image focal length and intensity, the exposure times varied from 1/1000 to 1/125 seconds. Image analysis used the same slides optically projected and magnified.

The reflectance characteristics of the object had to estimated inasmuch as specularly behaving objects could lead to image distances apparently much in excess of the true object to hologram range. (Chp.4)

AI.3.1 Lateral Impulse Response with Combined Subarrays

The antenna arrays were developed as four 10-element subarrays having two orthogonal polarisation designs. (Appendix II) The subarray functions were combined in both axes by directional couplers, and these unfortunately caused a gap between the 10th and 11th antennae due to the bulkiness of the necessary waveguide bends, flanges and spaces required to adjust the

antennae to a uniform grid. (See photograph of array, Fig.2.2) It is no simple matter mechanically to adjust both lateral offset and simultaneously ensure equal path lengths between subarray feed points and the common connection point of the directional couplers to source and preamplifier. Differential phase errors in signal combination at these points can cause pointing errors in the axial impulse responses of the vertical and horizontal arrays. From eq.AI.14 in the preceding analysis a subarray of length X' (measured in the reduced re-imaged hologram domain) resulted in a system axial impulse response in that axis:

$$f(r) \propto \operatorname{sinc}\frac{X'}{2}\left(\frac{rk'}{z'}\right)$$

Taking X' = X/K, and the expression for z' from a previous equation (eq.AI.17),

$$f(r) \propto \operatorname{sinc}\left(\frac{\pi X}{\lambda z}.rK\right)$$

The r-axis impulse response is simply a scaled version of the corresponding object domain function, and the response for combined subarrays is derived in that domain. There is a Fourier transform relationship linking aperture distribution and impulse response. The x-axis microwave array aperture distribution is:

$$h(x) = \operatorname{rect}\left(\frac{x}{X}\right)$$

Hence the non-reduced image plane (u',v') (sec.3.3.1) impulse response in the u'-axis is:

$$H(u') \propto \operatorname{sinc}\left(\frac{u'X\pi}{\lambda z}\right) \quad \text{---------- AI.23}$$

The arrays were used initially in an L arrangement (Chp.4) as this gave better isolation between transmitting and receiving antennae than the + arrangement used with the digital and enhanced optical reconstruction processes. (Chp.5) In the latter, cross-coupling was reduced to negligible proportions by a subtractive technique. (sec.5.3) The equivalent analogue operation has been reported[47] but was not used here. The array geometry is shown in Fig.AI.4. This deployment had a relative shift of 81.5mm in the axes of the vertical arrays caused by initial hardware limitations. The paraxial region approximation finds the orthogonal axes' impulse response by transforming the aperture occupancy in each axis separately.

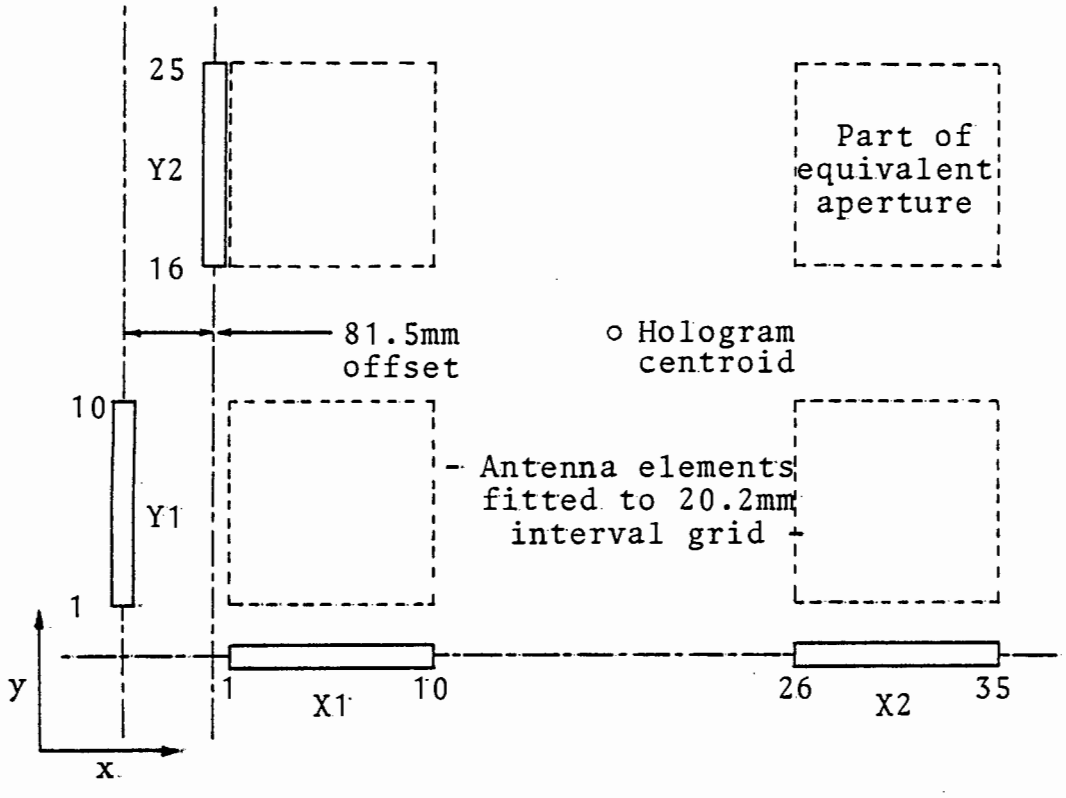

Fig. AI.4(a) Geometry of a preliminary 2 x 2 array

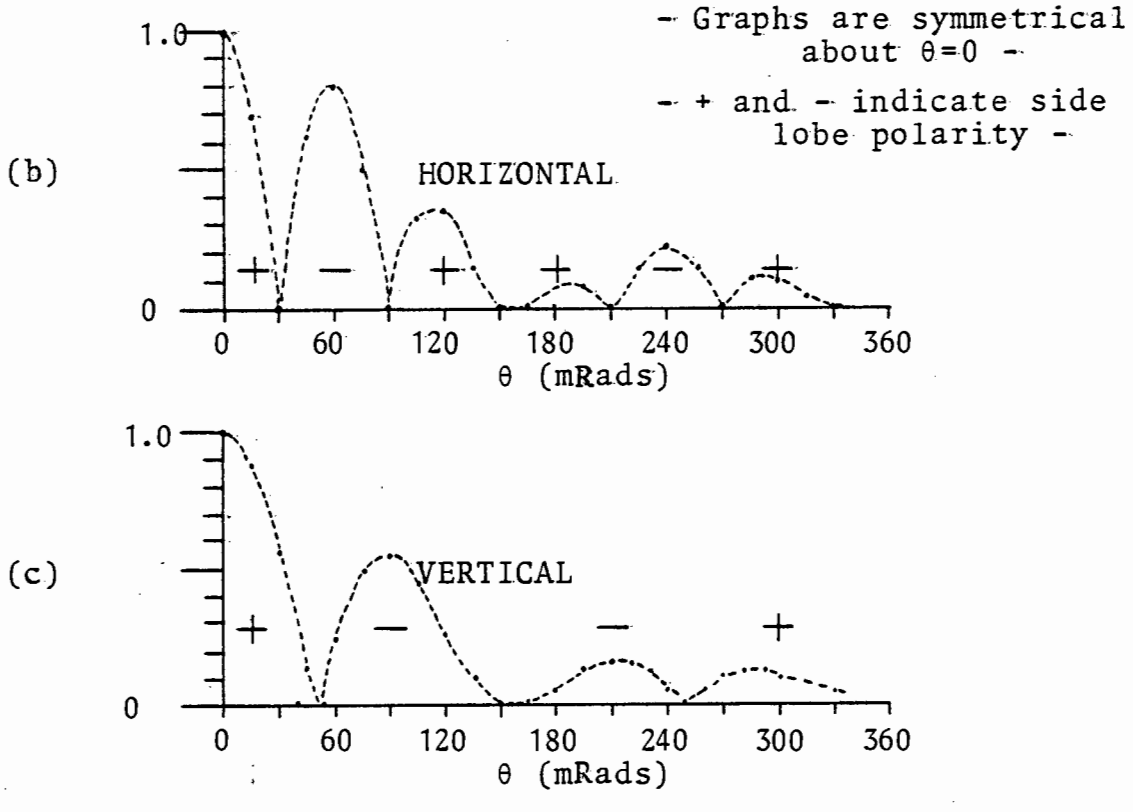

Figs. AI.4(b) and (c) Array impulse response

The horizontal array occupancy is:

$$h_h(x) = \text{rect}(\frac{x}{X}) \otimes (\delta(x \pm D_h.\Delta x))$$

$D_h = 12.5, \Delta x = 20.2\text{mm}$ and $X = 181.8\text{mm}$. The corresponding impulse response is:

$$H_h(u') \propto \text{sinc}(\frac{\pi u' X}{\lambda z}).\cos(\frac{2\pi u' D_h.\Delta x}{\lambda z})$$

The impulse response of the horizontal array (Fig.AI.4(b)) exhibits a narrow maximum flanked by slowly diminishing sidelobes. The resolution at the half-power points is:

$$u'_{-3dB} = \frac{\lambda z}{4D_h \Delta x}, \text{ or as an angular function:}$$

$$\theta_{-3dB} = \frac{\lambda}{4D_h \Delta x} = 30\text{mRads}.$$

The resolution of the system is higher than that of an array of equal overall aperture, but the sidelobe levels are much in excess of those expected of a filled array aperture. A filled array aperture would have 44mRads. resolution, but the first sidelobe pair in the combined array are at only -2dB level. (Fig.AI.4(b))

The vertical array had a smaller subarray gap ($D_v = 7.5$) and resulted in slightly wider central maximum (59mRads.) and lower amplitude (-6dB) sidelobe performance at a larger offset of ±100mRads. (Fig.AI.4(c))

AI.3.2 The Effect of Combination Phase Errors

The mechanical constraints imposed fitting antennae to a regular grid and ensuring that these are also collinear means that a phase error can be introduced between the signals of each subarray pair. Assuming a relative phase error of ε radians between the subarray ports, the array occupancy in an axis becomes:

$$h(x) = \text{rect}(\frac{x}{X}) \otimes (\delta(x \pm D.\Delta x).e^{\pm j\varepsilon/2})$$

Using the translation property of the Fourier transform:

$$H(u') \propto \text{sinc}(\frac{\pi u' X}{\lambda z}).\cos(\frac{2\pi u' D\ x}{\lambda z} - \frac{\varepsilon}{2})$$

A maximum error in the position of the central lobe of the impulse response function results if $\varepsilon = \pi$. The angular error would be $\lambda/4D\Delta x$ radians. The effect of phase errors in combination is to translate the oscillatory structure under the

sinc() envelope, and the regular nature of this structure means that a peak "pointing error" as large as the -3dB beamwidth is possible.

AI.3.3 Axial Offset in Vertical Subarrays

The x-axis relative offset of the vertical subarrays Y1,Y2 is d. (d = 81.5mm) This resulted from the E-plane divergence of the output ports of the directional coupler signal combiner. The hologram segment resulting from commutation of the sensors in subarrays X1 and Y1 and having a point scatterer target at (u,v,z) is approximately:

$$h_{X1Y1}(x,y) = e^{jp(x+y)} \cdot e^{j\frac{k}{2z}(u^2+(x-u)^2+v^2+(y-v)^2)}$$

The corresponding segment from the X1,Y2 subarray pair is:

$$h_{X1Y2}(x,y) = e^{jp(x+y)} \cdot e^{j\frac{k}{2z}((u-d)^2+(x-u)^2+v^2+(y-v)^2)}$$

The above expressions are similar, taken over their respective subarray y-axis values, but for a term:

$$\varepsilon(d,u,z) = e^{j\frac{k}{2z}(d^2-2ud)}$$

The effect of such an error term for a point object is to perturb the position of the impulse response maximum under the enveloping sinc() function in the same manner as the phase errors in combination in the orthogonal x-axis. The error is function of both range and object u-axis position, so that imaging of objects extended in that axis is additionally perturbed ; however, the array offset was corrected by additional hardware before any imaging of extended objects was attempted and used only in a preliminary "confidence test" with objects whose specular nature allowed point scatterer treatment.(Chp.4)

AI.4 Object Region Accessible to 10 and 20 Element Arrays

Differences in the lateral dimensions of the object region accessible to the crossed array microwave holographic system employing two 10 element, and, by way of comparison, two 20 element arrays are examined assuming the use of the paraxial

reconstruction process. The object region u- and v-axis accessibility is governed by both paraxial accuracy and sampling considerations, and is a function of range to that object plane.(secs.3.4 and 3.6) A criterion of paraxial approximation accuracy suggested (eq.3.36) a peak phase error of π radians:

$$u_{max} = \left(\frac{\phi .4z^3\lambda}{\pi}\right)^{\frac{1}{4}} - \frac{X}{2}, \text{ where } \phi = \pi, \text{ z is the range,}$$

λ = 30.3mm, X = .1818m (10 element) or .3838m(20 element) and the antenna element spacing is taken as $\Delta x = \Delta y$ = 20.2mm. The arrays are supposed to be assembled without "missing" antennae as filled arrays.

The Nyquist sampling criterion, based on a stationary phase estimate of hologram spectral extent, limits the u-axis accessibility according to:(sec.3.6)

$$u_{max} = \frac{\lambda z}{2\Delta x} - \frac{X}{2}$$

The axial half-power resolution is taken as $\frac{\lambda z}{X}$ in the conventional manner. An estimate of the number of resolved cells across the object region is taken as the u-axis limit divided by cell dimension and doubled.

The actual number of cells resolved on the areal object may be less than this number and would also depend on expected object contrast as the conventional apodising procedures used to control sidelobe levels on this account would also degrade linear resolution.[11] Examination of the shaded region of Figs.5(a) and (b) shows that the paraxial accuracy limitation ultimately restricts object region accessibility, and in the range interval below 2 metres used in the prototype system no more than 30 cells (for the 10 element array configuration) are available, but about 100 are available for a 20 element system which has slightly more than twice the linear aperture in either axis. The latter system could thus accept more complex objects but at the expense of an increase in the minimum usable range.

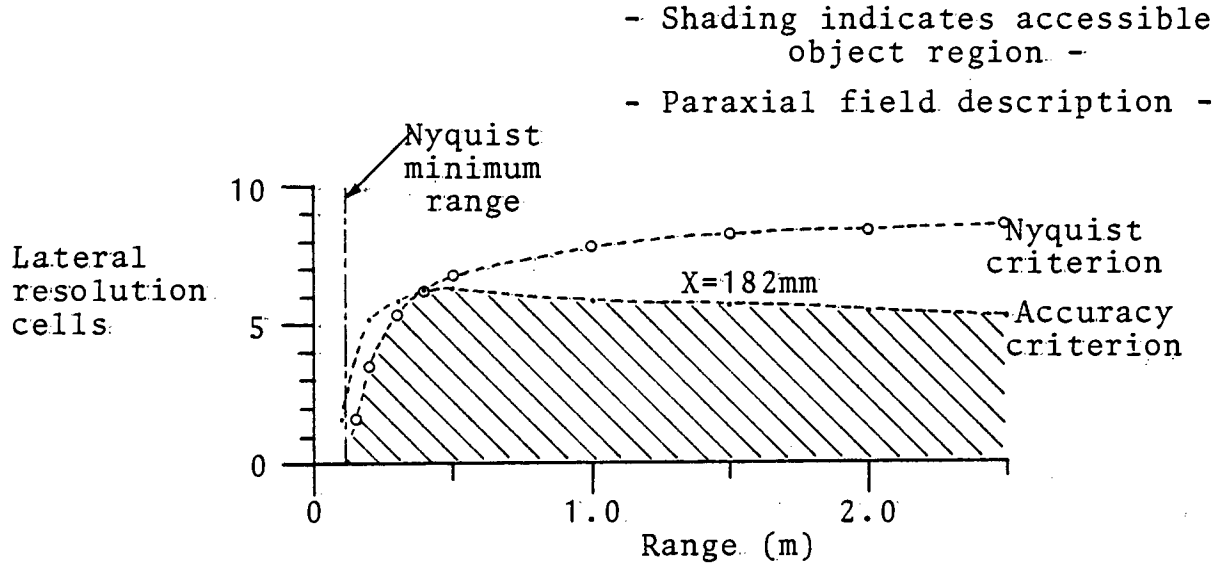

Fig. AI.5(a) Lateral resolution cells accessible to 10 x 10 array

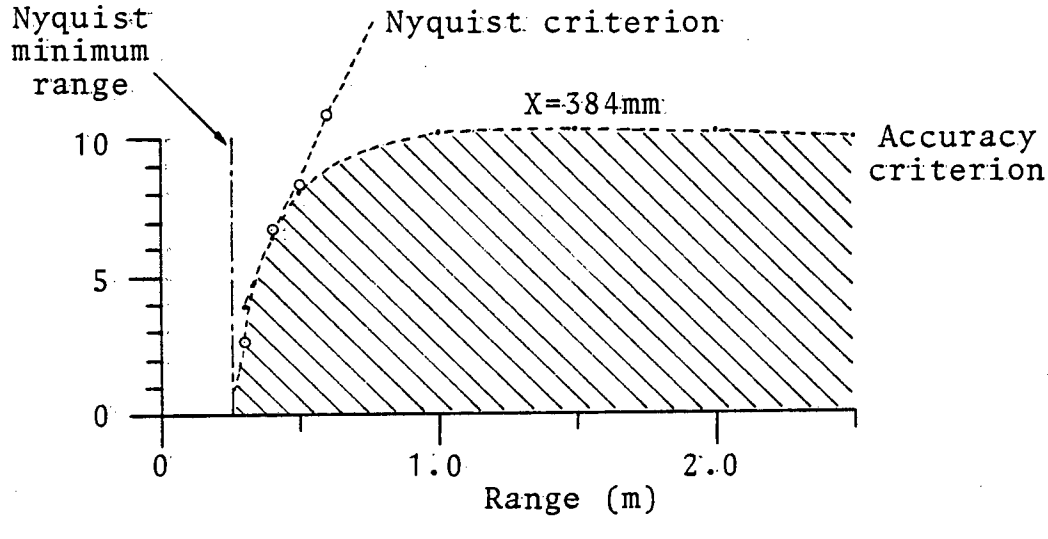

Fig. AI.5(b) Lateral resolution cells accessible to 20 x 20 array

Appendix II

System Design Features

The major hardware components of the circuitry responsible for selecting the active antennae, generating the required microwave power and processing the received signal are described in rather more detail than in Chp.2, and in addition, some of their design features are highlighted.

AII.1.1 The Antenna Arrays

The signal distributor for both transmitting and receiving arrays was a slotted waveguide operating as a resonant antenna. This type of distributor was felt to offer a simple and predictable method of obtaining a set of spatially separate signal fields with (ideally) zero relative phase shift and equal amplitudes. Other realizations of array antennae do not impose the same limitations in choice of slot spacings[89] but the price paid for this extra design parameter is a relative increase in insertion loss. The decision to base the antenna design on waveguide technology was made of necessity since more modern and compact stripline and microstrip technology demanded support equipment for fabrication and test measurement which was not available to this author. The narrow allowable frequency range imposed by the resonant slot length of approximately one half free-space wavelength and the adjustable short circuit used to reflect an open circuit condition as subarray termination was not a serious problem at the bandwidths (less than 0.01%) occupied by the system at the current stage.

Slots were cut in the broadwall of one subarray, (Fig.AII.1(a)) and in the narrow wall of the other, (Fig.AII.1(b)) so that the switches and associated radiators could be arranged for copolarised operation. Cross-polarised operation would be possible using identical arrays in both axes, although

Fig. AII.1(a)(Left) Subarray type with slots in broadwall of waveguide

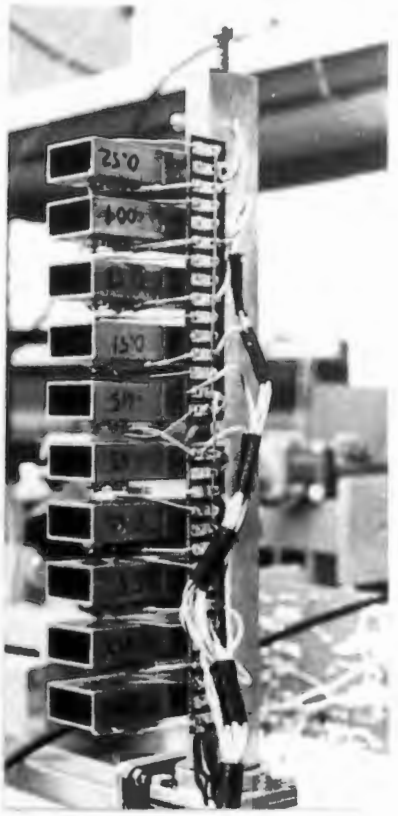

Fig. AII.1(b)(Right) Subarray type with slots in narrow wall of waveguide

Fig. AII.1(c) View of aperture shows diode switches and stubs

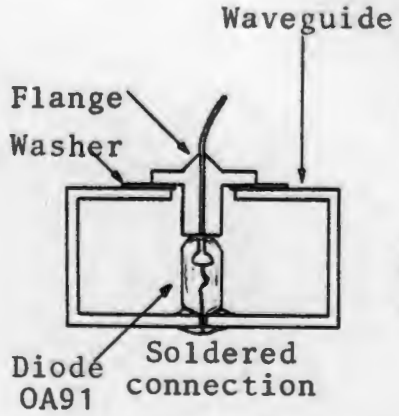

Fig. AII.1(d) Section of switch and flange

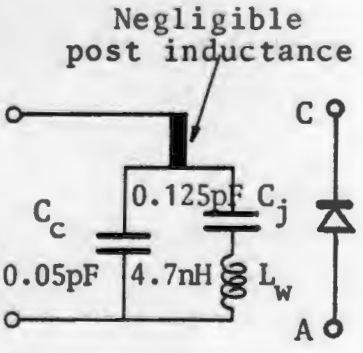

Fig. AII.1(e) Diode equivalent circuit (Switch in "ON" state)

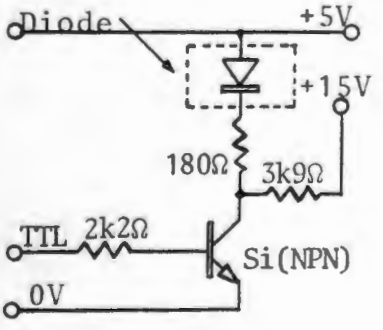

Fig. AII.1(f) Switch driver

polarisation filters have been developed for SAR use[126] and would be appropriate for generating co- and cross-polarised microwave holographic imagery as well.

The resonant distributor design assumes slot-to-slot spacings of multiples of one half waveguidelength(in this case 20.2mm) and almost exactly equal to two-thirds of the free space wavelength of 30.3mm. Lower spacings were not practical since the operating frequency would have approached the waveguide cut-off frequency.

AII.1.2 Switches

Shunt two diode switches were used in both axes. The negligible bandwidth requirements allowed device selection to be based on the diode parasitic reactances rather than having to try to minimise the effect of these parameters. In addition, the design was also required to yield a switch as simple as was possible, so that comparatively large numbers could be made without requiring individual adjustment. (Fig.AII.1(c))

Germanium point contact "signal" diodes were used in all switches. (The type used was OA91.) A short stub, equal in diameter to the diode, was mounted centrally in the waveguide and connected in series with the diode, so bridging the narrow dimension of the waveguide. The microwave circuit was completed by flanging this stub and inserting a plastic washer between flange and the outside broad wave guide wall so forming a bypass capacitor. The value of this bypass capacitor was less than 5pF and represented only -j3 ohms reactance at the operating frequency.(Figs.AII.1(d) and (e))The switch driver circuit is shown in Fig.AII.1(f). The transistor driver base was held at TTL logical zero level in the minimum transmissiom (quiescent) state, and , depending on which axis was selected, a 188kHz or 148kHz square tone-burst waveform was applied during the active epoch. The waveguide was as a result at TTL supply potential, and thus waveguide connection to source and preamplifier was made through thin low-loss

insulating washers between the mating flanges. The choice of germanium diode OA91 was only made after extensive tests of various units, including a variety of mechanically similar germanium point contact, silicon planar and hot carrier types. Silicon PIN diodes were not considered on the basis of the high costs of these devices . All diodes were tested in the same mount and where necessary the shorter diodes were extended by an equal diameter post so that all assemblies spanned the waveguide. The switches were terminated by a matched attenuator and following detector for repeatability of transmission measurements. Those diodes having the thinnest and longest "whiskers" within the envelope and the lowest capacitance under reverse-biased conditions proved to be best suited to waveguide switch service.

Slotted line admittance measurements also revealed that in all cases in both transmission states, the admittance in the diode plane was net inductive. The proposed equivalent circuit is shown in Fig.AII.1(e) and the quantities C_c and C_j refer to the fixed envelope and junction capacitance respectively. These are practically inseparable in a low frequency bridge measurement and the total value at -10 volts reverse bias was 0.15pF. The post inductance was negligible compared to that of the "whisker", denoted by L_w. The equivalent circuit in the "OFF" (lower transmission) state was not quite that of a series resonant circuit, the whisker reactance being twice that of the junction capacitive reactance, but a diode combining high whisker inductance and a junction capacitance of about 0.3pF could not be found.

It was possible to improve marginally the "ON" state transmission at the expense of the "OFF" state isolation, by including a (capacitive) adjustable screw reflected into the plane of the diode. In the "ON" state, the junction reactance represented by C_j is effectively removed from circuit by the action of the forward current then flowing and replaced by a low resistance term instead (of the order of 20 ohms), and the peaking of the "ON" state transmission by the screw is in

accordance with the equivalent circuit.

The switch also served as radiator without the addition of any external components. The interelement spacing of 20.2mm meant that standard RG-52/U waveguide was too wide for the broadwall subarray and a reduced width version with standard height (10mm) was fabricated from the solid with a 17.9mm internal dimension. The cut-off dimension at the system operating frequency was 15.15mm and tolerances on the width of the waveguide were held to 0.1mm over 20 switches in an attempt to minimise phase errors due to the increased waveguide phase velocity sensitivity so close to cut-off.

The development of the arrays as two pairs of 10 element subarrays was in retrospect unfortunate, since the combination into a single array function involved both a power loss of 3dB in the directional coupler and an inevitable gap between subarrays in a given axis which was caused by the bulky waveguide hardware and this adversely affected the form of the imaging system's impulse response.

AII.1.3 Array Evaluation

The evaluation of subarray and array performance was intended establish the array insertion losses and the relative phase and amplitude errors across the aperture. Any switch of either array functions both as commutator and amplitude modulator. This last process is performed in two steps, using different frequencies in each array. It is always convenient if the received signal is modulated either in amplitude or in phase as this enormously simplifies the recovery of small signals in the presence of a much larger amplitude reference field.[91]

The insertion loss is expressed as the loss in conversion of continuous wave power to power at a single sideband. Without modulation during the active epoch, the insertion loss of a switch varied. Using a matched termination (as opposed to an open waveguide) the subarrays having E-field polarisation parellel to their long axes(Fig.AII.1(b)) had an average

insertion loss of 4.6dB and the other type (Fig.AII.1(a)) had a loss of 3.5dB. Measurements were made using a microwave spectrum analyser (HP8555A) as a wideband receiver. The mean power of one fundamental sideband of the squarewave toneburst was, for an average element of the more efficient array, -13.6dB below the level a lossless switch would transmit. The high conversion loss was an unfortunate property of the simple shunt switch. By comparison, the reflective switch used in the cooperative target device could achieve higher performance since reflection of a continuous wave field alternately from planes spaced $\lambda_g/4$ apart amounts to suppressed-carrier DSB in the ideal case and even practically, the conversion loss was only 4dB.

The signal reflected from the object under investigation was remodulated by the shunt switches of the other array. The overall conversion loss including fixed losses in the switches and the modulation process itself was about 28dB. The synchronous detection process used recovered power in both fundamental sidebands and improved the insertion loss for practical purposes by 3dB.

The initial measurements of systematic phase errors in a subarray were made using a cooperative target[91-93], being a horn antenna terminated in a diode switch and short circuit. The device had impressive advantages, and the system could be used to determine the cooperative target's phase centre albeit in an environment far from anechoic.

The array test geometry is shown in Fig.AII.2(a) and a view of the source radiator and array as seen from the cooperative target is given in Fig.AII.2(b). The microwave source was unmodulated and the first subarray of 10 antennae was used as a receiver. No travelling wave tube preamplifier was necessary in the receive path since system losses were far lower than in a typical two-axis imaging situation. The output phases of the reflected signals are seen in Fig.AII.2(c) in order of the antennae. The cooperative target was just within the array far-field and normal to the antennae centreline. The signal

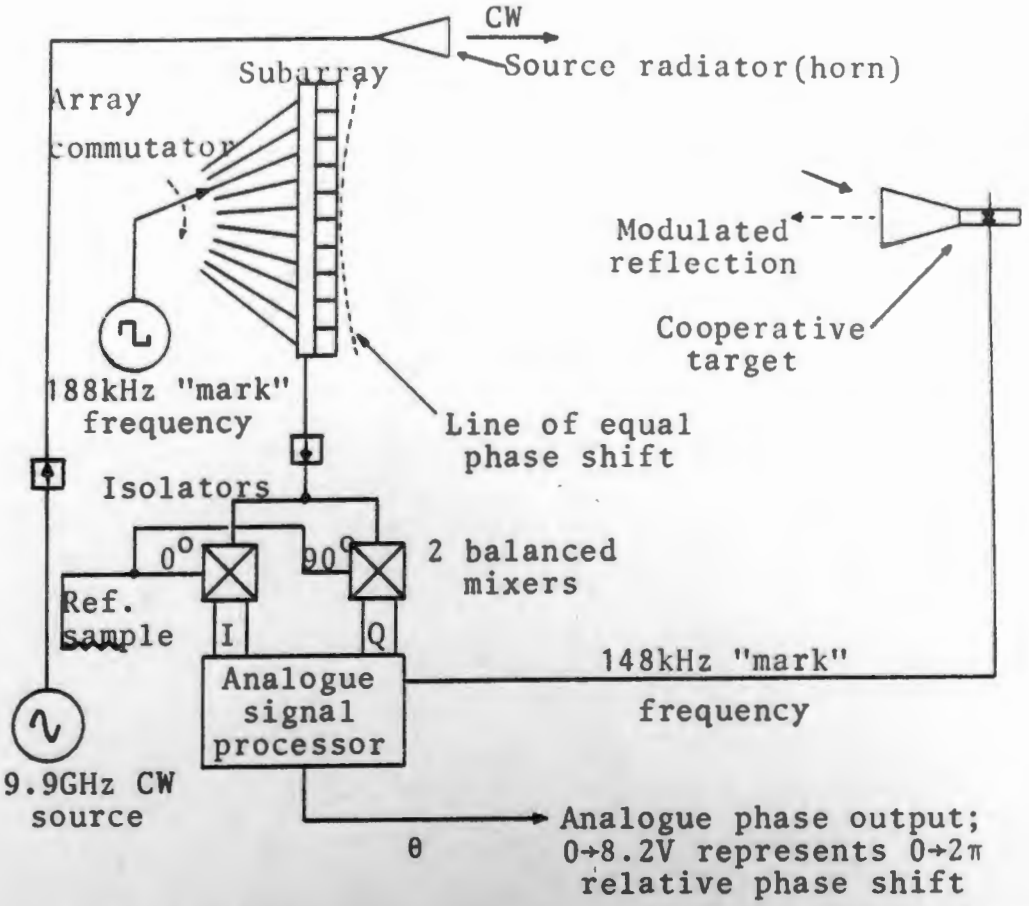

Fig. AII.2(a) Checking the performance of a subarray

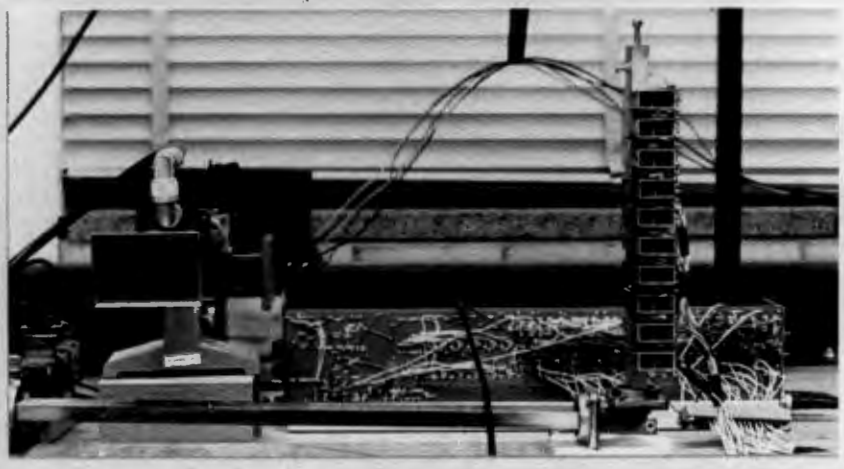

Fig. AII.2(b) A subarray seen from the cooperative target

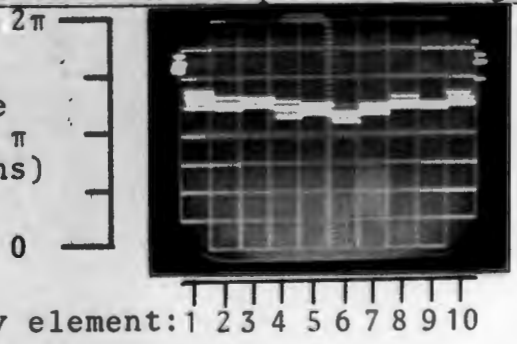

Fig. AII.2(c) Measured phases of individual subarray antenna elements

extracted for analogue measuring purposes was found at the output of an analogue sample-and-hold , which was arranged to follow the analogue processor (q.v.) phase output a variable time after the commutation of number 1 antenna, very much after the manner of a box-car detection system and possessing the signal averaging properties of this technique. Only the systematic phase errors were considered to remain after this stage.

This preliminary test showed that the first subarray had 40^{o} phase spread across the aperture at the farfield distance. In Fig.AII.2(c) the slight "concavity" of the phase data shown as analogous voltage quantities proved to be that expected, since this effect increased at shorter ranges. A least-squares parabolic fit of the phase data to that calculated for this range showed only 7^{o} r.m.s. phase error. This error is comparable with the "random errors of $\pm 12^{o}$ from a mean" accepted by Hayward, Rope, Tricoles and Yue[35] in their 16 x 16 antennae, mechanically switched, orthogonal array imaging system. These tests showed that the basic array design was sound and that optical reconstruction would be worthwhile if the cross-coupled (that is, coupled directly from transmit to receiving antenna) signals could be removed or otherwise kept to a sufficiently low level.

A more complete survey of the transmitting and receiving arrays was possible once the complete antenna system had been assembled with signal combining hardware (directional couplers), mounted on a suitably rigid frame and the interfaces to the Departmental minicomputer commissioned. The survey was performed under supervision as an undergraduate project.[38] The antennae system was deployed as shown in Fig.2.2 of Chp.2. This survey was geometrically quite similar to the previous test. A local normal to the plane of the arrays was established using a reflected beam from a low powered Helium-Neon laser and an optical mirror fixed in area of array intersection. The transmitting array was disconnected from the source feed and functionally replaced by a simple radiating element and

series switch placed a known distance along the array normal and linked to the source by coaxial cable. The arrays were surveyed separately and used as receive components. The commutation circuitry was switched so that in both cases commutation was at the same rate. This precaution simplified data capture. 1600 data points were recorded on paper tape for later analysis. These data corresponded to 40 frames each of 40 data, there being an I and Q component from every antenna of the 20 in a full array. Summation of these frames amounted to time domain averaging of the signal components and only systematic errors were considered to remain afterwards. A spherical wavefront was assumed to originate from the phase centre of the remote transmitter and a least-squares fit was applied to the mean measured data.

The system was also operated in its normal imaging mode, but using a large ($1m^2$) rigid aluminium sheet as a specular reflector and taking care to remove beforehand the (average) cross-coupled signal field. The specular "image" source found apparently behind the object was located in three dimensions and again a least-squares fit of the field considered to emanate from the "source" was applied to the mean measured data. The array phase errors derived from both separate and imaging surveys are shown in Fig.AII.3.

An obvious "step" between subarrays in the vertical axis is due to unequal path lengths in the directional coupler. The large discrepancy in phase error between the two methods for number 8 antenna was found to be caused by a defective array driver integrated circuit in the slower commutation circuit used only in the imaging mode investigation. It is also noteworthy that the lower combination phase error of the horizontal array is reflected in a remarkably symmetrical impulse response in this axis in the image; referral to the results of Chp.5 (Figs. 5.3(a),5.6(b),5.8,5.9(a) and5.10(b)) shows a central bright region flanked by symmetrical maxima as expect- of the array structure, (Appendix I)whereas the distinct combination error in the vertical axis has lead to an impulse

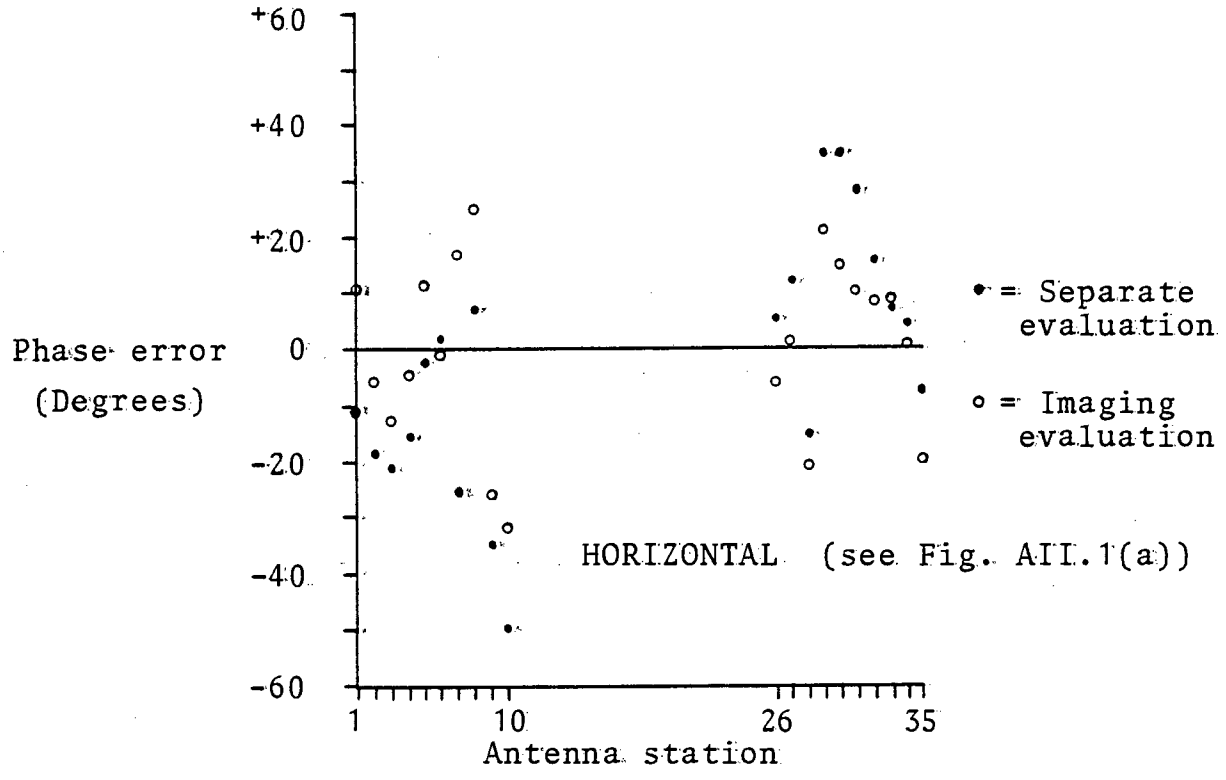

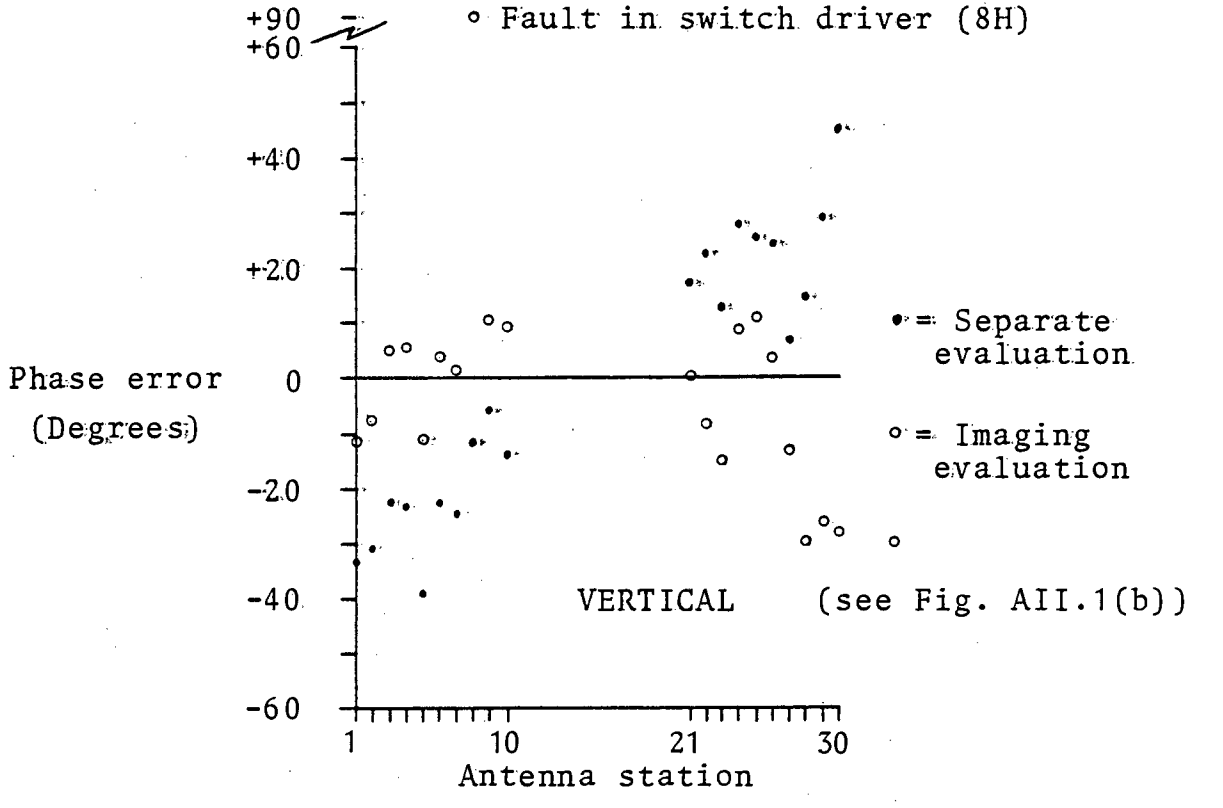

Fig. AII.3 Phase errors in the arrays

response where the maximum is slightly and consistently below the correct point.(Figs.5.7(b),5.8,5.9(a) and 5.10(b)) This conclusion applies to both optically- and numerically-based reconstuction of imageswhere the specular effect has been dominant.

The r.m.s. phase error for the vertical array was 24.5^{o} when tested separately but only 13^{o} when tested as an imaging system. The explanation of this discrepancy is quite simple. Assuming specular behaviour for the large flat object, any phase error in combination will produce a vertical offset in the image impulse response. Using the imaging notion, the wavefront supposed to emanate from that maximum will thus compensate for a linear phase error component across the respective array axis, and so produce a rather better r.m.s. phase error estimate. In like manner, the phase errors for the horizontal array were 2.2^{o}(tested separately) and 16^{o} (tested as an imaging system).

The imaging attempts prior to this survey had used optical reconstuction from unprocessed binary holograms and had shown that the effect of gaps in the array axes due to the bulky waveguide directional couplers and other hardware was a more serious defect than systematic phase errors. Compensation of such fixed errors was thus not routinely performed, but the procedure for doing so would require no more than three Fortran statements in a reconstruction program.

The procedure outlined here demonstrates the simple surveying and diagnostic features of the orthogonal axis imaging system. Correction of phase errors would involve only the storage in the reconstruction processor of M+N values, in a system having as many total elements, whereas an areal filled array of equivalent aperture and element density would require MN phase correction data.

AII.1.4 Amplitude Errors and Incomplete Elemental Isolation

The 10 element subarrays were individually tested using a simulated open circuit waveguide radiator and matched load with square law detector following. Tests were carried out at operational power levels and as an example, the vertical array (that is, having electric field polarisation parallel to the long axis) had only 1.5dB peak-to-peak variation among the "ON" elements, and the mean isolation of a switch element of this type was -23dB below the mean "ON" state level. The results of "ON" state level measurements made during the computer assisted survey were more scattered, and the same elements of the vertical array showed 6dB variation peak-to-peak, even allowing for the slight range differences to the source from element to element.

The most likely explanation of this discrepancy would account for the finite leakage of modulated signal components by nominally "OFF" antenna elements as a superposition of the spherical field due to that "ON" antenna and a lower level array of cophasal radiating elements. This background field would be encountered at a range of no more than 6% of its far-field distance in the geometry leading to Fig.AII.3, and would thus be approximately planar and uniform across the projected aperture. In this model, the spurious field components at the source position would be not more than 35% of the field generated by the "ON" antenna, which would lead to a peak additional apparent phase error of 21^{o} and amplitude errors up to +2.6dB and -3.7dB, which is in the range of errors observed in the free space experiment.

A direct test of this conjecture would involve imaging the aperture in all "ON" states possible (20), but such an undertaking is complicated by (a) a resolution reqirement rather less than $\lambda_g/2$ (the element spacing) and (b) simultaneous very low sidelobe level, since a very large dynamic range is required to separate "ON" and "leaking" antennae at this spacing.

In so far as practical imaging situations are concerned, it is noteworthy that the "range plane" imaging system considered in the latter part of Chp.5 should be particularly tolerant of errors arising from this source, as the beam focal position (which defines the image plane extent) is everywhere below the projected aperture of the system.

The array structure described here may not at first encounter appear likely to lead to low phase errors given the non-dissipative switching mode and consequent poor VSWR in the distributor. The resonant spacing of the antenna elements implies that all are (electrically) equal distant from the source, and the reflected signals are absorbed partly in the directional coupler load and in the source isolators. A signal reflected from an "OFF" antenna will always appear in the same relative phase to an "ON" antenna, regardless of such an antenna's position within the array. Attempts to reduce array insertion loss by increasing distribution slot coupling are likely to introduce series resistance elements into the shunt component model[89] and subsequent amplitude and phase taper across the array would be less suited to synthetic aperture use.

AII.2 Microwave Source

In view of the considerable losses in both transmitting and receiving arrays due to the complex signal modulation process, the microwave source was operated far above its rated voltages in an effort to increase the available power . A low power Varian klystron rated at 25-50mW (continuous wave) and intended for local oscillator service in radar equipment was made to deliver approximately 200mW. Forced air cooling was necessary and the klystron was mounted on a substantial heatsink. The anode potential was increased from the rated 250V to 450V. A number of similar devices were kept (pre-tuned) as spares, but no failure or reduction in radio-frequency power, as monitored by mixer bias current levels, was noted over approximately 300 hours of operation.

AII.3.1 The Microwave Mixer

The requirement for complex data representation of the hologram specified a two channel receiver to process the low level sum frequency signals from a pair of microwave mixers whose reference signals were in time quadrature and input signals were in phase. As the modulation process at transmitting and receiving antennae generated a variety of different frequency components in addition to that at the required sum frequency, a balanced mixer was indicated to optimise the rejection of unwanted components. The separation of signal and reference components was by conventional hybrid junctions (Fig.AII.4(a)) and signal distribution was by H-plane junctions, leading to cophasal signal components at all 4 mixer diodes. A slotted line signal sampler could be mechanically adjusted to ensure the quadrature reference field condition.

The mixer diodes (IN23C) were initially selected for equal response and impedance at a given bias current level of 200μA. The total available reference power was 2mW, and this was derived directly from the source via a 20.3dB directional coupler. Individual transresistance amplifiers incorporated feedback resistors so that mean voltage level and hence signal sensitivity could be equalised without affecting bias current or the waveguide to diode impedance match.(Fig.AII.4(b)) Signal subtraction after the transresistance amplifiers was by two identical , bifilar wound transformers, and the secondary outputs incorporated attenuators to compensate any remaining I and Q channel imbalance in amplitude.

AII.3.2 Phase and Amplitude Errors in the Mixer

The mixer diodes are taken to operate in the square law region. The subtraction of the outputs of a balanced mixer amounts to multiplication of the input and reference signals. If the input signal is:

$$f_{in}(t) = V_1(1 + a\cos\omega_s t).\cos(\omega_o t + \theta) \quad \text{------ AII.1}$$

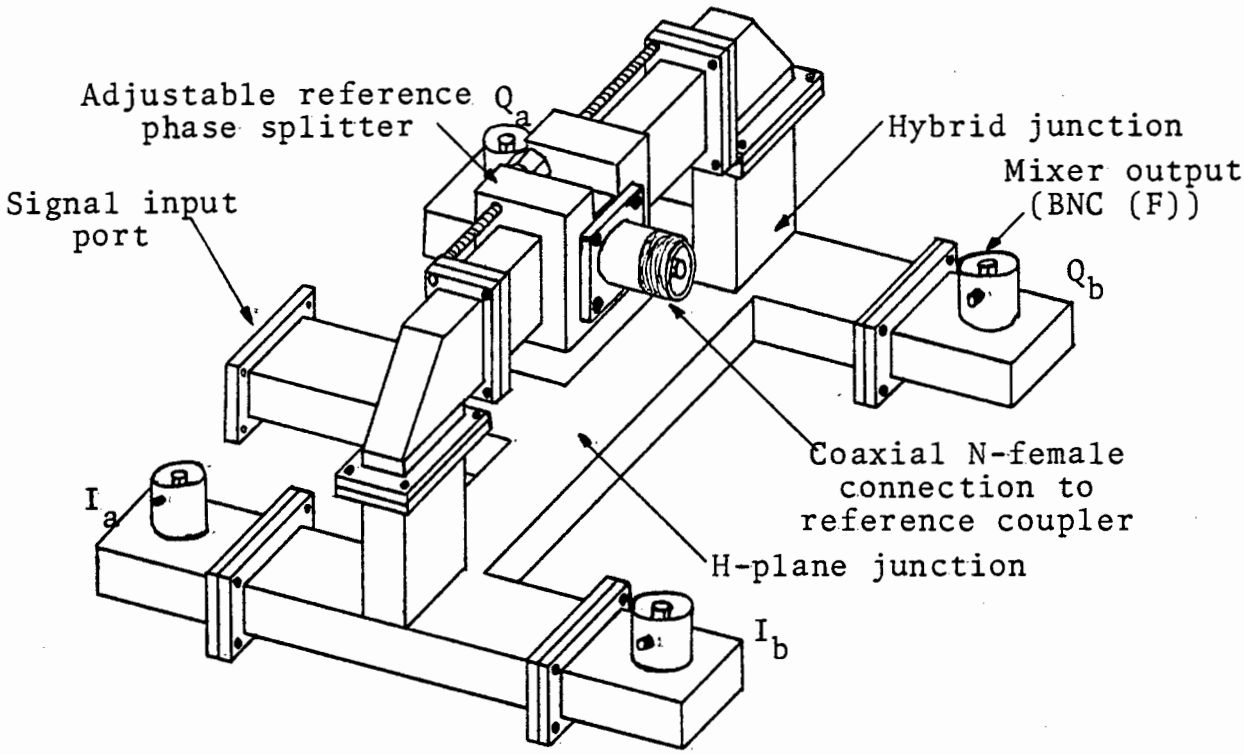

Fig. AII.4(a) Waveguide double mixer assembly

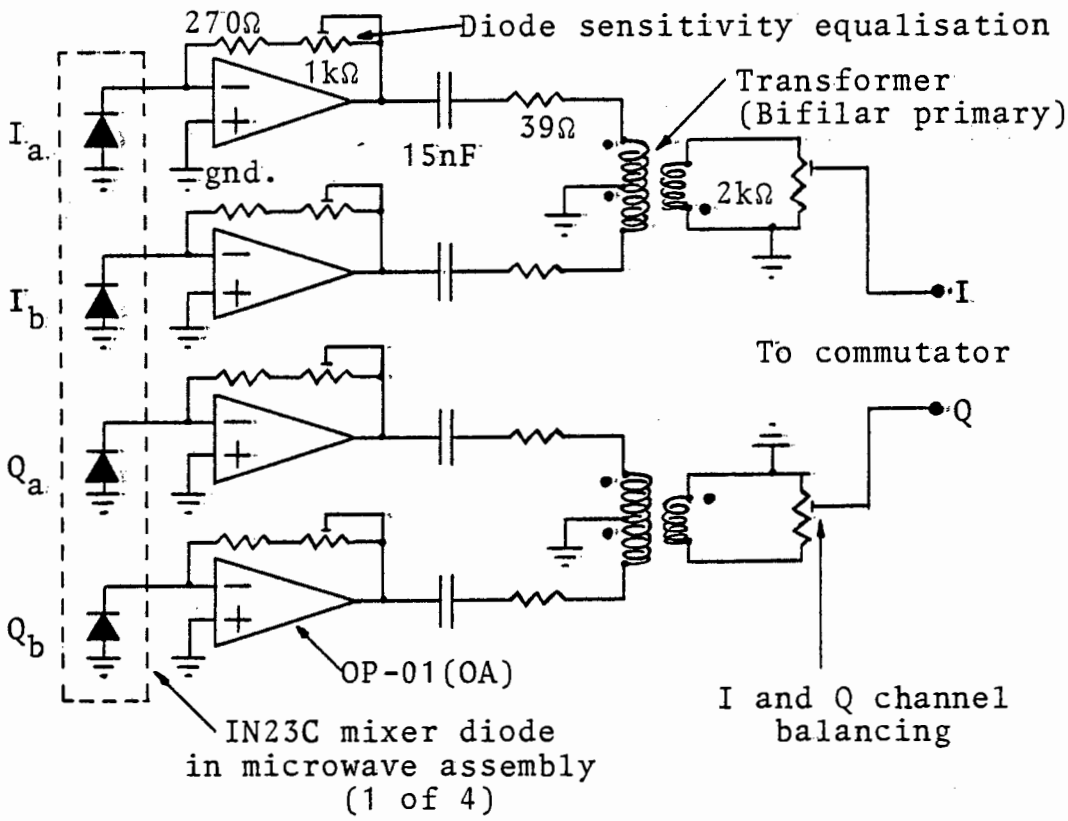

Fig. AII.4(b) Post-mixer signal combination

and the reference signal is:

$$f_{ref}(t) = V_2\cos(\omega_o t + \phi) \quad \text{---------- AII.2}$$

where: ω_o = 2π. 9.9GHz.,

ω_s = 2π. 336.9kHz,

θ = signal phase, ϕ = reference phase, and the factor a indicates the efficiency of the modulation process. The mixer output component at the frequency ω_s, the sum of the fundamental frequencies of the tonebursts applied to transmit and receive antennae, is:

$$f_I(t) \propto aV_1V_2\cos\omega_s t \,.\, \cos(\theta - \phi) \quad \text{-------- AII.3}$$

If the reference field is shifted $\pi/2$ radians at the other mixer, the Q component output is simply:

$$f_Q(t) \propto aV_1V_2\cos\omega_s t \,.\, \sin(\theta - \phi) \quad \text{-------- AII.4}$$

The same constant of proportionality is assumed, since this can be adjusted using the circuitry of Fig.AII.4(b). The amplitudes of the modulated I and Q components were extracted by synchronous detection, and the polar representation of the received signal follows from Euler's identity. The amplitude becomes aV_1V_2, and the phase is $(\theta - \phi)$.

In practice, amplitude imbalance and phase errors arise in mixer calibration. Ideally, the two(baseband) signals I and Q are given as: $(I,Q) = R(\cos\alpha,\sin\alpha)$. R is the amplitude, and α is the phase difference $(\theta - \phi)$between input and reference signals. Assuming that the reference in one mixer is in relative error by ψ radians and ε fractional amplitude, then the complex description of the reference field is multiplied by a factor $(1 + \varepsilon)e^{-j\psi}$. Hence:

$$(I,Q) = R(\cos\alpha, \sin\alpha) + R(0,\varepsilon\sin\alpha) + R(0,(1+\varepsilon)\sin\psi\cos\alpha) \quad \text{- AII.5}$$

The ratio of the unwanted and wanted components is:

$$\text{Ratio(unwanted:wanted sequence)} \doteq \left(\left(\frac{\varepsilon}{2}\right)^2 + \left(\frac{\sin\psi}{2}\right)^2\right)^{\frac{1}{2}} \quad \text{AII.6}$$

As an example, 10^o(.17 radians) and 20% amplitude error leads to a field conjugate to that of the wanted field and at a relative level of -18dB.

The required focussed image will, at worst, be found against a background of the diffuse conjugate field, and the relative amplitude will be greater than that measured at the hologram, and will depend on the object and holographic system geometry. The contrast of wanted image and unwanted background components arising from the conjugate hologram data can be illustrated for a point object if the reconstruction process is followed for both components. Initially equal amplitude wanted and unwanted hologram data are assumed-this corresponds to a reconstruction based on bipolar real data. A hologram aperture of area $XY(m^2)$ is considered to be generated by the orthogonal array system and the paraxial approximations are made. The reconstruction operation is, from sec.3.3 :

$$F(u',v') = \int_Y \int_X f(x,y).e^{\frac{-jk}{2z'}((x-u')^2+(y-v')^2)}.dxdy$$

The image and hologram plane coordinates are (u',v') and (x,y) respectively. The hologram data is taken as:

$$f(x,y) = \cos(\frac{k}{2z}(x^2 + y^2))$$

An object point on axis and at a range of z has been assumed. Real data hologram corresponds to equal amplitude of wanted and unwanted complex data. The approximate amplitude of the diffuse component is found using a stationary phase approach, and retaining only the amplitude of the result.[103] The contrast expressed as field amplitude ratio is:

$$\frac{\text{Focussed image component}}{\text{Diffuse background component}} = \frac{2XY}{\lambda z} \quad \text{---------- AII.7}$$

In the special case of real bipolar hologram data considered here, eq.AII.7 would also indicate the ratio of field amplitudes in the real and virtual image pair, where one of these has been reconstructed against a diffuse overlay of the other. The imaging mode survey of the arrays had X=.6868m, Y=.5858m λ=30.3mm and z=1.9m, and the image contrast ratio in addition to the inherent measured discrimination of the two channel receiver is approximately 23dB, so that the incomplete antennae isolation is a relatively more serious contributor to antennae phase and amplitude errors.

The contrast ratio is comparable with that found by Fargan and Newsome[128] in their analysis of the passage of wideband linear frequency modulated pulses through matched and conjugately mismatched filters. Their result for the ratio of outputs of matched and mismatched (one dimensional) filters is simply (2.Time-bandwidth product)$^{\frac{1}{2}}$. The spatial bandwidth of the hologram is $X/\lambda z$ m^{-1}, and duration corresponds to aperture dimension X. Including a second orthogonal axis of aperture Y, the same result for image contrast is obtained.

Most objects of interest will be composed of multiple point scatterers or will be of extended nature, and applying the principle of superposition, the image to background contrast will be less since the separate diffuse background attending each image point will be to a very large extent coincident.

AII.4 Post-mixer Signal Processing

AII.4.1 Sum Frequency Amplifier and Synchronous Detector

The I and Q mixer outputs were switched in turn to the input of a variable gain narrowband amplifier. The commutator was implemented using standard CMOS bilateral switches (type CD 4066) in a series changeover configuration. The feedthrough of higher order harmonic components of the switching frequency was minimised by briefly short-circuiting the commutator output during the changeover interval. The system clock frequency of 1.685kHz was derived by division by 200 of a signal phase-locked to the synthesised sum frequency reference. (Fig.AII.5(a)) The clock frequency was further divided by 4 to produce 421Hz and the antennae were switched at this rate. A given antenna pair was thus active for 2.374mS, and the first two periods of 594μS each were allocated to estimation of the I and Q signal components.(Fig.AII.5(b)) The phase-locking stratagem ensured that commutation frequency harmonic feedthrough gave rise to only direct voltage offsets in the demodulation stage, and the further use of the subtractive holographic mode (sec.5.3) removed even these components.

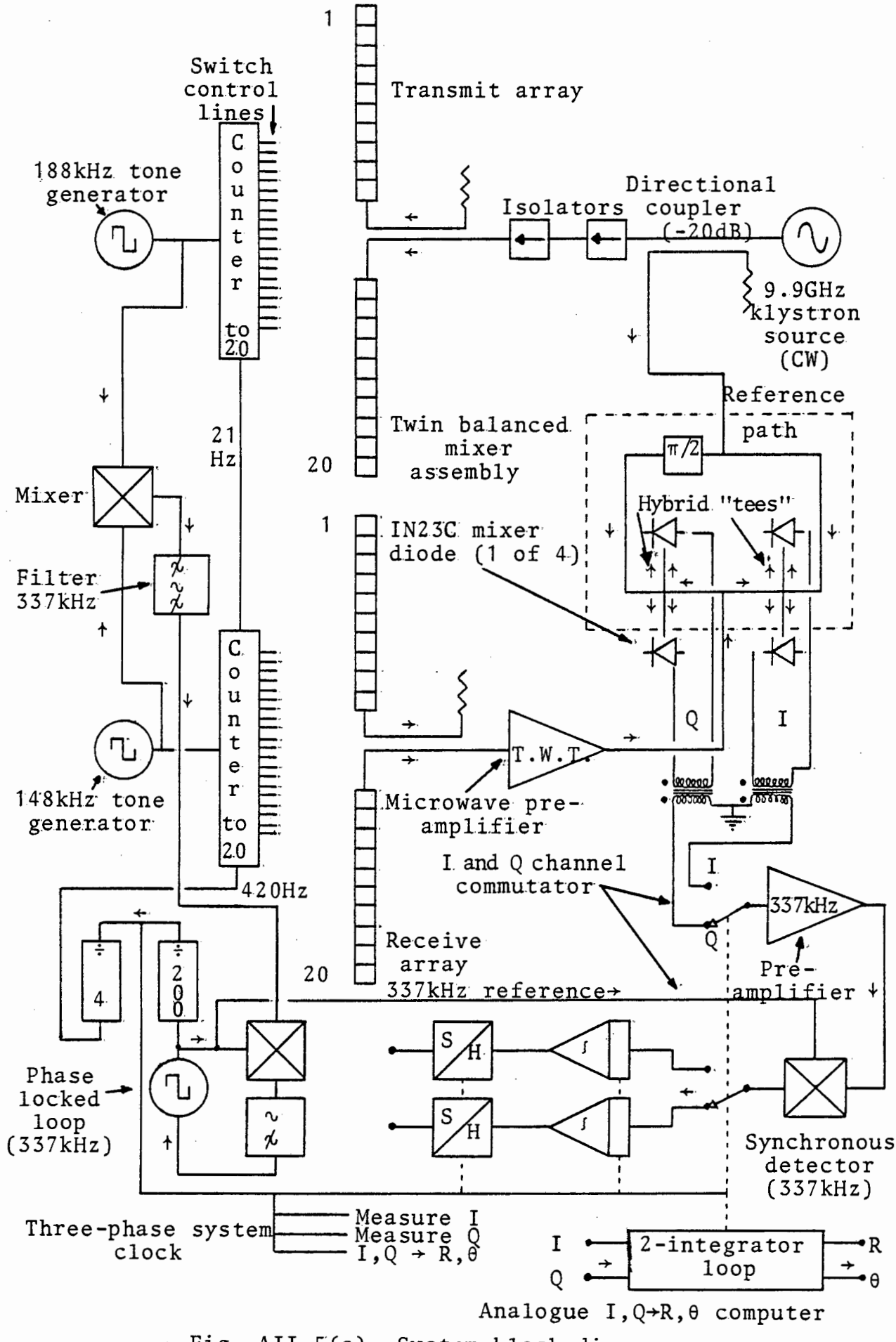

Fig. AII.5(a) System block diagram

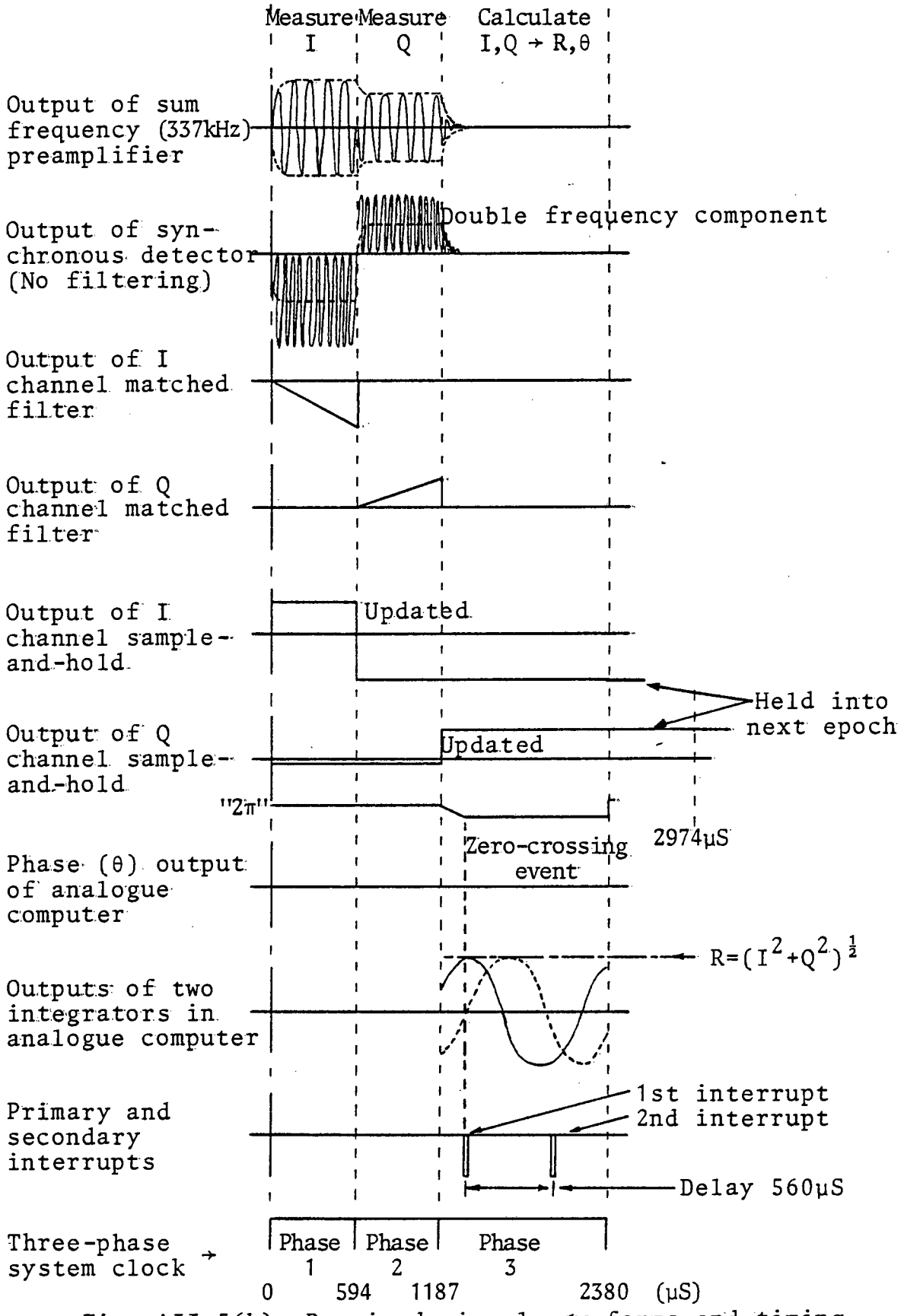

Fig. AII.5(b) Received signal waveforms and timing

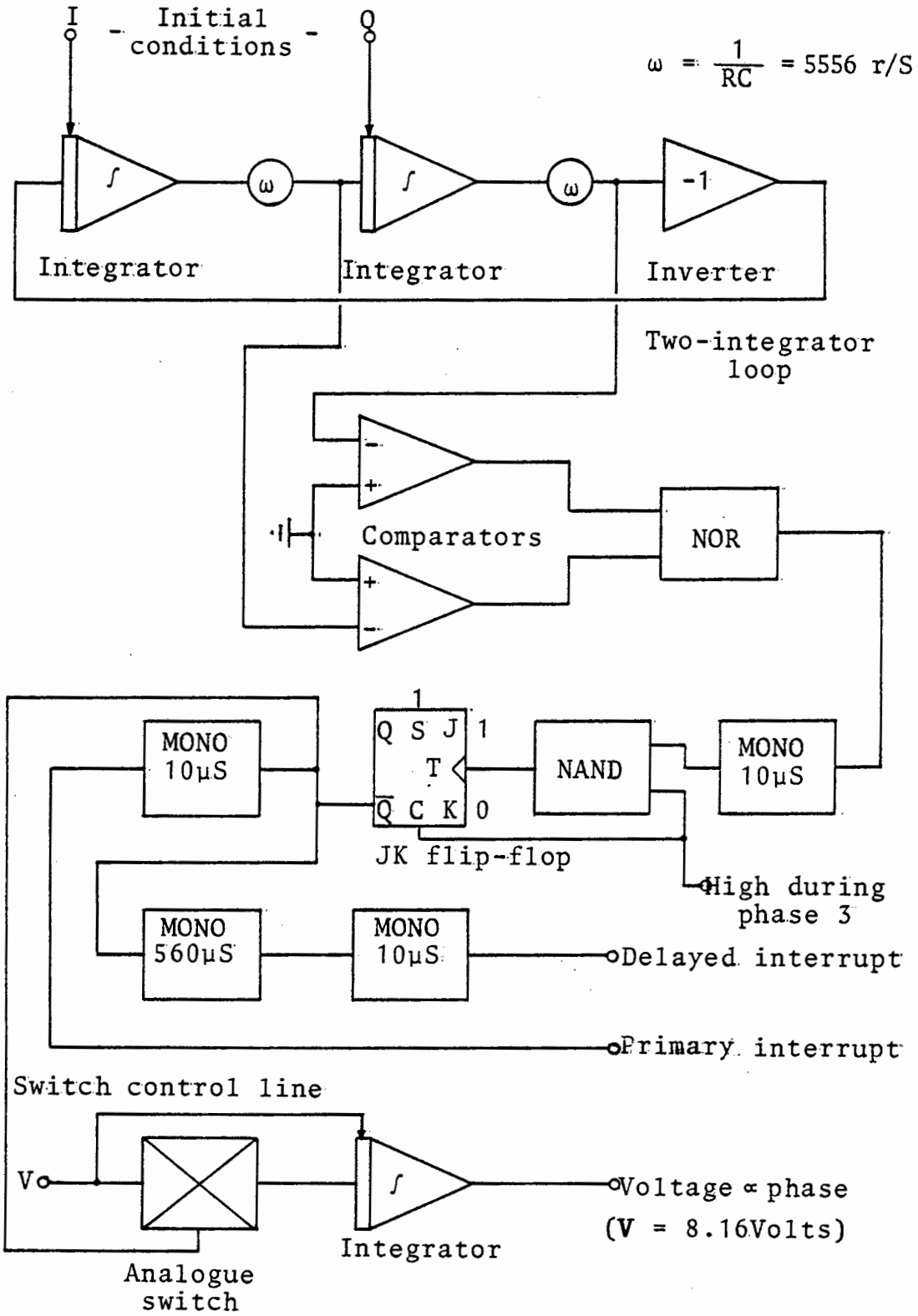

Fig. AII.5(c) Analogue computer block diagram

The latter procedure was repeatedly observed to be effective down to the system noise level in removing all offset voltages common to the two mapping stages.

The preamplifier was implemented as a cascode configuration using linear integrated circuits (type MC 1550G)and the gain was variable manually from 21.4 to 75.4dB in a 4kHz bandwidth centred at 336.928kHz. Normal operation was with a 60dB gain setting.

The synchronous detector was designed around a 4-quadrant variable transconductance multiplier (type MC 1495L) ,, and required a 2.8V r.m.s. sinusoidal reference signal derived from the filtered output of a logic gate whose inputs were the two antenna array toneburst frequencies 148.327kHz and 188.601kHz. These frequencies were in turn derived from two crystal controlled oscillators. The sum of the two frequencies was chosen as the processor carrier as bandpass filtering was more simply performed at the sum than at the difference frequency.

No explicit bandlimiting was performed in the synchronous detector, but the following stage comprised two parallel operational integrators. Since the received signal suffers essentially no delay and its duration is known, a linear matched filter is simply implemented by controlled integration. No separate commutator was required here as the FET reset transistor across the integrating capacitors performed this function. The I-component integrator was active from 0 to 594μS and the Q-component was found during the epoch 594 to 1187μS. The integrator outputs were both tracked by sample-and-hold devices (type LF 394) and the peak value, updated just before reset,, held until the following antenna pair epoch.

The sum frequency amplifier bandwidth of 4kHz was adequate for an early system[37] which had the entire antenna epoch of 2.5 mS available for a single component (I or Q, but not both) measurement. The limited bandwidth and extended impulse response implied "leakage" into the Q-epoch of I-epoch information. Since the dynamic range performance required at this

stage is very high (a Q estimate of zero is as significant as a maximum value), and extending bandwidth is an ineffective way of reducing this effect, a compensation procedure was sought. The amplifier is modelled as an underdamped second-order system and together with the following synchronous detector, has an overall "baseband" impulse response of :

$$h(t) = e^{-\frac{Rt}{2L}} = e^{-\frac{\omega_o}{2Q}t}$$ where: $\omega_o = 2\pi.336.9\text{kHz}$,
$Q = \omega_o/\Delta\omega$,
and $\Delta\omega$=bandwidth.

If the synchronously detected low frequency I component has unity amplitude, then the matched filter output is proportional to:

$$\frac{1}{T_0}\int_0^{594\mu S}(1 - e^{-\alpha t})dt = 0.873$$

The factor $\alpha = \omega_o/2Q$. The corresponding contribution of the I-component "leakage" into the Q-epoch filtered output is:

$$\frac{1}{T_0}\int_0^{594\mu S}(e^{-\alpha t})dt = 0.127$$

The process linearity implies that a constant fraction of the integrated I-filter output is "leaked" into the integrated Q-filter output. However, this is exactly the same effect as that produced by a non-orthogonal mixer reference field pair. (eq.AII.5) It implies that the compensation can be performed by purposely slewing the reference field pair's relative phase relationship. The phase adjustment needed is simply:

$$\text{Phase compensation} = \tan^{-1}(0.127/0.873) = 8.3^{o}$$

The complementary effect whereby Q_i components "leak" into a succeeding I_{i+1} epoch is entirely negligible, by virtue of the intervening dead time allocated to the analogue amplitude and phase processor.

AII.4.2 Analogue Amplitude and Phase Computer

The analogue phase and amplitude processor was originally intended to facilitate numerical reconstruction from phase-only data holograms, but in the event it proved more effective to use the component I and Q field data and a subtractive mode of hologram preparation.(sec.5.3) The analogue processor

did prove invaluable in the assessment of hardware as this was built and made possible a tomographic mode of microwave imaging. (Appendix III)

The processor was based on a two-integrator loop[90], where the mean I and Q components were loaded as initial conditions using summing amplifiers ahead of both integrators. After the end of the period allocated to Q component recovery, the loop was allowed to oscillate just more than one cycle of its natural frequency of 884.2Hz. A comparator detects the first positive-going zero crossing of the sinusoidal waveform at an integrator output and simultaneously generates a negative logic interrupt pulse intended to signal the Varian mini-computer to acquire data connected to one of its I/O channels. (Fig.AII.5(c)) The amplitude $R = (I^2 + Q^2)^{\frac{1}{2}}$ is that of the peak output of the second integrator. Also at this time, the output of an integrator set to have an initial output voltage analogous to 2π radians is sampled and this integration process halted. The result is an analogue direct voltage in the range 0 to 8.16 volts representing 0 to 2π radians of signal phase. A flip-flop memory element ensured that only one interrupt per computation cycle was possible. The computer dynamic range extended over two decades (40dB) and could accept component pairs leading to a maximum amplitude R of 7 volts, while at the other extreme a 70mV signal was subject to a 7^{o} (0.12 radians) maximum phase error. Linearity of the phase output was determined in practice by the microwave mixer calibration rather than by the analogue processor itself.

AII.4.3 Interface to Varian Computer

Some additional digital circuitry was necessary before operational use. A manually-operated switch signalled the start of data acquisition. The switch output was verified by a debouncing circuit, and after the recognition of the (1,1) antenna pair epoch, interrupt pulses appeared at the computer I/O interface continuously. Since two components I and Q constituted a single complex field measurement, the first

interrupt pulse originating in the analogue processor was followed by a second 560μS later. In the interim, a FET switch connected the Q sample-and-hold output to the analogue to digital convertor input. Suitably long delays were incorporated in the changeover switch to allow adequate settling of each output. This process delivered 800 interrupts per field (corresponding to components $I_1, Q_1, \ldots\ldots I_{400}, Q_{400}$) and software was used to demultiplex the components and to truncate the data stream after the desired number of fields. This arrangement was operationally convenient (requiring only two cable connections between the microwave system and the computer) and a necessary procedure in the case of suspected object motion, where field-sequential component data capture is meaningless.

AII.4.4 Motional Phase Errors in Sequential Processing

The sequential use of the sum frequency amplifier and following detector assured the tracking of transfer functions of both receiver channels irrespective of the manual gain setting of the amplifier and any parasitic phase shifts caused by such gain changes, but did cause an apparent error in reference orthogonality in the presence of object motion. For the purposes of discussion, the receiver is considered to be a matched two channel system with a 594μS delay incorporated in the Q channel. (Fig. AII.6)

Compared with an I component of a signal reflected from a stationary object, that derived from a signal Doppler shifted by ω (radians/second) will have an approximate relative amplitude $\cos\omega t.\mathrm{sinc}(\omega\tau/2)$. The quadrature channel will have an output $\sin\omega(t-\tau).\mathrm{sinc}(\omega\tau/2)$, where τ is 594μS. The analytic signal representation of the I and Q outputs is:

$$I + jQ = \mathrm{sinc}(\omega\tau/2)(e^{j\omega t}(1+e^{-j\omega\tau}) + e^{-j\omega t}(1-e^{j\omega\tau}))$$

For small ωτ, an approximate ratio of the positive and negative sequence components is just $2/\omega\tau$. Since ωτ has the dimensions of phase (that is, none) the ratio so derived is

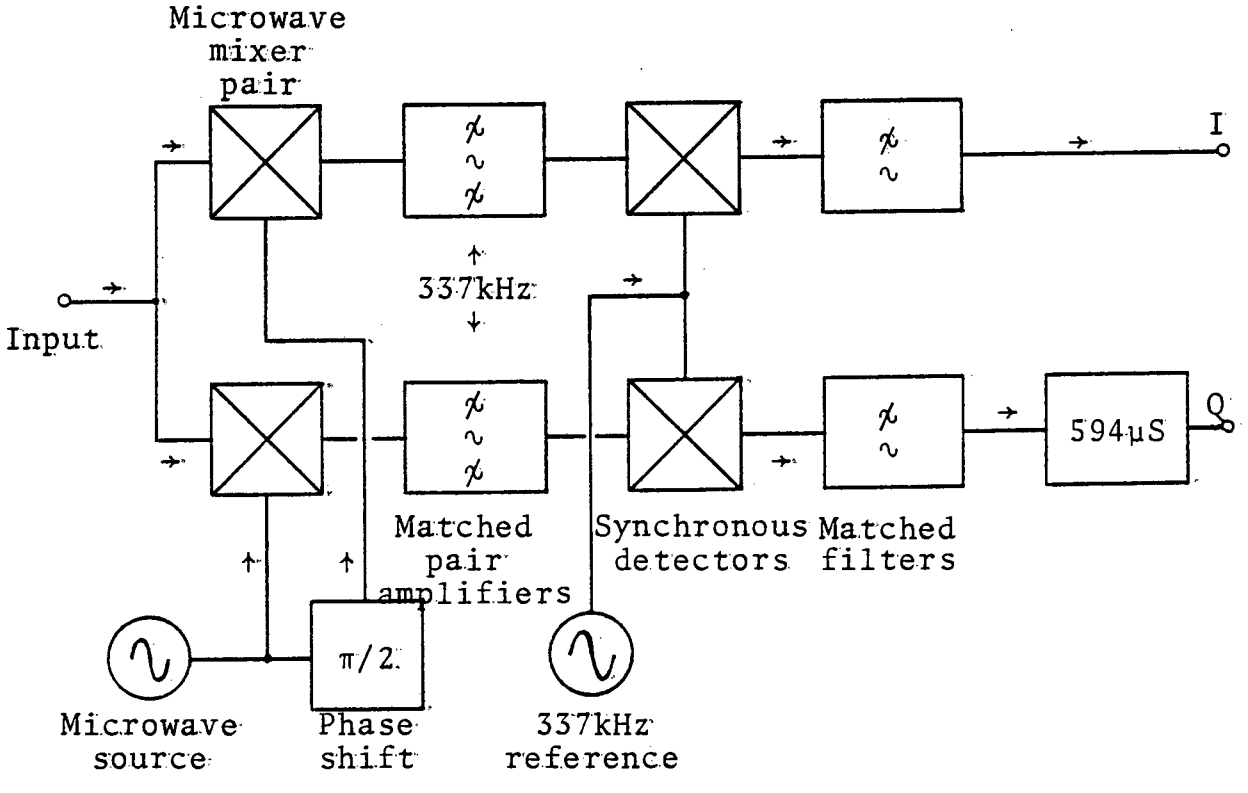

Fig. AII.6 On the equivalent two channel receiver

of the same form as that due to an error in phase orthogonality or amplitude imbalance of the mixer references.(sec.AII.3.2)

AII.5 Network Analyser Mode and Measurements

The basic analogue signal processor could be used alone with simple horn antennae replacing the transmitting and receiving arrays as a single frequency network analyser to monitor the performance of components developed and considered for development in the imaging system.

AII.5.1 Mixer Alignment

The hardware arrangement of Fig.AII.7(a) had an unmodulated source and the cooperative target device reflected essentially DSBSC modulated signals. The arrangement was initially used to align the mixer and the analogue processor phase output is shown in Fig.AII.7(b) adjusted for optimum linearity. To a first approximation, the orthogonality error in phase causes a sinusoidal perturbation in perceived phase, and a fit to the data of Fig.AII.7(b) reveals no more than 4^{o}(67mRads.) residual equivalent phase error. This would correspond to a conjugate hologram field accompanying the desired complex data hologram with a relative amplitude of -30dB.

AII.5.2 Antenna Phase Centre Location

The location of the apparent centre of radiation of the standard waveguide switch and antenna element was found by selecting a centre of azimuthal rotation which yielded least change in measured path phase with rotation of the device. The result indicated a phase centre 8mm behind the aperture in the electric field plane, and between 1mm and 2mm in the magnetic field plane when rotated in elevation. The difference was hardly significant given the depth resolution of the system, and in practice object-to-aperture plane ranges were taken to the antenna aperture.

Fig.AII.5 Microwave mixers

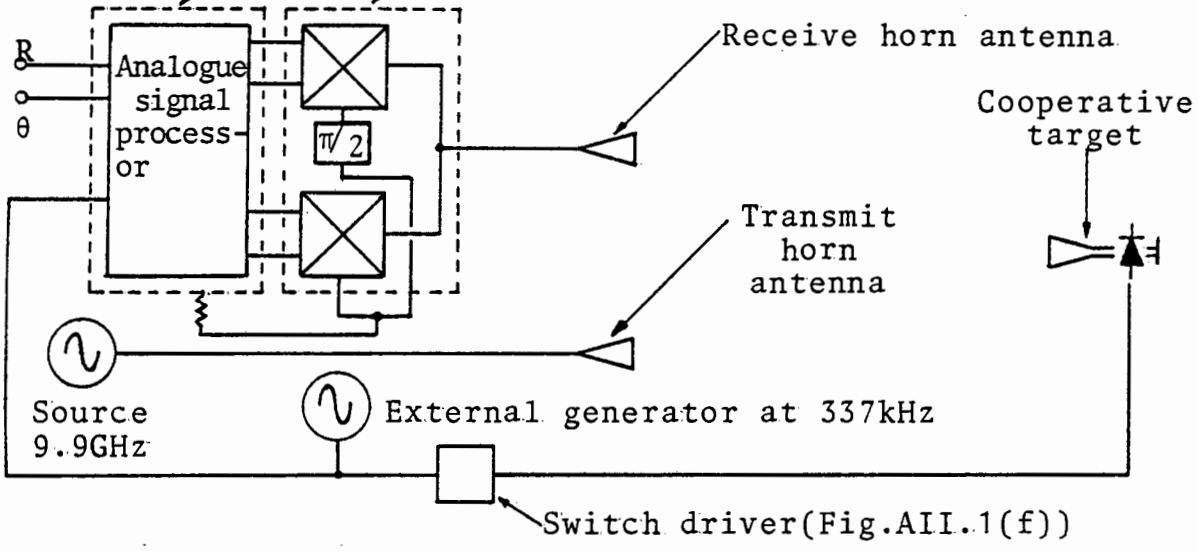

Fig. AII.7(a) Network analyser mode

Fig. AII.7(b) Alignment of the microwave mixer

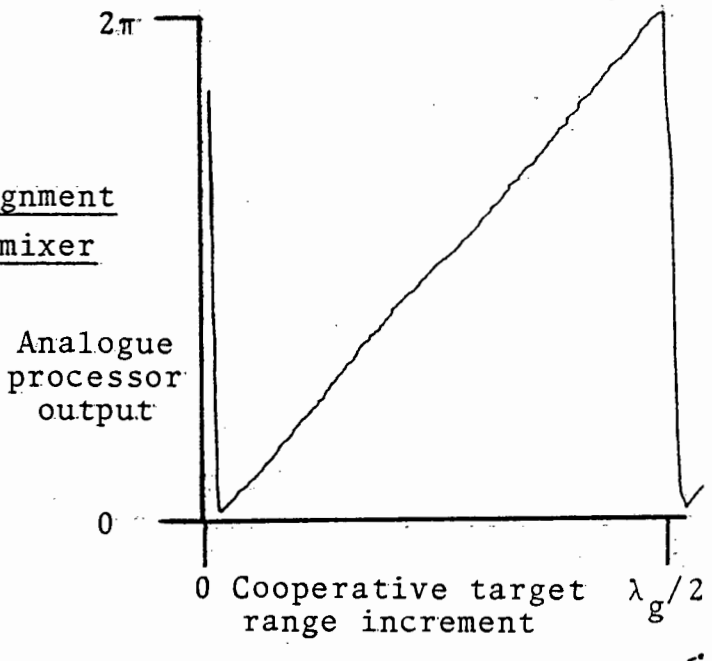

Fig. AII.7(c) Analogue microwave phase shifter

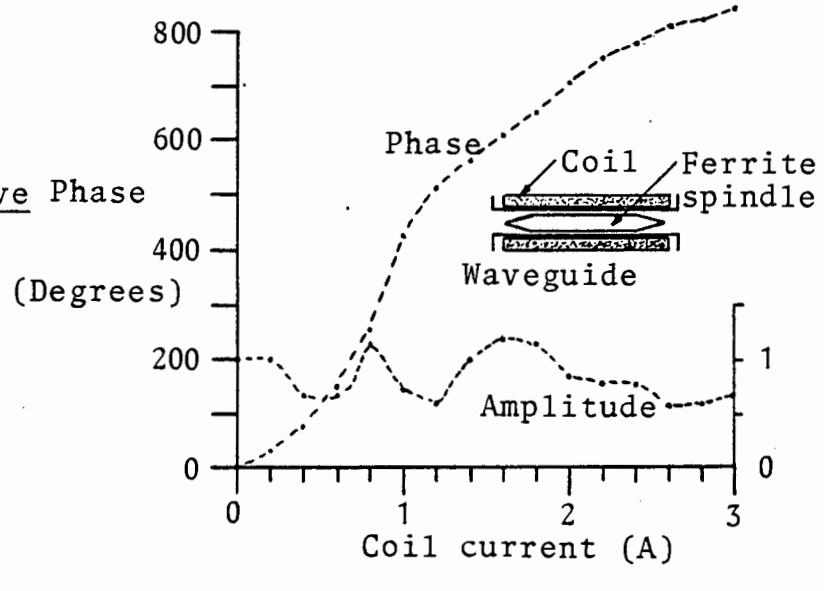

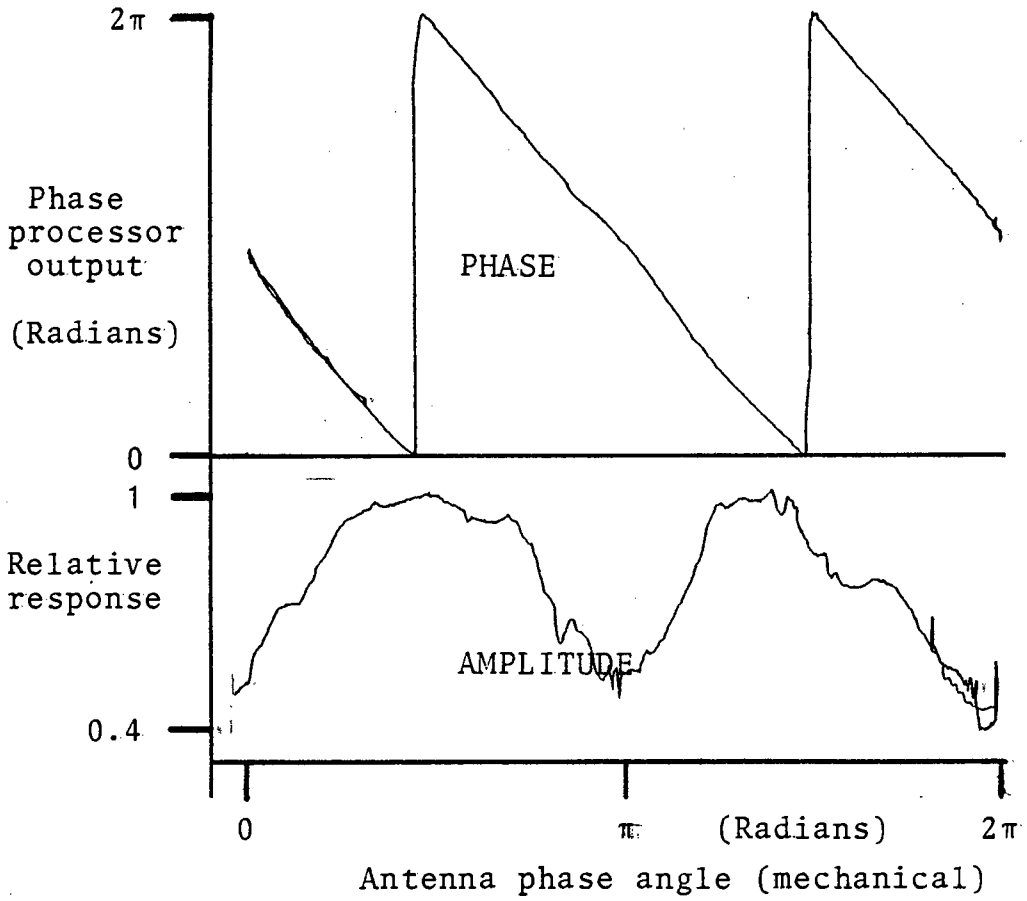

Fig. AII.7(d) Measurements on a helical antenna

AII.5.3 Analogue Microwave Phase Shifter

At an early stage of development, an analogue phase shifter operating on the principle of the Regia-Spencer device[129] was built to evaluate the possibility of using a single microwave mixer with a reference field switched in phase sequentially. This would have simplified the microwave mixer whilst retaining the existing analogue processor, but in the event the device failed to have adequate switching and settling time, despite all the precautions taken such as longitudinal slitting of the waveguide. Fig.AII.7(c) shows the differential phase shift and relative amplitude obtained with the device inserted in the cooperative target signal path and used in the reflection mode. The range of phase shifts shown would be halved in a transmission device. In practice, such a device would best be employed in the receive path to avoid mixer termination disturbance with varying reference levels. Insertion loss is not a serious problem given amplification ahead of the mixer, and hysteresis effects are easily avoided by resetting the ferrite magnetically just before every change of status.

AII.5.4 Helical Wire Antennae

An early deployment had helical wire antennae as radiating elements.[37] A distinct advantage of the type was the direct adjustment of phase shift by mechanical rotation of the body of the antenna which was a 6-turn reflector backed helix of constant radius. The array was not further developed because of the poor mechanical reliability. The 2:1 ratio between differential electrical phase shift and mechanical phase angle is obvious from Fig.AII.7(d). For this test, the antenna was terminated with a commutated diode switch based on coaxial line technology. The amplitude response shows considerable fluctuation the peaks of which coincided with the truncated radiator lying parallel to the incident field vector. Nested spiral circularly polarised antennae switched by PIN diodes

have been mooted in at least one phased array radar, in which these elements formed a variable phase reflector surface.[130]

Appendix III

Phase Object Imagery via Microwave Tomography

Transmission tomography using X-ray illumination has within the last decade developed into a mature technology.[131] Numerous applications of non-invasive plane imagery have been identified in medical diagnosis, and the significance of the technique has been recognized by the award in 1979 of a Nobel prize in Physics shared by Allan Cormack[132] and Godfrey Hounsfield.

AIII.1 The Motivation for Microwave Tomography

The commissioning of the analogue signal processor incorporated in the microwave holographic imaging system of this thesis presented the opportunity to exploit tomographic principles in the imaging of a type of object not practically accessible to microwave holography. By analogy with optical and acoustic practice, an object characterised by transmission approaching unity and a real dielectric constant a little greater than unity, is referred to as a "phase object". It was felt that measuring the small changes in total path length as differential phase shifts between a compact source/receiver and a cooperative target straddling the object region might well demonstrate high contrast imagery.

Microwave tomography might at first seem to be somewhat divorced from the primary theme of this thesis, but there are close links with aperture synthesis techniques, inasmuch as the fan-beam impulse response characteristic of a long linear array can be reduced to a pencil-beam response suitable for extended source mapping. Rotation of a linear array through 180^{o} (the array may possess physical aperture or may be generated by aperture synthesis) synthesises a rotationally symmetric aperture in the same way that rectangular aperture was developed by linear array translation.[133]

Tomographic techniques were, in fact, applied in all but name to the radioastronomical problem of reconstructing two-dimensional source brightness distributions from fan-beam scans taken at various aspect angles.[134] In the field of active radar astronomy similar techniques have been used to generate lunar radar reflectivity maps. A reflected continuous wave emission contains information relating to a particular area's reflectivity coded by the Doppler shift frequency resulting from lunar rotation. This technique is referred to as "supersynthesis".[103]

AIII.2 Principles of Tomography

The principles of tomographic imaging will be developed with the X-ray system as an example, although it is significant that the mathematical basis leading to the system impulse response, Fourier frequency domain reconstruction and the appropriate compensation schemes were developed by Bracewell and Riddle in radioastronomical context.[134]

Consider an object whose absorption at a point (x,y) is f(x,y). (Fig.AIII.1) The object extent is bounded and is assumed to be probed by a thin monoenergetic X-ray "ray-bundle". Source and receiver are fixed relative to each other and are translated past the object region at various angles θ to the object coordinate system. The intensity measured at R is $I_\theta(x')$:

$$I_\theta(x') = I_o \exp\left(-\int_S^R f(l)\,dl\right) \quad \text{-------- AIII.1}$$

The line integral is taken between source S and receiver R. (x',y') are rotated coordinates, such that:

$$\begin{vmatrix} x' \\ y' \end{vmatrix} = \begin{vmatrix} \cos\theta & \sin\theta \\ -\sin\theta & \cos\theta \end{vmatrix} \begin{vmatrix} x \\ y \end{vmatrix} \quad \text{---------- AIII.2}$$

I_o is the source intensity in object absence. Clearly such a measurement performed continuously along x' discards object position data in the direction RS; the measurement series forms a projection of the function f(x,y) at an angle θ. Such projections are taken for granted in single aspect X-ray radiography. It is intuitively obvious that if every point

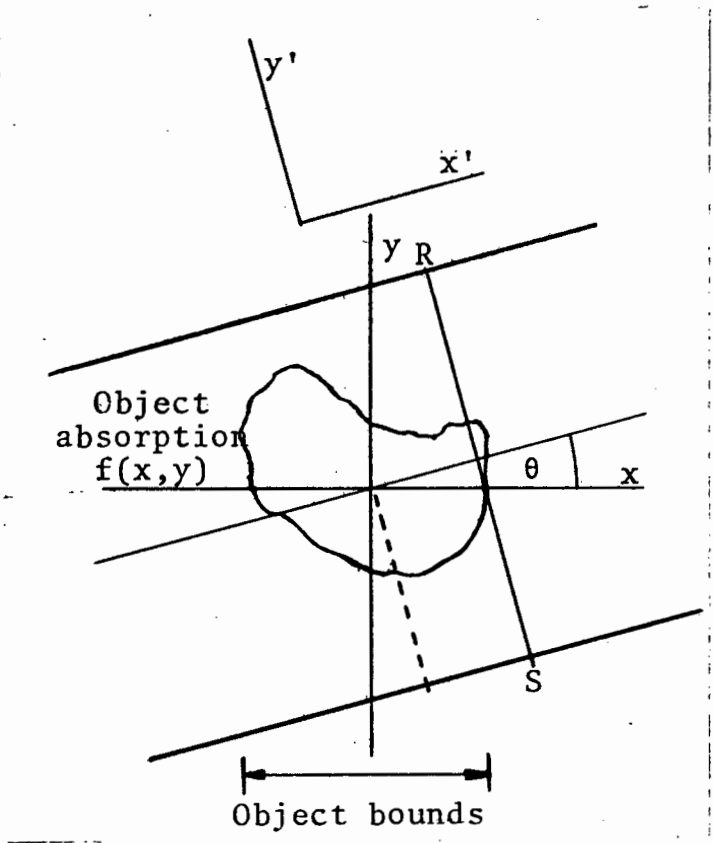

Fig. AIII.1 Generating projection data

in the object region could be made in turn the centre of object rotation (with respect to fixed source-receiver coordinates x',y') then that point's absorption could be measured albeit in the presence of motion-blurred and lower level data from regions outside the centre of rotation. The blurring could be reduced with increasing radius of rotation. Such systems are considered practical, and several such developments using purely analogue reconstruction have been reported by Barrett and Swindell[135] and Lindegaard-Andersen and Thuesen.[136]

Methods of image reconstruction from projection data fall into two general catergories; these are algebraic(ART) and filtered backprojection. ART reconstructions are based on iterative techniques and will not be considered here. The second technique is based on Fourier spatial frequency domain representation, although reconstruction is normally more efficiently performed by the equivalent data-domain operations. Fig.AIII.2 exemplifies unfiltered backprojection formation and summation to form an image from a finite projection data set. It is clear that the unfiltered backprojection-and-summation results in non-zero image amplitude outside the object boundaries; any point object will be imaged as a maximum density region surrounded by a spoked sidelobe region. In the limit of a large number of projections this leads to a radially symmetric and monotonically diminishing impulse response.

From eq.AIII.1 the projection data are:

$$f_\theta(x') = -\ln\left(\frac{I}{I_o}\right) = \int_{-\infty}^{+\infty} f(x',y').dy' \quad \text{------- AIII.3}$$

The quantity is assumed to be of limited extent. The backprojection data is obtained by extending $f_\theta(x')$ in the y' direction:

$$f_{b\,\theta}(x',y') = f_\theta(x') \quad \text{---------- AIII.4}$$

The one dimensional Fourier transform of eq.AIII.3 is:

$$F_\theta(u') = \int_{-\infty}^{+\infty}\int_{-\infty}^{+\infty} f(x',y').e^{-j2\pi u'x'}.dx'dy' \quad \text{AIII.5}$$

where u,v,u',v' are the independent variables of the unrotated and rotated spatial frequency domain respectively.

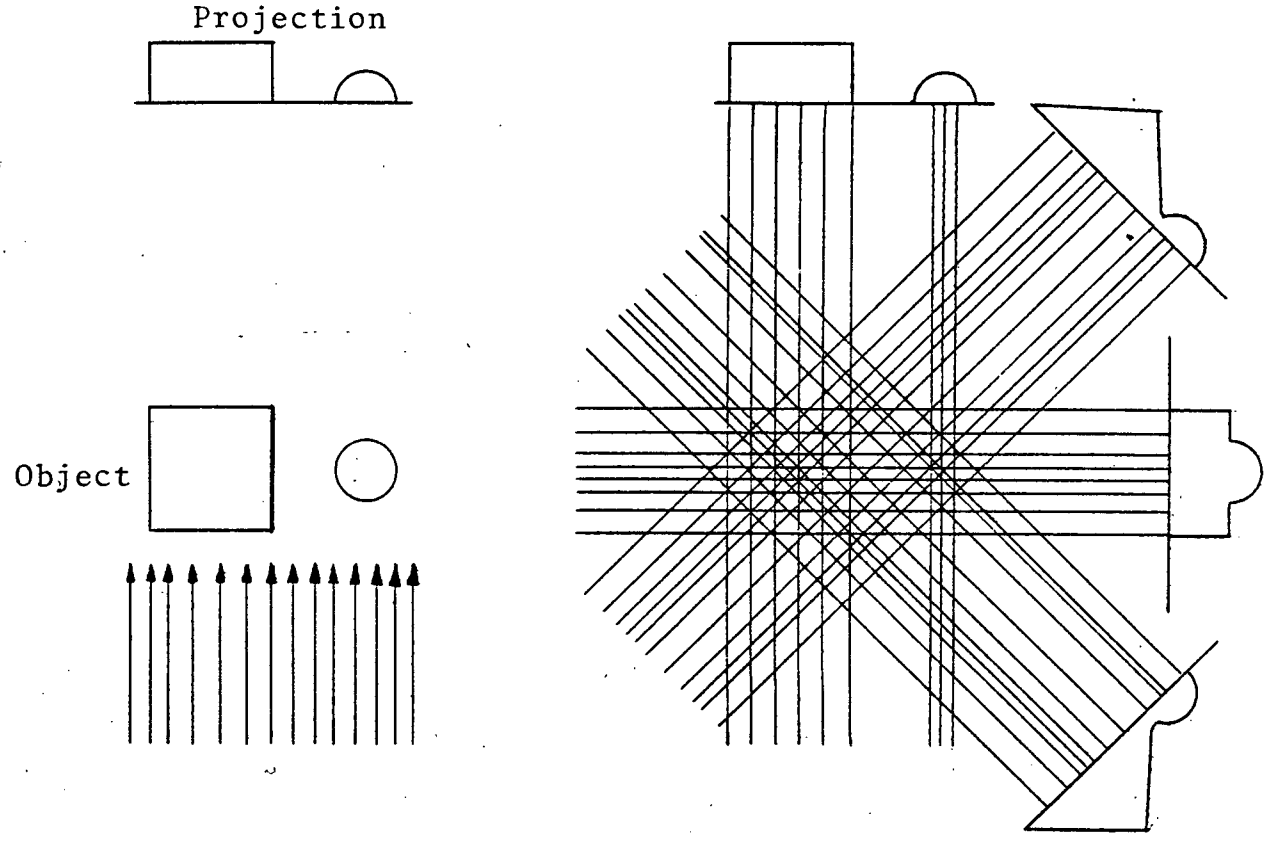

Generation of a projection data sequence

Backprojection of a few data sequences forms a crude image

Fig. AIII.2 Unfiltered backprojection-and-summation image formation

Eq.AIII.5 can also be expressed as a particular case of a general relationship:

$$F_\theta(u') = \int_{-\infty}^{+\infty}\int_{-\infty}^{+\infty} f(x',y').e^{-j2\pi(u'x'+v'y')}.dx'dy' \Big|_{v'=0} \quad \text{AIII.6}$$

In other words, the one dimensional transform of projection data taken at angle θ is the two-dimensional object $f(x,y)$ transform sampled at θ in the spatial frequency plane along the line $v'=0$. This result is generally known as the Central Slice Theorem. This result is intuitively appealing if a cosinusoidally corrugated surface is taken as an object. (Fig.AIII.3) At angles other than those in which the analysing beam traverses the object along a constant section, no periodicity will be noticeable in the object projection. In the spatial frequency domain, the periodicity is expressed by distributions along the line $v'=0$. Recalling eq.AIII.3:

$$f_\theta(x') = \int_{-\infty}^{+\infty} f(x',y').dy'$$

The spatial frequency transform of this projection, using polar spatial frequency ρ is:

$$F_\theta(\rho) = \int_{-\infty}^{+\infty} f_\theta(x').e^{-j2\pi\rho x'}.dx' \quad \text{------ AIII.7}$$

The Central Slice Theorem has been used here. Also:

$$u = \rho\cos\theta$$

$$\text{and} \quad v = \rho\sin\theta \quad \text{------------------ AIII.8}$$

Assembling all such $F_\theta(\rho)$ is equivalent to summing a back-projection continuum. It is sufficient to take a range of projections $0 \leqslant \theta \leqslant \pi$ to cover the complete (ρ,θ) spatial frequency region. Accordingly:

$$f_b(x,y) = \int_0^{\pi}\int_{-\infty}^{+\infty} F_\theta(\rho).e^{j2\pi(\rho x\cos\theta+\rho y\sin\theta)}.d\rho d\theta \quad \text{- AIII.9}$$

The subscript b denotes the backprojected continuum. By comparison, given the object distribution $f(x,y)$, the polar representation of the two-dimensional spatial frequency transform is just:(134)

$$f(x,y) = \int_{-\infty}^{+\infty}\int_{-\infty}^{+\infty} F(u,v).e^{j2\pi(ux+vy)}.dudv$$

$$= \int_0^{\pi}\int_{-\infty}^{+\infty} F_\theta(\rho).e^{j2\pi(\rho x\cos\theta+\rho y\sin\theta)}.|\rho|.d\rho d\theta$$

$$\text{---------- AIII.10}$$

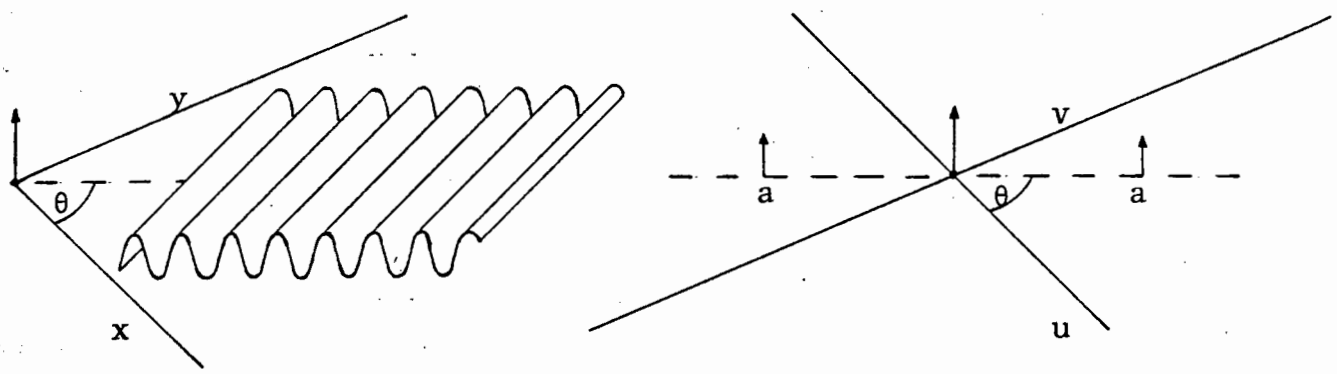

Corrugated object

Object spatial frequency spectrum
(peaks at a)

Fig. AIII.3 On the Central Slice Theorem

Comparing eqs.AIII.9 and AIII.10, the summation of back-projected data results in an image which has been filtered in the spatial frequency domain by a radially symmetric $1/|\rho|$ function. The procedure for reconstruction of a "perfect" image (that is, considerations of finite object size are temporarily neglected) is clearly multiplication of the back-projected data spectrum by a radially symmetric $|\rho|$ function before transformation back to the data domain. The back-projection-and-summation operation is equivalent to convolution of the true object by a function which is radially described by the transformation of $|\rho|$. Barrett and Swindell[135] show that the impulse response of a continuum of integrated back-projections is proportional to 1/R, where:

$$R = (x^2 + y^2)^{\frac{1}{2}} \quad \text{---------- AIII.11}$$

Hence:

$$f_b(\underline{R}) = f(\underline{R}) \otimes 1/R \quad \text{---------- AIII.12}$$

$\underline{R}$ denotes the object position vector whose magnitude is given by eq.AIII.11, and $\otimes$ indicates the convolution operation.

AIII.3 Impulse Response Compensation

It is generally considered necessary to correct the image degradation imposed by the nature of the projection and back-projection-and-summation operations. The radially symmetric ρ-filter $|\rho|$ can be synthesised by cascading two filters.

$$|\rho| = j\rho.\hat{\rho}$$

$$\text{where } \hat{\rho} = -j \text{ -----} \rho>0$$

$$= +j \text{ -----} \rho<0 \quad \text{---------- AIII.13}$$

The "exact" restoration technique involves pre-emphasis of projection data spectrum according to eq.AIII.13; the indicated operation is the derivative of the Hilbert transformation of the data.[137] The Central Slice Theorem allows operation on the one-dimensional data projections. Restoration of the image can thus be performed by two equivalent operations; either by multiplying the transformed data by a radially symmetric "high-pass" filter $|\rho|$, or by differentiating the Hilbert-transformed projection data. In the presence of finite

object spatial frequencies (since any data spectrum will have upper limits imposed by beam and source/receiver geometry) and projection data noise (such as radiation quantum noise and analogue-to-digital converter quantisation noise), this operation may degrade intolerably the image signal-to-noise ratio. Practical processors, whether digital or analogue, have dynamic range limitations which may be imcompatible with accurate differential Hilbert transform data representation. Bracewell and Riddle[134] considered that projection data were bandlimited in such a way that spatial frequencies beyond M (cycles/metre) were absent. In this case, the required ρ-filter is shown in Fig.AIII.4. This filter may be synthesised as:

$$|\rho| = \text{rect}(\tfrac{\rho}{2M}) - \tfrac{1}{M}(\text{rect}(\tfrac{\rho}{M}) \otimes \text{rect}(\tfrac{\rho}{M})) \quad \text{--------- AIII.14}$$

where:

$$\text{rect}(\tfrac{\rho}{2M}) = 1 \text{ -----} \rho < |M|$$
$$= 0 \text{ -----} \rho > |M| \quad \text{---------- AIII.15}$$

The equivalent (data) R-domain operation is a convolution of projection data with a function g(R), where:

$$g(R) = \delta(R) - M\text{sinc}^2(\pi MR) \quad \text{---------- AIII.16}$$

The simplification of the first term on the right hand side of eq.AIII.16 results from the assumption of strictly limited object spatial frequencies, $\delta(R)$ refers to the delta function, and the "sinc" function is defined: $\text{sinc}(x) = \frac{\sin x}{x}$.

The overall correction for bandlimited data is thus subtraction from the data of the data convolved with a low-pass function. This approach does not involve Fourier domain excursions and as the operation is performed before angular integration, it also makes efficient use of the reconstruction processor. There are tomographic beam and source/receiver geometries in which the data is not bandlimited to the extent assumed in the foregoing analysis, and data noise may require the use of an apodisation filter. There is a range of filters reported whose transfer functions approach $|\rho|$ at low ρ but which are rolled off at higher frequencies.[137] One such filter transform pair is shown in Fig.AIII.5.

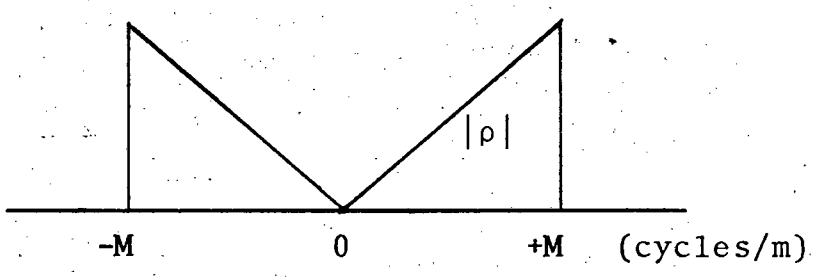

Fig. AIII.4 On impulse response compensation

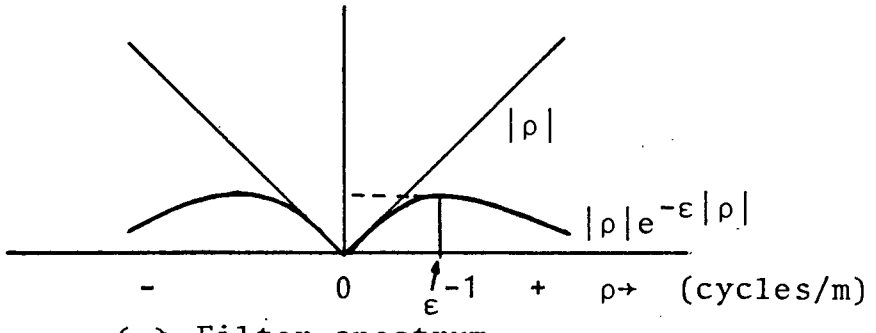

(a) Filter spectrum

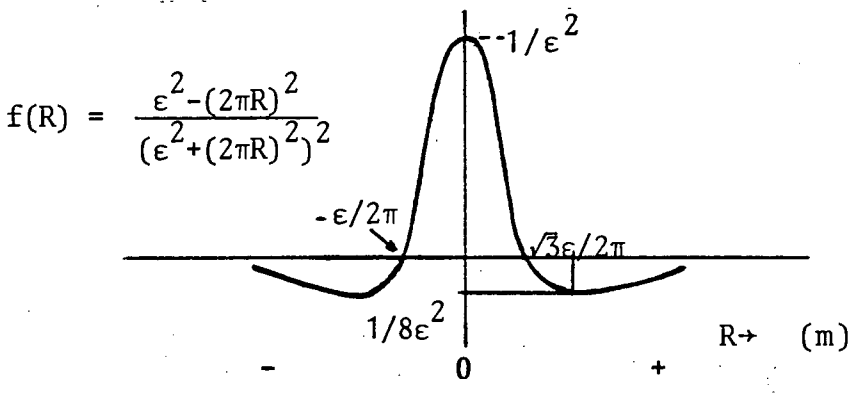

(b) Data domain filter

Fig. AIII.5 An approximation to the |ρ| filter

(after Scudder)

AIII.4 Experimental Microwave Tomography

The experimental geometry is shown in Fig.AIII.6. The microwave analogue signal processor was equipped with conventional horn radiators which were spaced as closely as possible. A cooperative target device (Appendix II) was placed opposite and the propagation path spanned the object region. This arrangement serependitiously both doubled the sensitivity compared to a single path system and required least disturbance of the existing signal processor. The cooperative target was no more than an available linear array with slots parallel to its long axis and measure of sidelobe control was inferred from the tapered slot excitation pattern. The array was at one end terminated by a simulated open circuit in the plane of the last slot, and at the other by a diode shunt switch and short circuit. The device reflected incident continuous wave (CW) illumination in an essentially DSBSC format. In addition to the normal advantages of the cooperative devices of this sort, the system inherently discriminated against reflections from the object interfaces.

A necessary property of a tomographic imaging system is high linear resolution. For a true three-dimensional imaging system, a narrow beam is required in the scan direction as well as normal to this direction and the object region. The object was translated past the source/receiver and cooperative target at aspect angles of 0^{o} to 90^{o} in steps of $22\frac{1}{2}^{o}$, as this was operationally more stable than moving the microwave hardware. A record of incident beam phase fluctuations corresponding to detail in a "phase" object of small depth in the beam direction can be obtained with arbitrarily high resolution using a small aperture surface probe; however, diffraction effects dictate that the projection data will be complicated by an impulse response which will be a function of along-beam position for objects having appreciable depth. A large aperture cooperative target brought to focus in the object region could provide high beam resolution but at the expense of depth of focus. Similar systems have been designed

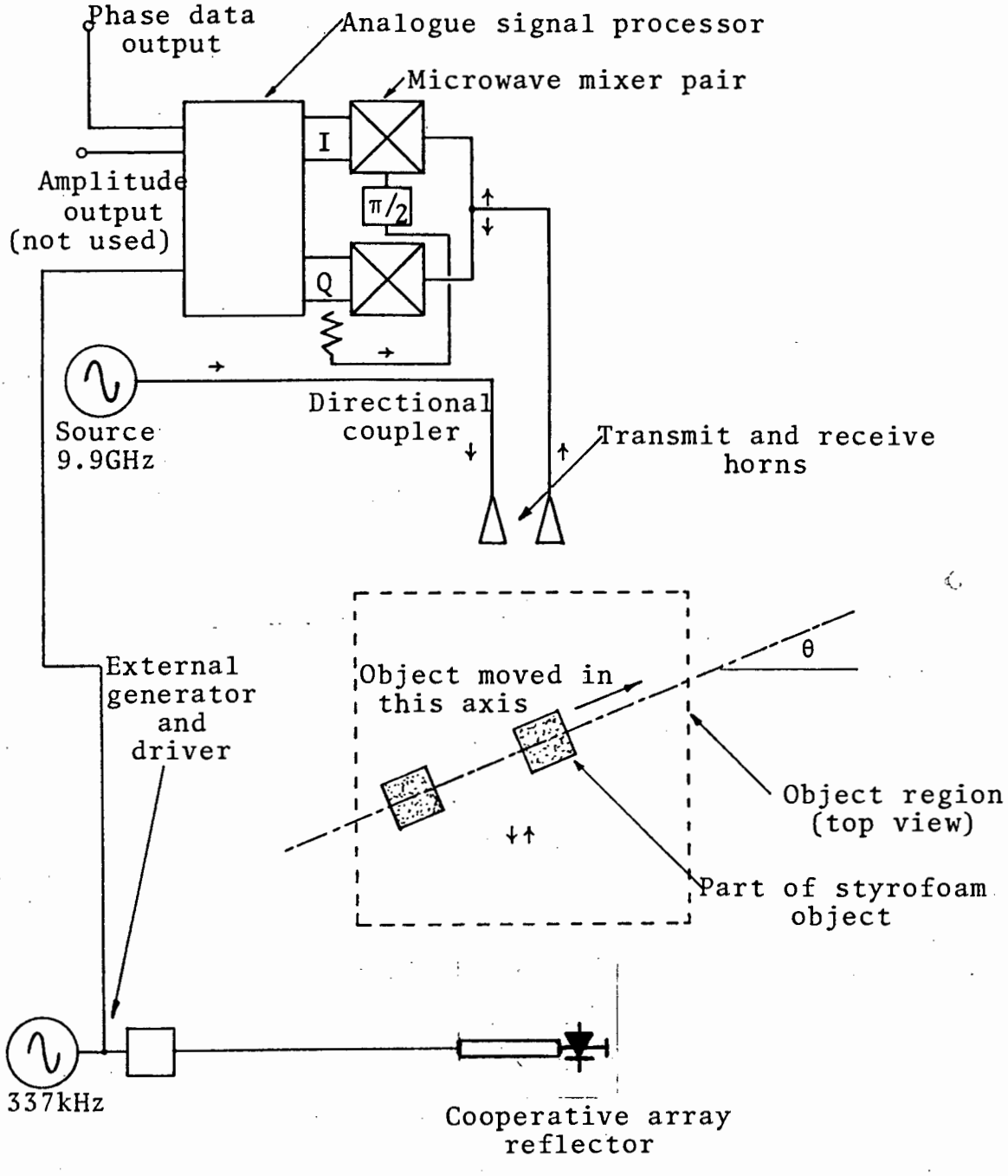

Fig. AIII.6 Experimental microwave tomography

for acoustic microscopy of "phase" objects where object depth is an insignificant parameter.[138]

The stratagem finally adopted was to choose object dimensions sufficiently large that the cooperative target lay essentially within the object near field. The projection data can be expected to be the "shadow" of the phase fluctuations imposed by the object on the source wavefront. Near-field projections were expected to be tolerant of object along-beam position. An attempt was made to extend linear resolution to smaller details within an object by physically narrowing the beam reflected from the cooperative target as much as possible consistent with the requirements of focal depth. The available linear slotted array had 220mm aperture, and with operation at a wavelength λ=30.3mm, about d^2/λ=1.6m depth of focus was available.(d is the aperture dimension.)

AIII.4.1 System Sensitivity

Preliminary testing was undertaken to determine the expected range of differential phase shifts for sample sheet polystyrene foam objects. The system had an unambiguous range of 0 to 2π radians (corresponding to an analogue output of 0 to 8.15 volts). A foam sheet one free space wavelength thick resulted in approximately 3^{o} differential phase shift when obscuring either source or receiver horns, but resulted in 5.5^{o} when totally obscuring the cooperative target aperture. These measurements are of the mean value of a few seconds' recorded phase, and are subject to 10% uncertainty. The foam relative dielectric constant is thus calculated as 1.015±.001 and taken as real. The signal attenuation through the foam was not measurable.

AIII.4.2 Linear Resolution of Overall System

Extracting the system impulse response in any domain by direct means is normally accomplished by specifying a pulse spectrum sufficiently broad to include the highest expected frequencies

in the transfer function. In this case, however, indefinite narrowing of the test object's dimensions will tend to produce projections outside the system's terms of reference. (sec.AIII.4) Fig.AIII.7 shows projection data produced using two foam blocks each 100mm square and 250mm high, standing on the small end and spaced by 200mm. The limited object depth means that the data represents beam cross-section convolved with an object which is essentially two-dimensional and smaller in cross-section than the expected beam profile. A conservative estimate of the half-height system resolution is 150mm. If furthermore the system impulse response is considered to be that of a Gaussian beam profile, then the system transfer function -3dB response is reached at $2.1m^{-1}$, and the 50% response is reached at $2.9m^{-1}$.

AIII.4.3 Reconstruction from Projection Data

The theoretical discussion of tomographic imaging has derived both system impulse response and the various compensation schemes available. The reconstruction strategy deconvolved projection data before backprojection-and-summation. Both operations are linear and operation order may be changed. Barrett and Swindell[135] have summarised the various equivalent backprojection and filtering stratagems, and have concluded that data deconvolution before summation of interpolated functions is most convenient. Furthermore, no Fourier domain excursions are required and the chosen operation order requires only one dimensional deconvolution although the output image after summation is two-dimensional.

The deconvolution kernel chosen was basically that of Fig.AIII.5(b), with the addition of a scaling factor ϵ^2 to control image dynamic range as the kernel width was varied. The second operation involved summation of successive backprojected data linearly interpolated to fit the underlying square data sampling grid. Truncation of backprojections beyond the 21 x 21 data grid was performed.

- Sample increment is 50mm -

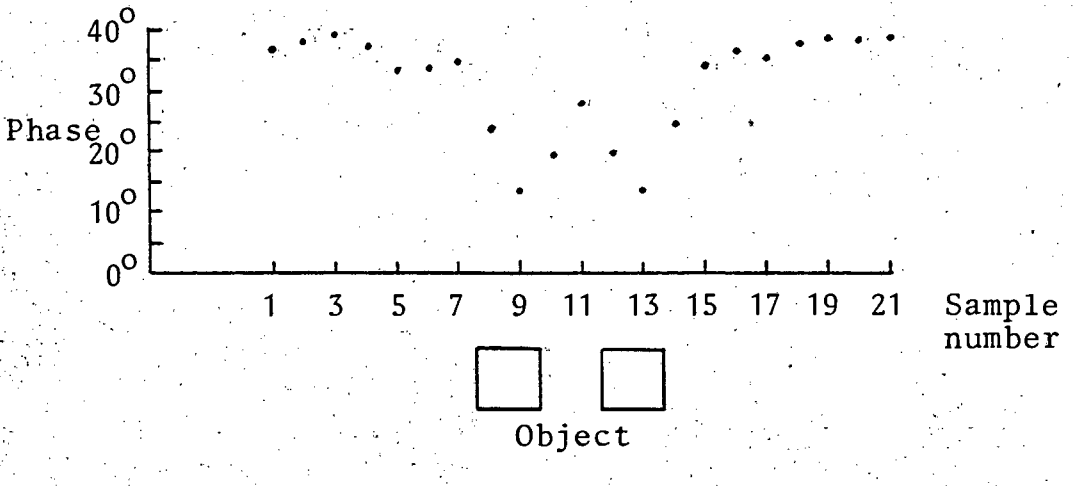

Fig. AIII.7 Projection data from two block object

Two objects were chosen for investigation by microwave tomography. Forsimplicity, they were symmetrical, as this eased data collection. Data for aspect angles greater than 90^{o} were obtained by re-ordering previous projections. Three projections were thus synthesised, covering $112\frac{1}{2}^{o}$ to $157\frac{1}{2}^{o}$. Transmission phase offsets were taken at 80mm intervals, with the mean of about ten seconds' recording subtracted from the mean phase recorded in the absence of the object. Each projection covered 1.6m in 21 samples. The simpler object comprised two styrofoam pillars 200mm square and 370mm high, elevated sufficiently to intersect the beam centreline. The pillars were spaced 590mm between centres. The corresponding backprojected-and-summed image without filtering (Fig.AIII.8(a)) is seen to possess rather more extended sidelobes than that image resulting from a filtering operation optimised in an empirical manner.(Fig.AIII.8(b)) The images have been linearly quantised to five levels and linearly stretched to this scale after every filtering operation. The pillar spacing in the latter figure is 90% of the correct value, and the resolution of the two individual pillars is markedly better than in the unfiltered image. Fig.AIII.8(c) shows the form of the deconvolving function used. The second object was a styrofoam box, rectangular in shape , 760mm long and 600mm wide and it had 40mm thick walls. The depth of the box was 300mm. Unfiltered and filtered backprojection images are shown in Figs. AIII.9(a) and (b) respectively; in this case the deconvolving operation has been less effective. The box size indicated in the image (720 x 560mm) is within one sampling unit of the correct values and the walls are represented as about two units thick, or 160mm. This is close to the estimated system resolution.(sec.AIII.4.2) In addition, the box interior is not excessively cluttered. The vertical and horizontal lines extending through the image seem to have been caused by reflection from a paper covering on these two sides as the beam incidence angle approached 90^{o}. This effect has emphasised the right vertical and lower horizontal walls and extended image contrast.

- . : # 1 2
  1 2 3 4 5 Image amplitude code -

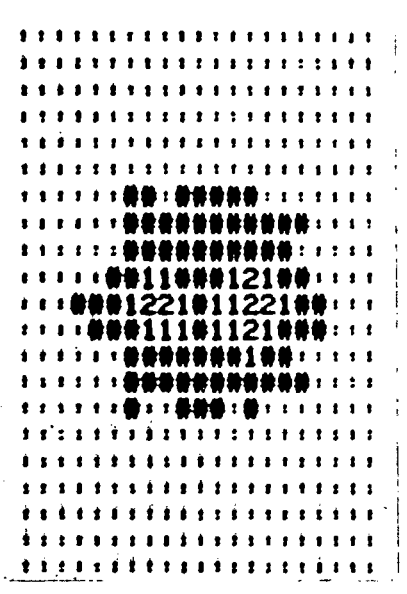

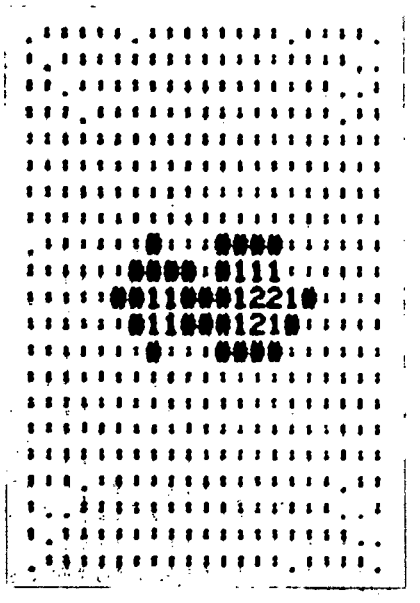

2-block object (to scale)

Fig. AIII.8(a) Backprojected-and-summed image

Fig. AIII.8(b) Deconvolved image

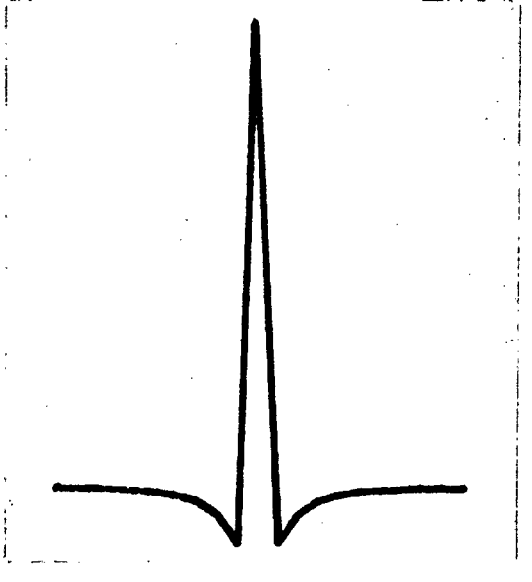

Fig. AIII.8(c) Deconvolution function used in Fig. AIII.8(b)

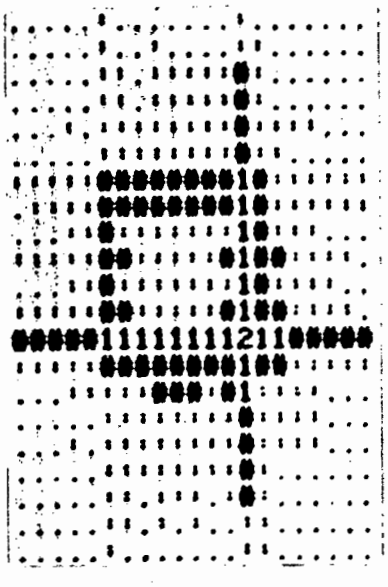

Fig. AIII.9(a) Backprojected-and-summed image

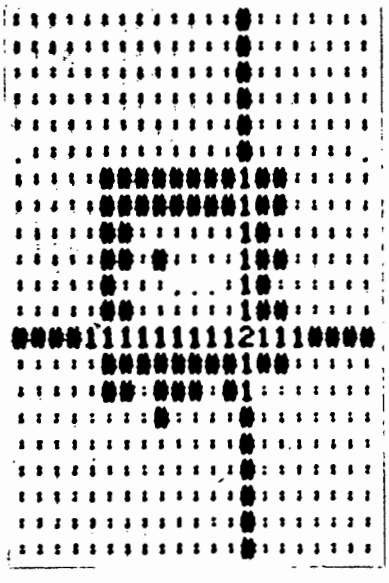

Fig. AIII.9(b) Deconvolved image

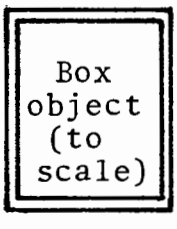

The deconvolving function (Fig.AIII.8(c)) was used with various values of ε (where $1/\varepsilon$ is the frequency of peak response) and the function which optimised the resolution of the two pillar object was also applied to the box image reconstruction operation. The optimum value of ε was 3.63 units which corresponded to 290mm, and implies a peak spatial frequency response at $3.4m^{-1}$. Comparative transfer functions of both system (assuming Gaussian beam profile) and the kernel function are given in Fig.AIII.10. The sampling interval of 80mm is equivalent to a spatial frequency of $12.5m^{-1}$, and to avoid aliasing effects, transfer functions should have small amplitude above the Nyquist frequency of $6.25m^{-1}$. Although the system transfer function has low (4%) amplitude at the Nyquist frequency, that of the compensating filter is hardly diminished (80%) at the same frequency compared to its value at the frequency of peak response.

The aliasing could be reduced by choosing a kernel function having a strictly limited spectral extent; in this regard the Lakshminarayanan kernel[137] is superior, although aliasing effects must always be present if the kernel is of finite length. From Fig.AIII.10, the filtering operations explicitly and implicitly performed on the projection data can be summarised as follows: (a) Multiplication in the frequency domain by $|\rho|$ to correct the inherent low-pass nature of summed backprojection imaging,

(b) Multiplication in the same domain by $e^{-\varepsilon|\rho|}$ arising from apodisation, sampling and data noise requirements,

and (c) Multiplication in the same domain by $e^{-\frac{\alpha^2\rho^2}{2}}$ to account for the estimated transfer function due to an assumed Gaussian beam of given half-height. (α=64mm) Filtering operations (b) and (c) combine to reduce the image resolution that is available. In particular, (b) represents a lower cut-off frequency than (c) so that image resolution should not be expected to be as good as that in the data projections; unfortunately filter (b) is essential in that it serves to reduce aliasing effects.

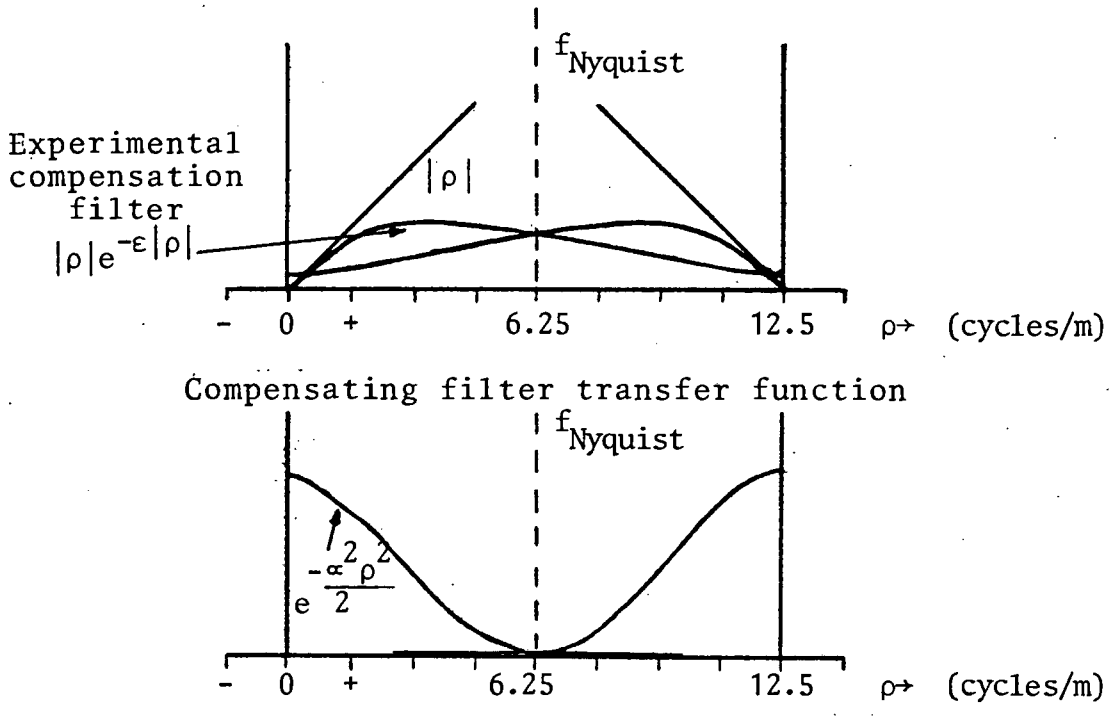

Fig. AIII.10 Experimental transfer functions for sampled data

AIII.4.4 Determination of Projection Angular Increment

The theoretical analysis of tomographic imaging assumed that a continuum of backprojections were available spread over 180^{o}. Obviously, real projection data must be angularly sampled in a practical numerically-based reconstruction. The analysis of the number of projection angles required for successful imaging of an object no bigger than D in largest dimension and containing spatial frequencies no higher than $M\ m^{-1}$ follows that advanced by Bracewell.[134] The object is considered determined if its two-dimensional Fourier transform is known at intervals D^{-1} on a rectangular lattice $M\ m^{-1}$ in radius.(Fig.AIII.11)

Assume N equi-angularly spaced projections are available, spread over 180^{o}. The transformed data is distributed along N diameters such that the frequency separation at the cut-off frequency M is no more than $\pi M/N\ m^{-1}$. Hence:

$$N > \pi MD \qquad \text{AIII.17}$$

The number of projections must be proportional to the spatial equivalent of the "time-bandwidth" product of the object. For the larger object used in sec.AIII.4.3, D was 760mm and linear resolution was about 150mm. Taking M as the 50% response point of $2.9m^{-1}$, then:

$$N > \pi .0.76 .2.9 \simeq 7 \qquad \text{AIII.18}$$

Experimentally, 5 real and 3 synthesised projections were distributed at $22\frac{1}{2}^{o}$ intervals over $157\frac{1}{2}^{o}$, which represents an adequate sampling density. The number of projections is small, but suffices to resolve the object quite adequately without compromising data resolution. Lindegaard-Andersen[136] found that the number of projections required for N^2 resolved picture elements to be about 1.5N. Applying this formula to the worst-case object dimension of 760mm and assuming 150mm resolution, then the 25 pixels describing the object need no more than 8 projections.

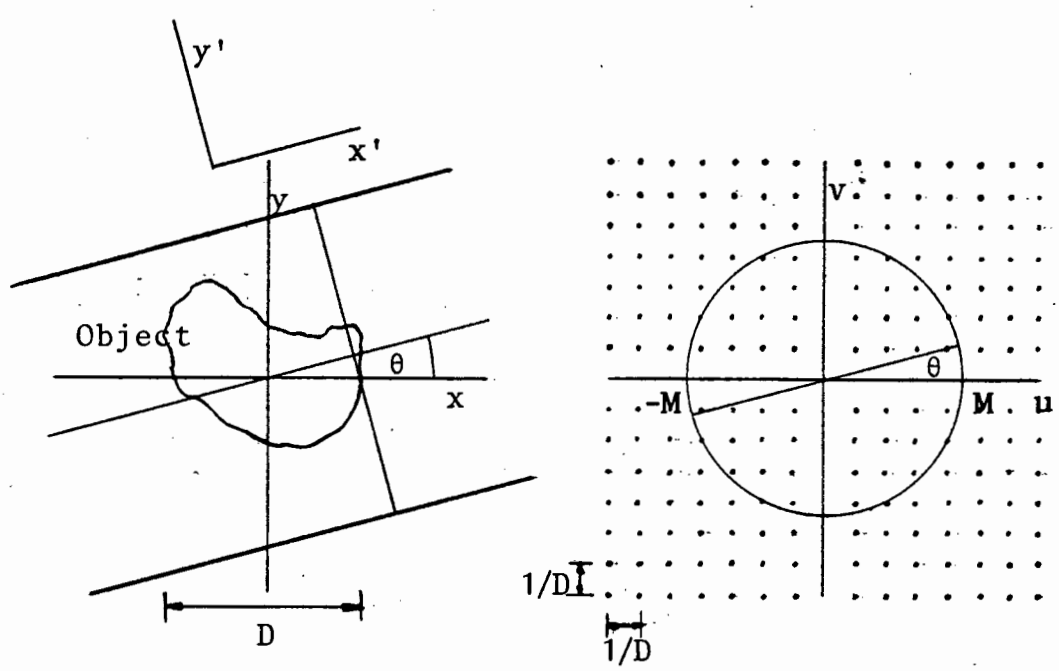

Generating projection data Spatial frequency plane

Fig. AIII.11 On the projection angular increment
(after Bracewell and Riddle)

AIII.5 Conclusion

A brief essay into microwave tomography has shown that imagery of "phase objects" not readily imaged by any system relying on reflected field processing may be imaged by recourse to tomography using complex transmision projection data.

Low frequency tomography is felt to be worthy of some attention since in this region quantum limitations on measurement accuracy are entirely negligible, both phase and amplitude information are usually available and safety considerations are much in favour of techniques using non-ionizing radiation of readily controllable strength. The disadvantages include initial ignorance of the propagation path in regions where characteristic impedances vary significantly (although this can be deduced by iterative techniques applied to successive image estimates[139]) and severely limited linear resolution by X-ray tomographic standards.

The choice of phase or amplitude information as the independent parameter in the projection data would be governed by the geometry of the object under investigation and the selection of operating frequency or frequencies. In regard to the latter pulsed emissions might be used to define linear resolution rather than relying on physical beamwidth of the interrogating antennae. An envisaged geometry uses a single source and distant receiver array; observation of the discrepancies in pulse arrival times among the array elements should yield information about the intervening object region using little more than a time domain reflectometry equipment. The requisite fan-beam could be derived from an established tomographic geometry.[137] Pulsed measurements need not be made explicitly if this is impractical, but could be realized by a posteriori Fourier decomposition of complex data (using a network analyser as a receiver) gathered over the frequency range appropriate to the required resolution.

An application of low frequency tomography in which some of the techniques suggested here may be useful and in which

limited resolution is satisfactory may be found in the plane imagery of sections of large structures such as buildings. Archeology might well be able to benefit from a non-invasive investigative technique, particularly as the characteristic "time constants" in this domain would allow low powered equipment to gather high quality data by observation over extended periods of time.